Etude d’un rotor d’hélicoptère sans plateau cyclique avec des servopaddles actives

Anne Brindejonc

To cite this version:

Anne Brindejonc. Etude d’un rotor d’hélicoptère sans plateau cyclique avec des servopaddles actives. Sciences de l’ingénieur [physics]. Arts et Métiers ParisTech, 2009. Français. NNT : 2009ENAM0037 . pastel-00005905

HAL Id: pastel-00005905
https://pastel.hal.science/pastel-00005905

Submitted on 1 Apr 2010

N°: 2009 ENAM 0037

Ecole doctorale n° 432 : Sciences des Métiers de l'Ingénieur

THÈSE

pour obtenir le grade de

Docteur
de
l'École Nationale Supérieure d'Arts et Métiers

Spécialité "Conception"

présentée et soutenue publiquement
par

Anne BRINDEJONC

le 15 Décembre 2009

ETUDE D'UN ROTOR D'HELICOPTERE SANS PLATEAU CYCLIQUE AVEC DES SERVOPADDLES ACTIVES

STUDY OF A SWASHPLATELESS HELICOPTER ROTOR WITH ACTIVE SERVOPADDLES

*Directeur de thèse : **Jean-Claude CARMONA***

*Co-encadrement de la thèse : François **MALBURET***

Jury :

Michel VERGÉ, Professeur, LMSP, Arts et Métiers ParisTech.. Examinateur
Marilena PAVEL, Assistant Professor, Department of AS & DM, T.U. Delft.................... Rapporteur
M. Yves GOURINAT, Professeur, Responsable de l'Unité de Formation SUPAERO de Mécanique, ISAE... Rapporteur
Rogelio FERRER, Docteur, EUROCOPTER .... Examinateur
André BARRACO, Professeur, LMSP, Arts et Métiers ParisTech .... Examinateur
François MALBURET, Maître de Conférences, LSIS, Arts et Métiers ParisTech.............. Examinateur
Jean-Claude CARMONA, Professeur, LSIS, Arts et Métiers ParisTech .... Examinateur
Oliver DIETERICH, EUROCOPTER.. Examinateur
Pierre-Antoine AUBOURG, Chef de département, EUROCOPTER................................. Invité

Laboratoire des Sciences de l'Information et des Systèmes
Arts et Métiers ParisTech, centre d'Aix-en-Provence

To my parents, to my
brother, my sister-in-law, my nephews and niece.

- ACKNOWLEDGMENTS -

I would like to thank the members of my examining committee, Prof. Michel Vergé, Prof. Marilena Pavel, Prof. Yves Gourinat, Prof. Jean-Claude Carmona, Maître de Conférence François Malburet, Dr. Rogelio Ferrer, Oliver Dieterich and Pierre-Antoine Aubourg for their time.

I would like to express my sincere gratitude towards Dr. Rogelio Ferrer from Eurocopter France for his guidance, advice and great help. He has been extremely generous with his time and resourceful with his suggestions. I would also like to thank Yves Favennec from Eurocopter France for the fundings he provided without which experimental testings would not have been performed. I thank Bernard Claret for his much appreciated advice and help on paddle manufacturing. Jacques Jauffret, Gaël Petillot and Yannick Unia for their support. I thank Pierre Berthié and Yves Coron who performed outdoors testings and provided me with great help and advice. I thank Oliver Dieterich, Bernhard Enenkl and Dieter Roth from Eurocopter Deutschland for taking time to listen to me and providing advice. Thanks to them, I had the great opportunity to examine the ADASYS rotor. I would like to acknowledge Tomasz Krysinski from Eurocopter France who provided the initial impetus for this research.

I would like to thank Gérard Coffignal for his professionalism and efficiency.

I owe a special thanks to Dr Jayant Sirohi for his great help, advice and patience without which, this thesis would not have materialized. I want to thank Dr. Anubhav Datta as well for his help and explanations.

My deepest thanks to my family - my parents, my brother and his wife have greatly supported me and provided encouragement and suggestions. I am also grateful to my friends, among whom Cédric for teaching me Survival 101, Guillaume for showing me how to put things into perspective, Julien for making me laugh and smile at all times, Sebastian for teaching me German, Bang, Laurène, Amélie, Chloé, Renata, Jayant, Arun and all the Bhaiyas, Maria, Karthik, Céline, Minica, Thibaut, Lionel, Abdou-Fadel, Frédéric, Vincent and Anne-Sylvie for all the discussions and support during difficult times. Finally, I would like to thank my three nephews: Marc, Benoît and Olivier, my niece Claire, my goddaughter Blanche and her siblings. I thank Paul for his Star Wars Lego that I dutifully kept under wraps for three years until the thesis reached its final stage.

Finally, I benefitted from my colleagues at the Ecole Nationale des Arts et Métiers and Eurocopter: Pierre-Antoine Aubourg, François Malburet, Jean-Claude Carmona, Claire Demassieux, Guillaume Roulois and Hervé

Morel.

It is impossible to remember all, and I apologize to those I have inadvertently left out.

Table of contents

List of Figures

Nomenclature

$ADASYS$	”ADAptive dynamische SYSteme” or adaptive dynamic systems.
ABC	Active Blace Concept.
AFR	Active Flap Rotor.
BVI	Blade Vortex Interaction.
c^A	Aileron section chord, m.
c^B	Blade section chord, m.
c^P	Paddle section chord, m.
c_{tot}	Paddle and aileron total chord, m.
CG	Center of gravity.
C_l	Lift coefficient, non-dimensional.
$C_{l\alpha}$	Blade lift curve slope, rad^{-1}.
$C_{l\delta}$	Aileron lift curve slope, rad^{-1}.
C_T	Rotor thrust coefficient, non-dimensional.
C_T/σ	Blade loading, non-dimensional.
dL	Elemental lift on a segment, N.
DOF	Degree of freedom.
dr	Beam segment width, m.
dy	Beam segment length, m.
$d\eta$	Aileron segment length, m.
e_β^B	Blade flap hinge offset, m.
e_θ^B	Blade pitch hinge offset, m.
e_β^P	Paddle flap hinge offset, m.
e_θ^P	Paddle flap hinge offset, m.
e_δ^A	Aileron pitch hinge offset, m.
F_b	Actuator blocked force, N.
FEM	Finite Element Method.
FM	Figure of Merit, non-dimensional.
HHC	Higher Harmonic Control.
I_β^B	Blade flapping inertia, kg/m^2.
I_β^P	Paddle flapping inertia, kg/m^2.

I_θ^B	Blade pitching inertia, kg/m^2.
I_θ^P	Paddle pitching inertia, kg/m^2.
I_a	Aileron pitching inertia, kg/m^2.
IBC	Individual Blade Control.
k_β^B	Blade flapping stiffness, Nm/rad.
k_β^P	Paddle flapping stiffness, Nm/rad.
k_θ^B	Blade pitching stiffness, Nm/rad.
k_θ^P	Paddle pitching stiffness, Nm/rad.
k_δ	Aileron pitching stiffness, Nm/rad.
k_{act}	Actuator stiffness, N/m.
LEF	Leading Edge Flap.
$MSMA$	Magnetic Shape Memory Alloy.
$MTOW$	Maximum Takeoff Weight.
M_b	Actuator blocked moment, N.
PZT	Piezoelectric material.
R^B	Rotor blade radius, m.
R^P	Paddle radius, m.
r	Paddle or blade or aileron segment radial location, m.
r_{in}	Aileron inboard radial location, m.
r_{out}	Aileron outboard radial location, m.
RPA	Rotor Pale Active or Active Blade Rotor.
S_β^B	Blade zeroth flap moment, Kg m.
S_β^P	Paddle zeroth flap moment, Kg m.
S_θ^B	Blade zeroth torsional moment, Kg m.
S_θ^P	Paddle zeroth torsional moment, Kg m.
S_a	Aileron zeroth torsional moment, Kg m.
$\bar{S}_\beta^B$	Blade first flap moment, Kg m.
$\bar{S}_\beta^P$	Paddle first flap moment, Kg m.
$\bar{S}_\theta^B$	Blade first torsional moment, Kg m.
$\bar{S}_\theta^P$	Paddle first torsional moment, Kg m.
$\bar{S}_a$	Aileron first torsional moment, Kg m.
$SHARCS$	Smart Hybrid Active Rotor Control System.
TEF	Trailing Edge Flap.
UAV	Unmanned Aerial Vehicule.
y	Distance between the paddle pitch axis and the chordwise element of the spanwise segment considered, m.
y_{CG}^P	Center of gravity location of the paddle segment considered, m.
$y_{CG}^{P,A}$	Center of gravity location of the paddle and aileron segment considered, m.
α	Angle of attack, deg.
β_{1s}	Lateral flapping angle.

β^B	Blade flap angle, deg.
β^P	Paddle flap angle, deg.
δ	Aileron deflection angle, deg.
η	Distance between the aileron hinge axis and chordwise element of the considered spanwise segment of the aileron, m.
η_{CG}	Center of gravity location of the considered aileron segment. Distance taken from the aileron hinge, m.
σ	Rotor solidity, non-dimensional.
θ_{1c}	Lateral cyclic pitch.
θ^B	Blade pitch angle, deg.
θ^P	Paddle pitch angle, deg.
ϕ	Aerodynamic angle, deg.
Ω	Blade rotational speed, RPM.
ρ_A	Mass per unit area of the aileron, kg/m^2.
ρ_B	Mass per unit area of the blade, kg/m^2.
ρ_P	Mass per unit area of the paddle, kg/m^2.

- Part I -

Basic Principles

Cette partie a pour but de situer la thèse dans le contexte aérodynamique, dynamique et mécanique de la conception des rotors d'hélicoptère. Elle situe en particulier la thèse par rapport aux travaux antérieurs, définit ses enjeux et rappelle sa contribution novatrice avant d'expliciter l'articulation de la thèse.

The present thesis deals with helicopter rotor design and involves aerodynamic, dynamic and mechanical aspects. In this first part, the state of the art is presented as well as the contributions from the present work. Finally, the thesis outline is exposed.

Chapter 1

Introduction

L'hélicoptère offre des capacités de vol uniques par rapport à d'autres types d'aéronefs, tels que les avions. Malgré de multiples progrès technologiques, de nombreux défis restent à résoudre concernant la stabilité et l'optimisation globale des hélicoptères. Le rotor principal permet d'assurer sa sustentation et son évolution dans l'espace, il est un élément fondamental et toujours un point clef pour les hélicoptéristes. La commande du rotor est la commande de la norme de la direction du vecteur de portance du rotor, c'est à dire la commande des angles du pas collectifs et cycliques de toutes les pales. C'est une fonction fondamentale car elle permet de réaliser toutes sortes de manoeuvres et donc de couvrir tous les cas de l'enveloppe de vol. Sa seule présence conditionne le décollage et la sustentation de l'appareil. Dans la majorité des hélicoptères conventionnels, cette commande est réalisée par un mécanisme appelé plateaux cycliques. Ces plateaux cycliques sont au nombre de deux, l'un est fixe en rotation tandis que l'autre tourne avec le mât rotor. L'ensemble des deux plateaux peut translater suivant le mât rotor. Ce dernier est connecté aux pales par des bielles de pas. Les plateaux sont actionnés par trois actionneurs. Si les actionneurs transmettent tous la même entrée au même moment, alors les plateaux translatent verticalement et le pas collectif de toutes les pales varie de la même manière. Si les actionneurs impriment une inclinaison aux plateaux, il en résulte une variation cyclique du pas de chaque pale à chaque rotation. A cause des efforts importants à supporter, on utilise aujourd'hui des servocommandes hydrauliques comme actionneurs.

Inventé par Boris Yuriev en 1910, les plateaux cycliques ont été ensuite incorporés par Sikorsky dans les premiers hélicoptères produits en grande série. Depuis, la plupart des hélicoptères commercialisés ont des plateaux cycliques. Ce concept a été bien étudié et son utilisation est très largement répandue, cependant il représente un mécanisme encombrant, lourd, complexe mécaniquement et coûteux. Il est formé d'un nombre important de pièces mobiles, sa maintenance est donc importante. D'un point de vue aérodynamique, il engendre une traînée importante: il représente avec le moyeu et le mât rotor, 35 % de la traînée totale d'un hélicoptère conventionnel.

L'élimination des plateaux cycliques et de leur actionnement hydraulique permettrait d'améliorer les performances de l'hélicoptère, notamment en réduisant son poids à vide, en diminuant la traînée parasite, en réduisant le nombre de pièces mobiles ainsi que les exigences de maintenance et la consommation de carburant. Les coûts d'acquisition et d'exploitation devraient également être réduits. Eurocopter a lancé un programme appelé *"hélicoptère vert" mettant l'accent sur toutes améliorations potentielles de l'hélicoptère afin qu'il ait un impact réduit sur l'environnement dans lequel il opère. Le travail présenté dans cette thèse devant mener à une diminution de la consommation de carburant, il a été inclus dans ce programme. Le concept proposé pour assurer une commande du rotor est appelé " rotor vert". Les nombreux avantages qu'un tel concept offre ont suscité un intérêt considérable pour la conception et le développement d'un rotor sans plateaux cycliques. La solution doit inclure la possibilité de mettre l'actionneur dans le système tournant pour éviter ce transfert mécanique entre le repère fixe et le repère tournant. L'actionneur a pour objectif de modifier l'incidence d'une partie de la surface aérodynamique assurant la portance.*

L'état de l'art montre qu'il existe des systèmes qui sont généralement utilisés pour la réduction des vibrations et du bruit, donc à d'autres valeurs de fréquences ou d'efforts que le système qui nous intéresse. On observe que ces systèmes utilisent souvent comme actionneurs des matériaux intelligents de types piezo-électrique implantés dans le repère tournant. Ces applications concernent la plupart du temps la commande du pas de la pale le long de son envergure ou en son pied par des bielles de pas de longueur variable (Ref. [2]) afin d'agir sur les charges aérodynamiques de la pale en fonction de son azimut. Ces techniques ont été appliquées sur des hélicoptères à l'échelle 1 (Ref. [3, 4, 5, 6, 7]) ou encore à l'échelle réduite (Ref. [8, 9, 10]). Beaucoup de concepts à petite échelle ne peuvent pas être implémentés à l'échelle 1 sans entraîner une augmentation importante du poids, ainsi que des problèmes de géométrie d'actionneurs et d'intégration à la pale. Il est important de noter qu'aucun hélicoptère sans plateaux cycliques n'a encore volé à l'échelle 1. Les différentes sortes de matériaux intelligents utilisés dans le cadre de ces études sont décrites dans ce chapître. Un modèle analytique est crucial au développement d'un concept visant à la commande du rotor car il permet d'en évaluer le comportement dynamique. Plusieurs analyses ont été développées pour étudier le comportement de diverses architectures pouvant réaliser la commande du rotor (Ref. [11, 12]). La représentation des charges aérodynamiques instationnaires est importante afin de prédire précisément la stabilité et les réponses aéroélastiques du système. Certaines méthodes utilisent par exemple les fonctions indicielles pour étudier ces charges aérodynamiques instationnaires. Il est intéressant de considérer les coefficients aérodynamiques de la théorie que Theodorsen a développée dans le cadre d'une étude sur le flottement (Ref. [13, 14, 15]). En effet ces coefficients sont fonction de la géométrie du système: ils intègrent par exemple la corde de la palette et de l'aileron ou encore la position de l'axe de rotation de l'aileron.

La commande du rotor exige des forces aérodynamiques beaucoup plus importantes que celles requises pour la réduction des vibrations. Par conséquent, ces efforts impliquent généralement une augmentation importante de la taille des gouvernes et des actionneurs piezo-électriques sur la pale. Incorporer des actionneurs et gouvernes de grandes tailles dans les pales de rotor pose des problèmes d'équilibre, de stabilité aéroélastique ou encore d'influence de l'actionneur. En outre, il est difficile de maintenir l'intégrité structurelle et la maintenabilité sur une longue période de temps d'une pale avec de grandes découpes pour accueillir les actionneurs et les gouvernes. Pour surmonter ces problèmes, il est souhaitable d'élaborer un concept de rotor qui minimise *ou ne provoque aucun changement de structure de la pale. Une manière d'y parvenir passe par un actionnement direct du pas de la pale en pied de pale. Cependant, ce concept nécessite des actionneurs de très haute puissance. En outre, les actionneurs doivent être très fiables car ils représentent des composants critiques du vol. Une autre approche serait d'utiliser de plus petites gouvernes aérodynamiques, nommées palettes, afin de parvenir à un changement de pas des pales par un effet de couplage.*

L'évaluation de ce nouveau concept à l'échelle 1 en vue de l'introduire dans la production d'hélicoptères, requiert un large éventail d'analyses à développer pour affiner sa représentation et étudier toutes les conditions de vol relatives à cet hélicopère. Ces études analytiques doivent être suivies et validées par des tests systématiques à différentes échelles. Chaque étape, l'analyse doit être validée par des expériences. L'analyse ainsi validée sera ensuite utilisée pour prédire le comportement du système lors des prochaines étapes expérimentales. L'architecture et une analyse de la dynamique du rotor à petite échelle doivent d'abord être validées par des tests en vol stationnaire, et ensuite par des essais en vol avant. Après la validation de l'analyse, une étude paramétrique doit être réalisée afin de déterminer la configuration optimum des pales et des palettes pour le développement d'un système à l'échelle 1. A ce stade, un algorithme de commande approprié doit être développé pour actionner les palettes et doit être incorporé dans le système de commande de vol. Les pales à grande échelle doivent être testées en vol stationnaire et en vol avant, avec en parallèle une validation de l'analyse. Le développement des pales à grande échelle implique une évaluation minutieuse de l'actionneur en fonction, par exemple, des fréquences et efforts requis. A ce stade, une décision peut être faite concernant le type d'actionneurs piézo-électrique ou électromagné-tique - requis pour le système. Une évaluation de la fiabilité et la maintenabilité doit également être menée à ce stade. Ce développement systématique devrait déboucher sur des essais en vol du concept sur un hélicoptère Ecureuil. La présente recherche jette les bases de ce développement en termes de modèle analytique aéroélastique et de tests d'un rotor d'échelle réduite en vol stationnaire. L'architecture choisie comprend deux pales, deux palettes et deux ailerons actionnés par des actionneurs piezo-électriques. Un couplage, entre l'angle de battement de la palette et l'angle de pas de la pale, est conçu en s'inspirant du concept des servopaddles de Hiller (Ref. [16, 17]). Les palettes sont situées dans le même plan que les pales, à 90° d'azimut avant par rapport à leur pale respective. Chaque aileron est positionné derrière le bord de fuite d'une palette. Quand l'actionneur fait défléchir l'aileron, une portance est générée qui résulte en un moment en pas autour de l'axe de pas de la palette. L'angle de pas de la palette varie donc ainsi que sa propre portance. Par conséquent, l'angle de battement de la palette change. Grâce au couplage mentionné plus haut, l'angle de pas de la pale varie. Comme chaque palette est indépendante de l'autre, la commande du pas collectif et cyclique de la pale est réalisée.

Les apports de la présente recherche sont nombreux. En effet, l'architecture proposée pour le rotor vert est novatrice et elle utilise des actionneurs intelligents, non pas pour la réduction des vibrations comme nombres de précédentes investigations, mais pour effectuer la commande du rotor. En outre, le rotor vert n'est pas équipé de plateaux cycliques comme l'est celui de Kaman (Refs. [18, 19, 20, 21]). Alors que la plupart des précédentes investigations *menées pour effectuer la commande du rotor impliquent de lourds et coûteux changements de conception de pale, dans le cas du rotor vert, la pale reste inchangée par rapport aux rotors conventionnels. Ceci permet de préserver l'intégrité structurelle de la pale. L'analyse développée pour prédire le comportement dynamique du système en vol stationnaire utilise la théorie de Theodorsen pour écrire les coefficients aérodynamiques en fonction de la géométrie du mécanisme.*

Cette thèse est composée de cinq chapitres.

1. *Le "Chapitre 1-Introduction" fournit une description du problème, un état-de-l'art du sujet et détaille la contribution qu'apporte la présente étude.*
2. *Le "Chapitre 2-Principes de fonctionnement" traite des principes physiques impliqués dans le fonctionnement du nouveau concept proposé pour réaliser la commande du rotor principal.*
3. *Le "Chapitre 3-Modèles analytiques" décrit les deux modèles analytiques développés afin de prédire le comportement dynamique du système en vol stationnaire.*
4. *Le "Chapitre 4-Expériences, résultats et discussion" présente la maquette de modélisme de petite échelle utilisée après modification lors de tests en extérieur et dans un banc rotor principal. Les vols en extérieur ont été réalisés afin de démontrer la faisabilité du concept en vol stationnaire. Les essais au banc rotor principal permettent de faire tourner le rotor dans un environnement plus maîtrisé et d'obtenir des résultats expérimentaux afin de valider l'analyse. Les difficultés rencontrées au cours de la mise en place et des phases d'essais sont décrites. Les résultats expérimentaux et les prédictions analytiques correspondantes sont comparés et discutés.*
5. *Le "Chapitre 5-Résumé, conclusions et activités futures" rappelle les principales caractéristiques de la conception proposée pour réaliser la commande du rotor. Les différentes études analytiques et expéri-mentales sont résumées. D'importantes conclusions sont tirées des résultats présentés. Enfin, des suggestions pour améliorer l'architecture du présent concept d'hélicoptère sans plateaux cycliques sont proposées. Les principales étapes pour développer ce concept sur un hélicoptère à grande échelle sont décrites.*

This chapter deals with the different aspects involved in swashplateless helicopter rotor primary control. Research on the following concepts are described: swashplateless rotor, primary control, blade control surfaces and smart actuators.

1.1 Problem statement

The helicopter offers unique flying capabilities over other kinds of aircrafts such as airplanes. However, many challenges remain to be solved regarding helicopter stability and overall optimization. While the main rotor produces thrust to counteract the aircraft weight, primary control is a fundamental function in a helicopter since it allows to perform all kinds of maneuvers thereby covering the whole flight envelop. Primary control consists of the magnitude and direction control of the rotor thrust vector.

- The magnitude of the rotor thrust depends on the lift generated by all blades. It is therefore controlled by the collective pitch of all the blades.
- The rotor thrust direction is perpendicular to the rotor tip path plane. Altering the tip path plane by tilting the hub of the shaft is not practical. On conventional helicopters, it is thus achieved by tilting a mechanical swashplate. The swashplate transfers blade pitch control inputs from the non-rotating frame to the rotating frame. Hence the inclined swashplate transmits different cyclic pitches to the blades depending on their azimuth thereby tilting the tip path plane.

Therefore, rotor primary control consists of collective and cyclic pitch control of all blades.

1.2 Motivation

First invented by Boris Yuriev in 1910, the swashplate was subsequently incorporated in mass-produced helicopters by Sikorsky. Since then, most of the commercialized helicopters by Kaman, Eurocopter or Sikorsky for instance, have featured a swashplate (Ref. [19, 21]). While this concept has been well studied and its utilization is widely spread, it is a bulky, heavy and mechanically complex mechanism and has a large number of moving parts. As a result, it is maintenance intensive, and is a significant contributor to the parasite drag of the helicopter. Prouty (Ref. [22]) and Leishman (Ref. [1]) estimate the swashplate along with the hub and shaft account for 35% of the entire aircraft parasitic drag.

Therefore, eliminating the mechanical swashplate and its hydraulic actuation, and introducing control inputs directly into the rotating frame, is expected to yield significant performance benefits. Such a swashplateless rotor is supposed to decrease the empty weight of the helicopter, decrease the parasite drag, decrease part count as well as maintenance requirements and reduce fuel consumption [1]. Moreover, acquisition and operating costs should also be reduced. Because of the numerous advantages such a concept

---

[1] Eurocopter has launched a program focusing on what it calls"green helicopters". This program concentrates on all potential improvements of rotorcraft so they have less impact

offers, there has been considerable interest in the design and development of a novel swashplateless rotor.

Over the past few decades, several concepts have been proposed to directly affect the aerodynamic loads produced on the rotor blade by means of either discrete on-blade control surfaces, or by changing the twist of the blade. These concepts were initially studied in conjunction with conventional swashplate control to generate small aerodynamic forces superimposed on the main rotor thrust. These small forces could be controlled as a function of rotor blade span and rotor disk azimuth to achieve vibration and noise control. Analytical results indicated the effectiveness of such a technique for vibration control, however, due to the stringent volumetric constraints in the rotor blade section and the severe loads (centrifugal, vibration) experienced at the outboard sections of the blade, practical implementation of on-blade aerodynamic control was elusive.

Recently, significant improvements in actuator technology has resulted in viable means of rotor vibration control using both discrete on-blade control surfaces as well as active rotor blade twist. Two major helicopter manufacturers - Eurocopter and Boeing have built and successfully tested full scale helicopter rotors with discrete flaps mounted at the trailing edge of the rotor blades. Eurocopter has also flight tested a helicopter with an active rotor system and demonstrated a substantial decrease in vibration. The flaps in these rotors were actuated by piezoelectric actuators. Due to their high power density, minimum of moving parts and wide variety of shapes, piezoelectric actuators are ideally suited for the application of on-blade control surface actuation. A number of piezoelectric actuator configurations have been developed over the past decade, and numerous researchers have used these actuators in experimental studies of active rotors at both small model scale and full scale. A special type of piezoelectric fiber based actuator has also been used as an 'active ply' integral with the composite skin of the rotor blades, to achieve active twist variation along the rotor blade span. However, these active twist blades have only been tested in small scale models due to the large increase in weight at full scale. In general, it has been observed that a given piezoelectric actuator configuration that works well in small scale models cannot be scaled up directly to full scale due to weight and blade integration issues. Similarly, an actuator that works well in full scale cannot be reduced in size to model scale. Therefore, scale model blades and

---

on the environment they operate in. Among the studies integrated into the program, some for instance investigate ways to reduce fuel consumption. Since the present work is expected to decrease fuel consumption, it is included in the Eurocopter green helicopter program. Hence, in the rest of the present thesis, the proposed concept to achieve primary control is called “green rotor”.

full scale blades typically use different piezoelectric actuator configurations.

While vibration control using rotors with piezoelectrically actuated trailing edge flaps has been proven, these rotors have a mechanical swashplate for primary control. Recent research efforts are focused on extending the on-blade actuation concept to achieve primary control without a swashplate. However, primary control requires much larger aerodynamic forces than that required for vibration control. Therefore, these efforts have typically involved a significant increase in the size of the on-blade control surfaces as well as the piezoelectric actuators. Incorporating such large actuators and control surfaces in the rotor blades result in several issues such as weight balance, aeroelastic stability and actuator control authority. In addition, it is challenging to maintain the structural integrity and maintainability over a long period of time of a blade with large cutouts to accomodate the actuators and control surfaces.

To overcome these issues, it is desirable to develop a swashplateless rotor control concept that minimizes or eliminates changes to the blade structure. One way to achieve this is by direct actuation of the blade root pitch. However, this concept require actuators with extremely high power density. In addition, such actuators must be very reliable because they are flight critical components. Another approach is to utilize smaller aerodynamic surfaces, or paddles, to achieve a change in blade pitch via a servo effect. This is similar to the servo paddle concept introduced by Hiller (Ref. [16, 17]) in the 50's to minimize the required rotor control forces. The present work is motivated by the servo paddle concept and the successful integration of actuators into the rotating frame. Accordingly, the present work describes a novel swashplateless rotor concept where the main blades are controlled by servo paddles. The servo paddles are controlled by means of on-blade trailing edge flaps with piezoactuators, thus eliminating the need for a mechanical swashplate. In addition, the important goal of retaining the existing blade structure is achieved.

The assessment of this novel concept for a full scale production helicopter such as the Ecureuil requires a wide range of analytical development followed by systematic testing at different scales. At each stage, the analysis needs to be validated by experiments. The validated analysis will then be used to predict the behavior of the system in the next stage of experiments. The design concept and physical principles of a servo paddle actuated rotor system must first be described. A detailed analysis of the dynamics of the system including unsteady aerodynamic effects, actuator dynamics and coupled blade-paddle response must be developed. Experiments must be performed on a small scale model in hover to validated the analysis. The scaled model should then be tested in forward flight. After validating the analysis, a parametric study must be performed to identify the optimum configuration of the blades and paddles for development of a full scale system. An appropriate controller must also be developed for actuating the paddles and must be incorporated into the flight control system. The full scale blades must be tested in hover and forward flight, in parallel with validation with the analysis. The development of full scale blades will involve a careful assessment of the actuator. At this stage a decision can be made regarding what kind of actuator - piezoelectric or electromagnetic - is required for the system. A reliability and maintainability assessment must also be conducted at this stage. This systematic development will culminate in flight testing of the concept on an Ecureuil helicopter. The present research effort lays the groundwork for this development in terms of the analytical aeroelastic model and the hover testing of a small scale rotor model.

1.3 Objectives of the Present Research

A novel rotor design, called “green rotor” hereafter, is envisaged to achieve primary control without any swashplate. The novel concept must be capable of providing both collective and cyclic pitch to the rotor blades. If viable, this system is expected to allow for implementation on the Ecureuil helicopter. The goals of the present research are to develop a novel swashplateless rotor concept that can be scaled up to full scale helicopters, to develop an analytical model of the system, and to demonstrate proof of concept on a small scale model.

Several architectures were considered to achieve primary control. A study was conducted on Kaman’s servoflaps that are located behind the blade trailing-edge, at around 75% of the blade radius. Kaman’s design still requires a swashplate (Ref. [19, 21]). Developing a swashplateless concept based on Kaman’s servoflap to achieve primary control would mean the outboard servoflap location would cause significant centrifugal load on any actuation system placed in the rotating frame to eliminate the swashplate and it would also imply dramatic blade design changes to accomodate for the actuation system to reach the servoflap. Therefore, this type of architecture was not retained to achieve blade collective and cyclic control without a swashplate.

Another concept was proposed to achieve primary control. It was inspired from the Hiller bar and addressed the shortcomings that a Kaman inspired concept would have involved. The Hiller bar configuration features two passive servopaddles, located close to the rotor hub, which provide pas-

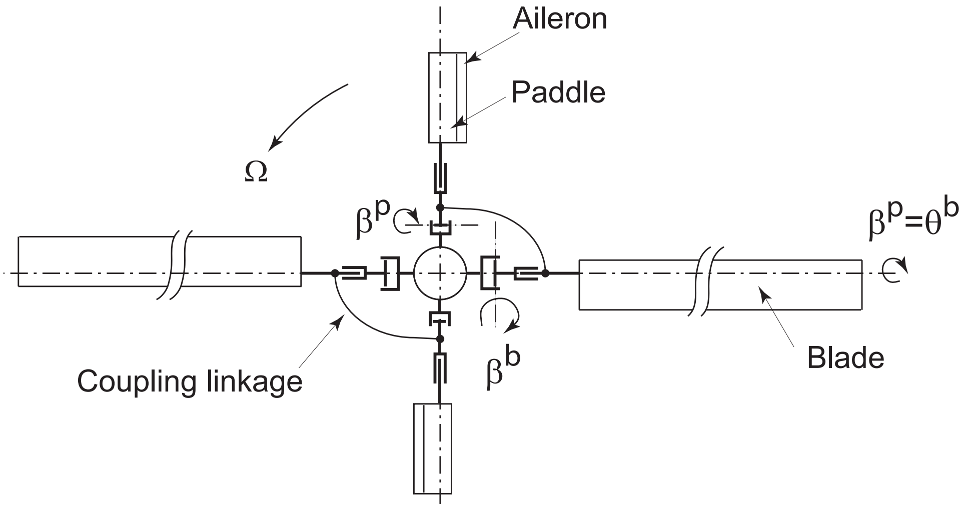

Figure 1.1: Schematic of the present swashplateless concept.

sive stabilization on full scale helicopters (Ref. [16, 17], model scale aircrafts (or RC models) and MAVs (Ref. [23]). This concept thus proves to be reliable at all scales. By replacing the passive servopaddles with actively controlled and independent paddles, all equipped with a piezoelectric-actuated aileron (see Fig. 1.1), it is envisaged that small control inputs can be introduced in the rotating frame to achieve swashplateless primary flight control. This concept was patented in 2008 (Ref. [24]). It presented the advantages of a low centrifugal load on the paddles, ailerons and actuation system and of no required blade design modifications. In addition, they could potentially be incorporated at low cost on existing full scale Ecureuil helicopters.

The servopaddle is coupled to a blade. When the piezoelectric actuator makes the aileron deflect, the aileron generates a lift. This, in turn, creates a pitching moment around the paddle feathering axis, thus making the paddle pitch vary. Hence, the paddle lift and flap angle change. Since the paddle flap and blade pitch are coupled, the blade pitch angle varies. In the case of a rotor with multiple blades, each paddle operates independently from the others. Therefore, the blades pitch angles are individually controlled by their correponding active servopaddle. The rotor primary control is thereby achieved.

This solution was retained and its ability to achieve primary control was studied. This chosen design consists of a two-bladed rotor along with two paddles, each equipped with an aileron. All lifting surfaces are located on the same plane. There is a 90° azimuth angle between a blade and its attached paddle. The objective of the present work is to assess the control authority of the paddle on the blade in hover flight. To this end, two analyses are developed to investigate the dynamic behavior of:

1. A two bladed rotor with two paddles commanded by piezoelectrically actuated aileron.
2. A two bladed rotor with two paddles commanded by a small swashplate.

Hover stand tests are performed to validate the latter analysis. This second method is then used to partially validate the first analysis in which only the paddle actuation differs.

1.4 State-Of-The-Art

The following section will describe the state-of-the-art of primary control and concepts using similar techniques on full scale aircraft, then for small scale applications. Most of these studies involve the use of smart materials. Hence, the main research in that field will be presented. Finally, the most significant analyses related to these topics will be exposed.

Achieving primary control was one the main challenges helicopter pioneers faced. Two concepts were developed early on: the swashplate and the servo-flap system. Most of the rotorcrafts developed and serialized today are based on the one or both of these mechanisms.

The different drawbacks of the swashplate were detailed in an earlier section. Because of numerous active rotor technology developments, there has been considerable interest in alternatives to the swashplate to alleviate the effects of its inherent drawbacks. Several different methods have been proposed to introduce control inputs directly in the rotating frame. These typically rely on blade pitch control, a change in the blade geometry, or variable length pitch links to affect the air loads on the blade as a function of azimuth. If ultimately all concepts are desired to be viable on full scale aircrafts for obvious economical reasons, only some of them have led to full scale applications. The following section focuses on the most significant ones.

1.4.1 Full scale applications

Several full scale helicopter rotors have been developed that generate a change in aerodynamic loads over the rotor blade by modifying the blade geometry. While most of these utilize a swashplate to achieve geometry change, some recent rotors use on-blade actuators. However, the on-blade actuators are designed to generate small changes in aerodynamic loads for vibration control. A review of recent developments in full scale helicopter rotors with on-blade control surfaces will yield considerable insight into the prefered swashplateless rotor design configuraiton.

Active-servo flaps in Kaman helicopters

A type of on-blade pitch control via control surfaces is the well known servo-flap. While introduced by d'Ascanio (Ref. [25]) in his co-axial helicopter, the servo-flap has become a staple feature in Kaman rotorcrafts and Unmanned Aerial Vehicules (UAVs) (Refs. [18, 19, 20, 21]). Figure. 1.2 shows a servo-flap on a K-Max helicopter. The servo-flap is located behind the blade trailing-edge, at apprimately 75% of the blade radius where it benefits from the lift peak. The flap is actuated by a swashplate via mechanical linkages running through the blade. This design involved exposed linkages located on the blade and hence generates significant amount of drag (Ref. [26]). This concept requires a soft in torsion rotor to ensure the servo-flap has enough control authority on the blade to achieve primary control. To fulfill this requirement, the rotor is equipped with soft torsional springs around the blades pitch bearings (Ref. [27]). The previous Kaman designs feature both advantages and drawbacks over conventional configurations with swashplates (Refs. [27, 28, 29]). In recent years, Kaman has focused on improved designs such as integrated flaps into the blades, improved airfoils (Refs. [28, 30, 31]). The wind tunnel tests that were performed showed performance improvements because of a reduced drag, increased lift and rotor control moments as well as a delayed stall (Ref. [32]).

The servo-flap remains in use in modern helicopters, however it still requires a swashplate as it utilizes mechanical linkages. Furthermore, the rotor instability issues created by the necessary soft in torsion rotor must be carefully assessed and dealt with (Ref. [33]).

Integrated ailerons

Another kind of on-blade surfaces are ailerons integrated into the blade. Two sorts exit: the leading-edge and trailing-edge flaps (LEF and TEF respectively). In most full scale cases, the TEF for instance are used to perform vibration and/or noise reduction. Similar basic techniques are used to achieve primary control. The main differences between primary and secondary control is that primary control requires an increased stroke and actuation and the targeted frequencies differ. Most of these full scale designs are equipped with smart actuators such as piezoelectric (PZT) actuators to

Figure 1.2: Close-up of the servo-flap on a K-Max helicopter by Kaman.

actuate the TEF. Figure. 1.3 presents the timeline of the main full scale active rotor projects. The design of these on-blade actuation systems is highly challenging due to the stringent volumetric constraints inside the blade cross-section, the large centrifugal loads due to the location of the actuator near the 75% span and the large deflections and vibrations occurring at the location of the actuators. In addition, the actuators integrated into the blade require additional balancing weights, which may result in a significant overall weight penalty.

Eurocopter France and Deutschland have led in-depth research to successfully perform vibration cancellation and blade-vortex-interaction (BVI) noise reduction on a full scale helicopter by means of :

1. First, electro-hydraulic blade pitch actuators replacing conventional pitch links. These actuators were of variable length. During flight tests, that design showed dramatic BVI noise reduction in descent flight (Ref. [35]) and significant vibration reduction in level flight (Ref. [36]). The controller developed for these investigations was then used in the ADASYS (Adaptive Dynamic Systems) research program at Eurocopter Deutschland which involve on-blade TEF to achieve vibration and noise reduction (Ref. [3, 4, 5]).
2. Second, Individual Blade Control (IBC) (see Section. 1.4.4) using PZT

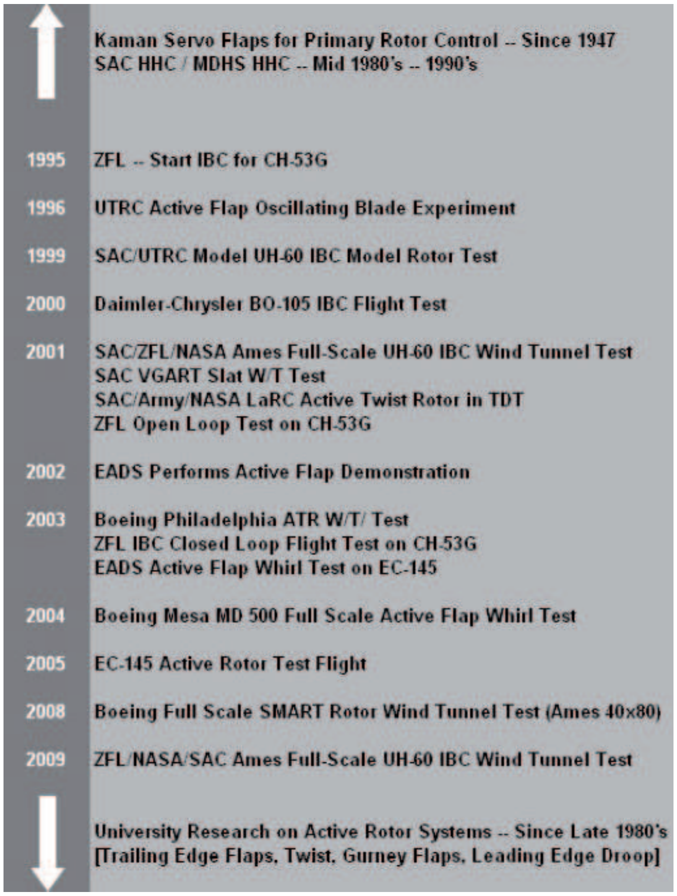

	Kaman Servo Flaps for Primary Rotor Control -- Since 1947 SAC HHC / MDHS HHC -- Mid 1980's -- 1990's
1995	ZFL -- Start IBC for CH-53G
1996	UTRC Active Flap Oscillating Blade Experiment
1999	SAC/UTRC Model UH-60 IBC Model Rotor Test
2000	Daimler-Chrysler BO-105 IBC Flight Test
2001	SAC/ZFL/NASA Ames Full-Scale UH-60 IBC Wind Tunnel Test SAC VGART Slat W/T Test SAC/Army/NASA LaRC Active Twist Rotor in TDT ZFL Open Loop Test on CH-53G
2002	EADS Performs Active Flap Demonstration
2003	Boeing Philadelphia ATR W/T/ Test ZFL IBC Closed Loop Flight Test on CH-53G EADS Active Flap Whirl Test on EC-145
2004	Boeing Mesa MD 500 Full Scale Active Flap Whirl Test
2005	EC-145 Active Rotor Test Flight
2008	Boeing Full Scale SMART Rotor Wind Tunnel Test (Ames 40x80)
2009	ZFL/NASA/SAC Ames Full-Scale UH-60 IBC Wind Tunnel Test
	University Research on Active Rotor Systems -- Since Late 1980's [Trailing Edge Flaps, Twist, Gurney Flaps, Leading Edge Droop]

Figure 1.3: Timeline of the main full scale active rotor projects over the last 15 years (Ref. [34]).

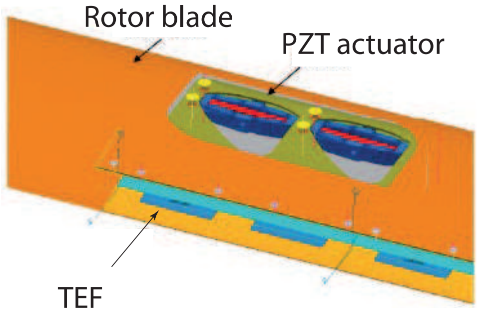

Figure 1.4: Piezoelectric actuators, on-blade trailing edge flaps on a $BK117$ main rotor blade. (Ref. [37])

actuated TEF (Ref. [37]).

In the latter case, two techniques were investigated to actuated on-blade flaps:

1. A PZT ceramic actuator called DWARF was used to actuated an integrated flap on modified $BK117$ blades. The flap chord was equal to 15% of the blade chord. The actuators and TEFs assembled on the blade are shown on Figure. 1.4. The modified $BK117$ flew for the first time with open loop control in 2005 (Ref. [4]).
2. An electromagnetic technology actuator called COCE was used to actuate a flap which chord was equal to 25% of the blade chord of a modified Dauphin helicopter.

The blade integration depended on the blade type and on the kind of actuator. It was observed that the energy density was greater in the case of the electromagnetic actuators. However, PZT actuator stiffness ensured no flutter would occure during flight.

The ADASYS program focused on active rotor control to perform vibration reduction and noise cancellation using on-blade PZT actuated TEF. The concept was implemented on a $BK117$ which features a 4-bladed rotor and a hingeless rotor hub. The ADASYS rotor blades were based on $EC145$ main rotor blades with advanced features such as ONERA airfoils and optimized planform. The blades were specially tailored so that the flap area could be customized with TEF modular design (Ref. [38, 39]). Depending on the chosen flap design, the stiffness, inertia and more generally blade aeroelastic and dynamic characteristics could vary. This in turn led to necessarily different blade tunning and varying lift and moment generated

Figure 1.5: $BK117$ with PZT actuated TEF to perform secondary control. (Ref. [4])

by the TEF. The blade torsional frequency was of $3.2/rev$ (Ref. [40])[2]. According to Ormiston (Ref. [41], see Section. 1.4.4), the torsional frequency should be considerably lower, in the neighborhood of $2/rev$, to ensure TEF control authority to achieve primary control. Wind-tunnel tests on a blade section equipped with embedded TEF were performed to establish the proof-of-concept of a PZT actuated TEF (Ref. [42]). Three different design parameters were considered and varied: the flap chord (Ref. [43]), span and radial location. Hover stand tests were carried out on the ADASYS rotor in 2004 and validated the chosen TEF design. In 2005, the first full scale active rotor flight ever was performed on a $BK117$ with open-looped PZT actuated flaps (see Figure. 1.5). The flight tests proved to be successful and brought considerable hindsight on the considerable influence of TEF radial location on vibration control effectiveness. Significant vibration reduction was achieved for moderate TEF actuation at airspeed of $60kts$ and $100kts$.

Further research was performed to assess if the ADASYS design could be used to perform primary control as well (Ref. [44], see Section. 1.4.4).

Eurocopter also worked on a full-scale active TEF using a piezo stack actuator with a shallow angle flextensional amplification mechanism (Ref. [45, 46, 47, 48]). The same concept was used to actuate a leading edge droop to delay dynamic stall (Ref. [49]).

Trailing edge flaps driven by on-blade hydraulic actuators have been tested on a Mach scaled model as part of an Active Rotor Control (ARC) test by Sikorsky (Ref. [6, 7]). The hydraulic fluid is supplied to the rotating frame through a hydraulic slip ring. State of the art servo-valves and custom

---

[2] In most papers, rotational speed values are not mentioned so that only non dimensional values are given in order to preserve confidential data. If the rotational speed in Hz is Ω_{Hz}, then $3.2/rev$ corresponds to a frequency of $(3.2 * \Omega_{Hz})$ Hz.

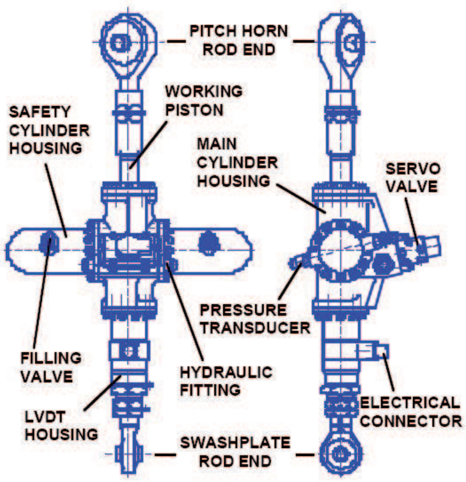

Figure 1.6: ZFL's IBC actuator schematic. (Ref. [50])

electronics enable operation of the hydraulic actuators at frequencies of upto 50 Hz. The Sikorsky research effort on active rotors is part of the Variable Geometry Rotor Technology (VGART) program, with the goal of developing next generation rotors with improved vibration and noise characteristics and enhanced performance. The rotor included a 20% chord TEF extending from 65% to 85% of the blade radius.

Arnold et. al. (Ref. [50, 2]) have developed active pitch links that can change their length and therefore change the blade pitch. Initially, a hydraulic actuator was designed (see Figure. 1.6). ZFL's hydaulic actuators were capable of providing up to 6° blade pitch input at 2/rev and ±1.6° at 7/rev. Full scale tests were later performed on a UH-60 equipped with ZFL's actuators in NASA Ames Research Center 24.38 by 36.58 m (i.e. 80 by 120 ft) wind tunnel. The goal of these experiments was to investigate the potential these actuators offered to achieve vibration and noise reduction as well as improved rotor performance. The IBC servo-mechanism, actuator characteristics and installation of into the US. Army/NASA Large Rotor Test Apparatus (LRTA) was described in Ref. [51]. The wind tunnel test showed that ZFL's concept was responsible for a 70% using 1° of 3/rev IBC and $12dB$ of BVI reduction. These hydraulic actuators have been only tested for vibration control, however primary flight control requires significantly larger actuators. In addition, the need for a hydraulic slip ring, as well as the bulky pitch links themselves, can result in an increase in maintenance requirements as well as parasite drag. Electrical actuators were then considered as a possible alternative to hydraulic actuators (Ref. [52, 2]). They would allow for the elimitation of the hydraulics from the aircraft

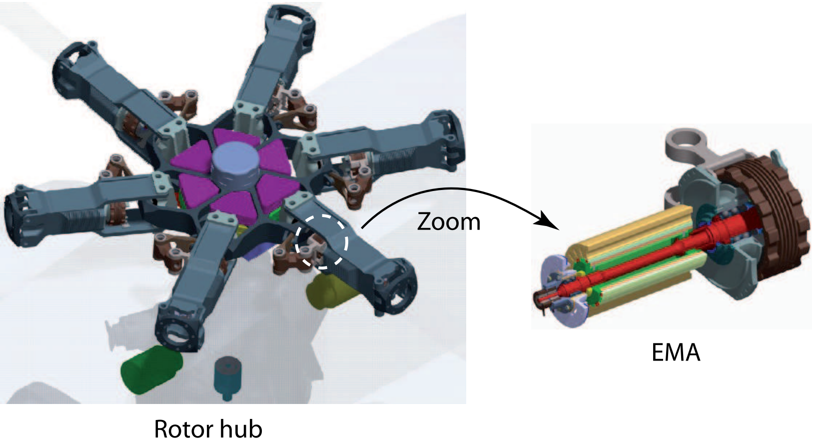

Figure 1.7: ZFL hub with integrated EMAs. (Ref. [50])

which would greatly reduce its weight. Electro-mechanical actuators were installed in the rotating frame in “force-carrying” tubes (see Figure. 1.7). This system including a retrofit IBC installation was estimated to be 3% lighter than the conventional control system that is the swashplate. This concept is expected to allow for primary control. However, as of 2007, it has not yet been tested.

McDonnell Douglas Helicopter Systems conducted studies on plain flaps to provide vibration and noise control as well as blade tracking for the $MD - 900$ helicopter (Ref. [8, 9]). This program was called the Active Flap Rotor (AFR). The development of the AFR rotor was accompanied by a detailed feasibility study and development program for the full scale active flap rotor program at McDonnel-Douglas/Boeing as well as a wind tunnel test campaign in NASA Ames wind tunnel and a correlation it allowed with CAMRADII predictions of the rotor loads (Ref. [53, 54, 55, 56, 57, 58, 59, 60, 61, 62, 63]). The application is for a MD900 Explorer helicopter, which is an 8-seat utility helicopter with a maximum takeoff weight (MTOW) of 2835 kg (i.e. 6250 lbs), with a 5 bladed, 10.3 m (i.e. 34 foot) diameter bearingless rotor. The final actuator design downselected consists of a 0.91 m (i.e.e 3 ft) span trailing edge flap driven by a bidirectional version of the X-frame actuator described above. The actuator has been scaled up from the model scale in order to meet full scale requirements (Ref. [57, 64]). Two X-frames are coupled together in order to obtain a positive force during both extension and retraction of the flap actuator push rod. The dual X-frame actuator is capable of a blocked force of 36.3 kg (i.e. 80 lbs) and a free displacement of approximately 2.54 mm (i.e. 100 mils). A dual X-frame actuator undergoing benchtop testing is shown in Figure 1.12.

A bi-directional flap actuator driven by piezostacks, based on lever arm amplification has been developed by Lee and Chopra (Ref. [65, 66, 67]). This actuator was designed to meet the requirements of a trailing edge flap on the blade section of a full-scale MD900 Explorer helicopter. The actuator was driven by 5 piezoceramic stack elements driven at a peak to peak voltage of 120 V and achieved a blocked force of approximately 4.08 kg (i.e. 9 lbs) with a free stroke of approximately 1.9 mm (i.e. 75 mils). This actuator was tested in a vacuum chamber spin test and in a wind tunnel, at frequencies of upto 5/rev. Spin testing results showed less than 10% degradation of actuator deflection at 710g's of centrifugal accelaration. In the wind tunnel, peak to peak flap deflections of upto 12° were measured at free stream velocities of 36.58 m/s (i.e. 120 ft/sec) and 12° collective. However, analytical predictions overpredicted the performance of the actuator as a result of the finite stiffness of the linkages. A bidirectional version of the same actuator has also been designed and is currently undergoing spin testing in vacuum.

While most full-scale smart rotor activities have centered around piezoelectric actuation systems, some electromagnetic actuation systems have also been proposed. The above mentioned COCE actuators used by Eurocopter are one example. Another example is the work of Fink et. al. (Ref. [68, 69]). In this study a proprietary electromagnetic actuator was used to drive a 11.3% span, 46% chord flap centered at 91% blade radius of an OH-58 (Kiowa Warrior) rotor blade. The actuator was designed to replace blade tip balance weights to minimize the weight penalty. Flap deflection amplitudes of ±6 deg were achieved at a tip Mach number of 0.48 (81% of design speed). Average flap power requirement was reported as $220W$, that represents less than 0.05% of the maximum installed power of an OH-58D.

A shear mode piezoelectric tube actuator has been developed to drive a trailing edge flap (Ref. [70, 71]). This actuation mechanism utilizes the d_{15} effect (see Section. 1.4.3) of the base piezoelectric material, which is the largest piezoelectric coupling effect. Design studies were conducted for a Boeing MD 900 helicopter with a plain trailing edge flap. It was estimated that flap deflections of ± 2.5° can be achieved at full speed. This is based on a 6% span flap, with a 25% chord, driven by a tube with an outer and inner diameter of 17.8 and $11.4mm$, respectively, and a length of $203mm$ (corresponding to 4% of rotor radius). Using a spring to simulate aerodynamics, $\pm\ 1.5^{circ}$ were measured in a bench top test, at 75% of the maximum electrical field, on the order of $1kV$.

A trailing edge flap actuator based on Magnetic Shape Memory Alloy (MSMA) as the active material was recently designed to provide primary flight control authority on a search and rescue helicopter (Ref. [72]). Two trailing edge flaps were used on each blade and flap deflections on the order of ± 5° at hinge moments of approximately 3 lb-ft were required for trim. Two permanent magnets were used in conjunction with two magnetic coils that provided a differential magnetic field of ±100 kA/m. The total actuator weight including the housing was 0.86 kg (i.e. 1.9 lbs), out of which 0.36 kg (i.e. 0.798 lbs) was the active MSMA material itself. The power requirement was 210 W, at a current of 4 A, which corresponds to approximately 0.2% of the total installed continuous power of the vehicle. This design study clearly demonstrates the feasibility and attractiveness of the swashplateless concept.

It is seen that there have been numerous investigations of full scale rotors capable of actively changing their blade geometry. Several important conclusions can be drawn from these studies. Firstly, it is seen that smart materials such as piezoceramics appear to be the material of choice for on-blade actuation due to their high power density, low number of moving parts and ability to be cast in different shapes. However, these materials typically suffer from an insufficient stroke, and different concepts for mechanically amplifying their output has been suggested. Secondly, all the full scale rotor investigations to date have been focussed on vibration and noise control. There is limited work in the literature on full scale swashplateless rotors. Studies appear to indicate that primary control using on-blade actuation would require much larger control surfaces and actuators than that required for vibration control. Such extensive changes to the rotor blade would compromise its structural integrity and aeroelastic stability.

There have also been numerous studies of on-blade actuation performed at a reduced model scale. These studies have been focussed on the development of appropriate analytical tools and their validation. The development of a small scale model is cheaper than full scale and is a step used to reduce the risk of new designs. A review of small scale applications will yield an understanding of the issues related to on-blade actuation with the constraint of the extremely small volume inside the blade.

1.4.2 Small scale applications

Numerous small scale applications have been developed for vibration and noise control. These typically precede the full scale development and serve as proof-of-concept for new designs. Initial small scale studies were performed by using on-blade control surfaces actuated by conventional swashplates. With the advent of smart structures technology, active materials, predomi-

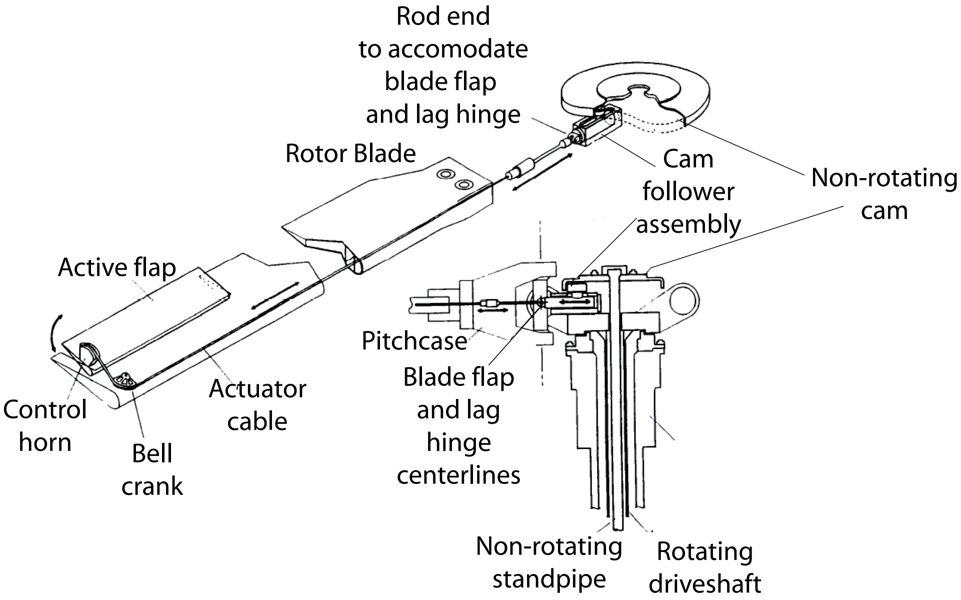

Figure 1.8: Actuation of the plain flap on the AFR. (Ref. [74])

nantly piezoceramics, were used to actuate the on-blade flaps or change the blade geometry. Each of these concepts has its advantages and disadvantages. Several of them were not pursued further because it was not feasible to scale the concept to full scale.

An important proof-of-concept investigation of the plain flap was conducted by McDonnell Douglas Helicopter Systems with their Active Flap Rotor (AFR) model (Ref. [73, 74, 75]. This rotor was a 3.66 m (i.e. 12 ft) diameter model, with plain flaps on the rotor blade that were driven by a cam and cable linkage (see Figure. 1.8). The goal of these experiments were to investigate the effectiveness of a plain flap in terms of vibration control, BVI noise reduction and power requirements. Tests were performed with open loop multicyclic flap control inputs, whose phasing could be adjusted by means of a mechanical arrangement.

The Japan Aerospace Exploration Agency (JAXA) and Kawada Industries, Inc. developed the "Active Tab" in a bid to reduce helicopter noise in approach, flyover and takeoff (Ref. [76]). The Active Tab is a control surface lodged in the in the trailing-edge of the blade. It is hinged at a single point located at 80% of the blade radius and is driven back and forth as shown on Figure. 1.9. Wind tunnel tests were carried out in a 2.5m by 2.5m section. A 2dB noise reduction was observed when the Active Tab was used.

A similar approach is being carried out in the "Rotor à Pale Active"

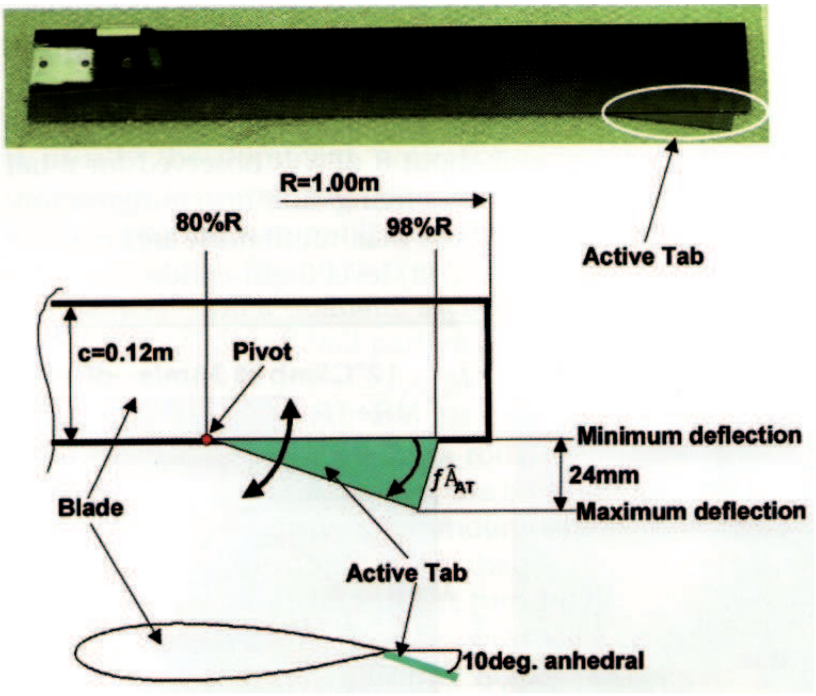

Figure 1.9: Active Tab by JAXA and Kawada Industries, Inc. (Ref. [76])

(*RPA*), or Active Blade Concept (*ABC*), research program conducted by ONERA, DLR, Eurocopter France and Deutschland. The aim of this program is to investigate, both analytically and experimentally, the concept of on-blade active TEF to achieve BVI noise and vibration reduction and to decrease power consumption in forward flight at cruise speed (Ref. [77, 78, 79, 80, 81]). After small scale studies (Ref. [10]), wind tunnel tests were performed in Modane (see Figure. 1.10) on a Mach-scaled rotor which includes TEFs. The TEFs were located outboard, from 69% to 90% of the blade radius. The TEFs were actuated by elliptical piezoelectric actuators developed by CEDRAT Recherche Company (See Figure. 1.11). Wind tunnel tests proved to be successful as a 15% vibration reduction on the $4/rev$ vertical force was observed.

The Smart Hybrid Active Rotor Control System (SHARCS) is being investigated by the Carleton University, the Universita di Roma and the DLR. This concept combines flow control as well as structural (or stiffness) control (see Figure. 1.12). It is expected to reduce vibration and noise on rotorcrafts. The design, prototyping, static and hover stand test of the concept have been performed (Ref. [82]). The SHARCS concept is also expected to improve the efficiency of a flow control device requiring low blade torsional stiffness (see Ormiston recommendations in Section. 1.4.4),

Figure 1.10: ABC rotor in Modane wind tunnel(Ref. [79])

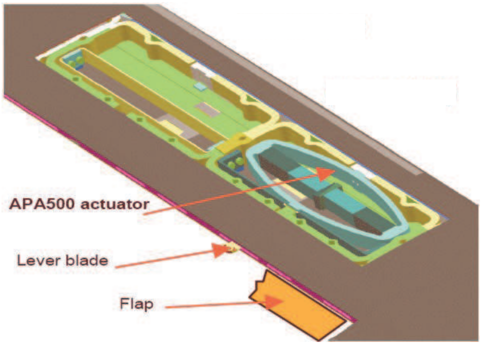

Figure 1.11: ABC Blade section including the PZT actuated TEFs. (Ref. [79])

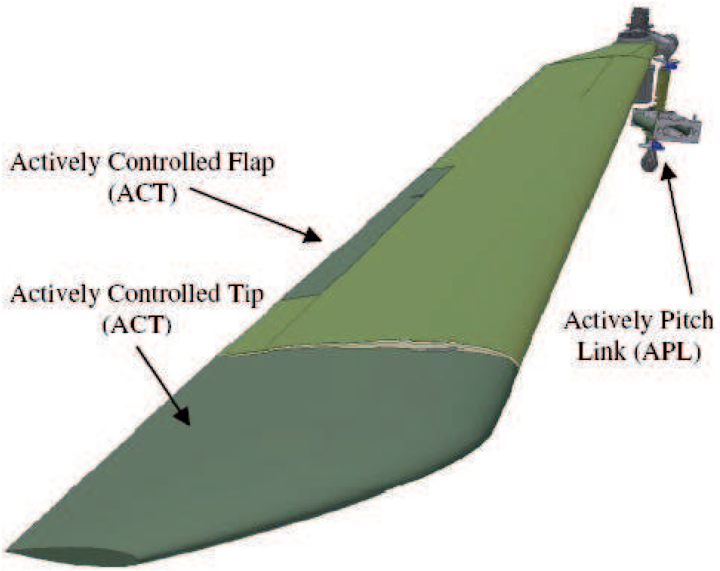

Figure 1.12: The SHARCS hybrid concept with 3 individual feedback systems (Ref. [82])

Barrett et. al. (Ref. [83]) developed a swashplateless rotor with Hiller servopaddles actuated by directionally attached piezoelectric torque-plates. The system was flight tested on a radio-controlled model helicopter with rotor diameter of 23.5 in. The active servopaddle system demonstrated deflections of up to 2.7 deg at full rotor RPM (1600 RPM), and a dynamic response of up to 2.5/rev. Experiments indicated that the helicopter with the swashplateless rotor system had a reduction in gross weight by 8% and a decrease in parasite drag of 26%, as well as a large reduction of the part count in the flight control system. The active servoflap was analysed using a one degree of freedom torsion model with quasi-steady aerodynamics. However, the small displacement of the twist actuators may constrain this system to model scale.

The first active twist rotor, using direct twist actuation was developed by Chen and Chopra (Ref. [84, 85, 86]). The rotor blade incorporated dual-layer monolithic piezo patch elements embedded at +45° under the upper skin and −45° under the lower skin of the rotor blade, see Figure 1.13. The piezo elements extended from approximately 17.5% to 70% chord and the ratio of the piezo to fiberglass skin thickness was of the order of 4:1. With both the upper and lower piezo elements excited in phase a net shear strain is induced in the skin, and blade twists. A 1.83 m (6ft) diameter Froude scale active twist rotor was tested in hover and in the wind tunnel. The tip Mach number of the reduced speed rotor was 0.28. Blade tip twist amplitudes

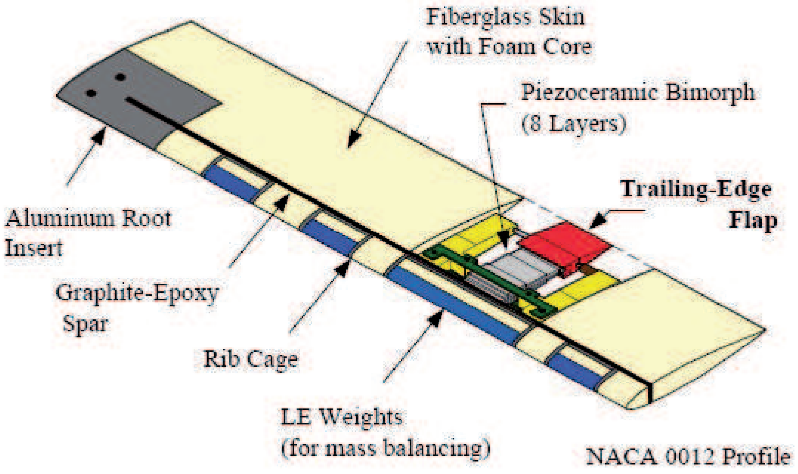

Figure 1.13: Active twist rotor with PZT elements embedded under the blade (Ref. [87])

of ± 0.25° were achieved (excitation field -560 to 1110 V/mm, excitation frequency below the torsional resonance frequency of 4.75/rev). The open loop wind tunnel tests demonstrated that despite the low blade tip twist amplitudes it was possible to appreciably alter the rotor hub loads.

Another active twist concept involves the integration of active piezofiber plies into the composite blade structure. Interdigitated electrodes are deposited on the active plies in order to utilize the larger d_{33} effect of the piezoelectric material. Active piezoceramic fibers replace the conventional graphite or glass fibers in a resin matrix, creating an active composite ply. When cured in a +45/-45 orientation on the blade, actuation of these active layers results in a linear twist along the blade section.

The piezo fiber concept was originally developed by Hagood et. al. (Ref. [88, 89, 90, 91]) and has subsequently been commercialized (Ref. [92]). A two bladed 1/6th Mach scale model of the CH-47 rotor with active piezofibers was tested by Rodgers et. al. (Ref. [91]). A tip twist of ±0.4° was measured at full rotor speed and 8° collective, with a mass penalty of 16%.

Actively changing the blade twist by bonding piezoelectric actuators on the surface of the blade has also been investigated by several researchers (Ref. [93, 94, 91]). Cesnik et. al. (Ref. [95, 96, 97]) have developed an

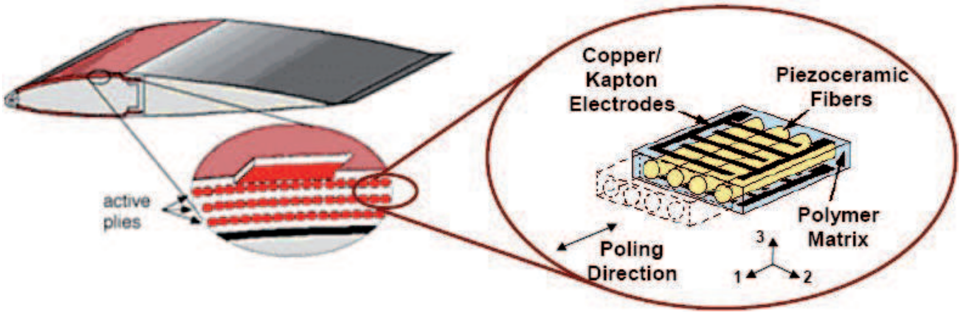

Figure 1.14: PZT fibers actuating the blade in torsion. (Ref. [99])

analytic model for active twist blades featuring active fiber composites. In parallel to this computational effort, a 1/6 Mach scale active fiber rotor blade was also designed and fabricated (Ref. [96, 98]). This rotor was hover tested in a heavy gas medium (Mach-scale) at the NASA Langley transonic wind tunnel. During the open loop hover test, oscillatory tip twist amplitudes of ±1° were achieved in the 3-5/rev frequency range. A team from Boeing/MIT has recently built and tested an advanced geometry active rotor model with piezo-fiber composites actuating the blade in torsion (Ref. [99, 100]). However, this method may also result in a significant weight penalty. In addition, obtaining sufficient twist for primary flight control is challenging.

Extensive research has been conducted on Froude and Mach scaled rotor models with trailing edge flaps actuated by piezo-bender elements to reduce vibrations. Early research efforts encountered problems with friction in the mechanical components as well as clamping problems in the actuator (Ref. [101, 102]). These problems limited the flap deflection to less than ±2° at full speed. Improvements made in the actuator mechanism by Koratkar and Chopra (Ref. [103, 104, 105, 106, 107, 108, 87]) enabled testing of Froude scaled and Mach scaled model rotors on the hover stand and subsequent testing of a Mach scaled model in the wind tunnel. In the wind tunnel, the rotor was tested at rotational speeds of upto 1800 RPM and an advance ratio of 0.3 and a collective pitch setting of 6°. The piezo-bender actuators were excited at 90 Vrms with a 3:1 bias, upto frequencies of 5/rev and generated a deflection on the order of ±4°. Further investigations were led on Koratkar's design by Roget and Chopra (Ref. [109]). It was found that the controller developed by Roget reduced the $1/rev$ component of the normal force by over 90% using small amplitude flap deflections (about ±2°) in hover at 1500RPM. Roget also conducted wind tunnel tests at a rotor speed of 1500RPM and advance ratio of 0.25 to reduce vibration in the fixed frame. It was observed that for a 2° collective blade angle, the hub normal force consisted mainly of $1/rev$, $3/rev$ components as well as a smaller $4/rev$ component. The controller reduced the $1/rev$ component by about 50%, although this was accompanied by an increase in the $1/rev$ component of other loads. The hub pitching moment vibration consisted mainly of a large $4/rev$ component, and a small $1/rev$ component. The $4/rev$ component could be reduced by over 60%. This was accompanied by a reduction in the 4/rev of the hub rolling moment and axial force, however, the $4/rev$ of the normal force was increased.

Fulton and Ormiston successfully tested an improved bimorph flap on a reduced speed rotor (tip Mach 0.27, diameter 2.23 m). The 12% span, 10% chord flap was centered at 75% radius and was driven by two 38.1 mm wide piezo bimorphs. The test program included a hover test (Ref. [110]), a wind tunnel test (Ref. [111]) and validation of the analytic model (Ref. [112, 11]). At full speed, open loop flap deflections of ±7.5° were achieved at an excitation of ±610 V/mm. The test program clearly demonstrated the ability of the trailing edge flap to alter the blade torsion and flap bending loads.

A scaled up version of the piezo-bender concept was also designed for a full scale MD900 rotor (Ref. [87]). Flap deflections on the order of ±5° were predicted with voltage inputs of 800 V. The weight of the full scale piezo-bender was predicted to be 1.54 kg (i.e. 3.4 lbs) and along with the mounting fixtures, 2.54 kg (i.e. 5.6 lbs). This actuation scheme appears suitable only for scaled rotor models.

Bernhard and Chopra have developed a novel actuation mechanism consisting of a bending-torsion coupled composite beam with piezoceramic sheet actuators bonded on its surface (Ref. [113, 114, 115, 116]). When the piezoceramic actuators are actuated in a bending configuration, the total bending in the beam cancels out and the total twist adds up. The resulting tip twist has been used to actuate trailing edge flaps as well as an all moving, 10% span blade tip (Smart Active Blade Tip, SABT). Froude and Mach scaled tests have been conducted on active rotors with this actuation mechanism. For the Froude scaled rotor, flap deflection amplitudes of ±2° were achieved at 900 RPM in hover in the 1-5/rev frequency range. In Mach scaled hover tests, at 2000 RPM, at 2° collective, and for an actuation voltage of 125 Vrms, the measured tip deflection at the first four rotor harmonics is between ±1.7° to ±2.8°, increasing to ±5.3° at 5/rev due to resonance amplification. The tip activation resulted in over 50% variation in the steady rotor thrust levels at 8° collective.

The Mach scale SABT rotor was also used as a testbed for a time domain neural network control algorithm, developed by Spencer et. al. (Ref. [117, 118, 119]). The same control algorithm was used to actively control vibrations on the Mach scaled active rotor with trailing edge flaps actuated by piezo-bimorphs described above, by Koratkar et. al. (Ref. [87]). The control algorithm and the active rotor system hardware were validated both in hover as well as in forward flight by means of wind tunnel experiments (Ref. [108, 120]).

Bothwell et. al. (Ref. [121]) researched the concept of actuating trailing edge flaps by means of an extension-torsion coupled composite tube, with an internal piezostack or magnetostrictive actuator. As a result of the composite coupling the tube extends and twists in response to extension of the actuator. Based on experimental success, it was proposed to stack multiple tubes in series to generate sufficient twist to deflect a trailing edge flap.

Modifications of the conventional straight bender have also been proposed, such as the C-block actuator (Ref. [122, 123, 124]). The C-block has a greater stroke capability than a conventional straight bender at the cost of reduced force output. A blade section incorporating a 10% chord trailing edge flap, with a 50% pivot overhang for aerodynamic balancing was wind-tunnel tested. With a driving voltage of 55% (of the maximum level), flap deflections of ±5° to 9° were measured, however the dynamic pressure was less than 3% of full scale dynamic pressure.

The X-frame actuator concept was pioneered by Prechtl and Hall (Ref. [125, 126, 127, 128, 129, 130]). The X-frame is a piezo-stack amplification mechanism that uses stroke amplification via shallow angles. The actuator was integrated into a 1/6th Mach-scale Boeing CH-47 (Chinook) blade and tested in hover (Ref. [127]). The flap is a slotted servo-flap with a 11.5% span, 20% chord and aerodynamic overhang 27.5% of flap chord. At the operating speed (tip mach number 0.63) and 8° collective, flap deflections of ±3.9° were achieved.

The above small scale rotor applications indicate that there are numerous ways to achieve changes in blade aerodynamic forces. However, only a few of these concepts can be scaled up to full scale due to actuator geometry, weight constraints and blade integration issues. For example, the piezofiber blade twist concept works well in model scale. At full scale, the active piezoceramic plies would make the blade weight prohibitively large and any damage to the blade would result in failure of the actuation. Examining all the above studies, it appears that the most successful in terms of control authority as well as scalability are those incorporating trailing edge flaps.

All the small scale active rotor studies and a majority of full scale active rotor studies utilized actuators based on smart materials. Therefore, a review of smart material actuation will be invaluable in developing the actuation scheme for the present research.

1.4.3 Smart materials

The goal of the present research is to demonstrate proof-of-concept on a small scale rotor model. While the emphasis is not on the development of an appropriate actuator, a review of smart materials technology will generate an awareness of the options available in terms of potential actuators. Consequently, future studies on this topic will have basic information on the consequences of a smart material actuator on the design, and can choose an appropriate smart material or electromagnetic actuator as needed.

Recent advances in active materials and smart structures technology open the door to a wide range of possibilities for on-blade actuators (Ref. [131, 132, 133, 134]). Active materials, with coupled electro-mechanical behavior create the possibility of combining the functions of sensors and actuators, resulting in opportunities for the application of collocated control algorithms that are known to have superior performance. This leads to the concept of a smart rotor, that has blades with embedded actuators and sensors, with a signal conditioning/controller unit on the fixed frame. The signal conditioning/controller unit sends control inputs to the on-blade actuators in response to parameters sensed by the embedded sensors, or other sensors on board the aircraft. The integration of actuators, sensors and control electronics into the rotor make it a smart rotor, as opposed to an active rotor concept, which would only include actuators (Ref. [135, 136, 131]).

In addition to achieving the primary goals of vibration and noise reduction, the smart rotor has potential benefits in other areas like handling qualities and performance enhancement, stall alleviation, aeromechanical stability augementation, minimization of dynamic stresses on rotor components and rotor health monitoring. For example, recent research has been conducted into the application of the trailing edge flaps on an active rotor as a means of interrogating the rotor, for the purposes of detecting helicopter rotor faults (Ref. [137]). The blade response is measured using the on-blade embedded sensors. It was shown that even a small amount of sensor noise adversely affects the damage detection methodology. High signal to noise ratio piezoelectric sensors could concievably provide large benefits in such applications.

Role of smart structures and active materials in the smart rotor

Recently there has been a growing interest in the application of smart structures technology to helicopter rotor systems (Ref. [138, 131]). A comprehensive review of the current state of the art in smart structures technology applied to rotorcraft systems can be found in Ref. [131].

Active materials such as piezoceramics and magnetostrictives are very attractive for the smart rotor concept because they are compact, light-weight, provide a high bandwidth, possess high energy densities and can provide actuation with a minimum of moving parts. Blade active systems using smart materials, such as rotors with trailing-edge flaps or controllable twist blades, offer the advantage of IBC, require lower actuation power, and eliminate the need for a hydraulic slip ring. All control inputs and sensor signals are transmitted between the fixed and rotating frame through an electrical slip ring, which is a very mature and reliable technology. Additionally, materials like piezoceramics, that exhibit electro-mechanical coupling, can be used both as sensors and actuators, leading to the possibility of collocated control techniques.

Numerous active control systems have been proposed and to some extent developed and tested, both in the model scale and for potential full scale rotors. At this stage a brief review of current active materials and their characteristics is warranted.

Active material actuators and sensors

Piezoelectric materials are one of the most popular candidates for smart actuators. These materials exhibit an electro-mechanical coupling. They undergo mechanical deformation in response to an electric field and generate an electric field in response to a mechanical strain field. Conventional piezoelectric actuators are typically based on piezoceramics. Piezoceramic actuators are typically as stiff as aluminum, and have a very high bandwidth, on the order of tens of kHz. Typical strain levels are on the order of $1000\mu\eta$ (for piezostacks) with stiffnesses on the order of 70 GPa. Depending on the configuration of the actuator, they can require excitation voltages on the order of 100 V, or even 1-2 kV. Due to their high energy density, high bandwidth, ease of embeddability and ease of integration into structures, they are extremely attractive for smart rotor systems. As a result of their electro-mechanical coupling, they can also be used as sensors.

Piezoceramic material is available in the form of sheets, rods and tubes, as well as in several other shapes. The base piezoceramic material can

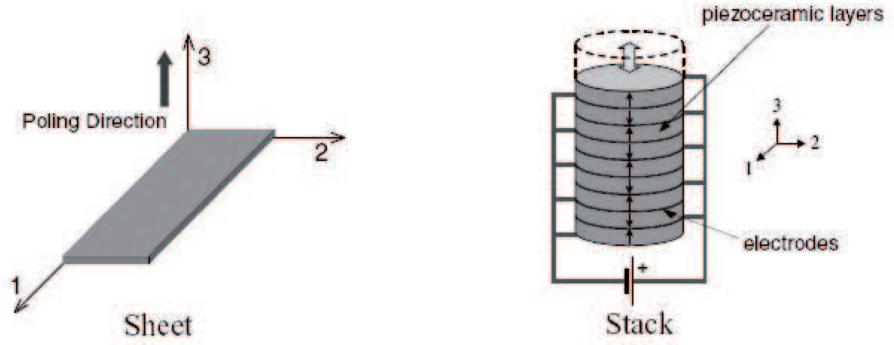

Figure 1.15: Types of piezoceramic actuators:sheet and stack. (Ref. [139])

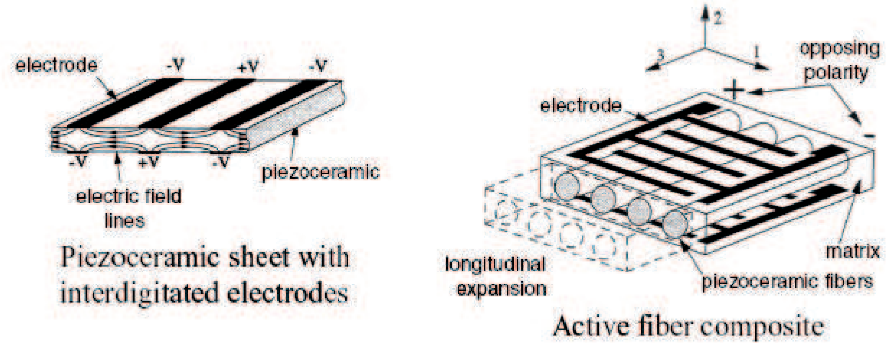

Figure 1.16: Types of piezoceramic actuators:special electrodes configuration. (Ref. [139])

be fashioned into solid state actuators, using either specific electrode configurations, or geometrical arrangements. Most of these actuators utilize the d_{31} mode of actuation or the d_{33} mode of actuation. However, some actuators are designed to utilize the d_{15} mode, or shear mode, which exhibits the largest electro-mechanical coupling. The basic types of such solid state piezoceramic actuators are shown in Figure. 1.15, 1.16 and 1.17. Figure 1.15 shows piezoceramic sheets and stacks, that consist of piezoceramic sheets with uniform electrodes on the 1-2 plane. These actuators use the d_{31} and d_{33} effect respectively. Figure 1.16 shows a piezoceramic sheet, and a composite with piezoceramic fibers (Ref. [140, 141]), both with interdigitated electrodes. The special electrode pattern enables these actuators to operate in the d_{33} mode. Figure 1.17 shows a bimorph and a C-block actuator (Ref. [122]), that achieve amplified output displacements as a result of their geometry. Several other actuators based on the same concept exist, such as the RAINBOW (Ref. [142]) and the THUNDER (Ref. [143, 144]) actuators. An overview of currently available piezoceramic materials and ac-

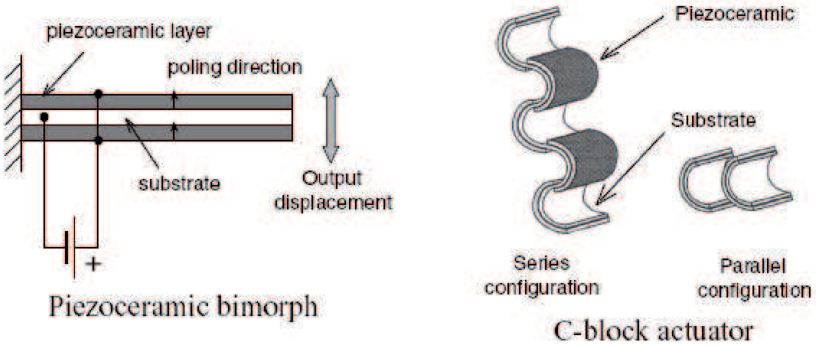

Figure 1.17: Types of piezoceramic actuators:geometrical amplification. (Ref. [139])

tuator geometries is presented by Near (Ref. [145]), from which Figure 1.18 is reproduced. It can be seen that piezoceramic stack actuators (MLAs) provide the highest energy density without mechanical amplification. A detailed discussion of piezoceramics and actuators based on piezoceramics can be found in Ref. [146] and Ref. [147]. Electrostrictive materials are similar to piezoelectric material, with slightly improved strain capability and lower hysteresis effect, but are highly temperature sensitive. In addition, the response of these materials to field is highly non-linear and depends only on the magnitude of the applied field, resulting in only uni-directional strains. Magnetostrictive materials (Terfenol-D) on the other hand respond to magnetic fields generated by coils located on or near the structure. These actuators generate low strain with high force over a large range of activation frequencies. The primary drawback of actuators based on magnetostrictive materials are that they are complex and very bulky due to the size of the magnetic coils required to create the magnetic fields.

Shape Memory Alloys (SMAs) are alloys of Nickel and Titanium that undergo phase changes depending on the their temperature. As a result, actuation can be achieved by means of heating and cooling the material. Their unique capacity to develop very large plastic strains (of the order of 5%) that is recoverable upon heating makes them attractive materials for use in low-frequency (less than 1Hz) actuators. For smart rotor applications, they are not very useful for vibration and primary flight control requirements as a result of their low bandwidth, but are excellent solutions for low bandwidth applications. As a result of their high stroke and high force capability, mechanical power transmission mechanisms are not required. SMA actuators have been used in trailing edge tab actuators (Ref. [148, 149]) and more recently, in active twist of tiltrotor blades (Ref. [150]). SMA torsional actu-

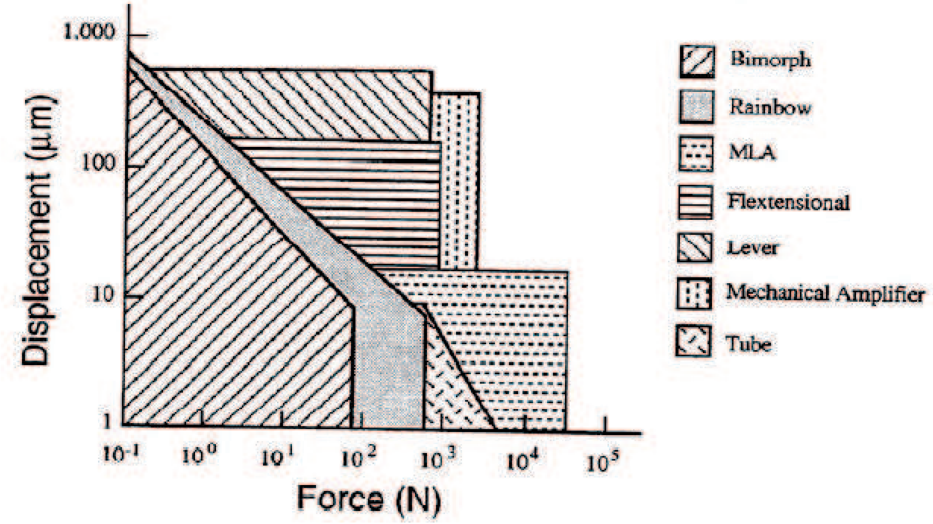

Figure 1.18: Divers PZT actuators output comparison. (Ref. [145])

ators have also been investigated to actuate a control surface on a fixed wing aircraft, in conjunction with the Smart Wing program (Ref. [151, 152]).

A new active material has recently been developed, called a Magnetic Shape Memory Alloy (MSMA). This material has the potential for large output strokes (5% strain) at moderate force levels, as well as a high bandwidth on the order of 100 Hz (Ref. [153]). An actuator based on this material has been designed to meet the requirements of a primary flight control system employing trailing edge flaps on a full scale helicopter rotor (Ref. [72]).

A comparison of various actuators based on their specific stress and strain output is shown in Figure 1.19. On the Y-axis, the quantity plotted is the stress of the actuator divided by its density, and on the X-axis is plotted the strain of the actuator. The product of the two gives a measure of the specific work output of the actuator, per unit mass. It should be noted that in a smart rotor application, in addition to the severe volumetric constraint, there is also a weight penalty limitation. Hence, an actuator has to be judged not only on the basis of its specific work output per unit mass, but also by its specific work output per unit volume. It can be seen that hydraulic actuators and shape memory alloy actuators have the highest specific energy density, however, the main drawback of hydraulic actuators is their complexity and large number of moving parts. This is one of the issues addressed by the present research on a piezoelectric hydraulic hybrid actuator, that focuses on the development of a hydraulic pump which is very compact and has a small number of moving parts. Shape memory alloys are

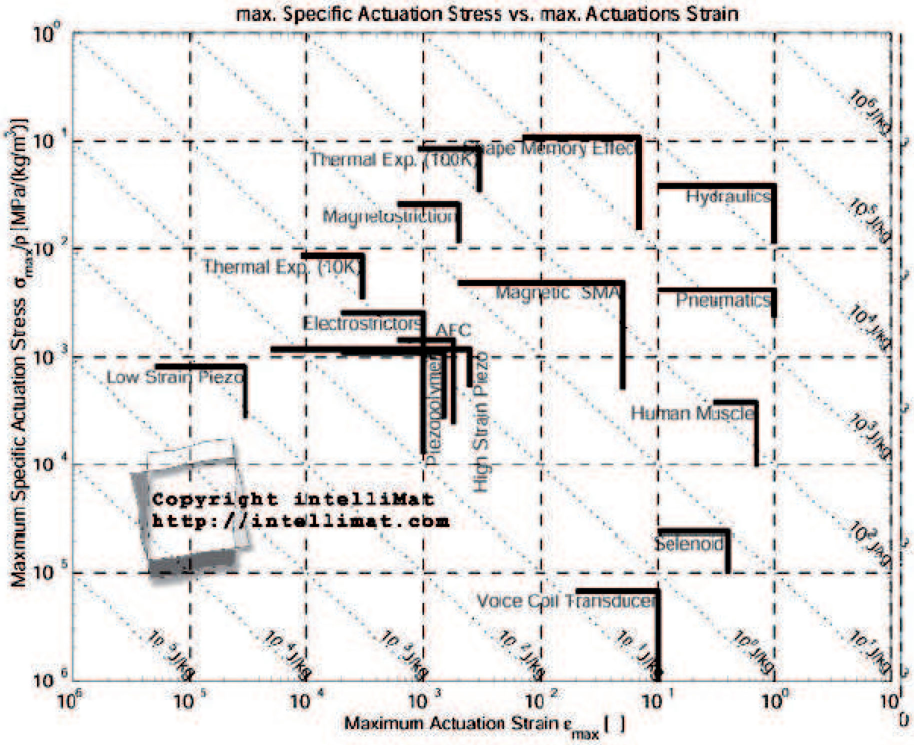

Figure 1.19: Comparison of the ouput characteristics of typical actuators, work output per unit mass. (Ref. [139])

limited by their low bandwidth. This can be seen from Figure 1.20, which compares various actuators on the basis of their stress-strain product, which is a measure of their output energy capability, and their frequency response. From these two comparsions, it can be seen that piezoelectric actuators offer the best combination of high energy density and high bandwidth.

It can be concluded that out of all the smart material actuators, piezoceramics such as PZT are the most feasible for on-blade actuation. However, they may not be the best choice for the present application for several reasons such as insufficient bandwidth, insufficient stroke and most importantly, unknown reliability under continuous operation. Future studies may result in the choice of an electromagnetic actuator for the present concept. Therefore, the analytical model that is developed in the present research must be designed to account for the specific load-stroke characteristics of any actuator.

A basic understanding of the dynamics of the coupled system is essential to the proper design of the experiments as well as assessment of the concept. In addition, modeling of the aeroelastic behavior will yield insight into the

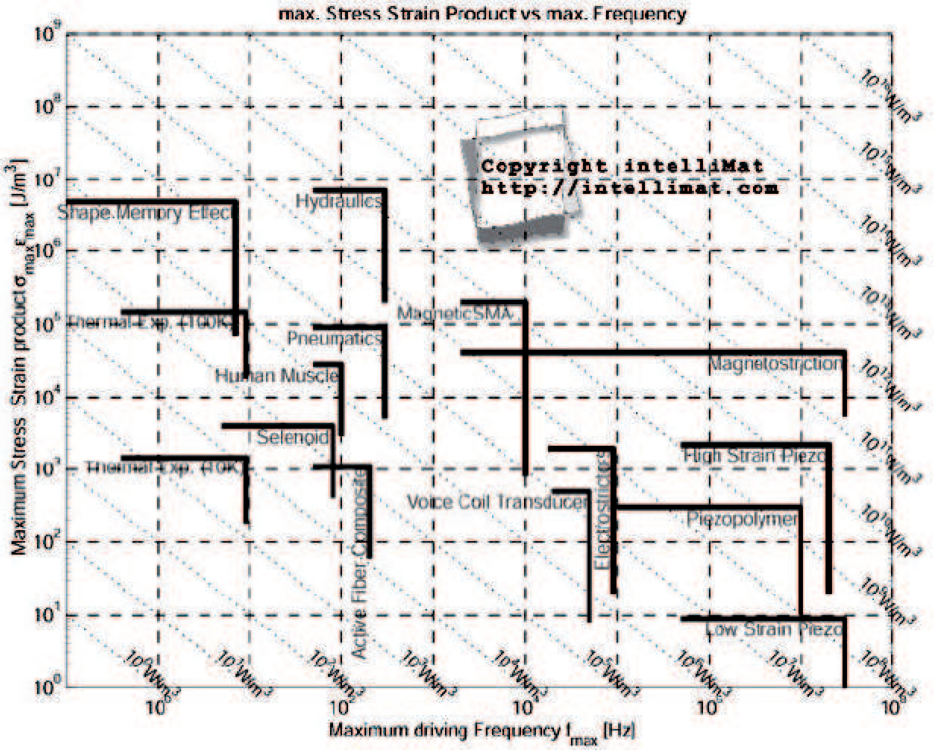

Figure 1.20: Comparison of the ouput characteristics of typical actuators, work output with frequency response (Ref. [139])

stability of the system for forward flight.

1.4.4 Analytical studies

Numerous on-blade actuators based on piezoelectrics have been investigated for deflecting control surfaces on the blade. Most of these studies have been carried out for vibration reduction. Analytical models have been developed to design these systems and to validate experiments. Some models include unsteady aerodynamics, while others assume quasi-steady aerodynamics. Similarly, some models incorporate actuator dynamics, while others use a local change in aerodynamic coefficients in an uncoupled fashion. A review of these analytical studies will enable an appropriate choice of physical phenomena to include in the present analytical model.

In recent years, most of the controllers developed to achieve vibration reduction rely on HHC or IBC (Ref. [154]). HHC stands for Higher Harmonic Control and IBC stands for Individual Blade Control. HHC is used in association with devices providing control inputs in the fixed frame. Thus studies using HHC still require a swashplate. HHC has been shown to be effective in terms of vibration reduction (Ref. [155, 156, 157]) and improved helicopter performance (Ref. [158]). This method however involve high power requirements, weight penalty, high pitch link loads. Most importantly, all blades experience the same pitch inputs through the conventional swashplate. Dissimilar blades vibration cannot be dealt with. In addition, vibratory aerodynamic loads are modified at their source. IBC is used with devices introducing time-varying control inputs in the rotating frame (Ref. [159]). Every blade is controlled individually at any desired frequency (Ref. [19]). The IBC approach can be implemented in different ways:

1. The entire blade is made to oscillate via an actuator located at its root.
2. One or two on-blade TEFs are actuated via on-blade actuators (Ref. [160, 161, 162])
3. The blade twist is modified by embedded PZT fibers as seen in an earlier section.

As seen in previous sections, numerous investigations have been carried out on single and dual flaps techniques to achieve vibration control. Vibration reduction is essentially the control of the aeroelastic response. Unsteady aerodynamic loads representation is critical when it comes to predict accurately the aeroelastic stability and response. It can be achieved using :

1. an approximate unsteady aerodynamic model for attached flow. A analytical model providing approximate unsteady aerodynamic loads

in the time domain was developed by Peters et. al. (Ref. [163, 164]). The finite state inflow model considerated global rotor disk downwash under unsteady conditions. This method is an exact representation of the three-dimensional incompressible potential flow equations of the wake. The wake was considered as a cylinder in hover and a skewed cylinder in forward flight. It includes the effect of wake contraction. Details of this theory are given in Ref. [165, 166]. An efficient free-wake model was developed to model BVI effects which account for an important part of the rotor vibratory loads at lower advance ratio (Ref. [167]). The Free-wake model was integrated into the UMARC (University of Maryland Advanced Rotorcraft Code) and has led to numerous studies.

2. dynamic-stall models. Dynamic stall has been explained by Leishman (Ref. [1]). A model has been developed by ONERA (Ref. [168]). It describes unsteady airfoil behavior both in attached flow and during dynamic stall realying on a set of nonlinear differential equations. The coefficients in the equations are determined from experimental data on oscillating airdoils. This model requires 22 empirical coefficients. The Leishman-Beddoes model (Ref. [169]) can represent unsteady lift, pitching moment and drag characteristics of an airfoil undergoing dynamic stall. It comprises three components: an attached flow model for the unsteady linear airloads, a separated flow model for the nonlinear airloads and a dynamic stall model for the leading edge vortex-induced airloads. This model uses only four coefficients derived from static airfoil data. This theory has also been included in the UMARC code.

The basic analysis of UMARC is detailed in Ref. [170]. Further refinements of UMARC included studies by Milgram et. al. (Ref. [171, 172, 173, 174]) and Shen et. al. (Ref. [175, 176, 177, 12, 178, 179, 180, 181, 182, 183]). The comprehensive aeroelastic analysis by Milgram et.al. studied plain TEFs to achieve vibration control. This method used a time domain unsteady aerodynamic model (Ref. [184]) using an indicial approach for both circulatory and non-circulatory unsteady airloads generated by both the airfoil and the flap motion. In addition, this theory captures the effects of compressibility on the non-circulatory airloads. Compressibility effect on the circulatory airloads are included using the Prandtl-Gauert rule. The gap between the flap leading edge and the base of the primay airfoil affects the flap efficiency as the flow leaks through the gap. This influence was modeled using flap effectiveness factors acting on the airfoil pitching moment and flap hinge moment. The gap effect is shown in CFD-generated views in Ref. [185, 186] and explained in Ref [187]. Milgram validated his analysis using on one hand the Comprehensive analytical Model of Rotorcraft Aerodynamics and Dynamics II (CAMRAD II), Ref. [188], and on the other hand experimental data from wind tunnel tests on McDonnell Douglas Active Flap Rotor (Ref .[73, 75]). UMARC trim controls predictions showed fair correlation with experiments. However, some discrepancies were observed in the case of both UMARC and CAMRAD regarding the steady components of some moments, the inplane bending, the effect of varying TEF phase angle. Shen further improved the Milgram model of a TEF for vibration control. His analytical model also investigated the TEF capability to achieve primary control. Shen used the unsteady Hariharan-Leishman model without aerodynamic balance and a quasi-steady Theodorsen theory (Ref. [13, 14, 15]) for and aerodynamic balanced TEF. The correlation studies of a typical bearingless rotor and an ultralight teetering rotor are respectively based on wind tunnel test data and simulations of another comprehensive analysis (CAMRAD II). Overall, good correlations are obtained. Parametric study identifies that the effect of actuator dynamics cannot be neglected, especially for a torsionally soft smart actuator system.

CAMRADII was used by Yeo to assess the capability of active controls to improve rotor performance. Yeo investigated seven different active concepts: leading edge slat, variable droop leading edge, oscillatory jets, Gurney flap, IBC, active twist and TEF (Ref. [189]). Two cases were considered for the study: 1)an airspeed sweep at $C_T/\sigma = 0.75$ to examine rotor lift-to-drag ratio 2) thrust sweep at fixed airspeeds (80 and 150 kt) to estimate maximum blade load capability. It was found out that the leading edge slat, the variable droop leading edge, the oscillatory jet and the Gurney flap increased the blade maximum loading capability when these concepts were used on the rotor retreating side. However, these methods did not improve rotor lift-to-drag ratio at $C_T/\sigma = 0.75$. IBC, active twist and TEF improved the rotor lift-to-drag ratio with a $2/rev$ harmonic control, but were not efficient to increase the blade loading maximum capability.

CAMRADII was also used by Priems (Ref. [44]) to investigate the possibility to achieve primary control using the ADASYS design. Priems studied the effect of several parameters: the blade pitch control stiffness, the blade pitch index angle (definition detailed in Ref. [12]), the TEF span and radial location. It was found that the TEF span and the blade pitch stiffness had the largest impact on the reduction of the TEF deflection angle requirement. An aeroelastic study was conducted for hover and several maneuvers. In some situation, the swashplateless ADASYS design tended to be unstable. This particular design offered a limited flight envelope with a blade torsion frequency near $2/rev$. However, the rotor performance were insufficient to perform safe autorotation and agressive turns. To achieve these two kinds of maneuver, large TEF angles resulting in low collective settings were required: in the present study, the TEF maximum authority was of 10°. An extra authority of factor 1.5 to 2.5 is required.

The actuation requirements for primary control are more severe than the requirements for vibration control. Recent studies indicate that on-blade elevon type control surfaces have the potential to provide sufficient collective and cyclic pitch authority to satisfy general requirements of primary flight control (Ref. [41]). An elevon type control surface, that is completely buried inside the blade structure, is favored due to the lower parasite drag penalty as compared to an exposed servo-flap type configuration. The torsional frequency of the rotor blade is reduced to between 1.5/rev-2.5/rev and the rotor blade works at freestream velocities well above the elevon reversal speed. Such a low blade torsion frequency might impair the blade structural integrity. This study used aerodynamic coefficients from thin airfoil theory which are not written as a function of the blade and TEF geometry. Moreover, this analysis did not unclude unsteady aerodynamics.

Theodorsen conducted a study on flutter (Ref. [13, 14, 15, 1]). To this end, he investigated aerodynamic forces on an oscillating airfoil-aileron combination. The aileron is located behind the airfoil trailing-edge as is a TEF. In Ref. [13], the unsteady lift, pitching moment and hinge moment coefficients in response to independent airfoil and aileron motions are given as a function of:

1. Half the total chord,
2. The aileron hinge location,
3. The axis of rotation of the airfoil, aileron
4. Theodorsen's function $C(k)$ is a circulatory term, hence which results from the flow circulation around the airfoil and aileron. $C(k)$ accounts for the effects of the shed wake on the unsteady airloads. $C(k)$ is written as a function of Bessel functions (Ref. [1]). k is the reduced frequency, $k = \frac{\omega c}{2U}$ where ω is the angular frequency at which the airfoil oscillates, c is the airfoil chord and U is the resultant velocity at the airfoil element.

While an analysis investigating the potential for primary control that an aileron offers will not focus on the flutter phenomenon, this study by Theodorsen is of high interest because of the possibility to integrate unsteady aerodynamics and aerodynamic coefficients written as functions of the system geometry into an investigation focusing on primary control.

From these studies, it is seen that an analysis that incorporates unsteady aerodynamics is very important to predict the rotor behavior. In addition, the coupling between blade and paddle is crucial. Finally, the actuator dynamics must be incorporated so that the correct outputs can be obtained for a given control input (such as voltage). Uniform inflow can be assumed as a first order approximation.

From the survey of the state-of-the-art on active rotor control, it is seen that numerous concepts that are developed for small scale models cannot be extended to full scale due to issues such as weight penalty, actuator geometry and blade integration. Therefore, a viable swashplateless rotor concept must be scalable so that it can be proven at reduced scale with minimum risk and also assessed at full scale. Piezoceramic actuators appear to be the most suitable for reduced scale models, however, at full scale they may not have sufficient stroke or force. Hence, electromagnetic actuators may need to be used at full scale. Finally, it is seen that an analytical model is crucial to the development of a novel rotor concept, incorporating coupled blade motion, actuator dynamics and unsteady aerodynamics. Based on the literature survey, it is concluded that the present swashplateless rotor concept of actively controlled paddles coupled to main rotor blades is a novel concept that appears feasible in the reduced scale and can be scaled up to full scale. Therefore, the present concept presents a viable solution to swashplateless primary control of a helicopter rotor, and the present analysis is sufficiently detailed to capture all the important physical phenomena of the coupled system.

1.5 Contribution of the present work

The servopaddle has been widely used in full scale helicopters (Ref. [16, 17]), as well as radio-controlled model helicopters for passive stabilization. The flapping motion of the servopaddle is coupled to the pitch of the main rotor blades. Therefore, a small change in the aerodynamic forces on the paddle results in a change in blade pitch, and a much larger change in aerodynamic forces on the main rotor blades. By replacing the passive servopaddles with actively controlled and independent paddles, it is envisaged that small control inputs can be introduced in the rotating frame to achieve swashplateless primary flight control. Most of the concepts mentioned in the previous section, while being innovative were developed to perform vibration and/or noise control: the ADASYS rotor system by Eurocopter Deutschland, the ARC concept by Sikorsky, the RPA project by ONERA, the "Active Tab" technique by JAXA and Kawada Industries, Inc. and the SHARCS project for instance. While the green rotor uses smart actuators, it must however perform primary control. To this end, the green rotor must not only be capable of cyclic pitch control, but also of collective pitch control. Some other concepts, such as the Kaman rotors, utilize control surfaces to achieve primary control. Instead of featuring a swashplate like the Kaman rotors, the green rotor must be swashplateless. Therefore, the control inputs must be introduced in the rotating frame. It should also be noted that most of the models described in the previous section involve modifications of the main rotor blades to achieve pitch variation. In order to preserve the blade structural integrity and to not add extra development and manufacturing costs, the present concept keeps the same blade design as in conventional helicopters. Only the paddle, aileron and coupling are introduced and require additional development and fabrication costs. The centrifugal load on the paddle, aileron and actuator should be less than the one experienced by on-blade trailing-edge flap located at 75% of the blade radius.

The analysis developed by Ormiston cannot be used in the present case since its aerodynamic coefficients are fixed and not function of the concept geometry. The theory developed to study the dynamic behavior of the green rotor must feature the paddle and aileron geometry as a parameter. This allows for a parameter study to be performed to determine the optimum configuration to maximize the blade pitch response. As a result, aerodynamic coefficents from Theodorsen's theory are used.

The present work consists of:

1. The design of a novel rotor primary control concept. The design must provide both cyclic and collective pitch control of all blades. The control inputs must be introduced directly in the rotating frame. The design should be adaptable on full scale helicopters.
2. The development of a theory to predict the dynamic behavior of the system. The analysis must include the system geometry as a parameter. Thus, Theodorsen's aerodynamic coefficients are used. The theory includes aileron dynamics. Theodorsen's function $C[k]$ permits to include unsteady aerodynamics.
3. Hover stand tests and validation of the theory, establishing proof-of-concept of the system.

1.6 Assumptions

Some assumptions are made in the present work. The analyses described in Chapter. 3 are based on the following assumptions:

1. The flow is considered purely axial. Only hover flight is considered, therefore, the advanced ratio is equal to zero. Eventual gusts are not

taken into account. Hence, the flow is considered purely axial.

2. Tip loss, caused by trail vortices at the tip of a lifting surface, is not taken into account. If included, the effective span of the blade, paddle or aileron decreases and hence their lifting capability at their tip is reduced (Ref. [1]).
3. The blade is considered rigid with two degrees of freedom,
4. The paddle is considered rigid with two degrees of freedom,
5. The aileron is considered rigid with one degree of freedom,
6. The aileron dynamics are included: the effects of centrifugal, inertial, aerodynamic loads are accounted for, a spring moment is also included in the aileron pitch equation.
7. In the present study, the actuator is supposed to be comparable to a spring of constant stiffness K_{act} (see Fig. 3.1). The actuator is thus represented as a stiffness.
8. The blade, paddle and aileron root stiffness coefficients are considered constant to keep the analysis simple. The aileron root stiffness coefficient is a function of K_{act}. Future work might include more refined analyses including Finite Element Method (FEM) representation of stiffness coefficients.
9. The forces and moments are being applied along the principal axes of the body, therefore only the diagonal terms of the inertia tensor are considered.
10. A constant and uniform inflow is used. We are interested in the effect of small changes in the paddle pitch or aileron pitch input on the rotor responses. The inflow is assumed to be constant during that process. This is because the analysis is a first order model. Hence the influence of the inflow on the rotor responses is not taken into account in the state space form. The rotor is operating in hover. Hence, the constant and uniform inflow is function of the rotor thrust. The thrust produced by the blades is greater than the one generated by the paddles. Thus, we consider the induced velocity in the blade equations.

1.7 Thesis outline

This thesis is composed of five chapters. A brief description of the chapters follows:

1. **Chapter 1 : Introduction**: A description of the problem statement, the previous work on the topic and the contribution of the present work is presented.

2. **Chapter 2 : Physical principles**: This chapter deals with the physical principles involved in the functioning of the proposed new concept to achieve rotor primary control.
3. **Chapter 3 : Analytical models**: A description of two analytical models predicting the dynamic behavior of the system is given.
4. **Chapter 4 : Experiments, results and discussion**: This chapter presents the small scale RC model which was modified to be tested outdoors and in a hover stand. Hover stand tests are conducted to validate the analysis. The difficulties encountered during the set-up and test phases are described. The experimental results and the corresponding analytical predictions are compared and discussed.
5. **Chapter 5 : Summary, conclusions and planned activities**: Main characteristics of the proposed design to achieve primary control are exposed. The different analytical and experimental studies are summed-up. Important conclusions are drawn from the presented results. The presented conclusions lead to future work suggestions to improve the design of the present concept of swashplateless helicopter. The main steps to develop the concept on full scale helicopter are described.

- Part II -

Present work

Cette partie détaille la solution considérée pour réaliser le contrôle primaire du rotor d'hélicoptère avec des surfaces de contrôle. Cette partie est divisée en trois chapîtres:

1. *Le chapître* 2 *discute des principes physiques du contrôle primaire. Le fonctionnement et la cinématique du nouveau concept sont décrits.*
2. *Le chapître* 3 *présente les modèles analytiques développés pour prédire le comportement dynamique du système. Le premier modèle comprend une pale, une palette et un aileron. Le second modéle compte une pale et une palette. Dans les deux cas, le battement de la palette est couplé au pas de la pale.*
3. *Le chapître* 4 *illustre la validation de concept ainsi que les tests en stationnaire réalisés. Une description de la conception et fabrication du prototype, de l'instrumentation et plus généralement des tests est donnée. Les résultats expérimentaux sont ensuite présentés avant d'exposer la corrélation avec le modéle théorique.*

The present part details the proposed solution to achieve primary control of the helicotper rotor with control surfaces. This part is divided into three chapters:

1. Chapter 2 deals with the physical principles involved in primary control. The funtioning and kinematics of the novel concept are described.
2. Chapter 3 presents the analytical models developed to predict the dynamic behavior of the system. The first model featured a blade, a paddle and an aileron, whereas the second is composed of a blade and a paddle. In both cases the paddle flap is coupled to the blade pitch. The second model is then tested in a hover stand.
3. Chapter 4 illustrates the proof-of-concept as well as the hover stand tests. A description of the prototype design and construction, of the instrumentation and of the tests is given. Sample analytical results are

presented. Then, experimental results are then detailed before exposing the analysis correlation.

Chapter 2

Physical principles

Dans les hélicoptères classiques, le rotor principal peut être incliné dans toutes les directions grâce aux plateaux cycliques. Cela permet à l'hélicoptère d'effectuer diverses manoeuvres afin de couvrir toute son enveloppe de vol. Les plateaux cycliques sont constitués de deux plateaux, l'un fixe et l'autre tournant. Cette conception a été largement utilisée pour réaliser le contrôle primaire du rotor. Comme mentionné dans le précédent chapitre, une traînée réduite devrait résulter en une diminution significative de la consommation de carburant, ce qui est économiquement très intéressant. Un nouveau concept de rotor principal sans plateaux cycliques est proposé dans le présent chapitre.

Dans la présente étude, le nouveau concept de rotor proposé compte deux pales et est équipé de deux palettes et de deux ailerons situés à l'extrémité de deux barres (Figure. 2.2). Les raisons expliquant le choix d'un rotor à deux pales sont exposées dans ce chapitre. Les palettes sont inspirées du mécanisme de servopaddle traditionnel de Hiller, qui est constitué d'une seule barre avec des masses profilées aux deux extrémités. Si l'une des masses bat vers le haut, la masse opposée bat donc vers le bas d'une quantité identique. Par conséquent, le servopaddle ne peut fournir que des entrées de type cyclique aux pales. Un rotor comprenant un mécanisme de servopaddles est généralement équipé de plateaux cycliques afin de réaliser le contrôle primaire du rotor principal. Dans la présente investigation, les barres sont alignées l'une par rapport à l'autre, perpendiculairement à l'axe de pas des pales. Les mouvements d'une barre ne sont pas couplés avec les mouvements de l'autre, par conséquent, les palettes et les ailerons peuvent fournir à la fois des entrées de pas collectif et cyclique aux pales et donc effectuer le contrôle primaire du rotor. Il est à noter que les pales peuvent se mouvoir indépendamment l'une de l'autre, le rotor présent n'est pas considéré comme un rotor "teetering".

L'aileron est situé derrière le bord d'attaque de la palette et sera actionné par un actionneur piezo-électrique. Lorsque l'aileron est incliné d'un angle δ *vers le bas, il génère une portance qui à son tour crée un moment en pas en piqué sur la palette. En supposant que la palette soit purement articulée, la réponse maximale en battement de palette se produit environ* 90° *d'azimut plus tard. Comme l'angle de battement de palette* β^p *est couplé avec l'angle de pas de la pale* θ^b*, l'angle de pas de la pale diminue. Il est à noter que des couplages impliquant les mouvements de battement de la pale ou de pas de la palette sont à éviter.*

La configuration proposée dans la présente thèse offre plusieurs avantages.

Les palettes améliorent la stabilité du rotor. Les palettes, comme dans le cas de la Barre stabilisatrice de Bell et dans le cas de la Barre de Hiller, tournent autour du mât rotor à la même vitesse que les pales du rotor. Les palettes ont une force inertielle et une force aérodynamique. L'inertie des palettes agit de la même façon qu'une Barre de Bell, on peut comparer l'action de l'inertie à celle qui fait tourner une toupie verticalement sur son axe. Par conséquent, les palettes montrent une résistance à tout changement de leur plan de rotation et donc présentent une stabilité gyroscopique. Par exemple, si le rotor subit une rafale de vent, les pales du rotor répondent à cette rafale. Etant donné que les pales et palettes sont liées, une certaine entrée sera transmise aux palettes. Le couplage mécanique, liant les palettes au pas des pales du rotor principal, est conçu de telle manière que les palettes introduisent une commande aux pales du rotor, ce qui compense les effets initiaux de la rafale sur les pales.

Le rotor proposé dans la présente étude ne comporte pas de plateaux cycliques actionnés hydrauliquement mais des surfaces de contrôle actionnées par des piezo-électriques. Par conséquent, le poids à vide, la traînée et la complexité mécanique d'un hélicoptère équipé d'un rotor vert devraient être inférieurs par rapport au cas d'hélicoptères classiques. Donc, le système serait plus fiable. Ses coûts d'acquisition, d'exploitation et d'entretien devraient baisser.

Du fait que la palette et son aileron sont situés à proximité de l'axe de rotation du rotor, ils subissent une charge centrifuge plus faible que les autres concepts de surfaces de contrôle sur les pales mentionnés dans le chapitre précédent, qui sont généralement situées aux alentours de 75% *de l'envergure de la pale. En conséquence, le système de commande et le câblage qu'il requière opèrent dans un environnement plus favorable.*

Les pales équipées de surfaces de contrôle requièrent généralement d'importantes modifications au niveau de leur conception. Dans le cas présent, les pales restent intactes. Aucun coût de développement ou de nouvelles lignes d'assemblage n'est nécessaire pour fabriquer les pales. Les palettes, dont l'envergure est beaucoup plus réduite que celle des pales, sont équipées d'actionneurs piezo-électriques et de leurs alimentations. Une liaison mécanique doit être montée entre les palettes et les manchons de pales.

Cependant, le système proposé présente quelques inconvénients. La palette et son aileron génèrent une traînée de profil qui diminue la Figure de Merit (FM) du rotor. Toutefois, ceci ne peut pas contrebalancer la réduction de traînée qui accompagne l'élimination des plateaux cycliques.

La palette et son aileron sont situés à proximité de l'axe de rotation du rotor. Donc, ils subissent une pression dynamique plus basse que des surfaces de contrôle sur la pale typiques se trouvant à 75% *de l'envergure de la pale. Par conséquent, l'efficacité de la palette et de son aileron s'en trouve réduite. En outre, l'assemblage de la palette et de l'aileron pourraient opérer dans la région d'écoulement inversé lorsque l'hélicoptère est en vol avant. Ceci pourrait aussi réduire l'efficacité du système. Ce problème n'est pas considéré dans la présente étude car elle se concentre sur le système en vol stationnaire. Pour éviter ces problèmes, il serait ncessaire d'optimiser la conception du rotor ou d'introduire de grands angles de contrôle en entrée.*

L'aileron peut être actionné par un actionneur piézo-électrique comme indiqué dans ce chapitre. Deux concepts d'actionnement possibles sont présentés: l aileron peut être soit contrôlé par un piezostack ou un piezobender. Dans le cas du piezostack, l'angle de pas de l'aileron est défini par la variation de la longueur de l'actionneur selon un axe. Une liaison mécanique est nécessaire afin de transformer ce mouvement en une rotation. Dans le cas du piezobender, comme son nom l'indique, l'actionneur fléchit. Il transmet ainsi un mouvement de rotation à l'aileron. On peut noter que les mêmes concepts peuvent être appliqués aussi bien à un aileron situé dans la palette elle-même qu'à un aileron positionné derrière le bord de fuite de la palette.

En première approche, il a été choisi que pour 1° *de battement de palette,* 1° *de pas de pale est obtenu. Toutefois, il est possible d'amplifier la réponse de pas des pales par des moyens dynamiques ou mécaniques par exemple. Si, pour un certain degré de battement de palette, la réponse de pas de la pale peut être amplifiée, les exigences sur l'angle de pas de la palette s'en trouvent réduites. Par conséquent, les exigences concernant l'actionneur piezo-électrique seront moins sévères et plus faciles à respecter.*

This chapter describes the design and kinematics of the new swashplateless concept proposed to achieve rotot primary control. A two-bladed rotor is equipped with two paddles and two ailerons. All elements are in the same plane of rotation. Each paddle is located 90° of azimuth forward with respect to its corresponding blade. The aileron is situated behind the paddle trailing-edge. The rotor primary control is achieved though a coupling of the blade pitch angle to the paddle flap angle. Both collective and cylic pitch of the blade are controlled by the paddle. The actuator and aileron dynamics are later exposed. The advantages and drawbacks of the system are then detailed. Finally, the case of three-plus-bladed rotors is investigated.

2.1 Primary control in conventional helicopters

In conventional helicopters, rotors can be tilted in all directions because of the swashplate. This allows the helicopter to perform various maneuvers to cover its entire flight envelop. The swashplate is constituted of a stationary swashplate and of a rotating one (see Figure. 2.1).

Three hydraulic actuators make the stationary swashplate tilt. This inclination is transmitted to the rotating swashplate via the bearings. Each pitch link is attached to the rotating swashplate and is connected to the blade via a pitch horn. When the rotating swashplate goes down (or up), it brings the pitch link down (or up) which transmits the motion to the blade, making it pitch down (or up). If the three actuators provide the same input to the swashplate, the swashplate does not tilt but move down (or up).

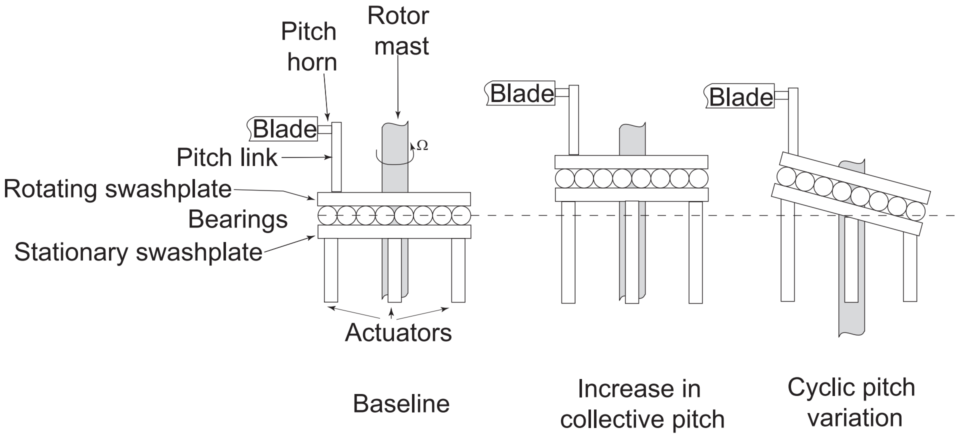

Figure 2.1: Schematic of a swashplate.

Collective pitch angles of all the blades are varied of the same amount at the same time (see Figure. 2.1). If the actuators provide different inputs to the swashplate, it tilts. The pitch input provided to a blade varies then as a function of its azimuth, thereby inducing a cyclic pitch change (see Figure. 2.1). The primary control of the blade is then achieved.

The three actuators permit to move the swashplate either up or down or sideways. Therefore the collective and cyclic pitch of the blade are both controlled by the swashplate. The operating principles behind the functioning of the swashplate are explained in Ref. [190].

This design has been widely used to achieved primary control. However, the main rotor hub and shaft account for 35% of an entire typical aircraft parasitic drag (Ref. [22]). Ref. [191] precises that the drag generated by the rotor hub alone accounts for 25% to 50% of the total parasitic drag area. It is therefore of great interest to reduce the drag generated by the swashplate. As mentionned in Chapter. 1, a decreased drag should prompt significant lower fuel consumption which is economically interesting. A novel swashplateless concept is proposed in the next section.

2.2 Present primary control concept

2.2.1 Design and Kinematics

In the present study, a two-bladed rotor is fitted with two paddles and ailerons located at the end of two bars. The reasons behind the choice of a two-bladed rotor are exposed in a later section.

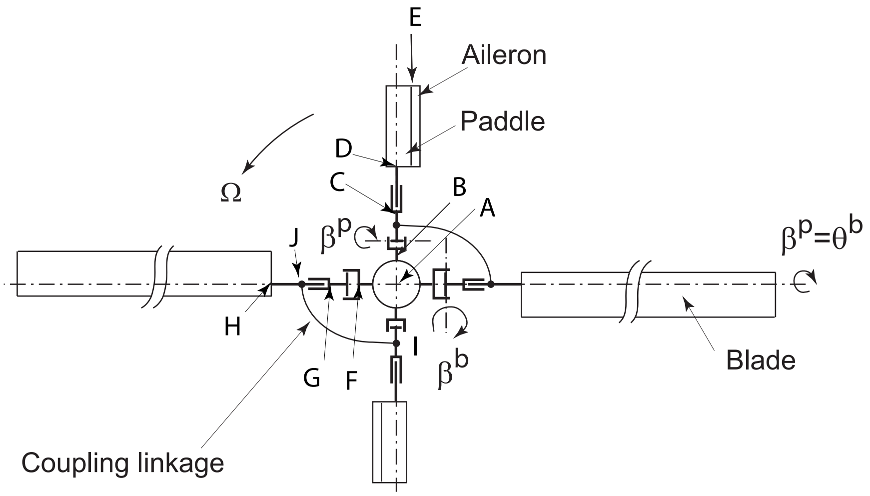

Figure 2.2: Two-bladed rotor equipped with paddles and ailerons.

A typical servopaddle is constituted of a single bar with profiled masses at both ends. If one mass flaps up, the opposite mass will flap down by the same amount. Therefore, the servopaddle can only provide cyclic pitch input to the blades. Thus, a rotor including a servopaddle is usually equipped with a swashplate in order to realize rotor primary control. In the present case, the bars are aligned with each other, perpendicular to the blades pitch axis (see Fig. 2.2). The bars motions are not coupled with each other, therefore the paddles and ailerons can provide both collective and cyclic blade pitch inputs and hence achieve rotor primary control. Note that the blades can move independently from one another, the considered rotor is not a teetering rotor. The system kinematics and links are presented in Figures. 2.3 and 2.4. As mentioned in a later chapter, the grips of the paddles and blades are divided into two parts. The most inboard part of a grip flaps only whereas the most outboard part of a grip can flap and pitch. This is to achieve easy measurements of the flap and pitch angles of the paddle and blade. The blade and paddle can lag about their attachment point to their respective grip.

A PZT-actuated aileron is located behind the trailing-edge of the paddle. When the aileron is deflected by, for instance, a downward angle δ (see Fig. 2.5), it generates an upward lift which in turn creates a nose down moment on the paddle. Assuming a purely articulated paddle, the maximum paddle flap response will occur approximately 90° of azimuth later. As the paddle flap angle β^p (Fig. 2.5) is coupled with the blade pitch angle θ^b (Fig. 2.6), the blade pitch angle will decrease. Note that the blade flap and paddle pitch motions are uncoupled.

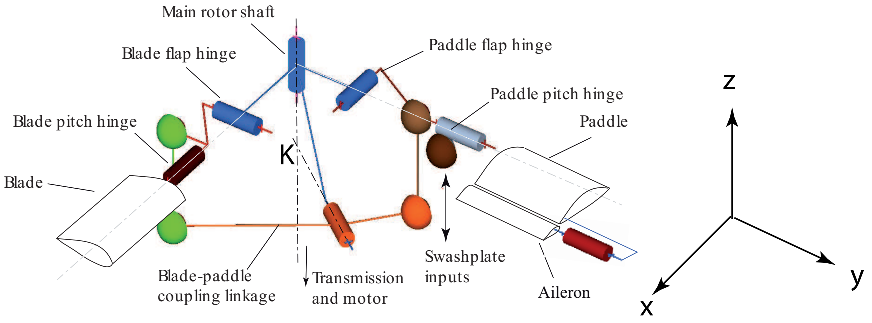

Figure 2.3: Kinematics schematic of the blade, its attached paddle and aileron.

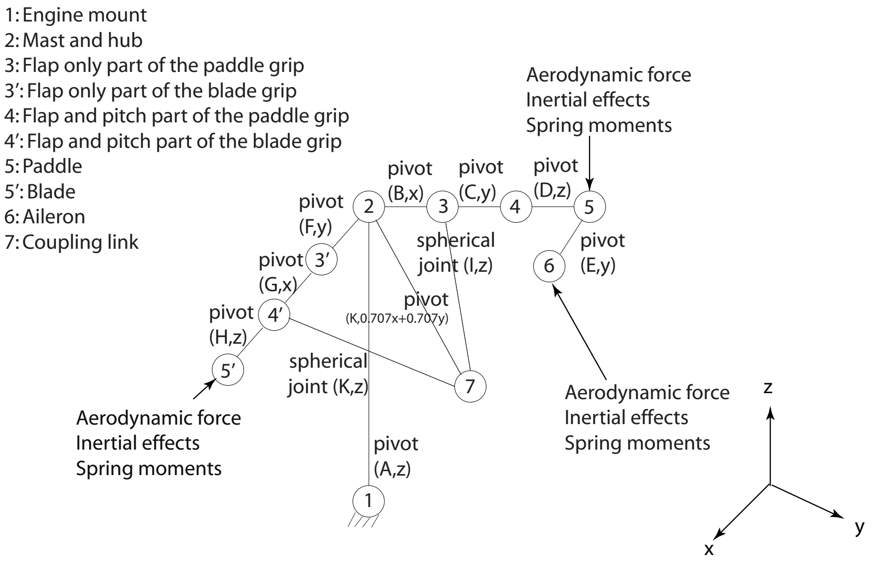

Figure 2.4: Kinematics schematic of the rotor links. Points are seen on Figure. 2.2

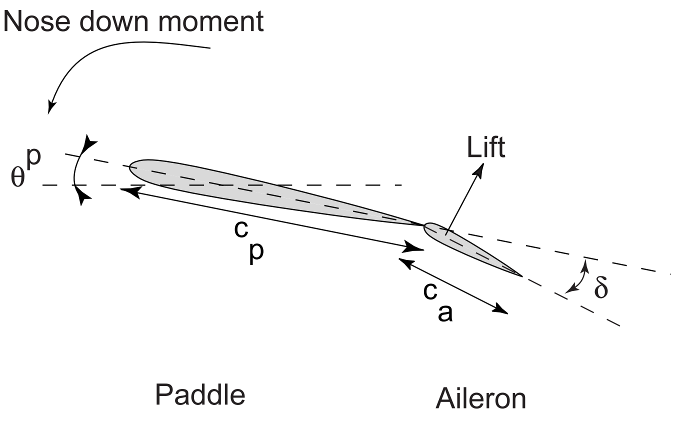

Figure 2.5: Paddle and aileron profiles.

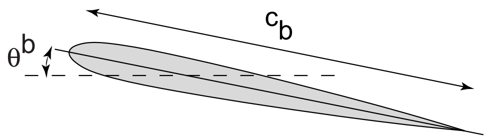

Figure 2.6: Blade profile.

2.2.2 Advantages and Drawbacks

The studied design features several advantages:

1. The servopaddles improve rotor stability (Ref. [1]). The servopaddles, as in the case of the Bell stabilizer and Hiller bar, rotate as the same speed of the rotor blades. The servopaddles have an inertia and aerodynamic force. The servopaddles inertia acts in the same way as a Bell stabilizer bar, it acts like a top. Hence, the servopaddles show a resistance to any change in their plane of rotation and therefore exhibit a gyroscopic stability.
   If the rotor experiences a gust for instance, the rotor blades will respond to that gust. Since the blades and servopaddles are linked, a certain input will be transmitted to the servopaddles. The linkage mechanism attaching the servopaddles to the main rotor pitch is designed in such a way that the servopaddles will input a command back to the rotor blades pitch which will compensate the initial gust effect on the blades.
2. The present rotor does not include a hydraulically actuated swashplate but a piezoelectric-actuated control surface. Consequently, the aircraft empty weight, the parasitic drag and mechanical complexity are expected to decrease compared to conventional helicopters. Hence, the

system would be more reliable and its acquisition, operating and maintenance cost would be lowered.

3. Because the paddle and aileron are located close to the rotor rotation axis, they undergo lower centrifugal loads than other on-blade control surfaces, which are typically located at around 75% of the blade span. As a result, the control system and wiring operate in a more benign environment.
4. On-blade control surfaces typically require extensive modifications of the blade construction. In the present case, the blades remain untouched. No development cost or new assembly lines are necessary to manufacture the blades. Only the paddles, whose span is much shorter than the blade span, are fitted with electrical wires and piezoelectric actuators. A mechanical linkage also needs to be mounted between the paddle and blade grips.

However, the proposed system presents some drawbacks:

1. The paddle and aileron generate a profile drag which decreases the Figure of Merit (FM) of the rotor [1]. However, it cannot counteract the drag decrease that accompanies the swashplate elimination.
2. The paddle and aileron are located close to the rotor rotation axis. Therefore they encounter lower dynamic pressure than typical on-blade control surfaces located at 75% of the blade span. Hence, the efficiency of the {paddle, aileron} system may be reduced [2]. Moreover, the paddle and aileron assembly could operate in the reversed flow region when the helicopter is in forward flight, which could further hamper its efficiency. This issue does not concern the present study as it focuses on hover flight. To avoid these issues, it would be necessary to optimize the design or input larger control angles.

2.2.3 Actuator, aileron dynamics

The aileron can be actuated by a piezoelectric actuator as shown in Fig.2.7. Two possible actuation concepts are presented: the aileron can be either controlled by a piezostack or a piezobender. In the case of the

---

[1] The Figure of Merit is the ratio of the ideal power required to hover over the actual power required to hover. It is an efficiency factor: the greater the aircraft energy losses, the greater the power needed to hover will be, the lower the FM will become. The FM can be used to compare the efficiency of two helicopters.

[2] The expression of the elemental lift dL at any blade section is approximated to $dL = \frac{1}{2}\rho_{air}\Omega^2 r^2 c C_l$ (see Chapter. 3, Ref. [1]). dL varies quadratically with the segment radial location r. If a paddle mid span radial location is at 30% of the blade span, it will encounter a dynamic pressure which is 40% lower than if it was located at 75%

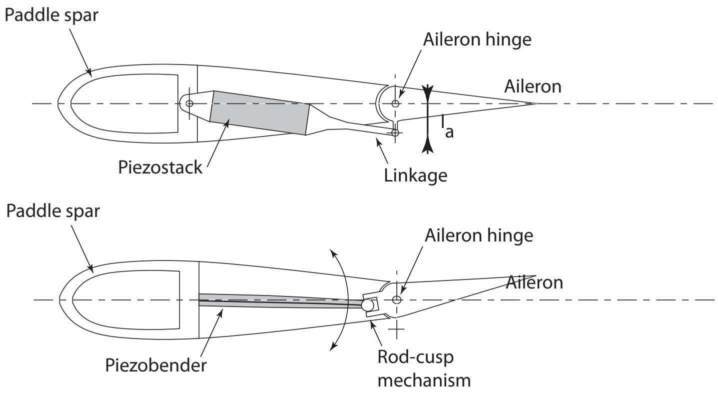

Figure 2.7: Schematic of two possible aileron actuation systems: via piezobender or piezostack.

piezostack, the aileron pitch angle is defined by the change in length of the actuator along an axis. A linkage is necessary to transform this motion into a rotation (see Fig.2.7). In the case of the piezobender, as its name explicitely mentions it: the actuator bends. It transmits, via a cusp on the aileron, a rotational motion to the aileron. It can be noted that the same concepts can be applied to an aileron located behind the trailing-edge of the paddle.

2.2.4 Amplification

As a first simple approach, it was chosen that for 1° of paddle flap, 1° of blade pitch is obtained. However, it is possible to amplify the blade pitch response by dynamic or mechanical means for instance. If for a certain degree of paddle flap, the blade pitch response can be amplified, the requirements on paddle pitch angle decreases. Hence, the requirements on the PZT actuator will be less drastic and more easily met.

2.2.5 Rotor with three or more blades

It is possible to apply the present system to rotors with more than two blades. Two solutions are then available:

1. Two distinct planes of rotation are used: one for the blades, one for the paddles and their attached ailerons. This solution, however, generates drag.
2. The blades, paddles and aileron remain on the same plane of rotation but the angle ζ between a blade and its paddle is reduced. This how-

ever changes the system time constant (Ref. [23]). A variation in time constant implies that an aircraft responsiveness might be altered depensing on the value of ζ. This could reveal to be dangerous if applied to military aircrafts or UAVs. Another consequence of a change in time constant is that the phases of rotor loads and hence responses will vary. In that case, the control system (mechanical or electronic) will have to adjust accordingly. For example, if the phase difference is 90°, then pure lateral cyclic pitch θ_{1c} causes pure β_{1s} (lateral flapping angle). If the phase differs, there will be a mixed response. In addition, a change in rotor loads and responses phases needs to be accounted for in analytical models to ensure correct predictions and controls of vibrations.

The present rotor is equipped with only two blades, two paddles and two ailerons to keep the design simple. If the project is proved to be viable, future work will necessarily include studies on a three-bladed rotor equipped with three paddles and aileron as the concept has to be feasible on the Ecureuil helicopters range.

2.3 Conclusion

This chapter detailed the kinematics and functioning of the swashplateless rotor design. It is equipped with two blades, two paddles and two ailerons. Each blade pitch angle is mechanically coupled to a paddle flap angle. The paddle is actuated by a PZT actuated aileron located behind its trailing-edge. This configuration is expected to increase the rotor stability, to lower the aircraft parasitic drag as well as its weight, mechanical complexity and acquisition, operating and maintenance cost. The paddle and aileron will experience lower centrifugal loads than typical on-blade control surfaces located at 75% of the blade radius. However, the paddle and aileron could decrease the Figure of Merit and if they operate in the reversed flow region in forward flight, their efficiency could be hampered. This flight case is not considered in the present study.

Chapter 3

Analytical models

Une étude complète du comportement du concept de rotor vert dans toutes conditions de vol sera nécessaire avant son application sur un hélicoptère d'échelle 1. Une première étape consiste en l'étude du comportement dynamique de cette configuration en vol stationnaire. Le vol en stationnaire présente une configuration simple de l'écoulement car il y est axisymétrique autour de l'axe rotor. Chaque pale évolue donc dans le même environnement aérodynamique. Le vol en stationnaire est de ce fait une condition de vol plus simple que le vol avant par exemple. La présente étude se concentre donc sur le vol en stationnaire. Si le concept du rotor vert se révèle viable en vol stationnaire, des travaux futurs pourront se concentrer sur d'autres conditions de vol.

Deux modèles analytiques sont présentés dans ce chapitre. Le but de ces modèles est de prédire le comportement dynamique du système étudié. La théorie est validée par des expériences menées sur une maquette de rotor d'échelle réduite en vol stationnaire. Les détails de la validation sont explicités au Chapitre 4. Ces deux modèles analytiques sont:

1. *Le modèle {Palette-Aileron-Pale}: le pas de la palette est commandé par un aileron actionné par des actionneurs PZT. Le battement de la palette est couplé au pas de la pale par un arbre mécanique. Les surfaces portantes de cette configuration sont la pale, la palette et l'aileron.*
2. *Le modèle {Palette-Pale}: identique à l'approche {Palette-Aileron-Pale} à l'exception de l'actionnement de la palette. Le pas de la palette est ici commandé par de petits plateaux cycliques. A ce stade du projet, des tests préliminaires sont nécessaires afin de démontrer la faisabilité du concept avant d'obtenir des financements supplémentaires pour pousser son développement plus avant. La configuration {Palette,Pale} qui représente une conception plus simple et moins coûteuse que l'approche {Palette-Aileron-Pale}, du fait de l'absence d'actionneur intelligent, est donc testée en vol stationnaire. Cette seconde configuration permet d'évaluer l'influence de la palette sur la pale. Le pas de la pale est gouverné par le battement de la palette. Les surfaces portantes de cette configuration sont la pale et la palette. Ce système est testé dans un banc rotor principal en vol stationnaire. Une palette actionnée par de petits plateaux cycliques est en effet moins coûteuse et plus sûre à développer et tester que si l'actionneur utilise des matériaux intelligents.*

Ces deux modèles présentent un certain nombre de caractéristiques communes : les hypothèses, les méthodes utilisées pour parvenir à l'équation de mouvement et celle pour la résoudre par exemple.

Dans les deux modèles, une analyse est menée sur chaque élément des sur-

faces portantes du rotor. Le but de cette analyse est d'étudier les effets de divers paramètres de commande et de la géométrie du système sur le comportement du rotor vert en vol stationnaire stable. Plusieurs méthodes peuvent être utilisées pour calculer l'équation du mouvement du rotor parmi lesquelles la méthode énergétique ou la méthode du principe fondamental de la dynamique par exemple. C'est cette dernière qu'il a été choisi d'utiliser dans la présente étude. De plus, le modèle développé à ce stade de prédimensionnement du projet est analytique et non numérique. En effet, une étude analytique est plus rapide à développer et maîtriser.

Dans le cas du modèle {Palette-Aileron-Pale}, le système compte cinq degrés de liberté: le battement et pas de la pale, le battement et angle de pas de la palette et l'angle de pas de l'aileron. L'élasticité de la pale, palette et de l'aileron n'est pas prise en compte dans ce chapitre. Le système possède un couplage mécanique entre le pas de la pale et le battement de la palette. Le nombre de degrés de liberté est donc réduit à quatre: battement de pale, pas de pale, pas de la palette et pas de l'aileron. Le modèle prédit les valeurs en régime établi :

1. *De la réponse en battement de la pale,*
2. *De la réponse en pas de la pale couplé au battement de la palette,*
3. *De la réponse en pas de la palette,*
4. *De la réponse en pas de l'aileron.*

La commande est le voltage d'entrée de l'actionneur piezo-électrique.

Dans le cas du modèle {Palette-Pale}, on compte quatre degrés de liberté : le battement et pas de la pale, le battement et pas de la palette. Comme dans le cas du modèle {Palette-Aileron-Pale}, le couplage du battement de la palette au pas de la pale réduit le nombre de degrés de liberté. Du fait de ce couplage, le modèle {Palette-Pale} possède trois degrés de liberté: le battement et pas de la pale et pas de la palette. L'approche {Palette-Pale} pronostique les valeurs en régime établi:

1. *De la réponse en battement de la pale,*
2. *De la réponse en pas de la pale couplé au battement de la palette,*
3. *De la réponse en pas de la palette,*

La commande est la force exercée par les petits plateaux cycliques.

Dans le cas de la méthode {Palette-Aileron-Pale} comme dans le cas de l'approche {Palette-Pale}, l'analyse utilise la représentation d'état pour résoudre l'équation du mouvement obtenue en considérant les différents moments des surfaces portantes. Chaque surface portante est ainsi divisée en un nombre précis de segments le long de son envergure. On calcule les charges: aérodynamique, inertielle, et donc centrifuge à chaque segment. Il est à noter qu'un moment de rappel est aussi inclus pour chaque degré de liberté d'une surface portante. La pale et la palette comptent chacune une moment de rappel en pas et en battement. L'aileron, dans le cas de la méthode {Palette-Aileron-Pale}, a un moment de rappel en pas.

Le développement des deux analyses est basé sur les mêmes hypothèses :

1. *L'écoulement est considéré axial car on étudie seulement le vol stationnaire dans la présente étude. On ne prend pas en compte d'éventuelles perturbations.*

2. *Les pertes marginales, causées par les tourbillons en bout de pales, sont négligées. On suppose donc que la portance en bout de pale, ou palette ou aileron, ne décroit pas.*
3. *La pale est considérée rigide avec deux degrés de liberté.*
4. *La palette est considérée rigide avec deux degrés de liberté.*
5. *Les raideurs équivalentes du rappel à plat des pales et palettes sont considérées constantes afin de simplifier l'analyse. Des travaux futurs pourront décrire de manière plus élaborée (en utilisant la méthode des éléments finis par exemple) les systèmes utilisés sur les axes de battement, pas et traînée, telle la butée sphérique sur l'Ecureuil.*
6. *Les forces et moments étudiés sont appliqués suivant les axes principaux. Donc on ne considère que les termes diagonaux de la matrice d'inertie.*

Dans le cas de la méthode {Palette-Aileron-Pale}, l'aileron est considéré rigide avec un degré de liberté. Les effets des charges aérodynamiques, inertielles, et donc centrifuges, sur l'aileron sont étudiés. L'aileron possède aussi un moment de rappel à plat, sa raideur équivalente est considérée constante afin de simplifier l'étude. On représente l'actionneur piezo-électrique de l'aileron comme un ressort au comportement linéaire, donc de raideur constante.

Dans les deux méthodes considérées, les coefficients aérodynamiques sont obtenus en utilisant la théorie de Theodorsen. Theodorsen a développé cette approche pour étudier le phénomène de flottement sur un profil équipé d'un aileron. Dans la présente étude, on utilise les coefficients de portance et de moment en pas du profil et de l'aileron écrit par Theodorsen. Comme précisé au Chapitre 1, les coefficients de Theodorsen présentent l'avantage d'être écrits en fonction de certaines caractéristiques géométriques comme la corde ou la position de l'axe de l'aileron. La présente étude inclut les coefficients de Theodorsen afin de rendre possible une étude paramétrique et la détermination d'une configuration optimale pour maximiser la réponse en pas de pale. Les forces aérodynamiques instationnaires peuvent être incluses à l'analyse à l'aide de la fonction de Theodorsen C(k). Cette fonction doit être intégrée à une étude si le vol avant est considéré. C(k) sera donc nécessairement incluse dans toute analyse future étudiant le comportement du concept proposé dans les conditions de vol avant. k, la fréquence réduite, caractérise le degré d'instabilité de l'écoulement et est exprimée de la manière suivante : $k = \frac{\omega c}{2U}$ *où c est la corde, U la vitesse expérimentée par le segment considéré sur la surface portante et* ω *la vitesse angulaire à laquelle le profil oscille. Si k = 0, l'écoulement est stationnaire, si* $0 \leq k \leq 0.05$ *l'écoulement est considéré comme quasi-stationnaire. Pour k = 0.05 et plus, l'écoulement est considéré instationnaire et les termes instationnaires dans les équations développées ne peuvent pas être négligés. La fréquence réduite est calculée à 75% du rayon de la surface portante considérée dans chacun des deux cas testés et exposés dans le Chapitre 4. Dans le cas de la pale* $k = 0.044$, $k = 0.108$ *pour la palette dans le cas* A' *(voir Chapitre 4) et* $k = 0.062$ *pour la palette dans le cas* B' *(voir Chapitre 4). Dans tous les cas, l'écoulement est ou est presque instationnaire. L'utilisation de la fonction de Theodorsen est donc justifiée.*

L'analyse dans le cas {Palette-Aileron-Pale} comme dans le cas {Palette-

Pale}, peut être divisée en quatre parties :

1. *La géométrie du rotor et les données de masse sont entrées dans le code. Le moyeu est conçu pour que les capteurs puissent y être insérés. De même, les manchons sont définis pour que les pales et palettes y soient introduites. Le rotor comporte des axes de battement et de pas séparés afin que les angles de battement et de pas soient facilement mesurés.*
2. *Les équations de pas et de battement de palette, les équations de pas et de battement des pales et dans le cas {Palette-Aileron-Pale} l'équation de pas de l'aileron sont écrites. Dans chaque équation, seuls les termes du premier ordre sont considérés. En outre, quand les effets d'inerties sont étudiés, pour le type de mouvements impliqués dans l'étude actuelle, deux quantités se dégagent: l'une liée à l'accélération angulaire (ci-après dénommée la force d'inertie) et une liée à la force centrifuge.*
3. *Le couplage entre le battement de la palette et le pas de la pale est écrit,*
4. *L'équation du mouvement est réécrite en utilisant la représentation d'état. La fonction de transfert est définie dans le cas {Palette-Aileron-Pale} comme dans le cas {Palette-Pale}. Les graphiques de Bode sont obtenus. Il est alors possible d'évaluer la réponse en pas de la pale. Cette étude est nécessaire pour s'assurer que de la faisabilité du concept et que les exigences en pas de la pale sont remplies en vol stationnaire. Les travaux futurs pourront se concentrer sur une analyse de stabilité par exemple et incluraient alors une étude des valeurs propres.*

Le détail des équations est donné dans ce chapitre. La configuration {Palette-Pale}, plus simple et moins coûteuse que l'approche {Palette,Aileron,-Pale}, est donc testé en vol stationnaire. Ces tests sont présentés au Chapitre 4. La configuration {Palette,Pale} permet d'évaluer l'influence de la palette sur la pale.

Two analytical models are presented in this chapter. The aim of the analysis is to predict the dynamic behavior of the system investigated. The analysis is validated with experiments performed on a model scale rotor in a hover stand. Details of the validation are presented in chapter 4. The final goal of this analysis is to develop tools to design an optimum paddle configuration to maximize the blade pitch response. The two analytical models described in this chapter are:

1. {Paddle-Aileron-Blade model}: the paddle pitch is controlled by a PZT actuated aileron. The paddle flap is coupled to the blade pitch through a mechanical arm.
2. {Paddle-Blade model}: the paddle pitch is controlled by a small swashplate. The blade pitch is governed by the paddle flap. This model will be tested in the hover stand.

3.1 Paddle-Aileron-Blade study

A comprehensive study of the proposed swashplateless concept behavior under all flight conditions will be necessary before applying it to full scale helicopters. A first step consists in the investigation of the dynamic behavior of this configuration in hover flight. Hover flight presents a simple flow field configuration as the flow field is azimuthally axisymmetric and so each blade encounter the exact same aerodynamic environment. Therefore, hover is a simpler flight condition than forward flight for instance. The present study thus focuses on hover flight. If the concept is found to be viable in hover then future work will focus on other flight conditions.

A paddle and blade element analysis was developed to study the effects of various control settings and system geometry on the system behavior during steady hover flight (Ref. [192], [193]). Several methods can be used to derive the equation of motion of the rotor among which the energy method or the force balance approach for instance. It was chosen to use the force balance approach in the present investigation. In addition, as the present study represent the early stage of the design investigation, the developed model is an analytical one as it is faster to develop and use than a numerical method for instance.

The system counts five degrees of freedom: the blade flap and pitch angles, the paddle flap and pitch angles and the aileron pitch angle. The elasticity of the blade, paddle and aileron is not taken into account as seen later in this section. The system features a mechanical coupling between the paddle flap and blade pitch angles (see Fig. 2.2). The number of degrees of freedom is thus reduced to four: blade flap, blade pitch, paddle pitch and aileron pitch. The model predicts the steady values of the:

1. Blade flap response,
2. Coupled blade pitch and paddle flap response,
3. Paddle pitch response,
4. Aileron pitch response,

to the actuator voltage input. The development of the analysis was based on the following assumptions:

1. The flow is considered purely axial. Only hover flight is considered, therefore, the advanced ratio is equal to zero. Eventual gusts are not taken into account. Hence, the flow is considered purely axial.
2. Tip loss, caused by trail vortices at the tip of a lifting surface, is not taken into account. If included, the effective span of the blade, paddle or aileron decreases and hence their lifting capability at their tip is reduced (Ref. [1]).
3. The blade is considered rigid with two degrees of freedom,
4. The paddle is considered rigid with two degrees of freedom,
5. The aileron is considered rigid with one degree of freedom,

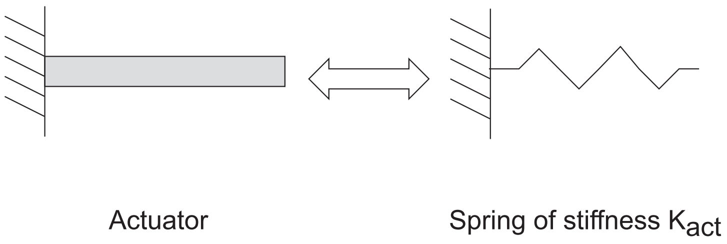

Figure 3.1: Equivalent model between a PZT actuator and a spring.

6. The aileron dynamics are included: the effects of centrifugal, inertial, aerodynamic loads are accounted for, a spring moment is also included in the aileron pitch equation.
7. In the present study, the actuator is supposed to be comparable to a spring of constant stiffness K_{act} (see Fig. 3.1). The actuator is thus represented as a stiffness.
8. The blade, paddle and aileron root stiffness coefficients are considered constant to keep the analysis simple. The aileron root stiffness coefficient is a function of K_{act}. Future work might include more refined analyses including Finite Element Method (FEM) representation of stiffness coefficients.
9. The forces and moments are being applied along the principal axes of the body, therefore only the diagonal terms of the inertia tensor are considered.
10. A constant and uniform inflow is used. We are interested in the effect of small changes in the paddle pitch or aileron pitch input on the rotor responses. The inflow is assumed to be constant during that process. This is because the analysis is a first order model. Hence the influence of the inflow on the rotor responses is not taken into account in the state space form. The rotor is operating in hover. Hence, the constant and uniform inflow is function of the rotor thrust. The thrust produced by the blades is greater than the one generated by the paddles. Thus, we consider the induced velocity in the blade equations.

The hub and grips are designed to fit the blades, paddles and sensors inserted in the hub. The rotor is articulated and the flap and pitch axes are independent so the flap and pitch deflections can be easily measured.

The analysis is based on a state space resolution of the moments applied on the blade, paddle and aileron. To this end, the blade, paddle and aileron are divided into N_{segb}, N_{segp} and N_{sega} elements respectively. Figure. 3.3 shows the blade segments. Centrifugal, inertial and aerodynamic loads are then computed at each segment.

Aerodynamic coefficients are obtained using Theodorsen's theory. This theory rely on the use of Theodorsen's coefficients to determine the aerodynamic lift, pitching moment and hinge coefficients of an airfoil equipped with an aileron. As precised in Chapter. 1, Theodorsen's coefficients present the advantage of being written as functions of certain geometry characteristics such as the chord or the hinge chordwise location. This allows for a parametric study to optimize the paddle geometry charateristics in order to maximize the blade pitch response. Therefore, the present analysis uses Theodorsen's coefficients to compute aerodynamic coefficients. Note that the aileron has a sealed hinge to avoid any significant gap effect between the paddle and its aileron. This is to prevent the pressure to go to zero at the trailing edge of the paddle and at the leading edge of the aileron. In addition, there is no change in airfoil shape in that region.

Unsteady aerodynamics can be included using Theodorsen function C(k) (Refs. [14] and [15]). Theodorsen function has to be incorporated in the study for forward flight calculations and will therefore be necessarily included in any future analysis investigating the concept behavior under forward flight conditions. Theodorsen function can be written as $C(k) = F(k) + iG(k)$ with $F(k)$ the real part, $G(k)$ the imaginary part and k the reduced frequency. k is non dimensional. $F(k)$ and $G(k)$ are both written as Bessel functions. k characterizes the degree of unsteadiness of the flow and is expressed as $k = \frac{\omega c}{2U}$ where c is the chord, U the flow velocity and ω the angular frequency at which the airfoil oscillates. If $k = 0$, the flow is steady, if $0 \leq k \leq 0.05$, the flow is considered quasi-steady. For $k = 0.05$ and above, the flow is considered unsteady and the unsteady terms in the governing equations cannot be neglected. In Chapter. 4, two cases are presented: the two features identical blades but different paddles. The blade radius is of 0.934 m, the first case paddle radius is of 0.374m and the second case paddle radius is of 0.654m. All are rotating at 900 RPM. The following reduced frequencies are computed at 75% of the lifting surface considered:

1. The reduced frequency of the blade at 75% blade radius is of 0.044. k is hence very close to 0.05. The blade is therefore close to encountering unsteady flow.
2. The reduced frequency of first case paddle at 75% paddle radius is of 0.108. The flow encountered by this paddle at this location is thus highly unsteady.
3. The reduced frequency of the second case paddle at 75% paddle radius is of 0.062. The flow encountered by the paddle at this location is thus unsteady.

The fact that all cases studied but one showcase unsteady flow justify the

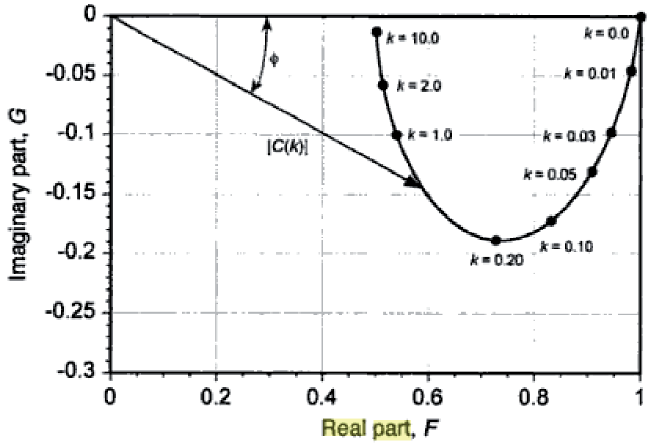

Figure 3.2: Theodorsen function plotted as real and imaginary parts. Ref. [1].

use of Theodorsen function. In the case of an Ecureuil blade, the reduced frequency at 75% blade radius is of 0.044. The flow encountered by the blade at this radial location is close to be unsteady. However, one can note that at more inboard locations, the flow velocity U decreases. This results in higher reduced frequencies. Therefore, more inboard blade radial locations are more at risk to experience unsteady flow. Figure. 3.2 shows the imaginary part of C(k), G, plotted as a function of its real part F. ϕ is the phase lag. Theodorsen function serves to introduce an amplitude reduction and phase lag effect on the circulatory part of the lift response compared to the results obtained in quasi-steady conditions. It is seen from Figure. 3.2 that if k increases up to $k = 0.2$, a phase lag of up to $-14.9°$ and a reduction in lift magniture can occur.

The analysis can be divided into four parts:

1. The rotor geometry and mass data are input into the code,
2. The paddle pitch and flap equations, the blade pitch and flap equations and the aileron equation are written. In each equation, only the 1^{st} order terms are considered. In addition, when investigating the effect of inertia for the type of motions involved in the present study, two quantities emerge: one linked to angular acceleration (hereafter called inertial force) and one linked to the centrifugal force.
3. The paddle flap-blade pitch coupling is written,
4. The equation of motion is rewritten using the state space form. The Bode plots and transfer functions of the degrees of freedom with respect

to the actuator voltage input are plotted. Transfer functions are needed to evaluate the blade pitch response. This first investigation is necessary to ensure the concept is feasible and blade pitch requirements in hover are met. Future work could focus on a stability analysis and include eigen value study.

3.1.1 Step 1 : Inputs

The model is given the following inputs:

1. The rotational speed of the blade, paddle and aileron are assumed to be constant and equal to Ω.
2. The hub, blade, paddle and aileron geometry (see Fig. 3.3).
3. The spring stiffnesses. Some helicopters, such as the Ecureuil, have bearingless hub. In such cases, the hub design features flexures about which flapping, lagging [1] and pitching occur. In the present case, however, the flapping and feathering motions are about hinges that are represented as combined with springs. These springs stiffness is an input of the present analysis. For a first-order analysis such as the present one, the design is kept simple, the spring stiffnesses are considered constant. Future work might lead to a more refined analysis including a Finite Element Method (FEM) analysis of the device providing flap or pitch stiffness.
4. The actuator stiffness. The aileron stiffness is linked to the actuator stiffness. Moreover, the forcing function of the system is written as a function of the actuator stiffness. It is thus necessary to input the actuator stiffness into the analysis.
5. Theodorsen's coefficients for the blade, paddle and aileron.
6. The mass of all elements of the blade, paddle and aileron.

3.1.2 Step 2 : Paddle flap equation

The paddle flap equation is constituted of the centrifugal, inertial, spring and aerodynamic moments. The centrifugal load arises due to the rotor rotation around its axis. The inertial load is generated in the present case whenever the paddle flaps up or down. The derivation for each of these moments is presented below. It is assumed the direction of positive flapping is upward (see Fig. 3.4). The moments that compose the paddle flap equation are determined about the paddle flap axis.

---

[1] Lagging motion is not taken into account in the present analysis but could be accounted for in future studies.

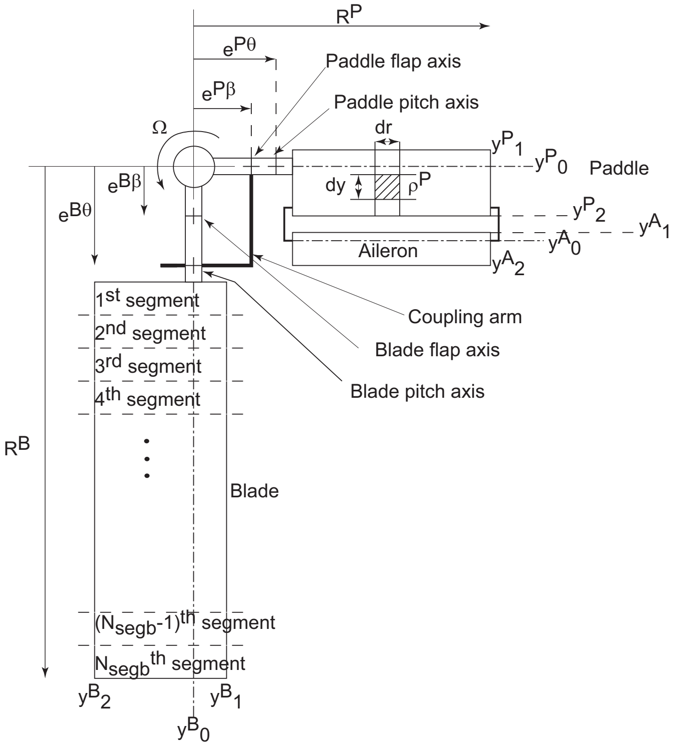

Figure 3.3: Geometry of a paddle, aileron and blade and paddle element characteristics.

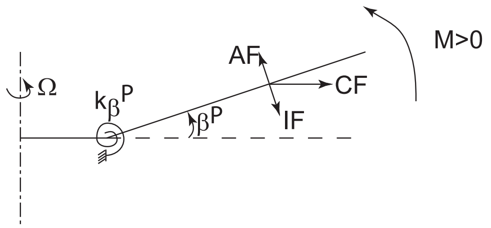

Figure 3.4: Centrifugal force, CF, aerodynamic force AF, inertia force IF of a paddle element undergoing a flapping motion.

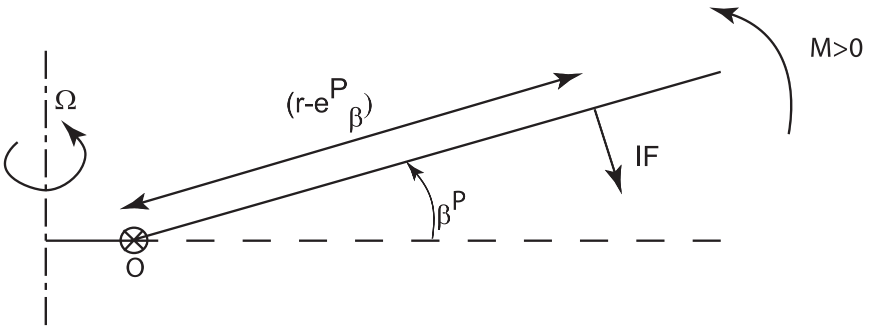

Figure 3.5: Paddle undergoing a flapping motion.

Spring moment

Let β_p^P be the paddle precone angle [1] and k_β^P the paddle flapping root stiffness. The paddle spring moment is written as follows:

$$M_{SP}^P = -k_\beta^P \left(\beta^P - \beta_p^P\right) \tag{3.1}$$

Inertial moment

The paddle inertial moment M_{IF}^P is obtained by summing up two inertial moments $M_{IF_\beta}^P$ and M_{IF_θ} taken about the hinge (point O in Fig. 3.5). $M_{IF_\beta}^P$ is generated when the paddle and aileron undergo a flapping motion and M_{IF_θ} is created when the paddle and aileron are subjected to a pitching motion.

Since the paddle flap equation is studied, the moments are taken about the flap axis (point O in Fig. 3.5). Hence the moment arm of all inertial moments is $\left(r - e_\beta^P\right)$ with r the radial location of the considered paddle segment. When a flapping motion is considered, the paddle and aileron move in the same fashion since the aileron does not have a flap hinge of its own. In addition, it is assumed the paddle and aileron have the same mass per unit area ρ^P. Therefore, the inertial moment created by a flapping motion can be written as follow:

$$M_{IF\beta}^P = -I_\beta^{P,A} \ddot{\beta}^P \tag{3.2}$$

with $I_\beta^{P,A}$ the flap moment of inertia of the paddle and aileron.

---

[1] When the rotor rotates, the centrifugal force causes a downward bending moment on the paddles. The paddles can be given a precone angle so that the aforementioned downward bending moment eliminates upward bending moment at the hub generated by aerodynamic loads.

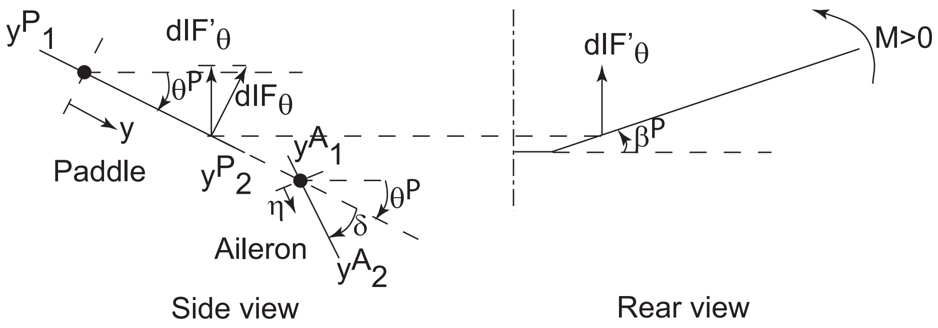

Figure 3.6: Inertial load on a paddle and aileron undergoing pitching motion.

When the paddle is subjected to a pitching motion, an inertial force dIF_θ appears (see Fig. 3.6). Its vertical component dIF'_θ (see Fig. 3.6) contributes to the paddle flap equation. Using the small angle assumption, we can write $dIF_\theta = dIF'_\theta$. The component dIF'_θ can thus be written as below:

$$dIF'_\theta = \rho^P dy dr \ddot{\theta}^P y \tag{3.3}$$

When a pitching motion occurs, the paddle moment of inertia is:

$$M^P_{IF_\theta} = \int_{e^P_\beta}^{R^P} \left(\int_{y^P_1}^{y^P_2} \rho^P y \ddot{\theta}^P \left(r - e^P_\beta\right) dy \right) dr \tag{3.4}$$

with R^P the paddle radius.

Similarly, when the aileron undergoes a pitching motion, the resulting inertial force has a component dIF'^A_θ contributing to the paddle flap equation:

$$dIF'^A_\theta = \rho^A d\eta dr \left(y\ddot{\theta}^P + \eta\ddot{\delta} \right) \tag{3.5}$$

The aileron moment of inertia when a pitching motion occurs is therefore:

$$M^A_{IF_\theta} = \int_{e^P_\beta}^{R^P} \left(\int_{y^A_1}^{y^A_2} \rho^A \left(y\ddot{\theta}^P + \eta\ddot{\delta} \right) \left(r - e^P_\beta\right) d\eta \right) dr \tag{3.6}$$

Summing up the paddle and aileron moments of inertia when under a pitching motion, we obtain:

$$\begin{aligned} M^P_{IF_\theta} + M^A_{IF_\theta} = & \int_{e^P_\beta}^{R^P} \int_{y^P_1}^{y^P_2} \rho^P y \ddot{\theta}^P \left(r - e^P_\beta\right) dy \\ & + \int_{e^P_\beta}^{R^P} \int_{y^A_1}^{y^A_2} \rho^A y \ddot{\theta}^P \left(r - e^P_\beta\right) d\eta + \int_{e^P_\beta}^{R^P} \int_{y^A_1}^{y^A_2} \rho^A \eta \ddot{\delta} \left(r - e^P_\beta\right) d\eta dr \end{aligned} \tag{3.7}$$

If m^P is the paddle mass per unit length, y_{CG} the center of mass of the paddle spanwise element considered, then $y_{CG}m^P = y_{CG}\sum_i \rho_i^P = \sum_i \rho_i^P y_i$. Equation. 3.7 becomes:

$$\begin{aligned} M_{IF_\theta} &= \int_{e_\beta^P}^{R^P} \left(r - e_\beta^P\right) \left(\ddot{\theta}^P \int_{y_1^P}^{y_2^A} \rho^P y dy + \ddot{\delta} \int_{y_1^A}^{y_2^A} \rho^A \eta d\eta\right) dr \\ &= \int_{e_\beta^P}^{R^P} \left(r - e_\beta^P\right) \left(\ddot{\theta}^P y_{CG}^{P,A}\, m^{P,A} + \ddot{\delta}\, \eta_{CG}\, m^A\right) dr \\ &= \overline{S_\theta^{P,A}}\, \ddot{\theta}^P + \overline{S_A}\, \ddot{\delta} \end{aligned} \tag{3.8}$$

with $\overline{S_\theta^{P,A}}$ the paddle and aileron first radial moment and $\overline{S_A}$ the aileron first radial moment. The paddle inertial moment M_{IF}^P is then obtained from Equations. 3.2 and. 3.8:

$$M_{IF}^P = -I_\beta^{P,A}\ddot{\beta}^P + \overline{S_\theta^{P,A}}\, \ddot{\theta}^P + \overline{S_A}\, \ddot{\delta} \tag{3.9}$$

Centrifugal moment

The centrifugal moment is created when the paddles rotate around the rotor shaft axis. If the paddle has flapped up, then the centrifugal load will generate a downward bending moment. At the contrary, if the paddle has flapped down, the centrifugal forces will generate an upward bending moment. The paddle centrifugal moment M_{CF}^P is composed of two centrifugal moments $M_{CF\beta}^P$ and $M_{CF\theta}^P$. The former is created when the paddle and aileron undergo a flapping motion and the latter is generated when the paddle and aileron are subjected to a pitching motion.

Let's investigate first a paddle and aileron subjected to a flapping motion (see Fig. 3.7). At any point A of the paddle or aileron, a centrifugal force dCF is applied. This force counts two components: dCF_s and dCF_2 (see top view in Fig. 3.7). dCF_s has a component dCF_d (see side view in Fig. 3.7) which contributes to the paddle flap equation. Using the small angle assumption, dCF_d is written as:

$$dCF_d = \sin\beta^P dCF_s = \beta^P dCF_s \tag{3.10}$$

Based on Fig. 3.7, dCF_s can be expressed as follow:

$$dCF_s = \cos\hat{w}\, dCF = \frac{r}{\sqrt{r^2 + y^2}} dCF \tag{3.11}$$

The mass per unit area of the paddle and aileron are assumed to be equal. dCF can then be written as:

$$dCF = \rho^P dydr\Omega^2\sqrt{r^2 + y^2} \tag{3.12}$$

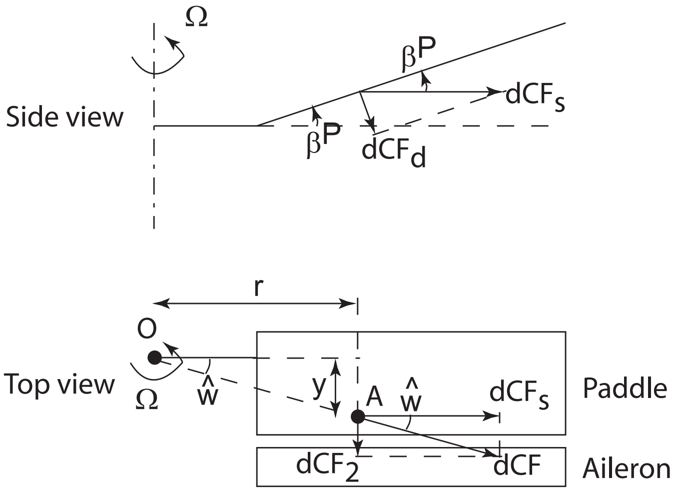

Figure 3.7: Centrifugal load on a paddle and aileron undergoing a flapping motion.

Hence, Equation. 3.10 becomes:

$$dCF_d = \rho^P dy dr \Omega^2 \beta^P r \tag{3.13}$$

Since the paddle flap equation is studied, the moment arm for the centrifugal moment considered is $\left(r - e^P_\beta\right)$. Using Equation. 3.13, the paddle centrifugal moment due to a flapping motion $M^P_{CF\beta}$ is expressed as below:

$$\begin{aligned} M^P_{CF\beta} &= -\Omega^2 \beta^P \int_{e^P_\beta}^{R^P} \left(r - e^P_\beta\right) r \left(\int_{y^A_2}^{y^P_1} \rho^P dy \right) dr \\ &= -\Omega^2 \beta^P \left[\int_{e^P_\beta}^{R^P} m^{P,A} \left(r - e^P_\beta\right)^2 dr + e^P_\beta \int_{e^P_\beta}^{R^P} m^{P,A} \left(r - e^P_\beta\right) dr \right] \\ &= -\beta^P \Omega^2 \left(I^{P,A}_\beta + e^P_\beta S^{P,A}_\beta \right) \end{aligned} \tag{3.14}$$

with $S^{P,A}_\beta = \int_{e^P_\beta}^{R^P} m^{P,A} \left(r - e^P_\beta\right) dr$ the paddle and aileron first flap moment.

If the paddle and aileron undergo a pitching motion, two different moments will be generated and contribute to the paddle flap equation: $M^P_{CF\theta}$

and $M^A_{CF\delta}$. These two moments are respectively written as:

$$\begin{aligned} M^P_{CF\theta} &= \int_{e^P_\beta}^{R^P} \int_{y^P_1}^{y^P_2} \rho^P dydr\Omega^2 ry\theta^P \\ &= \Omega^2\theta^P \left[\int_{e^P_\beta}^{R^P} y^P_{CG} m^P rdr\right] \\ &= \Omega^2\theta^P \left[\int_{e^P_\beta}^{R^P} y^P_{CG} m^P \left(r - e^P_\beta\right) dr + e^P_\beta \int_{e^P_\beta}^{R^P} y^P_{CG} m^P dr\right] \\ &= \Omega^2\theta^P \left(\overline{S^P_{theta}} + e^P_\beta S^P_\theta\right) \end{aligned} \tag{3.15}$$

with y^P_{CG} the paddle element center of gravity chordwise location, m^P the paddle mass per unit length, $\overline{S^P_{theta}}$ the paddle first radial moment and S^P_θ the paddle zeroth radial moment.

$$\begin{aligned} M^A_{CF\delta} &= \int_{e^P_\beta}^{R^P} \int_{y^A_1}^{y^A_2} \rho^A dydr\Omega^2 r\eta\delta \\ &= \Omega^2\delta \int_{e^P_\beta}^{R^P} \eta^A_{CG} m^A rdr \\ &= \Omega^2\delta \left[\int_{e^P_\beta}^{R^P} \eta^A_{CG} m^A \left(r - e^P_\beta\right) + e^P_\beta \int_{e^P_\beta}^{R^P} \eta^A_{CG} m^A dr\right] \\ &= \Omega^2\delta \left(\overline{S_a} + e^P_\beta S_a\right) \end{aligned} \tag{3.16}$$

where $\overline{S_a}$ is the aileron first radial moment and S_a is the aileron zeroth radial moment. When undergoing a pitching motion, the paddle and aileron centrifugal moments $M_{CF\theta}$ is therefore:

$$M_{CF\theta} = \Omega^2\theta^P \left(\overline{S^P_\theta} + e^P_\beta S^P_\theta\right) + \Omega^2\delta \left(\overline{S_a} + e^P_\beta S_a\right) \tag{3.17}$$

The paddle centrifugal moment is obtained from Equations. 3.14 and. 3.17:

$$\begin{aligned} M^P_{CF} = -\beta^P\Omega^2 \left(I^{P,A}_\beta + e^P_\beta S^{P,A}_\beta\right) + \Omega^2\theta^P \left(\overline{S^P_\theta} + e^P_\beta S^P_\theta\right) \\ + \Omega^2\delta \left(\overline{S_a} + e^P_\beta S_a\right) \end{aligned} \tag{3.18}$$

Paddle aerodynamic flapping moment

The aerodynamic moment about the flap hinge $M^P_{AF\beta}$ depends on the distribution of lift L across the blade:

$$M^{P\beta}_{AF} = \int_{e^{P\beta}}^{R^P} L \left(r - e^{P\beta}\right) \tag{3.19}$$

It is customary in first-order analyses like the present one to take the elementary lift on the paddle segment considered to be normal to the paddle to calculate flapping moments (Ref [1, 191]).

The aileron flapping motion is not independant from the paddle flapping motion. Thus, when the paddle flaps, it forces the aileron to flap as well. The following equation is using the lift coefficient for a thin airfoil and aileron in an incompressible flow. Thin airfoil theory implies the aerodynamic forces of the airfoil and aileron can be added up. As a result, the lift L is the one generated over the whole paddle and aileron:

$$L = \frac{1}{2}\rho_{air}U^2 c_{tot}(C_n + C_n^f)dr \tag{3.20}$$

with c_{tot} the total chord of the paddle and aileron. The aerodynamic coefficient $C_n + C_n^f$ consistst of C_n the unsteady lift coefficient on a thin airfoil and C_n^f the additional term due to the aileron. These two coefficients can be written as follow (Ref. [1]):

$$C_n = 2\pi C(k)\left\{\frac{\dot{h}^P}{U} + \alpha^P + b\left(\frac{1}{2} - a\right)\frac{\dot{\alpha}^P}{U}\right\} + \frac{\pi b}{U^2}\left(U\dot{\alpha}^P + \ddot{h}^P - ba\ddot{\alpha}^P\right) \tag{3.21}$$

$$C_n^f = 2\pi C(k)\left\{\frac{T_{10}\delta}{\pi} + \frac{bT_{11}\dot{\delta}}{2\pi U}\right\} + \frac{b}{U^2}\left(-UT_4\dot{\delta} - bT_1\ddot{\delta}\right) \tag{3.22}$$

with b the semi chord of the paddle and aileron. a is the distance in semichord between the paddle pitch axis and the mid chord of the paddle and aileron. The coefficients T_1, T_4, T_{10} and T_{11} come from Theodorsen's theory (Ref. [13]). As precised in Chapter. 1, Theodorsen's coefficients were initially developed to be used in a flutter study. However, since they are functions of certain geometry characteristics, such as the total chord for instance, they allow for a parametric study to be carried out to determine the optimum configuration to maximize the blade pitch response. Because of this, Theodorsen's aerodynamic coefficients are preferred over thin airfoil theory aerodynamic coefficients and used in the present analysis.

h^P is the heaving motion of the paddle (Fig. 3.8) and measured positive upwards. If the paddle flap angle is considered small, then h^P can be written as:

$$h^P = \left(r - e_\beta^P\right) sin(\beta^P) = \left(r - e_\beta^P\right)\beta^P \tag{3.23}$$

The paddle angle of attack is:

$$\alpha^P = \theta^P - \frac{U_P^P}{U_T^P} \approx \theta^P - \frac{\dot{\beta}^P}{\Omega} + \frac{v_i}{\Omega r} \tag{3.24}$$

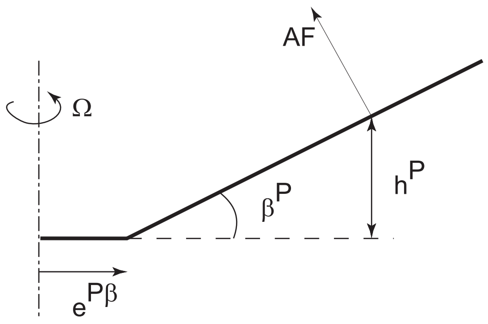

Figure 3.8: Paddle flapping motion.

because the out-of-plane velocity U_P^P is considered lesser than the in-plane velocity U_T^P (Fig. 3.9). v_i is the induced velocity. As we consider hover flight conditions, the induced velocity is assumed to be equal to the hovering velocity v_h, hence $v_i = \sqrt{\left(\frac{T}{2\rho_{air}A}\right)}$, with T the thrust, and A the area. The surface area of a blade is much larger than the one of a paddle. Hence, a small change in pitch will cause a negligible induced velocity of the paddle compared to the induced velocity of the blade. Therefore, the induced velocity is taken into account in the blade equations only.

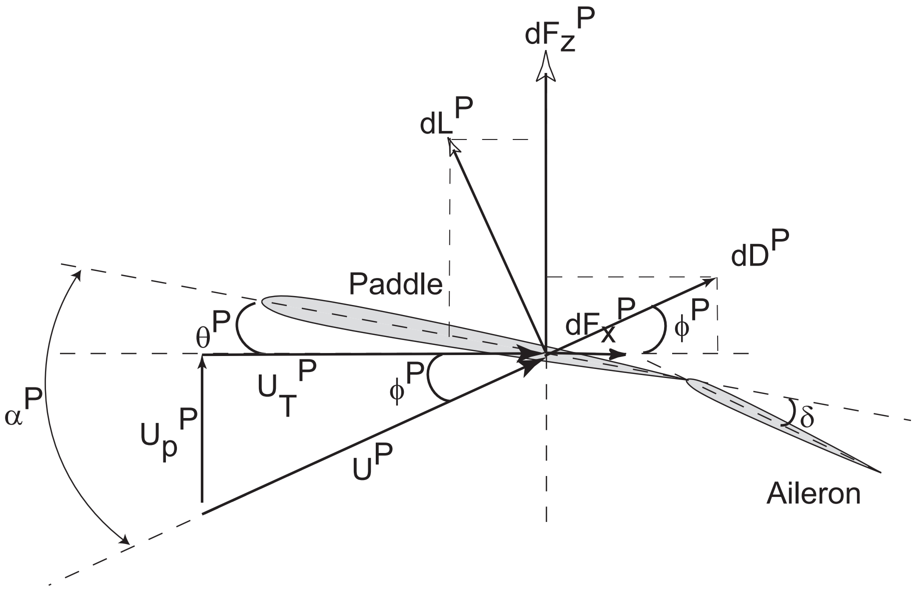

Figure 3.9: Paddle and aileron profile and aerodynamic angles.

The paddle aerodynamic moment is therefore written as follow:

$$\begin{aligned} M^P_{AF\beta} = & \int_{e^P\beta}^{R^P} \ddot{\beta}^P \left[\frac{1}{8}\, c_{tot}^2\, \pi\, \left(e_\beta^P - r\right) \left(2e_\beta^P + \left(2 + c^P - 2c_{tot}\right) C[k] r\right)\, \rho_{air}\right] dr \\ & + \int_{e^P\beta}^{R^P} \dot{\beta}^P \left[C[k]\, c_{tot}\, e_\beta^P\, \Omega\, \pi\, \left(e_\beta^P - r\right)\, r\, \rho_{air}\right] dr \\ & + \int_{e^P\beta}^{R^P} \ddot{\theta}^P \left[\frac{1}{32}\, \left(2c_{tot} - c^P\right)\, c_{tot}^3\, \pi\, \left(e_\beta^P - r\right)\, \rho_{air}\right] dr \\ & + \int_{e^P\beta}^{R^P} \dot{\theta}^P \left[\frac{1}{8}\, \left(2 + \left(2 + c^P - 2c_{tot}\right)\, C[k]\right)\, c_{tot}^2\, \Omega\, \pi\, \left(r - e_\beta^P\right)\, r\, \rho_{air}\right] dr \\ & + \int_{e^P\beta}^{R^P} \theta^P \left[C[k]\, c_{tot}\, \Omega^2\, \pi\, r^2\, \left(r - e_\beta^P\right)\, \rho_{air}\right] dr \\ & + \int_{e^P\beta}^{R^P} \ddot{\delta} \left[\frac{1}{8}\, c_{tot}^3\, \left(e_\beta^P - r\right)\, \rho_{air}\, T_1\right] dr \\ & + \int_{e^P\beta}^{R^P} \dot{\delta} \left[\frac{1}{4}\, c_{tot}^2\, \Omega\, \left(r - e_\beta^P\right)\, r\, \rho_{air}\, \left(C[k]\, T_{11} - T_4\right)\right] dr \\ & + \int_{e^P\beta}^{R^P} \delta \left[C[k]\, c_{tot}\, \Omega^2\, r^2\, \left(r - e_\beta^P\right)\, \rho_{air}\, T_{10}\right] dr \end{aligned} \tag{3.25}$$

The paddle flap equation is written from the moment equilibrium:

$$M^P_{SP} + M^P_{IF} + M^P_{CF} + M^P_{AF\beta} = 0 \tag{3.26}$$

We assume the paddle precone angle is equal to zero. Using Equations. 3.1, 3.9, 3.18 and 3.25, Equation. 3.26 becomes:

$$\begin{aligned} \ddot{\beta}^P C^{Pflap}_{\ddot{\beta}^P} + \ddot{\theta}^P C^{Pflap}_{\ddot{\theta}^P} + \ddot{\delta} C^{Pflap}_{\ddot{\delta}} + \dot{\beta}^P C^{Pflap}_{\dot{\beta}^P} + \dot{\theta}^P C^{Pflap}_{\dot{\theta}^P} & \\ + \dot{\delta} C^{Pflap}_{\dot{\delta}} + \beta^P C^{Pflap}_{\beta^P} + \theta^P C^{Pflap}_{\theta^P} + \delta C^{Pflap}_{\delta} & = 0 \end{aligned} \tag{3.27}$$

with the coefficients $C^{Pflap}_{\ddot{\beta}^P}$, $C^{Pflap}_{\ddot{\theta}^P}$, $C^{Pflap}_{\ddot{\delta}}$, $C^{Pflap}_{\dot{\beta}^P}$, $C^{Pflap}_{\dot{\theta}^P}$, $C^{Pflap}_{\dot{\delta}}$,

$C_{\beta^P}^{Pflap}$, $C_{\theta^P}^{Pflap}$ and C_{δ}^{Pflap} respectively defined as:

$$\begin{cases} C_{\ddot{\beta}^P}^{Pflap} = -I_\beta^{P,A} + \int_{e^{P\beta}}^{R^P} \left[\frac{1}{8}\, c_{tot}^2\, \pi\, \left(e_\beta^P - r\right) \left(2e_\beta^P + \left(2 + c^P - 2c_{tot}\right) C[k] r\right)\, \rho_{air}\right] dr \\ C_{\ddot{\theta}^P}^{Pflap} = \overline{S_\theta^{P,A}} + \int_{e^{P\beta}}^{R^P} \left[\frac{1}{32}\, \left(2c_{tot} - c^P\right)\, c_{tot}^3\, \pi\, \left(e_\beta^P - r\right)\, \rho_{air}\right] dr \\ C_{\ddot{\delta}}^{Pflap} = \overline{S_A} + \int_{e^{P\beta}}^{R^P} \left[\frac{1}{8}\, c_{tot}^3\, \left(e_\beta^P - r\right)\, \rho_{air}\, T_1\right] dr \\ C_{\dot{\beta}^P}^{Pflap} = \int_{e^{P\beta}}^{R^P} \left[C[k]\, c_{tot}\, e_\beta^P\, \Omega\, \pi\, \left(e_\beta^P - r\right)\, r\, \rho_{air}\right] dr \\ C_{\dot{\theta}^P}^{Pflap} = \int_{e^{P\beta}}^{R^P} \left[\frac{1}{8}\, \left(2 + \left(2 + c^P - 2c_{tot}\right)\, C[k]\right)\, c_{tot}^2\, \Omega\, \pi\, \left(r - e_\beta^P\right)\, r\, \rho_{air}\right] dr \\ C_{\dot{\delta}}^{Pflap} = \int_{e^{P\beta}}^{R^P} \left[\frac{1}{4}\, c_{tot}^2\, \Omega\, \left(r - e_\beta^P\right)\, r\, \rho_{air}\, \left(C[k]\, T_{11} - T_4\right)\right] dr \\ C_{\beta^P}^{Pflap} = -k_\beta^P - \Omega^2 \left(I_\beta^{P,A} + e_\beta^P S_\beta^{P,A}\right) \\ C_{\theta^P}^{Pflap} = \Omega^2 \left(\overline{S_\theta^P} + e_\beta^P S_\theta^P\right) + \int_{e^{P\beta}}^{R^P} \left[C[k]\, c_{tot}\, \Omega^2\, \pi\, r^2\, \left(r - e_\beta^P\right)\, \rho_{air}\right] dr \\ C_{\delta}^{Pflap} = \Omega^2 \left(\overline{S_a} + e_\beta^P S_a\right) + \int_{e^{P\beta}}^{R^P} \left[C[k]\, c_{tot}\, \Omega^2\, r^2\, \left(r - e_\beta^P\right)\, \rho_{air}\, T_{10}\right] dr \end{cases} \tag{3.28}$$

3.1.3 Paddle pitch equation

The paddle pitch equation obtained from the moment equilibrium of the spring, inertial, centrifugal and aerodynamic moments. The derivation of each of these moments is presented below. It is assumed the direction of positive pitching is nose up. The moments that compose the paddle pitch equation are defined about the paddle pitch axis.

Spring moment

Let θ_0^P be the initial paddle pitch angle and k_θ^P the paddle pitching stiffness. The paddle spring moment is written as follows:

$$M_{SP}^P = -k_\theta^P \left(\theta^P - \theta_0^P\right) \tag{3.29}$$

Inertial moment

The paddle inertial moment M_{IF}^P is obtained from the sum of three inertial moments $M_{IF\beta}^P$, $M_{IF\theta}^P$ and $M_{IF\delta}^P$. $M_{IF\beta}^P$ is generated when the paddle and aileron undergo a flapping motion. $M_{IF\theta}^P$ and $M_{IF\delta}^P$ are created when the paddle and aileron pitch.

As mentionned in a previous section, when a flapping motion is considered, the paddle and aileron move in the same fashion since the aileron does not have a flap hinge. The inertial force applied on an element of the paddle or of the aileron is $dIF_\beta = \rho^P dydr\ddot{\beta}^P \left(r - e^P_\beta\right)$. Therefore the inertial moment created by a flapping motion is:

$$\begin{aligned} M^{P,A}_{IF\beta} &= \int_{e^P_\theta}^{R^P} \int_{y^P_1}^{y^A_2} \rho^P dydr\ddot{\beta}^P \left(r - e^P_\beta\right) y \\ &= \ddot{\beta}^P \int_{e^P_\theta}^{R^P} y^{P,A}_{CG} m^{P,A} \left(r - e^P_\beta\right) dr \\ &= \ddot{\beta}^P \overline{S^{P,A}_\theta} \end{aligned} \tag{3.30}$$

with $\overline{S^{P,A}_\theta}$ the first radial moment of the paddle and aileron.

When the paddle is subjected to a pitching motion, an inertial force dIF_θ appears (see Fig. 3.6) and is defined as:

$$dIF_\theta = \rho^P dydry\ddot{\theta}^P \tag{3.31}$$

The inertial moment generated when the paddle undergoes a pitching motion is thus written as:

$$\begin{aligned} M^P_{IF\theta} &= -\int_{e^P_\theta}^{R^P} \int_{y^P_1}^{y^P_2} \rho^P dydry^2\ddot{\theta}^P \\ &= -\int_{e^P_\theta}^{R^P} i^P_\theta \ddot{\theta}^P dr \\ &= -I^P_\theta \ddot{\theta}^P \end{aligned} \tag{3.32}$$

with i^P_θ the paddle second moment of mass per unit span and I^P_θ the paddle zeroth radial moment.

Similarly when the aileron undergoes a pitching motion, an inertial force dIF^A_θ is applied on each of its element. Let dIF'^A_θ be the component of dIF^A_θ perpendicular to the paddle (see Fig. 3.10). dIF'^A_θ contributes to the paddle pitch equation and is defined by:

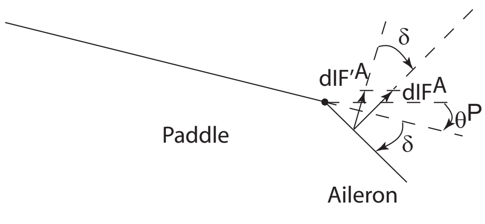

Figure 3.10: Paddle and aileron undergoing a pitching motion.

$$dIF'^A = dIF^A \cos\delta \; = dIF^A = \rho^A d\eta dr\eta\ddot{\delta} \tag{3.33}$$

The inertial moment generated when the aileron undergoes a pitching motion is hence written as:

$$\begin{aligned}
M_{IF\theta}^{A} &= -\int_{e_\theta^P}^{R^P}\int_{y_1^A}^{y_2^A} \rho^A d\eta dr \eta \ddot{\delta}\left(y_h+\eta\right) \\
&= -\ddot{\delta}\int_{e_\theta^P}^{R^P}\int_{y_1^A}^{y_2^A} \rho^A d\eta dr \eta y_h - \ddot{\delta}\int_{e_\theta^P}^{R^P}\int_{y_1^A}^{y_2^A} \rho^A d\eta dr \eta^2 \\
&= -\ddot{\delta}\left[\int_{e_\theta^P}^{R^P} m^A \eta_{CG}^A y_h dr + I_a\right] \\
&= -\ddot{\delta}\left(y_h S_a + I_a\right)
\end{aligned} \tag{3.34}$$

with I_a and S_a the aileron zeroth radial moments.

The inertial moment resulting from a pitching motion is obtained by summing up Equations. 3.32 and 3.34:

$$M_{IF\theta}^{P} + M_{IF\theta}^{A} = -I_\theta^P \ddot{\theta}^P - \ddot{\delta}\left(y_h S_a + I_a\right) \tag{3.35}$$

The paddle inertial moment M_{IF}^{P} is then obtained from Equations. 3.30 and 3.36:

$$M_{IF}^{P} = \ddot{\beta}^P \overline{S_\theta^{P,A}} - \ddot{\theta}^P I_\theta^P - \ddot{\delta}\left(y_h S_a + I_a\right) \tag{3.36}$$

Centrifugal moment

The paddle centrifugal moment $M_C^P F$ is composed of three centrifugal moments $M_{CF\beta}^{P}$, $M_{CF\theta}^{P}$ and $M_{CF\theta}^{A}$. $M_{CF\beta}^{P}$ is generated when the paddle and aileron are subjected to a flapping motion. $M_{CF\theta}^{P}$ and $M_{CF\theta}^{A}$ are created when the paddle and aileron undergo a pitching motion.

When the paddle and aileron are subjected to a flapping motion, a centrifugal force dCF is applied on each of their elements:

$$dCF = \rho^P dy dr \Omega^2 r \beta^P \tag{3.37}$$

The centrifugal moment resulting from dCF is therefore:

$$\begin{aligned}
M_{CF\beta}^{P} &= \int_{e_\theta^P}^{R^P}\int_{y_1^P}^{y_2^A} \rho^P dy dr \Omega^2 r \beta^P y \\
&= \Omega^2 \beta^P \int_{e_\theta^P}^{R^P} m^{P,A} y_{CG}^{P,A} r dr \\
&= \Omega^2 \beta^P \int_{e_\theta^P}^{R^P} m^{P,A} y_{CG}^{P,A}\left(r - e_\theta^P\right) dr + \Omega^2 \beta^P e_\theta^P \int_{e_\theta^P}^{R^P} m^{P,A} y_{CG}^{P,A} dr \\
&= \Omega^2 \beta^P \left(\overline{S_\theta^{P,A}} + e_\theta^P S_\theta^{P,A}\right)
\end{aligned} \tag{3.38}$$

with $S_\theta^{P,A}$ the paddle and aileron zeroth radial moment.

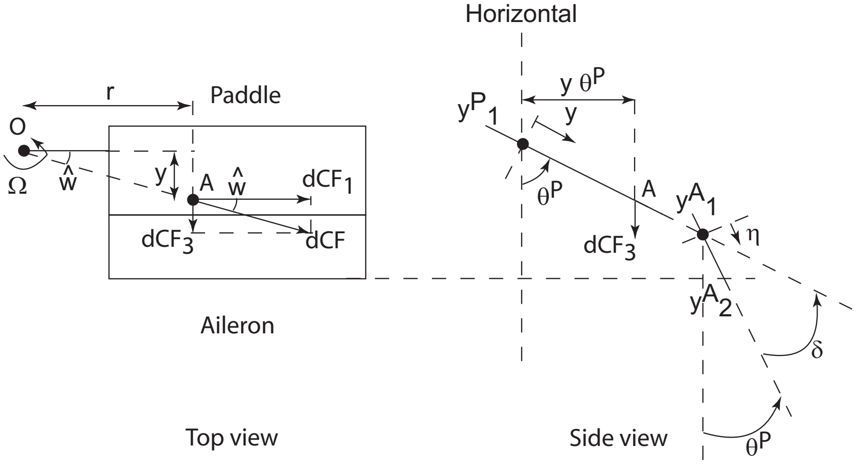

Figure 3.11: Paddle and aileron undergoing centrifugal load.

When the paddle undergoes a pitching motion, a propeller moment is generated (see Fig. 3.11). A centrifugal force dCF is applied on each element of the paddle. Its component dCF_3 contributes to the paddle pitch equation (see Fig. 3.11) and is defined as:

$$dCF_3 = \rho^P dydr\Omega^2 y \tag{3.39}$$

The centrifugal moment generated by dCF_3 on the paddle is thus written as:

$$\begin{aligned} M_{CF\theta}^P &= -\int_{e_\theta^P}^{R^P} \int_{y_1^P}^{y_2^P} \rho^P dydr\Omega^2 yy\theta^P \\ &= -\int_{e_\theta^P}^{R^P} i_\theta^P \Omega^2 \theta^P dr \\ &= -I_\theta^P \Omega^2 \theta^P \end{aligned} \tag{3.40}$$

Similarly, when a centrifugal force dCF is applied on an element of the aileron, its component dCF_3' contributes to the paddle pitch equation. The moment arm here is $y_h \sin\theta^P + \eta \sin\left(\theta^P + \delta\right)$. The propeller moment generated on the aileron is defined as:

$$\begin{aligned}
M_{CF\theta}^{A} &= -\int_{e_\theta^P}^{R^P}\int_{y_1^A}^{y_2^A} \rho^A d\eta dr \Omega^2 \left(y_h+\eta\right)\left[y_h\theta^P+\eta\left(\theta^P+\delta\right)\right] \\
&= -\int_{e_\theta^P}^{R^P}\int_{y_1^A}^{y_2^A} \rho^A d\eta dr \Omega^2 y\left[\left(y_h+\eta\right)\theta^P+\eta\delta\right] \\
&= -\int_{e_\theta^P}^{R^P}\int_{y_1^A}^{y_2^A} \rho^A d\eta dr \Omega^2 y^2\theta^P - \int_{e_\theta^P}^{R^P}\int_{y_1^A}^{y_2^A} \rho^A d\eta dr \Omega^2 y\eta\delta \\
&= -I_\theta^A\Omega^2\theta^P - \int_{e_\theta^P}^{R^P}\int_{y_1^A}^{y_2^A} \rho^A d\eta dr \Omega^2 y_h\eta\delta - \int_{e_\theta^P}^{R^P}\int_{y_1^A}^{y_2^A} \rho^A d\eta dr \Omega^2 \eta^2\delta \\
&= -I_\theta^A\Omega^2\theta^P - I_a\Omega^2\delta - S_a\Omega^2 y_h\delta
\end{aligned} \tag{3.41}$$

The centrifugal moment resulting from a pitching motion is obtained by summing up Equations. 3.40 and 3.41:

$$M_{CF\theta}^{P} + M_{CF\theta}^{A} = -I_\theta^{P,A}\Omega^2\theta^P - \left(I_a + S_a y_h\right)\Omega^2\delta \tag{3.42}$$

The paddle inertial moment M_{CF}^{P} is then obtained from Equations. 3.38 and 3.42:

$$M_{CF}^{P} = \Omega^2\beta^P\left(\overline{S_\theta^{P,A}} + e_\theta^P S_\theta^{P,A}\right) - I_\theta^{P,A}\Omega^2\theta^P - \left(I_a + S_a y_h\right)\Omega^2\delta \tag{3.43}$$

Paddle aerodynamic pitching moment

Let the aerodynamic pitch moment of the paddle be $M_{AF\theta}^{P}$. $M_{AF\theta}^{P}$ can be written as:

$$M_{AF\theta}^{P} = \int_{e_\theta^P}^{R^P} \frac{1}{2}\rho_{air} U^2 c_{tot}^2 C_m \tag{3.44}$$

with C_m the pitch aerodynamic coefficient (Ref. [1]). C_m is written as:

$$C_m = C_m^{nc} + \pi\left(a+\frac{1}{2}\right) C[k]\left(\alpha_{qs}+\delta_{qs}\right) + C_m^{qs} \tag{3.45}$$

with C_m^{nc} the non-circulatory aerodynamic moment coefficient, C_m^{qs} the quasi-steady aerodynamic moment coefficient and $\alpha_{qs}+\delta_{qs}$ the quasi-steady effective angle of attack (including the effect of aileron deflection). These terms are respectively defined as:

$$\begin{cases}
C_m^{nc} = -\frac{\pi}{2U^2}\left[\left(\frac{1}{8}+a^2\right)\ddot{\alpha} - ab\ddot{h}^P\right] - \frac{b^2\ddot{\delta}}{2U^2}\left[T_7 + \left(\frac{y_h}{b}-a\right)T_1\right] \\
C_m^{qs} = -\frac{1}{2U^2}\left[\pi U\left(\frac{1}{2}-a\right)b\dot{\alpha} + (T_4+T_{10})U^2\delta - \left[T_1 - T_8 - \left(\frac{y_h}{b}-a\right)T_4 + \frac{T_{11}}{2}\right]b\dot{\delta}U\right] \\
\alpha_{qs}+\delta_{qs} = \frac{\dot{h}^p}{U} + \alpha + b\left(\frac{1}{2}-a\right)\frac{\dot{\alpha}}{U} + \frac{T_{10}\delta}{\pi} + \frac{bT_{11}\dot{\delta}}{2\pi U}
\end{cases} \tag{3.46}$$

T_1, T_4, T_7, T_8, T_{10}, T_{11} are given by Theodorsen in Ref. [13].

The paddle aerodynamic pitch moment is therefore written as:

$$\begin{aligned}
M^P_{AF\theta} = & \int_{e^P_\theta}^{R^P} \ddot{\beta}^P \left[\frac{1}{64} c_{tot}^3 \pi \rho_{air} \left(2c^P e^P_\theta - 4c_{tot} e^P_\theta + 4r \right.\right. \\
& \left.\left. + \left(-4 + \left(c^P\right)^2 - 4c^P c_{tot} + 4c_{tot}^2\right) r C[k]\right)\right] dr \\
& + \int_{e^P_\theta}^{R^P} \ddot{\theta}^P \left[-\frac{1}{64} c_{tot}^2 \left(2 + \left(c^P\right)^2 - 4c^P c_{tot} + 4c_{tot}^2\right) \pi \rho_{air}\right] dr \\
& + \int_{e^P_\theta}^{R^P} \ddot{\delta} \left[\frac{1}{64} c_{tot}^3 \rho_{air} \left(-c^P c_{tot} T_1 + 2c_{tot}^2 T_1 - 4c_{tot} T_7 - 8T_1 y_h\right)\right] dr \\
& + \int_{e^P_\theta}^{R^P} \dot{\beta}^P \left[-\frac{1}{8} c_{tot}^2 \left(2 - c^P + 2c_{tot}\right) e^P_\theta \Omega \pi r \rho_{air} C[k]\right] dr \\
& + \int_{e^P_\theta}^{R^P} \dot{\theta}^P \left[-\frac{1}{64} \left(2 + c^P - 2c_{tot}\right) c_{tot}^3 \Omega \pi r \rho_{air} \left(2 + \left(c^P - 2\left(1 + c_{tot}\right)\right) C[k]\right)\right] dr \\
& + \int_{e^P_\theta}^{R^P} \dot{\delta} \left[\frac{1}{32} c_{tot}^2 \Omega r \rho_{air} \left(-2c_{tot}^2 T_4 + c_{tot}\left(-4T_1 - 2T_{11} + c^P T_4 + 4T_8\right) + 8T_4 y_h \right.\right. \\
& \left.\left. + c_{tot}\left(2 - c^P + 2c_{tot}\right) T_{11} C[k]\right)\right] dr \\
& + \int_{e^P_\theta}^{R^P} \theta^P \left[\frac{1}{8} c_{tot}^2 \left(2 - c^P + 2c_{tot}\right) \Omega^2 \pi r^2 \rho_{air} C[k]\right] dr \\
& + \int_{e^P_\theta}^{R^P} \delta \left[\frac{1}{8} c_{tot}^2 \Omega^2 r^2 \rho_{air} \left(-2\left(T_{10} + T_4\right) + \left(2 - c^P + 2c_{tot}\right) T_{10} C[k]\right)\right] dr
\end{aligned} \tag{3.47}$$

The paddle pitch equation is written from the moment equilibrium:

$$M^P_{SP} + M^P_{IF} + M^P_{CF} + M^P_{AF\theta} = 0 \tag{3.48}$$

The paddle initial pitch is assumed to be equal to zero. Using Equations. 3.29, 3.36, 3.43 and 3.47, Equation. 3.48 becomes:

$$\begin{aligned}
& \ddot{\beta}^P C^{Ppitch}_{\ddot{\beta}^P} + \ddot{\theta}^P C^{Ppitch}_{\ddot{\theta}^P} + \ddot{\delta} C^{Ppitch}_{\ddot{\delta}} + \dot{\beta}^P C^{Ppitch}_{\dot{\beta}^P} + \dot{\theta}^P C^{Ppitch}_{\dot{\theta}^P} \\
& \qquad + \dot{\delta} C^{Ppitch}_{\dot{\delta}} + \beta^P C^{Ppitch}_{\beta^P} + \theta^P C^{Ppitch}_{\theta^P} + \delta C^{Ppitch}_{\delta} = 0
\end{aligned} \tag{3.49}$$

with the coefficients $C^{Ppitch}_{\ddot{\beta}^P}$, $C^{Ppitch}_{\ddot{\theta}^P}$, $C^{Ppitch}_{\ddot{\delta}}$, $C^{Ppitch}_{\dot{\beta}^P}$, $C^{Ppitch}_{\dot{\theta}^P}$, $C^{Ppitch}_{\dot{\delta}}$,

$C_{\beta^P}^{Ppitch}$, $C_{\theta^P}^{Ppitch}$ and C_{δ}^{Ppitch} respectively defined as:

$$\begin{cases}
C_{\ddot{\beta}^P}^{Ppitch} &= \displaystyle\int_{e_\theta^P}^{R^P} \left[\frac{1}{64} c_{tot}^3 \pi \rho_{air} \left(2c^P e_\theta^P - 4c_{tot} e_\theta^P + 4r \right.\right. \\
& \quad + \left.\left. \left(-4 + \left(c^P\right)^2 - 4c^P c_{tot} + 4c_{tot}^2\right) rC[k]\right)\right] dr + \overline{S_\theta^{P,A}} \\
C_{\ddot{\theta}^P}^{Ppitch} &= \displaystyle\int_{e_\theta^P}^{R^P} \left[-\frac{1}{64} c_{tot}^2 \left(2 + \left(c^P\right)^2 - 4c^P c_{tot} + 4c_{tot}^2\right) \pi \rho_{air}\right] dr - I_\theta^P \\
C_{\ddot{\delta}}^{Ppitch} &= \displaystyle\int_{e_\theta^P}^{R^P} \left[\frac{1}{64} c_{tot}^3 \rho_{air} \left(-c^P c_{tot} T_1 + 2c_{tot}^2 T_1 - 4c_{tot} T_7 - 8T_1 y_h\right)\right] dr \\
& \quad - \left(y_h S_a + I_a\right) \\
C_{\dot{\beta}^P}^{Ppitch} &= \displaystyle\int_{e_\theta^P}^{R^P} \left[-\frac{1}{8} c_{tot}^2 \left(2 - c^P + 2c_{tot}\right) e_\theta^P \Omega \pi r \rho_{air} C[k]\right] dr \\
C_{\dot{\theta}^P}^{Ppitch} &= \displaystyle\int_{e_\theta^P}^{R^P} \left[-\frac{1}{64} \left(2 + c^P - 2c_{tot}\right) c_{tot}^3 \Omega \pi r \rho_{air} \left(2 + \left(c^P - 2\left(1 + c_{tot}\right)\right) C[k]\right)\right] dr \\
C_{\dot{\delta}}^{Ppitch} &= \displaystyle\int_{e_\theta^P}^{R^P} \left[\frac{1}{32} c_{tot}^2 \Omega r \rho_{air} \left(-2c_{tot}^2 T_4 + c_{tot} \left(-4T_1 - 2T_{11} + c^P T_4 + 4T_8\right)\right.\right. \\
& \quad + \left.\left. 8T_4 y_h + c_{tot} \left(2 - c^P + 2c_{tot}\right) T_{11} C[k]\right)\right] dr \\
C_{\beta^P}^{Ppitch} &= \Omega^2 \left(\overline{S_\theta^{P,A}} + e_\theta^P S_\theta^{P,A}\right) \\
C_{\theta^P}^{Ppitch} &= \displaystyle\int_{e_\theta^P}^{R^P} \left[\frac{1}{8} c_{tot}^2 \left(2 - c^P + 2c_{tot}\right) \Omega^2 \pi r^2 \rho_{air} C[k]\right] dr \\
& \quad - k_\theta^P - I_\theta^{P,A} \Omega^2 \\
C_{\delta}^{Ppitch} &= \displaystyle\int_{e_\theta^P}^{R^P} \left[\frac{1}{8} c_{tot}^2 \Omega^2 r^2 \rho_{air} \left(-2\left(T_{10} + T_4\right) + \left(2 - c^P + 2c_{tot}\right) T_{10} C[k]\right)\right] dr \\
& \quad - \left(I_a + S_a y_h\right) \Omega^2
\end{cases} \tag{3.50}$$

3.1.4 Blade flap equation

The blade flap equation is obtained from the paddle flap equation after removing all $\ddot{\delta}$, $\dot{\delta}$ and δ terms. The moments that compose the blade flap equation are defined about the blade flap axis.

Hence the blade flap equation is:

$$M_{SP}^B + M_{IF}^B + M_{CF}^B + M_{AF\beta}^B = 0 \tag{3.51}$$

$$\ddot{\beta}^B C_{\ddot{\beta}^B}^{Bflap} + \ddot{\theta}^B C_{\ddot{\theta}^B}^{Bflap} + \dot{\beta}^B C_{\dot{\beta}^B}^{Bflap} + \dot{\theta}^B C_{\dot{\theta}^B}^{Bflap} + \beta^B C_{\beta^B}^{Bflap} + \theta^B C_{\theta^B}^{Bflap} + v_i C_{v_i}^{Bflap} = 0 \tag{3.52}$$

where v_i is the induced velocity. The coefficients $C^{Bflap}_{\ddot{\beta}^B}$, $C^{Bflap}_{\ddot{\theta}^B}$, $C^{Bflap}_{\dot{\beta}^B}$, $C^{Bflap}_{\dot{\theta}^B}$, $C^{Bflap}_{\beta^B}$, $C^{Bflap}_{\theta^B}$ and $C^{Bflap}_{v_i}$ are respectively defined as:

$$\begin{cases} C^{Bflap}_{\ddot{\beta}^B} = -I^B_\beta + \int_{e^{B\beta}}^{R^B} \left[\frac{1}{8}\ \left(c^B\right)^2\ \pi\ \left(e^B_\beta - r\right)\left(2e^B_\beta - \left(-2 + c^B\right) C[k] r\right)\ \rho_{air}\right] dr \\ C^{Bflap}_{\ddot{\theta}^B} = \overline{S^B_\theta} + \int_{e^{B\beta}}^{R^B} \left[\frac{1}{32}\ \left(c^B\right)^4\ \pi\ \left(e^B_\beta - r\right)\ \rho_{air}\right] dr \\ C^{Bflap}_{\dot{\beta}^B} = \int_{e^{B\beta}}^{R^B} \left[C[k]\, c^B\, e^B_\beta\, \Omega\, \pi\ \left(e^B_\beta - r\right)\ r\, \rho_{air}\right] dr \\ C^{Bflap}_{\dot{\theta}^B} = \int_{e^{B\beta}}^{R^B} \left[\frac{1}{8} \left(c_B\right)^2 \left(-2 + \left(-2 + c^B\right)\ C[k]\right)\ \Omega\, \pi\ \left(e^B_\beta - r\right)\ r\, \rho_{air}\right] dr \\ C^{Bflap}_{\beta^B} = -k^B_\beta - \Omega^2 \left(I^B_\beta + e^B_\beta S^B_\beta\right) \\ C^{Bflap}_{\theta^B} = \Omega^2 \left(\overline{S^B_\theta} + e^B_\beta S^B_\theta\right) + \int_{e^{B\beta}}^{R^B} \left[C[k]\, c^B\, \Omega^2\, \pi\, r^2\ \left(r - e^B_\beta\right)\ \rho_{air}\right] dr \\ C^{Bflap}_{v_i} = c^B C[k] \Omega \pi \left(r - e^B_\beta\right) r \rho_{air} \end{cases} \tag{3.53}$$

where c^B is the blade chord, R^B is the blade radius, e^B_β is the blade flap hinge offset, k^B_β is the blade flap stiffness. ρ^B is the blade mass per unit area. The remaining terms are:

$$\begin{cases} I^B_\beta = \int_{e^B_\beta}^{R^B} \left(r - e^B_\beta\right)^2 \left[\int_{y^B_1}^{y^B_2} \rho^B dy\right] dr & \text{the blade flap moment of inertia} \\ \overline{S^B_\theta} = \int_{e^B_\beta}^{R^B} \left(r - e^B_\beta\right) \left[\int_{y^B_1}^{y^B_2} y \rho^B dy\right] dr & \text{the blade first radial moment} \\ S^B_\beta = \int_{e^B_\beta}^{R^B} \left(r - e^B_\beta\right) \left[\int_{y^B_1}^{y^B_2} \rho^B dy\right] dr & \text{the blade first flap moment} \\ S^B_\theta = \int_{e^B_\beta}^{R^B} \left[\int_{y^B_1}^{y^B_2} y \rho^B dy\right] dr & \text{the blade zeroth radial moment} \end{cases} \tag{3.54}$$

3.1.5 Blade pitch equation

The blade pitch equation is obtained from the paddle pitch equation after removing all $\ddot{\delta}$, $\dot{\delta}$ and δ terms. The moments that compose the blade pitch equation are taken about the blade pitch axis.

Hence the blade pitch equation is:

$$M^B_{SP} + M^B_{IF} + M^B_{CF} + M^B_{AF\theta} = 0 \tag{3.55}$$

$$\ddot{\beta}^B C^{Bpitch}_{\ddot{\beta}^B} + \ddot{\theta}^B C^{Bpitch}_{\ddot{\theta}^B} + \dot{\beta}^B C^{Bpitch}_{\dot{\beta}^B} + \dot{\theta}^B C^{Bpitch}_{\dot{\theta}^B} + \beta^B C^{Bpitch}_{\beta^B} + \theta^B C^{Bpitch}_{\theta^B} + v_i C^{Bpitch}_{v_i} = 0 \tag{3.56}$$

with the coefficients $C^{Bpitch}_{\ddot{\beta}^B}$, $C^{Bpitch}_{\ddot{\theta}^B}$, $C^{Bpitch}_{\dot{\beta}^B}$, $C^{Bpitch}_{\dot{\theta}^B}$, $C^{Bpitch}_{\beta^B}$, $C^{Bpitch}_{\theta^B}$ and

$C_{v_i}^{Bpitch}$ respectively defined as:

$$\begin{cases} C_{\ddot{\beta}^B}^{Bpitch} & = \int_{e_\theta^B}^{R^B} \left[\frac{1}{64}\left(c^B\right)^3 \pi\rho_{air}\left(-2c^B e_\theta^B + 4r + \left(-4 + \left(c^B\right)^2\right) rC[k]\right)\right] dr + \overline{S_\theta^B} \\ C_{\ddot{\theta}^B}^{Bpitch} & = \int_{e_\theta^B}^{R^B} \left[-\frac{1}{64}\left(c^B\right)^2\left(2 + \left(c^B\right)^2\right)\pi\rho_{air}\right] dr - I_\theta^B \\ C_{\dot{\beta}^B}^{Bpitch} & = \int_{e_\theta^B}^{R^B} \left[-\frac{1}{8}\left(c^B\right)^2\left(2 + c^B\right) e_\theta^B \Omega\pi r\rho_{air} C[k]\right] dr \\ C_{\dot{\theta}^B}^{Bpitch} & = \int_{e_\theta^B}^{R^B} \left[-\frac{1}{64}\left(-2 + c^B\right)\left(c^B\right)^3 \Omega\pi r\rho_{air}\left(-2 + \left(c^B + 2\right) C[k]\right)\right] dr \\ C_{\beta^B}^{Bpitch} & = \Omega^2\left(\overline{S_\theta^B} + e_\theta^B S_\theta^B\right) \\ C_{\theta^B}^{Bpitch} & = \int_{e_\theta^B}^{R^B} \left[\frac{1}{8}\left(c^B\right)^2\left(2 + c^B\right)\Omega^2\pi r^2\rho_{air} C[k]\right] dr - k_\theta^B - I_\theta^B\Omega^2 \\ C_{v_i}^{Bpitch} = 0 \end{cases} \tag{3.57}$$

with e_θ^B the blade pitch hinge offset, k_θ^B the blade pitch stiffness and $I_\theta^B = \int_{e_\theta^B}^{R^B}\left[y^2\rho^B dy\right] dr$ the blade zeroth radial moment.

3.1.6 Aileron pitch equation

The aileron pitch equation is obtained from the moment equilibrium of the spring, inertial, centrifugal and aerodynamic moments. The derivation for each of these moments is presented in the following sections. The direction of positive pitching is assumed to be nose up. The moments that compose the aileron pitch equation are defined about the aileron pitch axis.

Spring moment

Let δ_0 be the initial aileron pitch angle and k_δ the aileron pitch stiffness. The aileron spring moment is written as:

$$M_{SP}^A = -k_\delta\left(\delta - \delta_0\right) \tag{3.58}$$

Inertial moment

The aileron inertial moment M_{IF}^A is obtained from the sum of three inertial moments $M_{IF\beta}^A$, $M_{IF\theta}^A$ and $M_{IF\delta}^A$. $M_{IF\beta}^A$ is generated when the aileron undergoes a flapping motion. $M_{IF\theta}^A$ and $M_{IF\delta}^A$ are created when the aileron pitches.

When the aileron is subjected to a flapping motion, an inertial force dIF_β^A is applied on each of its elements. dIF_β^A is defined as:

$$dIF_\beta^A = \rho^A d\eta dr\ddot{\beta}^P\left(r - e_\beta^P\right) \tag{3.59}$$

The moment arm is here η as the moment considered is about the aileron hinge (see Fig. 3.12). The inertial moment on an aileron undergoing a flapping motion is therefore:

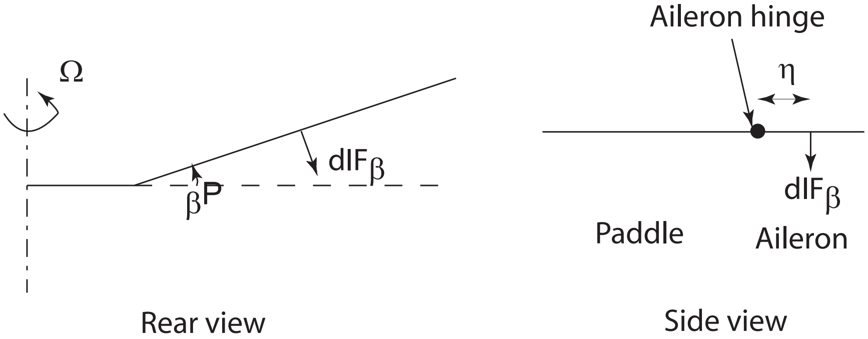

Figure 3.12: Inertial load on an aileron element undergoing a flapping motion.

$$\begin{aligned} M^A_{IF_\beta} &= \int_{e^A_\delta}^{R^P} \int_{y^A_1}^{y^A_2} \rho^A d\eta dr \ddot{\beta}^P \left(r - e^P_\beta\right) \eta \\ &= \ddot{\beta}^P \overline{S_a} \end{aligned} \tag{3.60}$$

with $\overline{S_a}$ the aileron first radial moment ,e^A_δ the aileron pitch hinge offset. It is assumed $e^A_\delta = e^P_\theta$.

When the aileron undergoes a pitching motion, an inertial force dIF^A_δ is applied on each of its elements. dIF^A_δ is defined as:

$$dIF^A_\delta = \rho^A d\eta dr \ddot{\delta} \eta \tag{3.61}$$

The moment arm is of η. Hence the inertial moment on an aileron element when the aileron is pitching is written as:

$$\begin{aligned} M^A_{IF_\delta} &= -\int_{e^A_\delta}^{R^P} \int_{y^A_1}^{y^A_2} \rho^A d\eta dr \ddot{\delta} \eta^2 \\ &= -\ddot{\delta} I_a \end{aligned} \tag{3.62}$$

where I_a is the aileron zeroth radial moment.

When the paddle is pitching, it makes the aileron pitch of an angle θ^P. Hence an inertial force dIF^A_θ is generated on each aileron element. dIF^A_θ can be written as:

$$dIF^A_\theta = \rho^A d\eta dr \ddot{\theta}^P y \tag{3.63}$$

The moment arm is of η. The inertial moment on the aileron when the paddle pitches is therefore:

$$\begin{aligned} M^A_{IF_\theta} &= -\int_{e^A_\delta}^{R^P}\int_{y^A_1}^{y^A_2} \rho^A d\eta dr \ddot{\theta}^P y\eta \\ &= -\int_{e^A_\delta}^{R^P}\int_{y^A_1}^{y^A_2} \rho^A d\eta dr \ddot{\theta}^P \left(y_h+\eta\right)\eta \\ &= -\ddot{\theta}^P \left[\int_{e^A_\delta}^{R^P}\int_{y^A_1}^{y^A_2} \rho^A d\eta dr y_h \eta + \int_{e^A_\delta}^{R^P}\int_{y^A_1}^{y^A_2} \rho^A d\eta dr \eta^2\right] \\ &= -\ddot{\theta}^P \left(I_a + S_a y_h\right) \end{aligned} \tag{3.64}$$

with S_a the aileron zeroth radial moment.

The aileron inertial moment is thus obtained from Equations. 3.60, 3.62 and 3.64:

$$M^A_{IF} = \ddot{\beta}^P \overline{S_a} - \ddot{\delta} I_a - \ddot{\theta}^P \left(I_a + S_a y_h\right) \tag{3.65}$$

Centrifugal moment

The aileron centrifugal moment is obtained from the sum of two centrifugal moments $M^A_{CF\beta}$ and $M^A_{CF\theta,\delta}$. The former is generated when the aileron is subjected to a flapping motion and the latter is created when the paddle and aileron pitch.

When the aileron undergoes a flapping motion, a centrifugal force dCF^A_β is applied on each of its elements. dCF^A_β can be written as:

$$dCF^A_\beta = \rho^A dy dr \Omega^2 r \beta^P \tag{3.66}$$

The moment arm is here again η. The centrifugal moment on the aileron when it is flapping is therefore:

$$\begin{aligned} M^A_{CF\beta} &= \int_{e^A_\delta}^{R^P}\int_{y^A_1}^{y^A_2} \rho^A dy dr \Omega^2 r \beta^P \eta \\ &= \beta^P \Omega^2 \left[\int_{e^A_\delta}^{R^P} s_a \left(r - e^A_\delta\right) dr + e^A_\delta \int_{e^A_\delta}^{R^P} s_a dr\right] \\ &= \beta^P \Omega^2 \left(\overline{S_a} + e^A_\delta S_a\right) \end{aligned} \tag{3.67}$$

When the paddle and aileron are subjected to a pitching motion, a propeller moment is generated on the aileron. The centrifugal force which is applied to each aileron element is:

$$dCF^A_{\theta,\delta} = \rho^A d\eta dr \Omega^2 y \tag{3.68}$$

The moment arm is $\eta\left(\theta^P+\delta\right)$. The centrifugal moment on the aileron when the paddle and aileron are pitching is therefore:

$$
\begin{aligned}
M^A_{CF\theta,\delta} &= -\int_{e^A_\delta}^{R^P}\int_{y^A_1}^{y^A_2}\rho^A d\eta dr\Omega^2 y\eta\left(\theta^P+\delta\right)\\
&= -\left(\theta^P+\delta\right)\Omega^2\int_{e^A_\delta}^{R^P}\int_{y^A_1}^{y^A_2}\rho^A d\eta dr\Omega^2\left(y_h+\eta\right)\eta\left(\theta^P+\delta\right)\\
&= -\left(\theta^P+\delta\right)\Omega^2\left[\int_{e^A_\delta}^{R^P}\int_{y^A_1}^{y^A_2}\rho^A d\eta dr y_h\eta+\int_{e^A_\delta}^{R^P}\int_{y^A_1}^{y^A_2}\rho^A d\eta dr\eta^2\right]\\
&= -\left(\theta^P+\delta\right)\Omega^2\left(y_hS_a+I_a\right)
\end{aligned}
\tag{3.69}
$$

The aileron centrifugal moment M^A_{CF} is thus obtained from Equations. 3.67 and 3.69

$$
M^A_{CF}=\beta^P\Omega^2\left(\overline{S_a}+e^A_\delta S_a\right)-\left(\theta^P+\delta\right)\Omega^2\left(y_hS_a+I_a\right) \tag{3.70}
$$

Aileron aerodynamic pitching moment

Let the aerodynamic pitching moment of the aileron be $M^A_{AF\delta}$. $M^A_{AF\delta}$ can be written as:

$$
M^A_{AF\delta}=\int_{e^A_\delta}^{R^P}\frac{1}{2}\rho_{air}U^2c^2_{tot}C_h \tag{3.71}
$$

with C_h the aileron hinge aerodynamic coefficient (Ref. [1]). C_h is defined as:

$$
C_h=C^{nc}_h+\frac{T_{12}}{2}C[k]\left(\alpha_{qs}+\delta_{qs}\right)+C^{qs}_h \tag{3.72}
$$

where C^{nc}_h is the non-circulatory part of the hinge moment coefficient and C^{qs}_h is the quasi-steady part of the hinge moment coefficient. T_{12} is obtained from Theodorsen's theory (Ref. [13]). C^{nc}_h and C^{qs}_h are written below:

$$
\begin{cases}
C^{nc}_h &= -\frac{1}{2U^2}\left(2T_{13}b^2\ddot{\alpha}-T_1b\ddot{h}^P-\frac{T_3b^2}{\pi}\ddot{\delta}\right)\\
C^{qs}_h &= -\frac{1}{2U^2}\left[\left[-2T_9-T_1+T_4\left(a-\frac{1}{2}\right)\right]Ub\dot{\alpha}+\frac{U^2}{\pi}\left(T_5-T_4T_{10}\right)\delta-\frac{Ub}{2\pi}\dot{\delta}T_4T_{11}\right]
\end{cases}
\tag{3.73}
$$

where T_5 and T_9 come from Theodorsen's theory (Ref. [13]). The aileron hinge moment is therefore written as:

$$\begin{aligned}
M^A_{AF\delta} = &\int_{e^A_\delta}^{R^P} \ddot{\beta}^P \left[\frac{1}{32}c^3_{tot}\rho_{air}\left(-4e^A_\delta T_1 - r\left(\left(2+c^P-2c_{tot}\right)T_4+8T_9\right)\right.\right. \\
&- \left.\left.\left(2+c^P-2c_{tot}\right)rT_{12}C[k]\right)\right]\,dr \\
&+ \int_{e^A_\delta}^{R^P} \dot{\beta}^P \left[-\frac{1}{4}c^2_{tot}e^A_\delta \Omega r\rho_{air}T_{12}C[k]\right]\,dr \\
&+ \int_{e^A_\delta}^{R^P} \ddot{\theta}^P \left[-\frac{1}{8}c^4_{tot}\rho_{air}T_{13}\right]\,dr \\
&+ \int_{e^A_\delta}^{R^P} \dot{\theta}^P \left[-\frac{1}{32}c^3_{tot}\Omega r\rho_{air}\left(-4T_1-2T_4-c^PT_4+2c_{tot}T_4-8T_9\right.\right. \\
&\left.\left.-\left(2+c^P-2c_{tot}\right)T_{12}C[k]\right)\right]\,dr \\
&+ \int_{e^A_\delta}^{R^P} \theta^P \left[\frac{1}{4}c^2_{tot}\Omega^2 r^2\rho_{air}T_{12}C[k]\right]\,dr \\
&+ \int_{e^A_\delta}^{R^P} \ddot{\delta} \left[\frac{c^4_{tot}\rho_{air}T_3}{16\pi}\right]\,dr \\
&+ \int_{e^A_\delta}^{R^P} \dot{\delta} \left[\frac{c^3_{tot}\Omega r\rho_{air}T_{11}\left(T_4+T_{12}C[k]\right)}{16\pi}\right]\,dr \\
&+ \int_{e^A_\delta}^{R^P} \delta \left[\frac{c^2_{tot}\Omega^2 r^2\rho_{air}\left(T_{10}T_4-T_5+T_{10}T_{12}C[k]\right)}{4\pi}\right]\,dr
\end{aligned} \tag{3.74}$$

The aileron pitch equation is then written using the moment equilibrium:

$$M^A_{SP} + M^A_{IF} + M^A_{CF} + M^A_{AF\delta} = F_{act}V \tag{3.75}$$

$F_{act}V$ is the input provided to the aileron by the piezo electric actuator. V is the actuator voltage. The initial aileron angle is assumed to be equal to zero. Using Equations. 3.58, 3.65, 3.70 and 3.74, Equation. 3.75 becomes:

$$\begin{aligned}
&\ddot{\beta}^P C^{Apitch}_{\ddot{\beta}^P} + \ddot{\theta}^P C^{Apitch}_{\ddot{\theta}^P} + \ddot{\delta} C^{Apitch}_{\ddot{\delta}} + \dot{\beta}^P C^{Apitch}_{\dot{\beta}^P} + \dot{\theta}^P C^{Apitch}_{\dot{\theta}^P} \\
&\qquad + \dot{\delta} C^{Apitch}_{\dot{\delta}} + \beta^P C^{Apitch}_{\beta^P} + \theta^P C^{Apitch}_{\theta^P} + \delta C^{Apitch}_{\delta} = 0
\end{aligned} \tag{3.76}$$

with the coefficients $C^{Apitch}_{\ddot{\beta}^P}$, $C^{Apitch}_{\ddot{\theta}^P}$, $C^{Apitch}_{\ddot{\delta}}$, $C^{Apitch}_{\dot{\beta}^P}$, $C^{Apitch}_{\dot{\theta}^P}$, $C^{Apitch}_{\dot{\delta}}$,

$C^{Apitch}_{\beta^P}$, $C^{Apitch}_{\theta^P}$ and C^{Apitch}_{δ} respectively defined as:

$$
\left\{
\begin{aligned}
C^{Apitch}_{\ddot{\beta}^P} &= \int_{e^A_\delta}^{R^P} \Big[\frac{1}{32}c^3_{tot}\rho_{air}\left(-4e^A_\delta T_1 - r\left(\left(2+c^P-2c_{tot}\right)T_4+8T_9\right)\right. \\
&\qquad \left. -\ \left(2+c^P-2c_{tot}\right)rT_{12}C[k]\right)\Big]\,dr + \overline{S_a} \\
C^{Apitch}_{\ddot{\theta}^P} &= \int_{e^A_\delta}^{R^P} \left[-\frac{1}{8}c^4_{tot}\rho_{air}T_{13}\right] dr - I_a - S_a y_h \\
C^{Apitch}_{\ddot{\delta}} &= \int_{e^A_\delta}^{R^P} \left[\frac{c^4_{tot}\rho_{air}T_3}{16\pi}\right] dr - I_a \\
C^{Apitch}_{\dot{\beta}^P} &= \int_{e^A_\delta}^{R^P} \left[-\frac{1}{4}c^2_{tot}e^A_\delta \Omega r\rho_{air}T_{12}C[k]\right] dr \\
C^{Apitch}_{\dot{\theta}^P} &= \int_{e^A_\delta}^{R^P} \Big[-\frac{1}{32}c^3_{tot}\Omega r\rho_{air}\left(-4T_1-2T_4-c^PT_4+2c_{tot}T_4-8T_9\right. \\
&\qquad \left.-\left(2+c^P-2c_{tot}\right)T_{12}C[k]\right)\Big]\,dr \\
C^{Apitch}_{\dot{\delta}} &= \int_{e^A_\delta}^{R^P} \left[\frac{c^3_{tot}\Omega r\rho_{air}T_{11}\left(T_4+T_{12}C[k]\right)}{16\pi}\right] dr \\
C^{Apitch}_{\beta^P} &= \Omega^2\left(\overline{S_a}+e^A_\delta S_a\right) \\
C^{Apitch}_{\theta^P} &= \int_{e^A_\delta}^{R^P} \left[\frac{1}{4}c^2_{tot}\Omega^2 r^2\rho_{air}T_{12}C[k]\right] dr - \Omega^2\left(y_h S_a + I_a\right) \\
C^{Apitch}_{\delta} &= \int_{e^A_\delta}^{R^P} \left[\frac{c^2_{tot}\Omega^2 r^2\rho_{air}\left(T_{10}T_4-T_5+T_{10}T_{12}C[k]\right)}{4\pi}\right] dr - k_\delta - \Omega^2\left(y_h S_a + I_a\right)
\end{aligned}
\right.
\tag{3.77}
$$

3.1.7 Step 3 : Blade pitch and paddle flap coupling

As exposed in Chapter. 2, the blade pitch angle and the paddle flap angle are coupled using a mechanical arm. The coupling $\theta^B = \beta^P$ is used to combine Equation. 3.27 and Equation. 3.56. These two equations are added to obtain the following equation:

$$
\begin{aligned}
&\ddot{\beta}^B C^{Bpitch}_{\ddot{\beta}^B} + \ddot{\theta}^B\left(C^{Bpitch}_{\ddot{\theta}^B}+C^{Pflap}_{\ddot{\beta}^P}\right) + \ddot{\theta}^P C^{Pflap}_{\ddot{\theta}^P} + \ddot{\delta}C^{Pflap}_{\ddot{\delta}} \\
&\qquad + \dot{\beta}^B C^{Bpitch}_{\dot{\beta}^B} + \dot{\theta}^B\left(C^{Bpitch}_{\dot{\theta}^B}+C^{Pflap}_{\dot{\beta}^P}\right) + \dot{\theta}^P C^{Pflap}_{\dot{\theta}^P} + \dot{\delta}C^{Pflap}_{\dot{\delta}} \\
&+ \beta^B C^{Bpitch}_{\beta^B} + \theta^B\left(C^{Bpitch}_{\theta^B}+C^{Pflap}_{\beta^P}\right) + \theta^P C^{Pflap}_{\theta^P} + \delta C^{Pflap}_{\delta} = 0
\end{aligned}
\tag{3.78}
$$

3.1.8 Step 4 : Equation of motion, state space form and transfer function

Equation of motion

The number of unknowns has now been reduced from five to four. The unknows are now:

1. The blade flap angle, β^B,
2. The blade pitch angle, θ^B,
3. The paddle pitch angle, θ^P,
4. The aileron pitch angle, δ,

The equation of motion is obtained from the four following equations:

1. The blade flap equation (Equation. 3.52),
2. The blade pitch and paddle flap coupling equation (Equation. 3.78),
3. The paddle pitch equation (Equation. 3.49),
4. The aileron pitch equation (Equation. 3.76).

The equation of motion is therefore written as:

$$[M]\begin{Bmatrix}\ddot{\beta}^B\\ \ddot{\theta}^B\\ \ddot{\theta}^P\\ \ddot{\delta}\end{Bmatrix}+[C]\begin{Bmatrix}\dot{\beta}^B\\ \dot{\theta}^B\\ \dot{\theta}^P\\ \dot{\delta}\end{Bmatrix}+[K]\begin{Bmatrix}\beta^B\\ \theta^B\\ \theta^P\\ \delta\end{Bmatrix}=\begin{Bmatrix}0\\ 0\\ 0\\ F_{act}\end{Bmatrix}V+[C_{constant}]v_i \qquad (3.79)$$

where M is the mass matrix, C is the damping matrix, K is the stiffness matrix and V is the actuator voltage input. The $C_{constant}$ matrix regroups the terms related to the induced velocity. The M matrix contains terms from Theodorsen's theory. Once numerical values are input is the M matrix, it is clear it is symmetric and positive definite. It is inversible as its determinant is not equal to zero. The M, C and K matrices are defined below:

$$[M]=\begin{bmatrix}C^{Bflap}_{\ddot{\beta}^B} & C^{Bflap}_{\ddot{\theta}^B} & 0 & 0\\ C^{Bpitch}_{\ddot{\beta}^B} & \left(C^{Bpitch}_{\ddot{\theta}^B}+C^{Pflap}_{\ddot{\beta}^P}\right) & C^{Pflap}_{\ddot{\theta}^P} & C^{Pflap}_{\ddot{\delta}}\\ 0 & C^{Ppitch}_{\ddot{\beta}^P} & C^{Ppitch}_{\ddot{\theta}^P} & C^{Ppitch}_{\ddot{\delta}}\\ 0 & C^{Apitch}_{\ddot{\beta}^P} & C^{Apitch}_{\ddot{\theta}^P} & C^{Apitch}_{\ddot{\delta}}\end{bmatrix} \qquad (3.80)$$

$$[C]=\begin{bmatrix}C^{Bflap}_{\dot{\beta}^B} & C^{Bflap}_{\dot{\theta}^B} & 0 & 0\\ C^{Bpitch}_{\dot{\beta}^B} & \left(C^{Bpitch}_{\dot{\theta}^B}+C^{Pflap}_{\dot{\beta}^P}\right) & C^{Pflap}_{\dot{\theta}^P} & C^{Pflap}_{\dot{\delta}}\\ 0 & C^{Ppitch}_{\dot{\beta}^P} & C^{Ppitch}_{\dot{\theta}^P} & C^{Ppitch}_{\dot{\delta}}\\ 0 & C^{Apitch}_{\dot{\beta}^P} & C^{Apitch}_{\dot{\theta}^P} & C^{Apitch}_{\dot{\delta}}\end{bmatrix} \qquad (3.81)$$

$$[K] = \begin{bmatrix} C_{\beta^B}^{Bflap} & \theta^B C_{\theta^B}^{Bflap} & 0 & 0 \\ C_{\beta^B}^{Bpitch} & \left(C_{\theta^B}^{Bpitch} + C_{\beta^P}^{Pflap}\right) & C_{\theta^P}^{Pflap} & C_{\delta}^{Pflap} \\ 0 & C_{\beta^P}^{Ppitch} & C_{\theta^P}^{Ppitch} & C_{\delta}^{Ppitch} \\ 0 & C_{\beta^P}^{Apitch} & C_{\theta^P}^{Apitch} & C_{\delta}^{Apitch} \end{bmatrix} \tag{3.82}$$

State space form

Now that the equation of motion has been established, the associtated state space form is written to solve the equation of motion. The induced velocity influences the angle of attack. A simple inflow model is used in the present investigation, rather than a dynamic one for instance (Ref. [194]). In the present case, the inflow is considered constant and uniform throughout the rotor disk. The rotor operates in hover. Since we want to study the dynamic behavior of the system, the induced velocity is not taken into account in the state space form. Let

$$[X] = \begin{Bmatrix} \beta^B \\ \theta^B \\ \theta^P \\ \delta \end{Bmatrix} \tag{3.83}$$

and

$$\begin{cases} \dot{X}_1 = \dot{X} = X_2 \\ \dot{X}_2 = \ddot{X} \end{cases} \tag{3.84}$$

Then Equation. 3.79 can be written as:

$$[M]\dot{X}_2 + [C]\dot{X}_1 + [K]X_1 = [F] \tag{3.85}$$

$$\dot{X}_2 = [M]^{-1}\left([F] - [C]X_2 - [K]X_1\right) \tag{3.86}$$

with $[F] = \begin{Bmatrix} 0 \\ 0 \\ 0 \\ F_{act} \end{Bmatrix} V$.

The state space form can be written as an 8^{th} order system:

$$\begin{aligned} \begin{Bmatrix} \dot{X}_1 \\ \dot{X}_2 \end{Bmatrix} &= \begin{bmatrix} [0]_{4*4} & [I]_{4*4} \\ -[M]^{-1}[K] & -[M]^{-1}[C] \end{bmatrix} \begin{Bmatrix} X_1 \\ X_2 \end{Bmatrix} + \begin{bmatrix} [0]_{4*4} \\ -[M]^{-1}[F] \end{bmatrix} [I]_{4*1} \\ \dot{\chi} &= [A]\chi + [B]u \end{aligned} \tag{3.87}$$

with 0_{4*4} a four-by-four zero matrix, $[I]_{4*4}$ a four-by-four identity matrix, $[I]_{4*1}$ a four-by-one identity matrix and $u = \delta$ the input. $[A]$ and $[B]$ are the state space matrices. χ is defined as:

$$\chi = \begin{Bmatrix} X_1 \\ X_2 \end{Bmatrix} \tag{3.88}$$

The state space form is therefore defined as:

$$\begin{cases} \dot{\chi} & = [A]\chi + [B]u \\ y & = [\zeta]\chi \end{cases} \tag{3.89}$$

where $u = \delta$ controls $y = \theta^P$.

Transfer function H(s) between δ and θ^P

The transfer function is finally obtained from Equation.3.89 using the Laplace transform:

$$\begin{cases} s\chi & = [A]\chi + [B]U(s) \\ Y(s) & = [\zeta]\chi \end{cases} \tag{3.90}$$

Equation.3.90 can be written as:

$$\begin{cases} \chi & = \left(s[I]_{8*8} - [A]\right)^{-1}[B]U(s) \\ Y(s) & = [\zeta]\left(s[I]_{8*8} - [A]\right)^{-1}[B]U(s) \end{cases} \tag{3.91}$$

with $[I]_{8*8}$ an eight-by-eight identity matrix. The transfer function $H(s)$, can then be defined as:

$$H(s) = \frac{Y(s)}{U(s)} = [\zeta]\left(s[I]_{8*8} - [A]\right)^{-1}[B] \tag{3.92}$$

Bode plots can then be computed.

The analytical model of the {blade, paddle, aileron} design features two main characteristics:

1. The paddle control authority on the blade, i.e. how much blade pitch is created for one degree of paddle pitch.
2. The aileron control authority on the paddle pitch: does the piezoelectric actuator have the capability to generate aileron deflection at desired frequencies and amplitudes.

At this stage of the project, some preliminary testings are required to ensure the concept is viable before allocating more fundings to its development. To this end, a simpler design is tested in hover. This second configuration is identical to the one described earlier except for the paddle actuation: in the latter design, the paddle pitch is not achieved by means of a PZT actuated aileron but by a small swashplate. As it does not include a PZT actuator, the second configuration is simpler and faster to test. However, the second design still permits to assess the paddle control authority on the blade.

3.2 Simplified model : Paddle-Blade study

A second analytical model is developed from the method presented in the previous section. This second model is constituted of a paddle and a blade. The coupling between the blade pitch angle and the paddle flap angle remains the same as described earlier. The difference between the two models resides in the paddle actuation. In the {paddle,blade} method, the paddle pitch is actuated by a small swashplate. This configuration is investigated to later perform hover stand tests. A swashplate actuated paddle is indeed cheaper and safer to develop and test than a piezoelectic-actuated one. Tests on a {paddle, blade} configuration permits to check and quantify the paddle control authority on the blade.

The goal of this model is to study the effects of various control settings and system geometry on the system behavior during steady hover flight. The system features four degrees of freedom:

1. The blade flap angle,
2. The blade pitch angle,
3. The paddle pitch angle,
4. The paddle flap angle.

A mechanical coupling links the paddle flap and blade pitch angles. The number of degrees of freedom is thus reduced to three: blade flap, blade pitch and paddle pitch. The model predicts the steady values of the:

1. Blade flap response,
2. Paddle pitch response,
3. Coupled blade pitch and paddle flap response,

to the system input: the force exerted by the swashplate. Similarly to the previous method, the development of the {paddle, blade} analysis is based on the following assumptions:

1. The blade is considered rigid with two degrees of freedom,
2. The paddle is considered rigid with two degrees of freedom,

3. The flow is considered purely axial.

The hub and grips are designed to fit the blades, paddles and sensors inserted in the hub. The rotor is articulated and the flap and pitch axes are independent so the flap and pitch deflections can be easily measured.

Similarly to the 4 degree-of-freedom analysis presented in the previous section, it was chosen to use the force balance approach in the present investigation to derive the equation of motion of the rotor. The present analysis is based on a state space resolution of the moments applied on the blade and paddle. To this end, the blade and paddle are divided into N_{segb} and N_{segp} elements respectively. Centrifugal, inertial and aerodynamic moments are then computed at each segment. Aerodynamic coefficients are obtained using Theodorsen's theory. Unsteady aerodynamics can be included using Theodorsen's coefficient C[k]. The model can be divided into four parts:

1. The rotor geometry and mass data are input into the code,
2. The paddle pitch and flap equations and the blade pitch and flap equations are written,
3. The paddle flap-blade pitch coupling is written,
4. The equation of motion is defined using the state space form. The Bode plots and transfer functions of the degrees of freedom with respect to the swashplate input are plotted.

3.2.1 Step 1 : Inputs

Inputs are similar to the ones exposed earlier:

1. The rotational speeds of the blade and of the paddle are assumed to be equal to Ω.
2. The hub, blade and paddle geometry (see Fig. 3.13).
3. The spring stiffnesses.
4. Theodorsen's coefficients for the blade and paddle.
5. The mass, center of gravity and density of all elements of the blade and paddle.

3.2.2 Step 2 : Paddle flap equation

The paddle flap equation is obtained from the paddle flap equation of the {paddle, aileron, blade} model after removing all terms related to $\ddot{\delta}$, $\dot{\delta}$ and δ. The moments that compose the paddle flap equation is this model

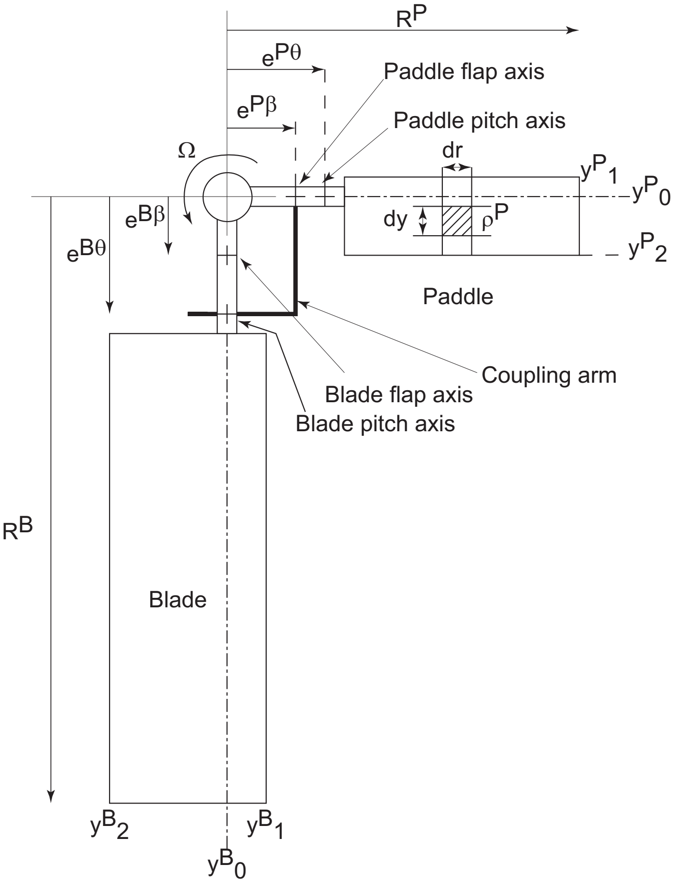

Figure 3.13: Geometry of a paddle and a blade and paddle element characteristics.

are obtained about the paddle flap axis.

$$\ddot{\beta}^P C_{\ddot{\beta}^P}^{Pflap} + \ddot{\theta}^P C_{\ddot{\theta}^P}^{Pflap} + \dot{\beta}^P C_{\dot{\beta}^P}^{Pflap} + \dot{\theta}^P C_{\dot{\theta}^P}^{Pflap} + \beta^P C_{\beta^P}^{Pflap} + \theta^P C_{\theta^P}^{Pflap} = 0 \quad (3.93)$$

with the coefficients $C_{\ddot{\beta}^P}^{Pflap}$, $C_{\ddot{\theta}^P}^{Pflap}$, $C_{\dot{\beta}^P}^{Pflap}$, $C_{\dot{\theta}^P}^{Pflap}$, $C_{\beta^P}^{Pflap}$ and $C_{\theta^P}^{Pflap}$ respectively defined as:

$$\begin{cases} C_{\ddot{\beta}^P}^{Pflap} = -I_\beta^P + \int_{e^P\beta}^{R^P} \left[\frac{1}{8}\ \left(c^P\right)^2\ \pi\ \left(e_\beta^P - r\right) \left(2e_\beta^P + \left(2 - c^P\right) C[k] r\right)\ \rho_{air}\right] dr \\ C_{\ddot{\theta}^P}^{Pflap} = \overline{S_\theta^P} + \int_{e^P\beta}^{R^P} \left[\frac{1}{32}\ \left(c^P\right)^4\ \pi\ \left(e_\beta^P - r\right)\ \rho_{air}\right] dr \\ C_{\dot{\beta}^P}^{Pflap} = \int_{e^P\beta}^{R^P} \left[C[k]\ c^P\ e_\beta^P\ \Omega\ \pi\ \left(e_\beta^P - r\right)\ r\ \rho_{air}\right] dr \\ C_{\dot{\theta}^P}^{Pflap} = \int_{e^P\beta}^{R^P} \left[\frac{1}{8}\ \left(2 + \left(2 - c^P\right)\ C[k]\right)\ \left(c^P\right)^2\ \Omega\ \pi\ \left(r - e_\beta^P\right)\ r\ \rho_{air}\right] dr \\ C_{\beta^P}^{Pflap} = -k_\beta^P - \Omega^2 \left(I_\beta^P + e_\beta^P S_\beta^P\right) \\ C_{\theta^P}^{Pflap} = \Omega^2 \left(\overline{S_\theta^P} + e_\beta^P S_\theta^P\right) + \int_{e^P\beta}^{R^P} \left[C[k]\ c^P\ \Omega^2\ \pi\ r^2\ \left(r - e_\beta^P\right)\ \rho_{air}\right] dr \end{cases} \quad (3.94)$$

3.2.3 Paddle pitch equation

The paddle pitch equation is obtained from the paddle flap equation of the {paddle, aileron, blade} model after removing all terms related to $\ddot{\delta}$, $\dot{\delta}$ and δ. The moments that compose the paddle pitch equation in this model are determined about the paddle pitch axis.

$$\ddot{\beta}^P C_{\ddot{\beta}^P}^{Ppitch} + \ddot{\theta}^P C_{\ddot{\theta}^P}^{Ppitch} + \dot{\beta}^P C_{\dot{\beta}^P}^{Ppitch} + \dot{\theta}^P C_{\dot{\theta}^P}^{Ppitch} + \beta^P C_{\beta^P}^{Ppitch} + \theta^P C_{\theta^P}^{Ppitch} = 0 \quad (3.95)$$

with the coefficients $C_{\ddot{\beta}^P}^{Ppitch}$, $C_{\ddot{\theta}^P}^{Ppitch}$, $C_{\dot{\beta}^P}^{Ppitch}$, $C_{\dot{\theta}^P}^{Ppitch}$, $C_{\beta^P}^{Ppitch}$ and $C_{\theta^P}^{Ppitch}$

respectively defined as:

$$\left\{\begin{aligned} C^{Ppitch}_{\ddot{\beta}^P} &= \int_{e^P_\theta}^{R^P} \left[\frac{1}{64}\left(c^P\right)^3 \pi \rho_{air}\left(-2c^P e^P_\theta + 4r\right.\right. \\ &\quad + \left.\left.\left(-4 + \left(c^P\right)^2\right) rC[k]\right)\right] dr + \overline{S^P_\theta} \\ C^{Ppitch}_{\ddot{\theta}^P} &= \int_{e^P_\theta}^{R^P} \left[-\frac{1}{64}\left(c^P\right)^2\left(2 + \left(c^P\right)^2\right)\pi\rho_{air}\right] dr - I^P_\theta \\ C^{Ppitch}_{\dot{\beta}^P} &= \int_{e^P_\theta}^{R^P} \left[-\frac{1}{8}\left(c^P\right)^2\left(2 + c^P\right) e^P_\theta \Omega\pi r\rho_{air} C[k]\right] dr \\ C^{Ppitch}_{\dot{\theta}^P} &= \int_{e^P_\theta}^{R^P} \left[-\frac{1}{64}\left(2 - c^P\right)\left(c^P\right)^3 \Omega\pi r\rho_{air}\left(2 - \left(c^P + 2\right) C[k]\right)\right] dr \\ C^{Ppitch}_{\beta^P} &= \Omega^2\left(\overline{S^P_\theta} + e^P_\theta S^P_\theta\right) \\ C^{Ppitch}_{\theta^P} &= \int_{e^P_\theta}^{R^P} \left[\frac{1}{8}\left(c^P\right)^2\left(2 + c^P\right)\Omega^2\pi r^2\rho_{air} C[k]\right] dr - k^P_\theta - I^P_\theta \Omega^2 \end{aligned}\right. \tag{3.96}$$

3.2.4 Blade flap equation

The blade flap equation is obtained from the blade flap equation of the {paddle, aileron, blade} model. The moments that compose the blade flap equation are taken about the blade flap axis.

$$\begin{aligned} \ddot{\beta}^B C^{Bflap}_{\ddot{\beta}^B} + \ddot{\theta}^B C^{Bflap}_{\ddot{\theta}^B} + \dot{\beta}^B C^{Bflap}_{\dot{\beta}^B} + \dot{\theta}^B C^{Bflap}_{\dot{\theta}^B} \\ + \beta^B C^{Bflap}_{\beta^B} + \theta^B C^{Bflap}_{\theta^B} + v_i C^{Bflap}_{v_i} = 0 \end{aligned} \tag{3.97}$$

with the coefficients $C^{Bflap}_{\ddot{\beta}^B}$, $C^{Bflap}_{\ddot{\theta}^B}$, $C^{Bflap}_{\dot{\beta}^B}$, $C^{Bflap}_{\dot{\theta}^B}$, $C^{Bflap}_{\beta^B}$, $C^{Bflap}_{\theta^B}$ and $C^{Bflap}_{v_i}$ respectively defined as:

$$\left\{\begin{aligned} C^{Bflap}_{\ddot{\beta}^B} &= -I^B_\beta + \textstyle\int_{e^{B\beta}}^{R^B} \left[\frac{1}{8}\left(c^B\right)^2 \pi \left(e^B_\beta - r\right)\left(2e^B_\beta - \left(-2 + c^B\right) C[k] r\right) \rho_{air}\right] dr \\ C^{Bflap}_{\ddot{\theta}^B} &= \overline{S^B_\theta} + \textstyle\int_{e^{B\beta}}^{R^B} \left[\frac{1}{32}\left(c^B\right)^4 \pi \left(e^B_\beta - r\right) \rho_{air}\right] dr \\ C^{Bflap}_{\dot{\beta}^B} &= \textstyle\int_{e^{B\beta}}^{R^B} \left[C[k]\, c^B\, e^B_\beta\, \Omega\, \pi \left(e^B_\beta - r\right) r\, \rho_{air}\right] dr \\ C^{Bflap}_{\dot{\theta}^B} &= \textstyle\int_{e^{B\beta}}^{R^B} \left[\frac{1}{8}\left(c_B\right)^2\left(-2 + \left(-2 + c^B\right) C[k]\right) \Omega\, \pi \left(e^B_\beta - r\right) r\, \rho_{air}\right] dr \\ C^{Bflap}_{\beta^B} &= -k^B_\beta - \Omega^2\left(I^B_\beta + e^B_\beta S^B_\beta\right) \\ C^{Bflap}_{\theta^B} &= \Omega^2\left(\overline{S^B_\theta} + e^B_\beta S^B_\theta\right) + \textstyle\int_{e^{B\beta}}^{R^B} \left[C[k]\, c^B\, \Omega^2\, \pi\, r^2 \left(r - e^B_\beta\right) \rho_{air}\right] dr \\ C^{Bflap}_{v_i} &= c^B C[k]\Omega\pi\left(r - e^B_\beta\right) r\rho_{air} \end{aligned}\right. \tag{3.98}$$

3.2.5 Blade pitch equation

The blade pitch equation is obtained from the blade pitch equation of the {paddle, aileron, blade} model. The moments that compose the blade pitch equation are taken about the blade pitch axis.

$$\begin{aligned}\ddot{\beta}^B C_{\ddot{\beta}^B}^{Bpitch} + \ddot{\theta}^B C_{\ddot{\theta}^B}^{Bpitch} + \dot{\beta}^B C_{\dot{\beta}^B}^{Bpitch} + \dot{\theta}^B C_{\dot{\theta}^B}^{Bpitch} & \\ + \beta^B C_{\beta^B}^{Bpitch} + \theta^B C_{\theta^B}^{Bpitch} + v_i C_{v_i}^{Bpitch} = 0 & \quad (3.99)\end{aligned}$$

with the coefficients $C_{\ddot{\beta}^B}^{Bpitch}$, $C_{\ddot{\theta}^B}^{Bpitch}$, $C_{\dot{\beta}^B}^{Bpitch}$, $C_{\dot{\theta}^B}^{Bpitch}$, $C_{\beta^B}^{Bpitch}$, $C_{\theta^B}^{Bpitch}$ and $C_{v_i}^{Bpitch}$ respectively defined as:

$$\begin{cases} C_{\ddot{\beta}^B}^{Bpitch} & = \int_{e_\theta^B}^{R^B} \left[\frac{1}{64}\left(c^B\right)^3 \pi\rho_{air}\left(-2c^B e_\theta^B + 4r + \left(-4 + \left(c^B\right)^2\right) rC[k]\right)\right] dr + \overline{S_\theta^B} \\ C_{\ddot{\theta}^B}^{Bpitch} & = \int_{e_\theta^B}^{R^B} \left[-\frac{1}{64}\left(c^B\right)^2 \left(2 + \left(c^B\right)^2\right) \pi\rho_{air}\right] dr - I_\theta^B \\ C_{\dot{\beta}^B}^{Bpitch} & = \int_{e_\theta^B}^{R^B} \left[-\frac{1}{8}\left(c^B\right)^2 \left(2 + c^B\right) e_\theta^B \Omega\pi r\rho_{air} C[k]\right] dr \\ C_{\dot{\theta}^B}^{Bpitch} & = \int_{e_\theta^B}^{R^B} \left[-\frac{1}{64}\left(-2 + c^B\right)\left(c^B\right)^3 \Omega\pi r\rho_{air}\left(-2 + \left(c^B + 2\right) C[k]\right)\right] dr \\ C_{\beta^B}^{Bpitch} & = \Omega^2\left(\overline{S_\theta^B} + e_\theta^B S_\theta^B\right) \\ C_{\theta^B}^{Bpitch} & = \int_{e_\theta^B}^{R^B} \left[\frac{1}{8}\left(c^B\right)^2 \left(2 + c^B\right) \Omega^2 \pi r^2 \rho_{air} C[k]\right] dr - k_\theta^B - I_\theta^B \Omega^2 \\ C_{v_i}^{Bpitch} = 0 & \end{cases} \tag{3.100}$$

3.2.6 Step 3 : Blade pitch and paddle flap coupling

As described in the previous method, the blade pitch angle and the paddle flap angle are coupled. The coupling is assumed to be $\theta^B = \beta^P$. It is used to combine Equations. 3.93 and 3.99. These two equations are added to obtain the coupling equation:

$$\begin{aligned}\ddot{\beta}^B C_{\ddot{\beta}^B}^{Bpitch} + \ddot{\theta}^B \left(C_{\ddot{\theta}^B}^{Bpitch} + C_{\ddot{\beta}^P}^{Pflap}\right) + \ddot{\theta}^P C_{\ddot{\theta}^P}^{Pflap} & \\ + \dot{\beta}^B C_{\dot{\beta}^B}^{Bpitch} + \dot{\theta}^B \left(C_{\dot{\theta}^B}^{Bpitch} + C_{\dot{\beta}^P}^{Pflap}\right) + \dot{\theta}^P C_{\dot{\theta}^P}^{Pflap} & \\ + \beta^B C_{\beta^B}^{Bpitch} + \theta^B \left(C_{\theta^B}^{Bpitch} + C_{\beta^P}^{Pflap}\right) + \theta^P C_{\theta^P}^{Pflap} = 0 & \quad (3.101)\end{aligned}$$

3.2.7 Step 4 : Equation of motion, state space form and transfer function

Equation of motion

The number of degrees of freedom has now been reduced from four to three. The degrees of freedom are now:

1. The blade flap angle, β^B,
2. The blade pitch angle, θ^B,
3. The paddle pitch angle, θ^P.

The equation of motion is obtained from the three following equations:

1. The blade flap equation (Equation. 3.97),
2. The blade pitch and paddle flap coupling equation (Equation. 3.101),
3. The paddle pitch equation (Equation. 3.95).

The equation of motion is therefore written as:

$$[M]\left\{\begin{matrix}\ddot{\beta}^B\\ \ddot{\theta}^B\\ \ddot{\theta}^P\end{matrix}\right\}+[C]\left\{\begin{matrix}\dot{\beta}^B\\ \dot{\theta}^B\\ \dot{\theta}^P\end{matrix}\right\}+[K]\left\{\begin{matrix}\beta^B\\ \theta^B\\ \theta^P\end{matrix}\right\}=\left\{\begin{matrix}0\\ 0\\ F_{swash}+[C_{constant}]v_i\end{matrix}\right\} \tag{3.102}$$

where M is the mass matrix, C is the damping matrix, K is the stiffness matrix, F_{swash} is the pitch input from the swashplate and the $C_{constant}$ matrix regroups the terms related to the induced velocity. Once numerical values are input is the M matrix, it is clear it is symmetric and positive definite. It is inversible as its determinant is not equal to zero. The M, C and K matrices are defined below:

$$[M]=\begin{bmatrix}C^{Bflap}_{\ddot{\beta}^B} & C^{Bflap}_{\ddot{\theta}^B} & 0\\ C^{Bpitch}_{\ddot{\beta}^B} & \left(C^{Bpitch}_{\ddot{\theta}^B}+C^{Pflap}_{\ddot{\beta}^P}\right) & C^{Pflap}_{\ddot{\theta}^P}\\ 0 & C^{Ppitch}_{\ddot{\beta}^P} & C^{Ppitch}_{\ddot{\theta}^P}\end{bmatrix} \tag{3.103}$$

$$[C]=\begin{bmatrix}C^{Bflap}_{\dot{\beta}^B} & C^{Bflap}_{\dot{\theta}^B} & 0\\ C^{Bpitch}_{\dot{\beta}^B} & \left(C^{Bpitch}_{\dot{\theta}^B}+C^{Pflap}_{\dot{\beta}^P}\right) & C^{Pflap}_{\dot{\theta}^P}\\ 0 & C^{Ppitch}_{\dot{\beta}^P} & C^{Ppitch}_{\dot{\theta}^P}\end{bmatrix} \tag{3.104}$$

$$[K]=\begin{bmatrix}C^{Bflap}_{\beta^B} & \theta^B C^{Bflap}_{\theta^B} & 0\\ C^{Bpitch}_{\beta^B} & \left(C^{Bpitch}_{\theta^B}+C^{Pflap}_{\beta^P}\right) & C^{Pflap}_{\theta^P}\\ 0 & C^{Ppitch}_{\beta^P} & C^{Ppitch}_{\theta^P}\end{bmatrix} \tag{3.105}$$

The input matrix $[F]$ is defined as:

$$\left\{\begin{matrix} 0 \\ 0 \\ F_{swash} \end{matrix}\right\} \tag{3.106}$$

with F_{swash} the force exerted by the swashplate.

State space form

As in Section. 3.1.8, the state space form of the {paddle, blade} model is written from its equation of motion (Equation. 3.102). For the same reasons stated in the {paddle, aileron, blade} model, the induced velocity is not taken into account in the state space form. It is here a 6^{th} order system:

$$\begin{cases} \dot{\chi} & = [A]\chi + [B]u \\ y & = [\zeta]\chi \end{cases} \tag{3.107}$$

with $[A]$ and $[B]$ state space matrices and $y = \theta^P$ the output. The input u is F_{swash} the force input provided by the swashplate and controls θ^P.

The matrix $[A]$ is obtained from Matrices. 3.103, 3.104 and 3.105:

$$\begin{bmatrix} [0]_{3*3} & [I]_{3*3} \\ -[M]^{-1}[K] & -[M]^{-1}[C] \end{bmatrix} \tag{3.108}$$

The matrix $[B]$ is obtained from Matrices. 3.103 and 3.106:

$$\begin{bmatrix} [0]_{3*3} \\ -[M]^{-1}[F] \end{bmatrix} \tag{3.109}$$

$[0]_{3*3}$ and $[I]_{3*3}$ are a three-by-three zero matrix and af three-by-three identity matrix respectively.

Transfer function H(s)

The transfer function is finally obtained from Equation.3.107, using the Laplace transform:

$$\begin{cases} s\chi & = [A]\chi + [B]U(s) \\ Y(s) & = [\zeta]\chi \end{cases} \tag{3.110}$$

Equation.3.110 can be written as:

$$\begin{cases} \chi & = \left(s[I]_{6*6} - [A]\right)^{-1}[B]U(s) \\ Y(s) & = [\zeta]\left(s[I]_{6*6} - [A]\right)^{-1}[B]U(s) \end{cases} \tag{3.111}$$

where $[I]_{6*6}$ is a six-by-six identity matrix. The transfer function $H(s)$, can then be defined as:

$$H(s) = \frac{Y(s)}{U(s)} = [\zeta] \left(s[I]_{6*6} - [A]\right)^{-1} [B] \qquad (3.112)$$

Bode plots can then be computed.

3.3 Conclusion

The two models exposed in this chapter predict the dynamic behavior of the respective configurations:

1. {Paddle, aileron, blade}. The blade pitch is coupled to the paddle flap. The paddle flap is controlled via the aileron deflection.
2. {Paddle, blade}. The blade pitch is coupled to the paddle flap. The paddle flap is commanded by a small swashplate.

A parametric study based on the first model is presented in the next chapter. The second configuration is tested in a hover stand to check the authority of the paddle on the blade.

Chapter 4

Experiments, results and discussion

Ce chapître décrit les études expérimentales qui ont été menées ainsi que les résultats analytiques et expérimentaux. Premièrement, une série d'essais en vol en plein air a été effectuée pour établir la faisabilité du système. Puis, le comportement du "Rotor Vert" simplifié a été étudié lors d'essais en vol stationnaire. Ces derniers essais ont été réalisés sur un banc rotor principal qui est un environnement beaucoup plus maîtrisé, des capteurs ont été utilisés pour mesurer certaines caractéristiques du rotor, tels que les angles de battement et de pas des pales et palettes. Certains résultats analytiques ainsi que les résultats expérimentaux des tests en vol stationnaire sont présentés. Ensuite, une validation de l' analyse est exposée.

L'objectif des essais en vol était de démontrer le bien-fondé du concept de couplage entre le battement de la palette et pas des pales afin de réaliser la régulation primaire du rotor. Ces tests ont été effectués en plein air sur un modèle réduit d'hélicoptère (ou hélicoptère RC) disponible dans le commerce (ou sur étagère). Le rotor d'hélicoptère a été modifié pour inclure le couplage mécanique entre le battement de la palette et le pas de la pale. Le rotor ne comportait pas d'ailerons actionnés par des PZT. Les palettes étaient actionnées par de petits plateaux cycliques pour simplifier le design. Ce rotor reflète donc la configuration exposée dans l'analyse {Palette, pale} au Chapitre 3. Le diamètre du rotor est de $1,853$ *m. L'hélicoptère a volé dans un environnement de vents quelconques où l'amplitude et la direction du vent n'étaient pas maîtrisées. L'hélicoptère était stable dans ces conditions et des vols en stationnaire ont été réalisés avec succès et à plusieurs reprises*

Les essais en vol n'ont pas été effectués dans un environnement maîtrisé et aucun capteur n'équipait le rotor. Ces inconvénients sont traités par des essais sur un banc rotor principal afin d'évaluer le comportement dynamique du système en vol stationnaire.

Des tests en vol stationnaire ont été effectués sur un rotor d'échelle réduite. Les objectifs des essais en vol stationnaire étaient les suivants:

1. *Déterminer l'influence du pas d'une palette sur le pas d'une pale en régime établi,*
2. *Faire en sorte que la palette permette que toute la plage de pas de la pale soit atteignable,*
3. *Recueillir des données expérimentales pour valider l'analyse,*
4. *Evaluer la Figure de Merit de la configuration actuelle et déterminer si elle est meilleure que dans le cas d'une conception classique.*

Les tests ont été effectués dans la soufflerie d'Eurocopter France. Le vent n'étant pas utilisé, la soufflerie s'apparente à un banc rotor principal d'échelle réduite. Le support de la maquette est équipé d'un moteur de 400 *Hz et d'un renvoi d'angle. Une balance six-axes est montée sur le support. Cette balance est utilisée pour mesurer les forces et les moments du rotor. Si la balance n'est pas utilisée, elle est remplacée par une fausse balance. La fausse balance est une masse de métal insérée dans le support à l'emplacement réservé à la balance six-axes. Ses caractéristiques sont déterminés afin que la fréquence propre du support soit sensiblement similaire quelle que soit la balance utilisée. La fréquence propre du support équipé de la balance et d'un rotor à deux pales et deux palettes est de* $8,5$ *Hz. La même configuration, cette fois avec la fausse balance, présente une fréquence propre de* $9,5$ *Hz.*

Afin que la palette réalise avec succès la commande de la pale, les essais ont été effectués sur un modèle plus simple que la configuration {Palette, Aileron, Pale} décrite dans le Chapitre 3. Dans le modèle expérimental actuel, les palettes sont actionnées par de petits plateaux cycliques et non pas par un aileron actionné par des actionneurs piézo-électriques. Cela simplifie la conception et réduit le temps de développement et le coût des tests. Afin de réduire davantage les coûts, les plateaux cycliques utilisés sont ceux d'un modèle expérimental d'un autre projet.

Le rotor testé est un rotor de petite échelle, qui était équipé de deux pales, deux palettes et d'un couplage battement de palette-pas de pale. Pour simplifier la conception, les pales et leurs palettes correspondantes sont situées sur le même plan, avec un angle de 90° *d'azimut entre chaque pale et sa palette. Le couplage a été conçu de telle sorte que* 1° *de battement de palette donne* 1° *de pas de pale. Le diamètre du rotor a été limité pour éviter les effets de sol. Le diamètre du rotor est de* $1,868m$*. Les axes du battement et du pas sont dissociés pour que les mesures soient faciles à effectuer et que le couplage soit limité au pas de la pale-battement de la palette. En outre, la biellette de pas de la pale, qui est reliée au mécanisme de couplage, est située sur l'axe du battement de la pale pour éviter tout effet* δ_3*. La rotation autour des axes du battement et du pas est obtenue en utilisant des bagues en bronze autolubrifiantes.*

Les pales utilisées sont disponibles sur étagère. Leur profil offre l'avantage de réduire le moment en pas de la pale. Les palettes sont obtenues, elles aussi, à partir de pales disponibles sur étagère. Le fournisseur de ces pales a percé des trous le long de l'envergure et de la corde des pales. Des poids en plomb ont été ensuite introduits dans ces trous et recouverts de résine. Ceci assure un même moment statique au sein d'une paire de pales. Une pale a été radiographiée afin de connaître l'inertie exacte de cette pale. Cependant les pales sont coupées en envergure pour obtenir les palettes. On modifie aussi l'inertie des palettes en introduisant par leur saumon, des poids en plomb sur leur axe de pas, afin de ne pas altérer leur moment en pas. Le dernier paramètre relatif aux palettes est la position radiale du milieu de la palette. Il est varié en utilisant des manchons de palettes de différentes longueurs.

Comme les axes du pas et du battement sont dissociés sur les pales et palettes, tous les manchons sont constitués de deux parties : une partie battante qui est située plus proche du moyeu et une partie plus éloignée du moyeu *qui peut battre et prendre du pas. Par ailleurs, si la palette bat vers le haut, le couplage a été conçu de telle façon que l'angle de pas de la pale augmente. Les pales et palettes sont attachées à leur manchon par une vis unique permettant le recul de pale et palette.*

La force exercée par les plateaux cycliques sur la bielle de pas de la palette commande le pas de la palette. La sortie du système est l'angle de pas de la pale. Le banc rotor principal offre un environnement maîtrisé, qui permet d'évaluer l'influence de plusieurs paramètres sur le comportement dynamique du système. Dans la présente étude, les paramètres variés sont : l'inertie de la palette, son envergure et sa position radiale. Pour évaluer l'influence d'un de ces paramètres, les deux autres doivent rester constants. Si l'envergure et la position radiale varient et que l'inertie reste constante, alors l'effet des forces aérodynamiques peut être déterminé. Il s'agit essentiellement d'une variation du nombre de Lock. Les différentes valeurs prises par les paramètres sont spécifiées dans ce chapitre. Pour chaque configuration {inertie,position radiale, envergure}, des angles collectifs et cycliques de palette sont introduits. L'angle de pas collectif varie entre $[-8^\circ, 14^\circ]$. *L'angle de pas cyclique de palette varie entre* $[-8^\circ, 8^\circ]$.*Ces angles ont été définis par l'encombrement entre les plateaux cycliques et le moyeu. Ces angles collectifs peuvent ne pas permettre d'observer le comportement du système proche du décrochage.*

Les mesures sont prises tant que le régime établi n'est pas atteint. On mesure la vitesse de rotation du rotor en utilisant un capteur de Hall. Les angles de pas et de battement des palettes et pales sont mesurés en utilisant des potentiomètres rotatifs installés sur les axes du pas et du battement. La balance à 6 axes permet de mesurer la portance, les moments et les couples. Les mesures de couple sont importantes puisqu'elles permettent le calcul de la Figure de Merit. Toutes les données enregistrées dans le repère tournant sont transmises au repère fixe par l'intermédiaire d'un collecteur.

Quand un rotor est mis en rotation, il rencontre des modes avant d'atteindre sa vitesse de rotation nominale. Afin d'assurer de bonnes conditions de vol stationnaire et de mesures, aucun mode ne devrait être présent près de la vitesse de rotation du rotor. On utilise le critère de Coleman pour déterminer si le système peut subir une résonance sol. Pour ce faire la fréquence du premier mode de traînée est calculée pour une vitesse de rotation rotor de 15 *Hz. Il est démontré que si la balance 6 axes est utilisée, il existe un risque de résonance sol. Plusieurs solutions sont tour à tour implémentées pour résoudre ce problème.*

1. *Des câbles sont d'abord attachés entre le support rotor et le sol. Cette solution empêche tout mouvement intempestif du support. Elle permet d'éviter toute résonance sol. Cependant, les câbles étaient soumis à des vibrations durant les rotations rotor. Les points d'attache au sol des câbles ont de ce fait été endommagés. Cette solution n'a donc pas été retenue.*
2. *Des masses ont été ajoutées au support afin de baisser sa fréquence propre. Il a été observé que même en utilisant des masses importantes (jusqu'à* 22.4 *kg), les risques de résonance sol étaient toujours importants. Abaisser de manière satisfaisante la fréquence propre du support nécessitant des masses trop importantes, il a été décidé de ne pas*

implémenter cette solution.

3. *La vitesse de rotation rotor pourrait être abaissée à* 14*Hz par exemple. Cependant, les règles de sécurité des installations interdisaient l'utilisation de la balance.*

Les test ont donc été réalisés avec la fausse balance, avec le rotor tournant à 15 *Hz. Aucun câble, aucune masse n'ont été utilisé. L'utilisation de la fausse balance implique que les forces et moments au moyeu n'ont pu être mesurés. La Figure de Merit du rotor vert n'a donc pas été déterminée expérimentalement.*

Comme mentionné ci-dessus, l'architecture de la maquette inclut des bagues en bronze autolubrifiantes sur chaque axe du pas et du battement des pales et palettes. Il a été observé que les bagues ont généré d'importants frottements. Par conséquent, l'utilisation des bagues autolubrifiantes a causée des vibrations. Des vibrations ont également été générées au cours de la mise en rotation du rotor, jusqu'à ce qu'il atteigne son régime nominal. Durant la mise en rotation, le rotor est "passé par des modes". Si la vitesse de rotation du rotor était augmentée rapidement jusqu'à 15 *Hz, le rotor passait très vite les modes. Il a été ainsi constaté que le niveau des vibrations n'est pas reproductible d'un essai à l'autre. Il convient de noter que les certains capteurs ont cessé de fonctionner correctement après le premier test en raison des vibrations. Un capteur mesurant le pas de pale par exemple, a cessé de fonctionner. Dans ce cas, il a été supposé que l'angle de pas des pales était égal à l'angle du battement de la palette.*

Du fait des problèmes mentionnés ci-dessus, la séquence de tests a été réduite. Seulement deux paires de palettes ont été testées. L'une possède une envergure de 20% *du rayon de la pale et son point d'attachement à son manchon est situé à* 20% *du rayon de la pale. Son inertie de battement est de* $0.00579\ kg.m^2$*. L'autre paire de palette a une envergure de* 40% *du rayon de la pale et son point d'attachement à son manchon est situé à* 20% *du rayon de la pale. Son inertie de battement est de* $0.01046\ kg.m^2$*.*

Un exemple de résultat d'analyse est ensuite présenté. L'analyse {*Palette-Aileron-Pale*} *a été simplifiée, l'écoulement est considéré quasi-stationnaire, afin de vérifier si une fréquence calculée de manière analytique et une fréquence donnée par le code sont similaires. Il est à noter que le système dans cett section est basé sur un hélicoptère Ecureuil, la vitesse de rotation du rotor est d'environ 40 rad/s. Si un mouvement de battement de pale est considéré, la valeur analytique de la première fréquence de battement, avec des vibrations libres amorties est* 41, 18 *rad/s et la fréquence du code est* 41.25 *rad/s. On constate donc que les quantités en sortie du code sont réalistes. Une étude paramétrique est effectuée. La palette a la même corde et masse par unité de surface que la pale. L'aileron a la même envergure et masse par unité de surface que la palette. La corde de l'aileron est égale à* 25% *de la corde de la palette. On évalue par exemple l'effet de la position radiale de la palette (centrée à* 30% R^B*,* 40% R^B *et* 50% R^B*) et de la masse de la palette (en maintenant sa surface constante). Il est constaté que quand la palette est eloignée du moyeu, la réponse en pas de pale baisse. Cela est attribué à la masse relativement importante de la palette, ce qui cause de faibles angles de battement de palette et par conséquent, de faibles angles de pas de pale. La densité de la palette est variée. Si cette densité* *décroît et les dimensions de paddle restent constantes, la masse de la palette diminue. Par conséquent, la fréquence propre de la palette augmente et est alors supérieure à 1/ rev. De ce fait, la norme de la réponse cyclique de la palette baisse. Donc, la portance générée par la palette est réduite, ce qui entraîne une diminution de la réponse en battement de la palette. La réponse en pas de pale diminue puisqu'elle est couplée avec le battement de la palette. Comme décrit ci-dessus, l'analyse à 4 degrés de liberté qu'est l'approche {Palette, Aileron, Pale} a été mise en oeuvre dans MATLAB et les conclusions suivantes peuvent être tirées:*

1. *Le concept de couplage pas de pale-battement de palette a été représenté sous une forme analytique. L'analyse inclut des caractéristiques de l'architecture d'un hélicoptère Ecureuil. Plusieurs cas ont été étudiés et des fonctions de transfert des réponses à une tension unité appliquée à un actionneur PZT ont été obtenues. Les réponses en collectif et cyclique peuvent être extraites des fonctions de transfert*
2. *Lorsqu'un mouvement de battement, par exemple, est considéré, la fréquence de battement obtenue par le modèle numérique 4 degrés de liberté est en accord avec la fréquence obtenue à partir d'une analyse simplifiée basée sur les premiers principes.*
3. *L'analyse à 4 degrés de liberté à démontré l'effet de la position radiale de la palette ainsi que l'effet de sa masse (pour une superficie de palette constante). Il a été montré que quand la palette est éloignée du moyeu, elle est soumise à une augmentation des efforts centrifuges et bat donc moins. Cela conduit à une diminution de la réponse en pas de pale dû au couplage pas de pale-battement de palette. L'effet de la masse de la palette a été montré sur la fréquence propre de la palette. Si la fréquence propre de la palette est augmentée, alors la réponse en pas cyclique de la palette décroît comme le font les réponses en battement de palette et en pas de pale.*
4. *L'influence des forces aérodynamiques est observée en termes d'amortissement.*
5. *L'actionneur PZT n'est pas choisi pour le moment. On ne peut donc s'appuyer sur les normes des réponses pour concevoir et définir la configuration optimum pour maximiser la réponse de pas des pales. L'amplitude des réponses est informative et indique les performances relatives des différentes configurations.*
6. *Les normes relatives des réponses analytiques des différentes configurations fournissent une orientation concernant le choix des paramètres expérimentaux.*

Comme mentionné ci-dessus, deux cas de palettes ont été testés en vol stationnaire : cas A' et B'. Les résultats sont donnés sous la forme d'angles collectifs (appelés aussi statiques) et de normes d'angles cycliques (appelés dynamiques). Les variations temporelles du pas statique et dynamique des pales et palettes durant les deux tests sont présentées. On remarque que dans le test B', certaines données sont manquantes. Ceci est dû à la perte de capteurs causée par des vibrations excessives lors du test A'. On note aussi que les mesures d'une même quantité, par exemple l'angle de pas collectif, provenant des deux palettes ne sont pas identiques. Cela veut dire que les palettes ne répondent pas de la même façon à une même entrée provenant des plateaux cycliques. De même, dans le cas des pales, la même *entrée ne produit pas la même réponse des deux pales. Ceci est dû aux frottements générés par les bagues autolubrifiantes situées sur les axes du battement et du pas des pales et palettes. En effet, quand le rotor est en rotation, tout lubrifiant subit l'effet de la charge centrifuge et ne lubrifie donc pas toute la bague, génèrant du frottement. Les variations des angles de pas statique et dynamique de la pale en fonction des angles de pas statique et dynamique, respectivement, de la palette sont aussi présentées. Il est noté que ces courbes montrent une forme d'hystérésis. Par exemple, pour une valeur de pas statique de palette, il existe deux valeurs de pas statique de pale correspondantes. Ce phénomène apparaît lors de la variation en pas de palette sur sa plage prédéfinie. La réponse en pas de pale n'est pas toujours la même pour un pas de palette donné. Ceci prouve la présence de frottements dans les bagues en bronze mentionnées précédemment. De plus, puisque les réponses des deux pales ne sont pas confondues, cela indique que les pales ne sont pas alignées. Par ailleurs, la réponse en pas statique des pales est plus importante dans le cas B'. Ceci peut être expliqué par le fait que les palettes dans le cas B' ont une plus grande surface et donc génèrent plus de portance et ainsi plus de battement de palette. Donc, le pas de la pale est plus important dans le cas B'. L'erreur de mesure peut être aussi incriminée dans les résultats du cas A' : les angles sont réduits, l'erreur est donc prédominante. Une courbe linéaire accompagnée d'un facteur de régression est tracée à partir des variations en pas statique et dynamique de la pale en fonction des pas statique et dynamique de la palette. Plus le facteur de régression est proche de 1, plus les données expérimentales sont proches de leur courbe linéaire correspondante. Il est observé que les pales dans le cas B' ont un comportement plus linéaire que dans le cas A'. Moins de frottements ont dû être générés dans le cas B'.*

L'analyse {Palette, Pale}, aussi appelée analyse 3 degrés de liberté, est utilisée pour obtenir des résultats analytiques afin de les comparer aux résultats expérimentaux. Comme de très importants frottements ont été observés dans le cas A', seul le cas B' est considéré dans la présente étude de corrélation. L'analyse {Palette, Pale} produit des diagrammes de Bode à partir desquels sont extraites les composantes statiques et dynamiques des données de pas de palette et de pale. Les composantes du pas de la pale sont divisées par les composantes du pas de la palette. On obtient donc les valeurs de pentes analytiques pour les pas de pale statique et dynamique respectivement en fonction des pas de palette statique et dynamique. Les pentes analytiques et expérimentales, pour les pas statique et dynamique, sont comparées. Les pentes analytiques et expérimentales sont différentes. Ceci peut être causé par :

1. *Les pales RC utilisées pour fabriquer les palettes incluent des cavités remplies de plombs et de résine. Par conséquent, les caractéristiques des palettes fabriquées à partir des pales RC ne sont pas connues avec précision et varient de palette en palette.*
2. *Les bagues sur les axes du pas et du battement des pales et palettes génèrent d'importants frottements.*
3. *Les pales et palettes ne sont pas alignées.*
4. *Plusieurs capteurs ont cessé de fonctionner dans le cas B'. Le manque de mesures provenant des capteurs susmentionnés a empêché une bonne lecture des angles des pales et palettes.*

Il est donc nécessaire d'évaluer quels résultats de l'analyse {*Palette, Pale*} *ou expérimentaux sont plus viables. Une analyse simplifiée fondée sur les principes premiers est développée pour être utilisée comme référence. Ce modèle simplifié peut être développé pour mieux comprendre le comportement du système en vol stationnaire. Cette approche néglige les excentricités de pas et de battement, les efforts aérodyna-miques sont considérés quasi-stationnaire et les raideurs de rappel à plat sont considérées comme infinies. Les pentes statiques et dynamiques de l'analyse* {*Palette, Pale*}*, du modèle simplifié et de l'expérience sont comparées. Il est clair que les pentes de l'analyse* {*Palette, Pale*} *sont plus proches des pentes du modèle simplifié que des pentes expérimentales. L'analyse* {*Palette, Pale*} *présente donc des résultats plus dignes de confiance que les résultats expéri-mentaux. Les raisons sont celles exposées ci-dessus : les caractéristiques des palettes ne sont pas précisément connues et varient de palette en palette, les bagues en bronze créent d'importants frottements, les pales et palettes ne sont pas alignées et des capteurs ont cessé de fontionner dans le cas B'. Enfin, les différences entre les pentes du modèle* {*Palette, Pale*} *et celles de l'analyse simplifiée montrent l'importance de prendre en compte les excentricités de pas et de battement, la position du centre de gravité des pales et palettes et les termes aérodynamiques instationnaires.*

Les conclusions tirées de ce chapitre sont enfin présentées. Le nouveau concept de couplage de pas de pale-battement de palette a d'abord été testé en vol en extérieur, sur des une version modifiée d'un hélicoptère RC. Ces essais en vol ont validé le concept de commande du rotor à l'aide du couplage mentionné ci-dessus. Les observations qualitatives du pilote ont indiqué une bonne efficacité de la commande en vol stationnaire, même en présence de forts vents de travers.

Une maquette d'échelle réduite comprenant deux pales a été conçue et fabriquée pour effectuer des tests en stationnaire dans un environnement maîtrisé. Les pales et palettes ont été construites en utilisant des pales d'hélicoptère de modélisme disponibles dans le commerce. Le système a été équipé de capteurs pour mesurer les angles de pas et de battement des pales et palettes. Pour éviter toute résonance sol, une fausse balance est utilisée, les forces et moments au moyeu ne sont donc pas mesurés. Deux configurations sont ainsi testées en vol stationnaire. Les tests ont été sévèrement limités par les vibrations du système générées par d'importants frottements dans les bagues présentes sur chaque axes du pas et du battement des pales et palettes. Les pales et palettes ne sont donc pas alignées. Pour une palette d'envergure égale à 40 % du rayon de la pale, avec une angle de pas dynamique de 9°*, un angle de pas dynamique de la pale de* 5° *a été obtenu.*

L'analyse {*Palette, Aileron, Pale*} *est utilisée pour mener une étude paramétrique en incluant les caractéristiques de l'Ecureuil. La méthode* {*Palette, Aileron, Pale*} *a démontré les effets de la masse et de la position radiale de la palette sur les réponses du rotor. Les résultats de cette analyse indiquent quels paramètres ont un effet sur les performances. Les normes relatives des réponses fournissent des orientations quant au choix des paramètres expérimentaux.*

Les résultats de l'analyse {*Palette, Pale*} *ont ensuite été comparés aux résultats expérimentaux. Les résultats expérimentaux montrent une hystéré-*

sis et une importante non-linéarité due aux frottements sur les axes du pas et battement. Un modèle simplifié a donc été conçu pour évaluer la précision de l'analyse {Palette, Pale}. Ce modèle simplifié suppose que les efforts aérodynamiques sont quasi-stationnaires, que le centre de gravité de la pale et celui de la palette se trouve sur leur axe de pas respectif et néglige les excentricités de pas et battement. Les résultats de l'analyse simplifiée sont en bonne corrélation avec les résultats de l'analyse {Palette,Pale} et montrent l'importance de considérer les excentricités, la position du centre de gravité des pales et palettes et des termes aérodynamiques instationnaires. Ces résultats indiquent par ailleurs les effets des frottements relevés dans les données expérimentales. Par conséquent, il a été conclu qu'il est nécessaire d'effectuer de nouvelles expériences avec un rotor soigneusement conçu où les frottements sont minimisés et les paramètres rotor sont bien définis.

This chapter describes the experimental studies that have been carried out as well as analytical and experimental results. First, a series of outdoor flight tests were performed to establish the proof-of-concept of the system. Then, the behavior of a simplified Green Rotor was studied in a hover stand. This facility offers a much more controlled environment and sensors were used to measure some rotor characteristics, such as the blades and paddles pitch and flap angles. Analytical sample results and hover stand results are presented. Then an analytical validation is exposed.

4.1 Experimental studies

4.1.1 Flight tests

The goal of the flight tests was to establish the proof-of-concept of the paddle flap-blade pitch coupling. These tests were performed outdoors on a off the shelf RC helicopter.

The helicopter rotor was modified to include the paddle flap-blade pitch coupling arm. The rotor did not include a PZT-actuated aileron. The paddles were actuated by a small swashplate to keep the design as simple as possible (see Figure. 4.1). Hence this rotor reflects the configuration exposed in the analysis {blade, paddle} in Chapter. 3. The rotor diameter was of 1.853 m. The helicopter was flown in a windy area where the amplitude and direction of the wind were not controlled parameters. The helicopter proved to be stable under these conditions and hover was achieved successfully and repeatedly (see Figure. 4.2).

The flight tests were not performed in a controlled environment and lacked on board-sensor measurements. These short-comings are addressed

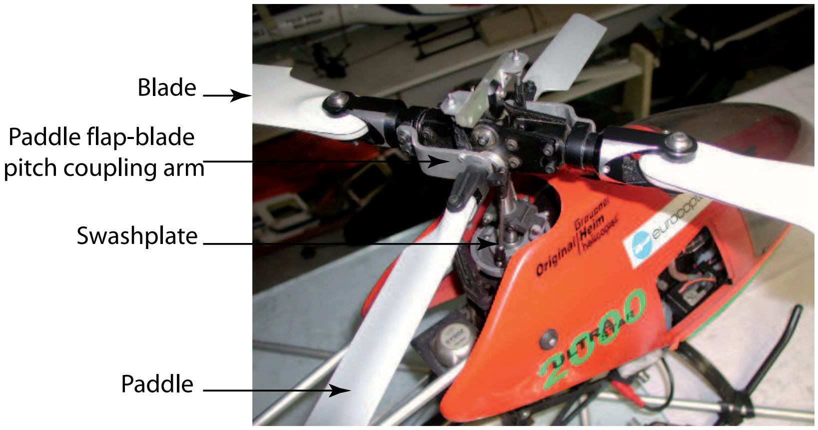

Figure 4.1: Flight tests rotor close-up.

Figure 4.2: RC helicopter outdoor flight test.

by the hover stand tests in order to assess the dynamic behavior of the system.

4.1.2 Hover stand tests

Hover stand tests were performed on a model scale rotor in a hover stand.

Goals

The goals of the hover tests were:

1. To determine the influence of the paddle pitch on the final steady state value of the blade pitch,
2. To ensure that the paddle allows for the whole blade pitch range to be covered,
3. To gather experimental data to validate the analysis,
4. To assess the present configuration Figure of Merit and determine if it is better than in the case of a conventional design.

Testing facility

The tests were performed in the wind tunnel of Eurocopter France. The wind was turned off so that the stand could be used as a small scale whirl tower. The stand is equipped with a 400 Hz motor and a bell crank (see Figure. 4.3). A six-axes balance is mounted on the stand (see Figure. 4.3). This balance is used to measure the hub forces and moments. If the balance is not used, it is replaced by a dummy one to keep the natural frequency of the system fairly similar. The natural frequency of the stand with the balance and a rotor equipped with two blades and two paddles is of 8.5Hz. The same setup, this time with the dummy balance, showcases a natural frequency of 9.5 Hz.

The dimensions of the facility dictated the rotor diameter in order to avoid any ground effect.

Rotor design

To ensure the paddle achieved successful blade primary control, the tests were conducted on a simpler model than the {blade, paddle, aileron} configuration described in Section. 3.1. In the present experimental model, the

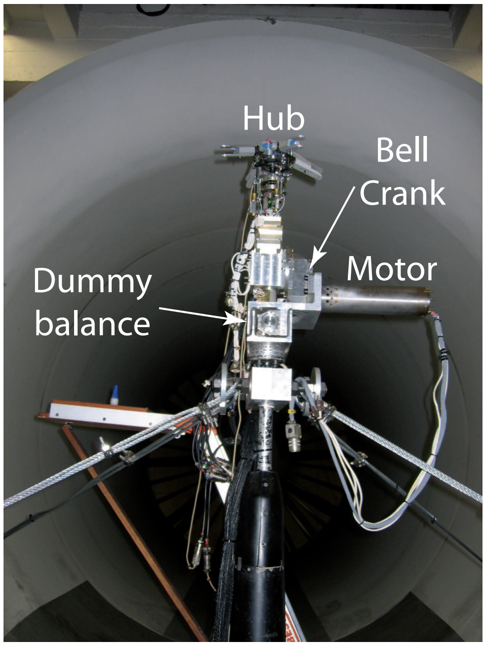

Figure 4.3: Small scale rotor hub mounted on its stand in the testing facility.

paddles are actuated by a small swashplate and not by a piezoelectric actuated aileron. This simplifies the design and reduces the development time and cost of the present testings. To further reduce costs, the swashplate that is used is from another project experimental model.

The tested rotor was a small scale rotor which featured two blades, two paddles and a coupling arm linking the paddle flap and blade pitch angles (see Figure. 4.4 and 4.5). To keep the present study simple, the blades and paddles are located on the same plane 90° of azimuth apart (see Figure 4.5). The coupling was designed so that a 1° of paddle flap results in a 1° of blade pitch. The maximum rotor diameter was limited to avoid ground effect and ceiling effect in the testing facility. The rotor diameter was of 1.868m. The flap and pitch axes are places at two different locations for the following reasons:

1. It is easy to measure the flap and pitch angles when they are disassociated. A potentiometer is located on each flap and pitch axes of the blades and paddles. The rotor is thus equipped with eight potentiometers.
2. The blade pitch is coupled only to the paddle flap. Hence the flap axis is located more inboard than the pitch axis. This prevents the paddle pitch from interfering with the aforementioned coupling.

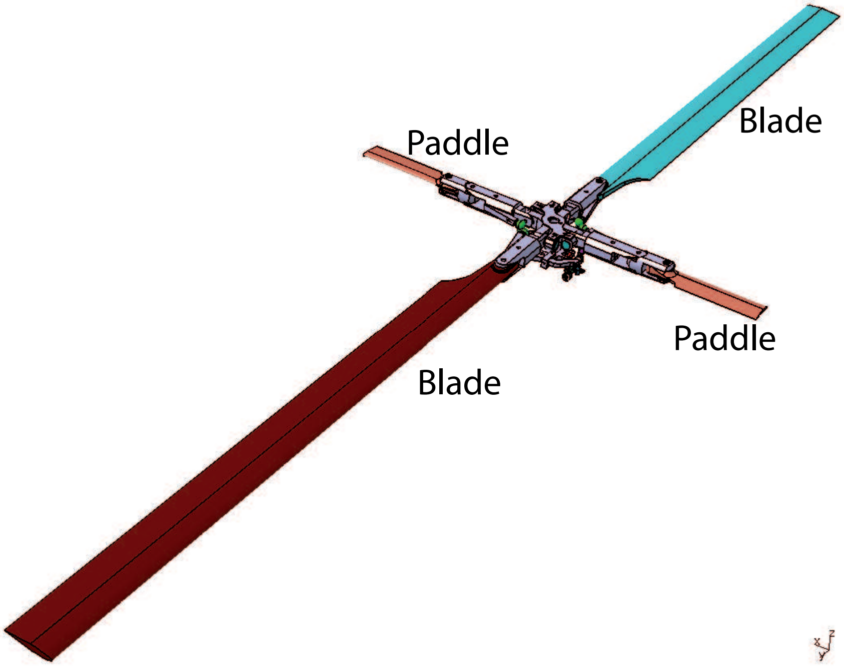

Figure 4.4: Isometric view of the entire small scale rotor.

The rotation about the pitch and flap axes of the blades and paddles is achieved by using self lubricating bronze bushings (see Figure. 4.6). In addition, the blade pitch link which is connected to the coupling arm is located on the blade flap axis to avoid any δ_3 effect (see Figure. 4.7).

The blades are off the shelf RC blades. Their span is of 0.740 m, their chord is of 0.062 m and their mass is of 0.222 kg. The blade thickness is of 0.007 m. In the present design, the blade radius R^B is of 0.934 m. The blades feature an untwisted reflex cambered profile. This type of profile offers the great advantage of reducing the blade pitching moment.

Sets of identical blades are modified to obtain paddles. The paddles are thus untwisted (Figure. 4.8). RC blades available on-shelf present usually additional weights that are inserted at any blade radial location by the manufacturer to ensure blade static balance. An x-ray of an RC blade was thus performed to ensure exact locations, diameter and material of the extra weights were known to allow for paddle inertia computation. Pairs of paddles with different spans and masses were then manufactured:

1. Different spans are obtained by cutting the blades spans short (see three of the seven pairs of manufactured paddle on Figure. 4.9. Paddles within a pair are identical).

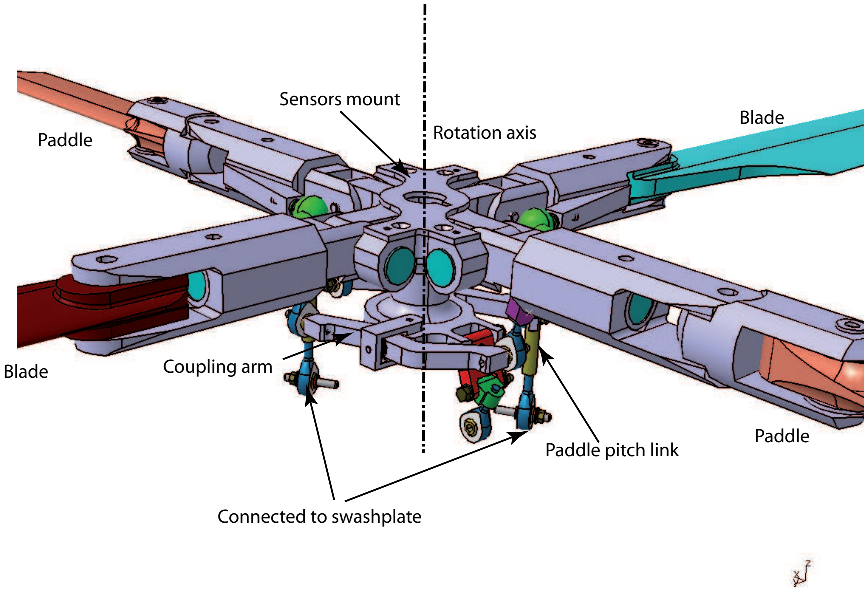

Figure 4.5: Isometric view of the rotor to be tested in the hover stand.

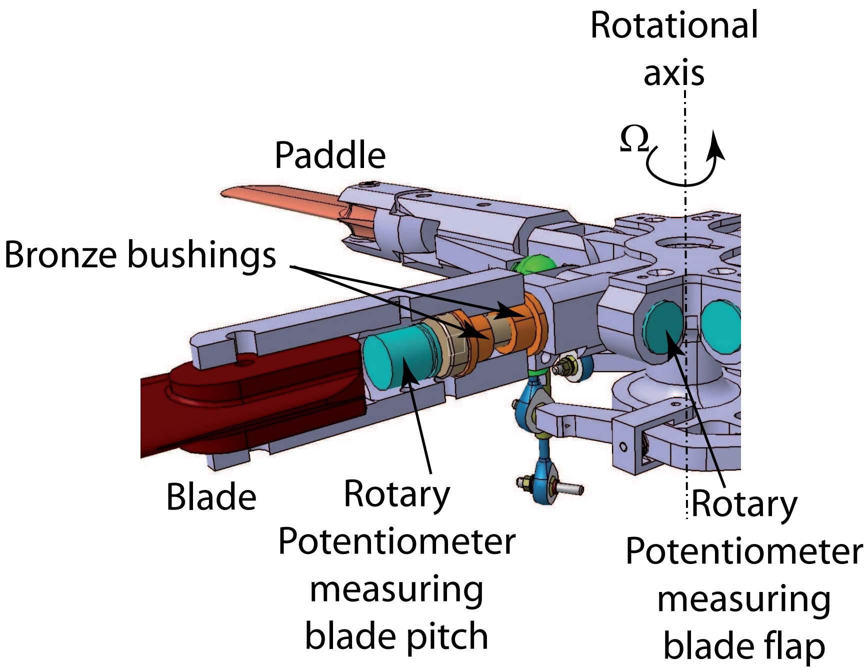

Figure 4.6: View of a blade grip.

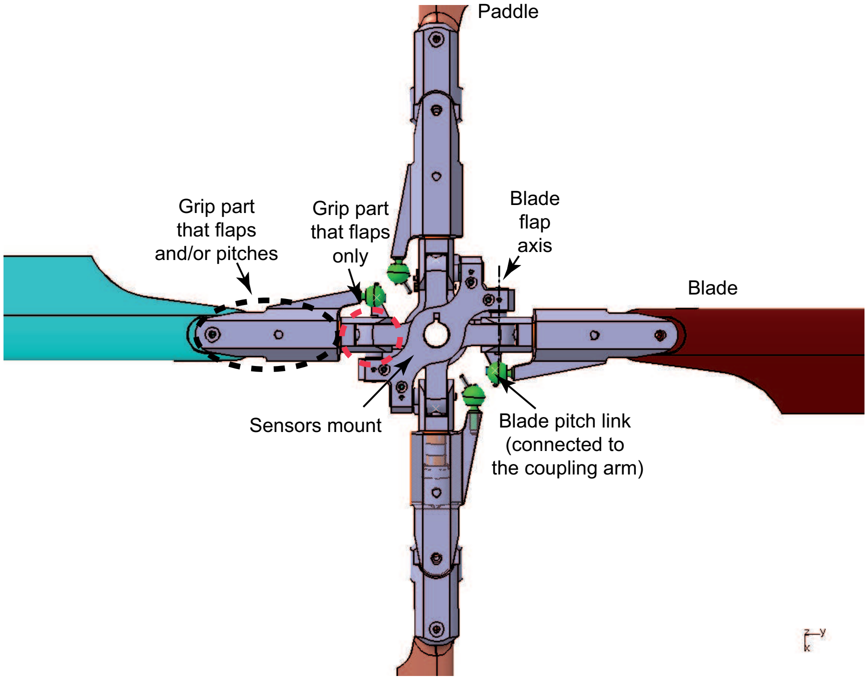

Figure 4.7: Top view of the rotor to be tested in the hover stand.

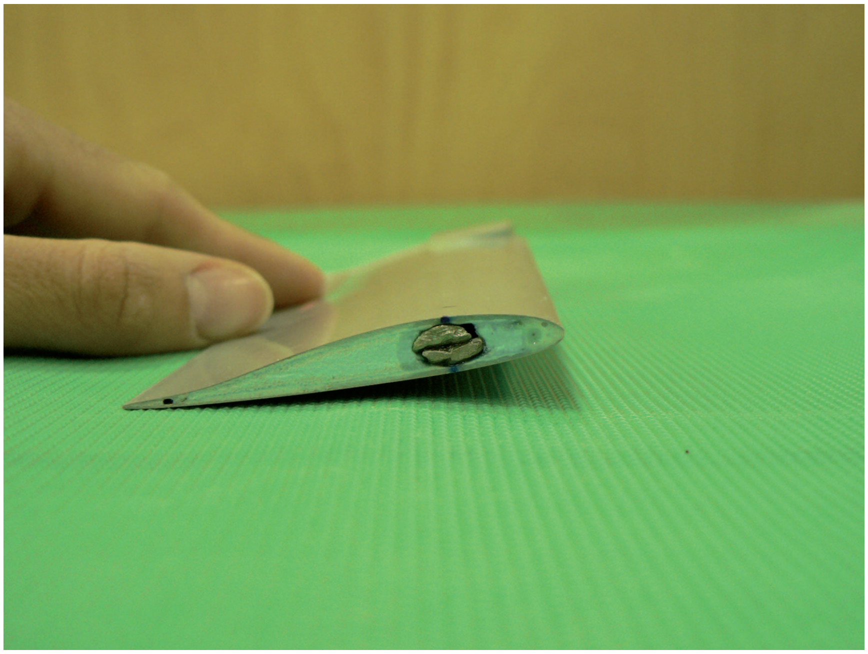

Figure 4.8: The paddles are untwisted.

2. Various masses are achieved by drilling a 0.006 m (0.24 in) diameter hole at the quarter chord on the outboard side of the paddle. This hole is then filled up with lead weights and resin (see Figure. 4.10). Resin is finally added over the whole profile on the outboard side of the paddle and screws are inserted across the blade skin and lead weights (see Figure. 4.11) to ensure the weight do not fly off when the rotor spins. Too much weight is to be avoided to prevent it from flying off. In addition, a weight located too deep within the paddle is to be averted to preserve the paddle structural integrity. Precise weight location is required to obtain particular inertias as detailed in the following section.

In addition, tape is added on the leading edge of some paddles to ensure the static moment is the same within a pair of paddle (Figure. 4.11).

Another parameter that can be varied is the paddle radial location. This is achieved by a grip extension part (see Figure. 4.12) that is inserted between a paddle and its grip. Grip extension parts of two different length are manufactured: one of 0.059m and one of 0.152m.

Kinematics

Since the flap and pitch axes are dissociated on both the paddle and blade, the grips are separated into two parts: the most inboard part only flaps and the most outboard part pitches and flaps (see Figure. 4.7). The coupling arm is linked to the paddle flap horn and the blade pitch horn (see Figure. 4.13 and 4.14). If the paddle flaps up, the paddle flap horn goes up (see Figure. 4.14). Since the central part of the coupling arm is fixed, the coupling arm drives the blade pitch horn down. The blade pitch horn is attached to the rear side of the blade grip. Hence, if the blade pitch horn goes down, the blade pitches up. Therefore, if the paddle flaps up, it results in a blade nose up motion. The blades and paddles are attached at their roots to their respective grips by a single screw each. Attachment screws are not screwed tightly so the blades and paddles can lag about their attachment point.

Inputs and parameters

The force exerted by the swashplate on the paddle pitch link controls the paddle pitch angle. The output is the blade pitch angle. The whirl tower offers a controlled environment which allows for assessment of the influence of several parameters on the dynamic behavior and time constant of the system response. In the present study, the parameters that are varied are:

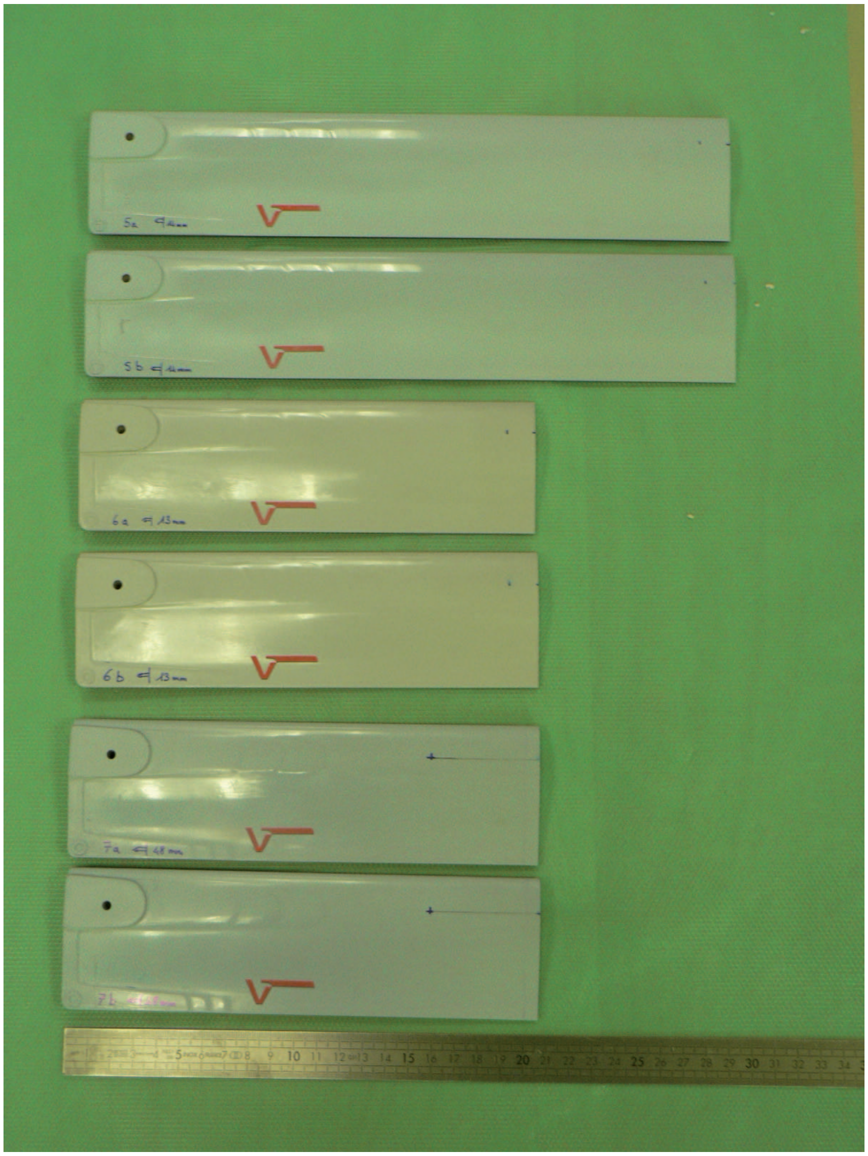

Figure 4.9: Three pairs of paddles with spans of 20% and 30% of the blade radius.

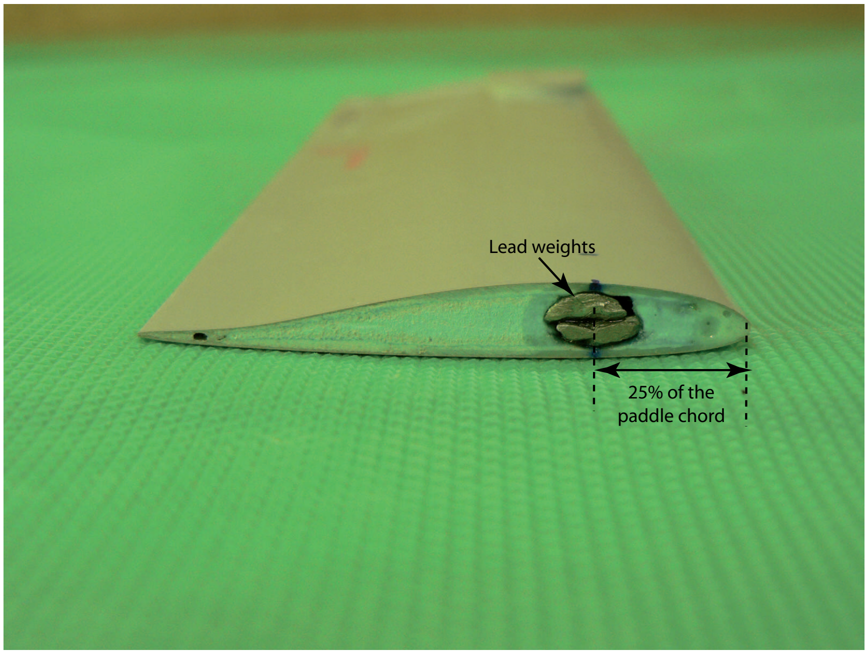

Figure 4.10: Lead weights are incorporated into the paddle on its feathering axis.

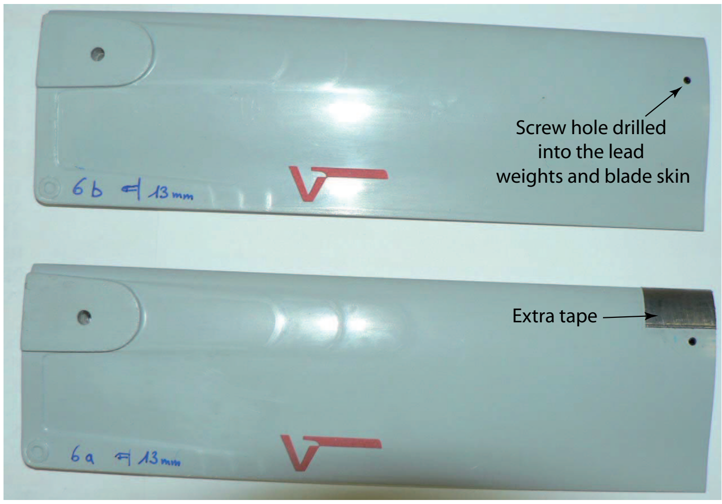

Figure 4.11: Screws holes in a pair of paddle. Tape is added to keep the static moment equal within a pair of paddle.

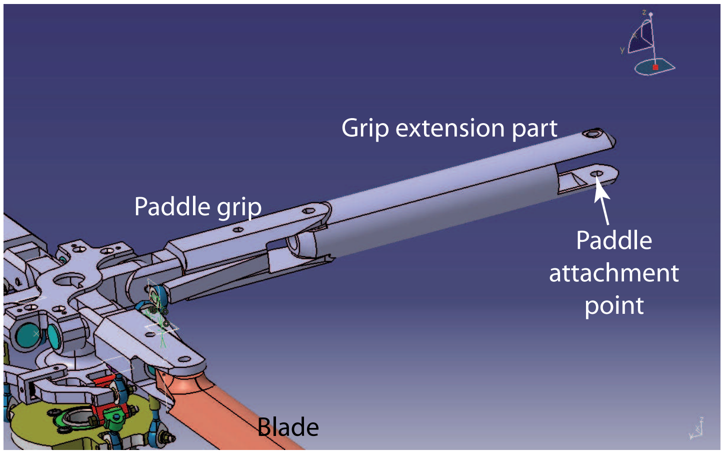

Figure 4.12: Grip extension part.

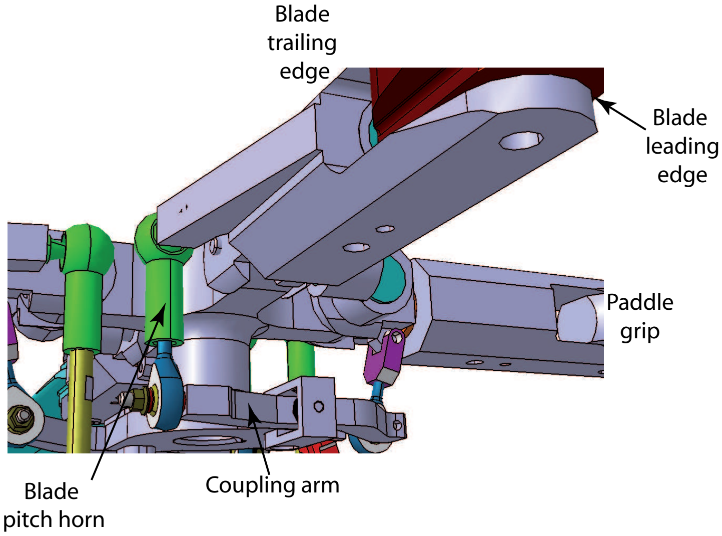

Figure 4.13: Coupling arm.

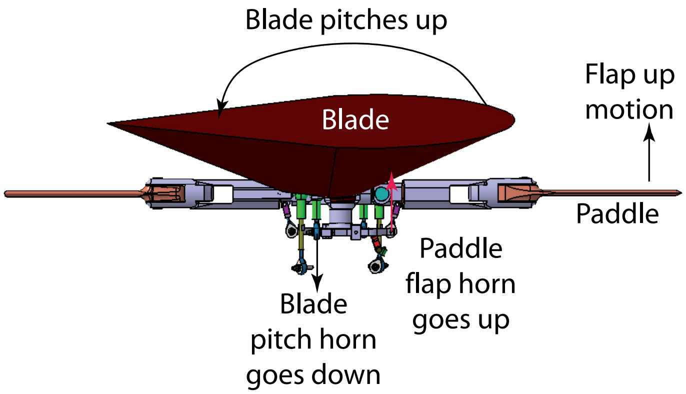

Figure 4.14: Coupling kinematics.

Table 4.1: Hover stand tests parameters

Paddle flapping inertia ($kg.m^2$)	Paddle span ($\%R^B$)	Paddle attachment point radial location ($\%R^B$)
0.00579	20 %	20 %
0.00752	30 %	30 %
0.00826	40 %	
0.01042		
0.01045		
0.01125		
0.01239		

1. The paddle inertia,
2. The paddle span, i.e. the paddle geometry,
3. The paddle radial location.

The paddle radial location is varied using the grip extension part that is inserted between the paddle and its grip (see Figure 4.15). Two different sorts of these parts are manufactured to achieve the desired radial locations specified below. To evaluate the influence of one of these parameters, the other two must remain constant. If the paddle span and radial location both vary and the inertia remains constant, then the effect of aerodynamic forces can be determined. This is essentially a variation of the Lock number. Table 4.1 describes the different values taken by the aforementioned parameters.

The test matrix is explicited in Table 4.2.

For each {inertia, span, radial location} configuration, a set of collective and cyclic paddle pitch angles are introduced as inputs. Collective pitch inputs vary between $[-8°; 14°]$. Cyclic inputs vary between $[-8°; 8°]$. These angles were defined by the clearance between the swashplate and the hub.

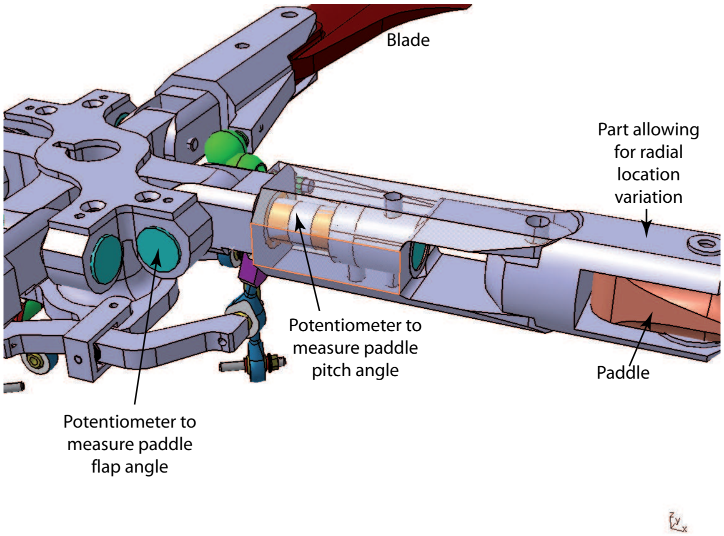

Figure 4.15: Detailed view of the potentiometers locations.

Table 4.2: Hover stand test matrix

Case #	Paddle flapping inertia ($kg.m^2$)	Paddle span ($\%R^B$)	Paddle attachment point radial location ($\%R^B$)
A	0.00579	40 %	20 %
B	0.00752	20 %	30 %
C	0.00826	30 %	30 %
D	0.01042	40 %	30 %
E	0.01045	30 %	30 %
F	0.01125	20 %	30 %
G	0.01239	20 %	30 %

The present collective angles might not permit to observe the system behavior under stall.

Measurements and sensors

The following quantities are measured and recorded at discrete times (64 times per rotation) until the steady state values are reached:

1. Rotor RPM using a Hall sensor.
2. Flap and pitch angles of all blades and paddles using 8 potentiometers located in the rotating frame as explained in a previous section (see Figure. 4.15).
3. Rotor thrust, moments and torque using a 6-axis balance. The rotor torque measurements are critical as it is used to determine if the Figure of Merit of the system is better than in the case of a conventional design.

All data originating from the rotating frame are transmitted to the non-rotating frame using a slip ring.

Ground resonance

When a rotor is spun up, it goes through modes that makes the whole system vibrate. To ensure good hovering and measurement conditions, no mode should be present at the rotor rotational speed Ω. It is important to ensure the system does not encounter any ground resonance. To this end, Coleman stability criterion is studied (Ref. [195]). This criterion states that if the frequency of the first mode of blade lag, ω_l, is lesser than the rotor rotational speed, Ω, the system is stable if the two following equations are verified:

$$\begin{cases} \omega_{structure} \neq \Omega + \omega_l \\ \omega_{structure} \neq \Omega - \omega_l \end{cases} \tag{4.1}$$

with $\omega_{stucture}$ the stand natural frequency. The rotor spins at 15 Hz, i.e. 900 RPM. The first lag mode frequency of the blade can be written as:

$$\omega_l = \Omega \sqrt{\frac{e_l + m_s}{I_l} + \frac{k_l}{I_l \Omega^2}} \tag{4.2}$$

with e_l, the lag hinge offset, m_s the blade static moment, I_l the lag inertia. It is assumed the blades can lag about their attachment point to their grips, hence their lag stiffness $k_l = 0$. The static moment is written as:

$$m_s = m_b d \tag{4.3}$$

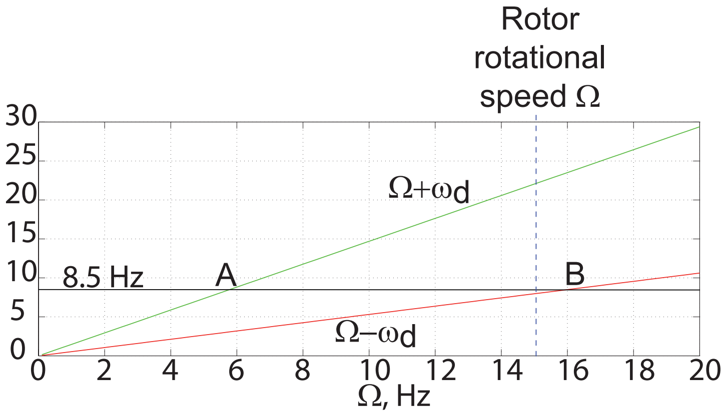

Figure 4.16: $\Omega+\omega_l$, $\Omega-\omega_l$ and the stand natural frequency of 8.5 Hz, with the balance.

where m_b is the blade mass and d the distance between the blade attachment point and its center of gravity. The lag inertia is approximated to:

$$I_l = \left(\frac{T_l}{2\pi}\right)^2 m_b g d \tag{4.4}$$

with T_l the lag period and g the acceleration due to gravity. T_l was measured by hanging the blade down and make it oscillate around its attachment point. The first lag mode frequency ω_l was found out to be $\omega_l = 0.47\Omega$, i.e. ≈ 7 Hz if $\Omega = 15$Hz. Figures. 4.16 and 4.17 show the $\Omega+\omega_l$ and $\Omega-\omega_l$ equations at all rotational speeds during spin-up. In Figure. 4.16, the 8.5 Hz constant equation is the stand natural frequency when it is equipped with the balance. In Figure. 4.17, the 9.5 Hz constant equation is the stand natural frequency when it is equipped with the dummy balance. The x-coordinate of point A and B (in Figure. 4.16) and point C and D (in Figure. 4.17) show at which rotational speed the rotor should not hover to avoid vibrations. It is seen that if the stand equipped with the balance and the rotor hovers at $\Omega = 15$Hz, there is a risk of instability since the x-coordinate of point B is 16 Hz, i.e. 1 Hz from Ω in hover.

Several potential solutions were implemented in an attempt to avoid ground resonance:

1. Stiffening the stand with cables connected to the stand and to the ground (see Figure. 4.18). Using this method with the balance, the stand natural frequency was increased to 15 Hz. This means the intersection points, much as A and B in Figure. 4.16, between the stand natural frequency and $\Omega+\omega_l$ and $\Omega-\omega_l$ would have x-coordinate of 10 Hz and 28.3 Hz respectively. These values are very different from

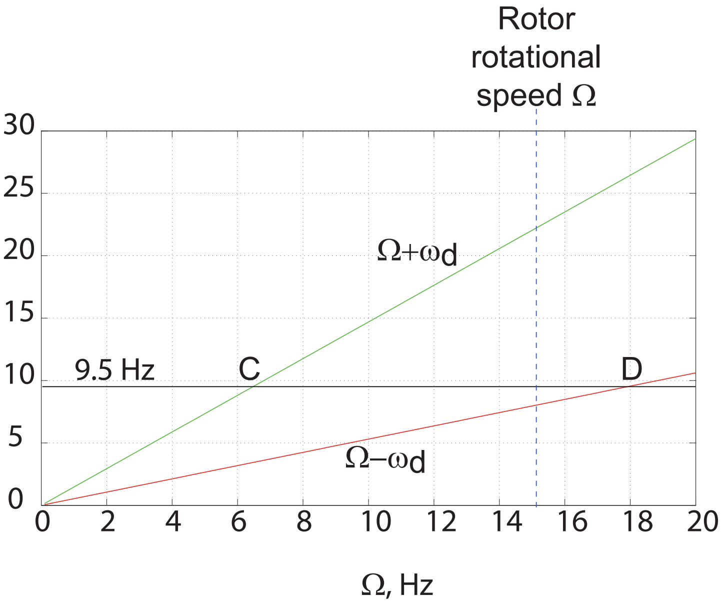

Figure 4.17: $\Omega + \omega_l$, $\Omega - \omega_l$ and the stand natural frequency of 9.5 Hz, with the dummy balance.

the rotor rotational speed of 15 Hz. Ground resonance would thus be avoided using this method. Unfortunately, cables vibrated during rotations and the ground anchor of one of the cables got damaged. Hence, this configuration was not safe and was therefore not used.

2. Increasing the stand mass by adding different masses : 18.4kg (see Figure. 4.19) and 22.4kg respectively. This method resulted in lower stand natural frequency: 7.5Hz and 7.2Hz respectively. This means the intersection points, between the stand natural frequency and the most critical $\Omega - \omega_l$ equation, would have x-coordinate of 14.17 Hz and 13.57 Hz respectively. These values are too close to the rotor rotational frequency $\Omega = 15$ Hz. Lowering further the stand natural frequency would require a mass too important. Hence, this method was not used.

3. The rotor rotational speed could be lowered to 14Hz for instance. However, even doing so, safety guidelines forbade the use of the balance.

The tests were thus performed with the dummy balance, with the rotor rotating at 15Hz with no extra mass and no cables. The use of the dummy balance means that the hub forces and moments could not be measured. Therefore, the Figure of Merit of this configuration cannot be computed from experimental data.

Figure 4.18: Cables are used to stiffen the stand to increase its natural frequency.

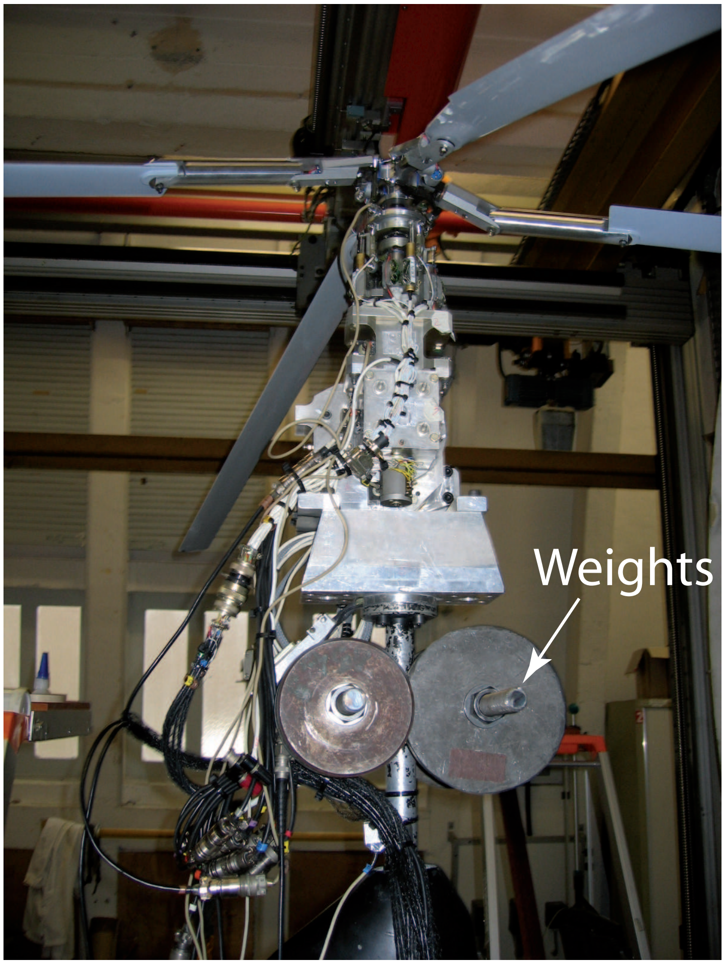

Figure 4.19: Extra weights added to decrease the stand natural frequency.

Table 4.3: Hover stand reduced test matrix

Case number	Paddle flapping inertia ($kg.m^2$)	Paddle span ($\%R^B$)	Paddle attachment point radial location ($\%R^B$)
A'	0.00579	20 %	20 %
B'	0.01046	40 %	20 %

Vibrations

As mentioned earlier, the experimental design included bronze bushings to allow for rotation of the blades and paddles about their flap and pitch axes. It was observed that the bushings generated significant amount of friction (see later section). Hence, vibrations resulted from the use of the bushings.

Vibrations were also generated during spin-up, while "going through" modes. The faster the rotor was spun up to 15 Hz, the fastest it would "go through" a mode. It was thus observed that the level of vibration was not repeatable from one test to another.

It should be noted that some sensors stopped functioning correctly after the first test due to vibrations. A blade pitch sensor for instance stopped functioning, thus in this case it was assumed that the blade pitch angle was equal to the paddle flap angle.

Reviewed test matrix

Because of the issues described above, only two test cases were performed (see Table 4.3). These two cases show the effect of inertia and span on the blade pitch response.

4.2 Results and discussion

4.2.1 Sample analytical results

The analysis {Paddle, Aileron, Blade} was simplified to use quasi-steady aerodynamics in order to check if a frequency calculated analytically and a frequency given by the code match. Note that the system in this section is based on the Ecureuil helicopter, the rotational speed of the rotor is approximately 40 rad/s (i.e. 6.36 Hz). If the blade flap motion is considered, the

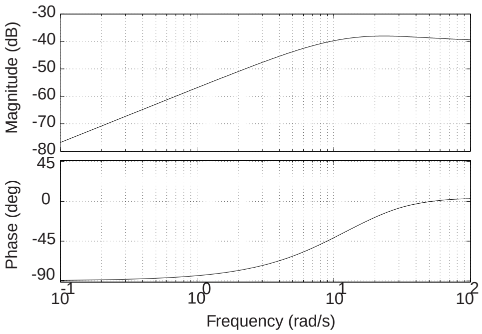

Figure 4.20: Blade response in the baseline case.

analytical value of the first resonance frequency for damped free vibrations is 41.18 rad/s and the code frequency is 41.25 rad/s (i.e. 6.57 Hz). It is thus found that the code outputs can be trusted. A parametric study is therefore performed.

The baseline case for the parametric study is taken as a paddle of span 30% R^B, centered at 40% R^B. The baseline paddle has the same chord and the same mass per unit area as the rotor blade. The aileron has the same mass per unit area and span as the paddle. Its chord is equal to 25% of the paddle chord. In addition, a purely articulated rotor is analysed by setting the flap stiffnesses of the blade and paddle to zero. In the present swashplateless concept, there is no control stiffness in the torsional degree of freedom for either the blade or the paddle. The blade pitch response to an applied voltage for the baseline case is shown in Fig. 4.20, and the paddle pitch response is shown in Fig. 4.21. It can be seen that the response is highly damped due to the aerodynamic forces. The two main points of interest are the blade pitch at zero frequency, which corresponds to the collective pitch of the blade and the blade pitch at 1/rev (i.e. 6.57 Hz), which corresponds to the cyclic pitch of the blade. For the baseline case, it can be seen that the collective pitch response is very small, at around -77 dB and the cyclic pitch response is around -38 dB. Note that the present analysis assumes a generic piezoceramic actuator, and calculates the frequency response to an input voltage. In order to assess the feasibility of the concept, the actual change in blade pitch angle for a realistic swashplateless rotor must be calculated, which can be performed only after a specific piezoceramic actuator is selected.

Several cases were evaluated using the parametric analysis, such as the effect of the paddle radial location (centered at 30%R^B, 40%R^B and 50%R^B) and the paddle mass (keeping the area constant). For example, the effect of the paddle radial location is shown in Fig. 4.22. It can be seen that as the

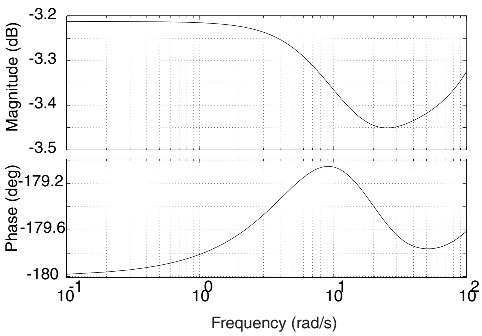

Figure 4.21: Paddle pitch response in the baseline case.

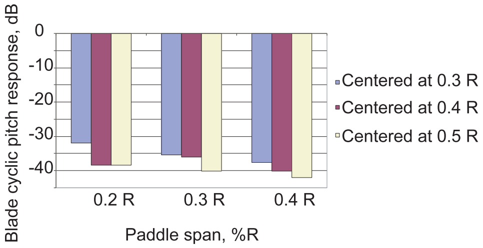

Figure 4.22: Effect of the paddle span and center radial location on blade pitch response.

paddle moves outboard, the resulting blade pitch response decreases. This is attributed to the relatively large mass of the paddles, which results in low paddle flapping angles and consequently, low blade pitch.

The effect of the paddle mass on the coupled blade pitch and paddle flap and on the paddle pitch responses is shown in Fig. 4.23 and Fig. 4.24. The paddle density value is varied: it is first chosen as equal to half the blade density (case #1), as equal to the blade density and as twice the blade density. If the paddle density decreases and the paddle dimensions remain constant, then the paddle mass decreases. Therefore, the paddle natural frequency increases and is thus greater than 1/rev. Hence, the magnitude of the paddle cyclic response at 1/rev is decreasing (Fig. 4.23). Consequently, the lift generated by the paddle is reduced which results in a paddle flap response diminution. The blade pitch response decreases as well because it is coupled with the paddle flap (Fig. 4.24).

Conclusions drawn from the sample analytical results

As described above, the 4 DOF analysis that is the {Paddle, Aileron, Blade} model was implemented in matlab and the following conclusions can

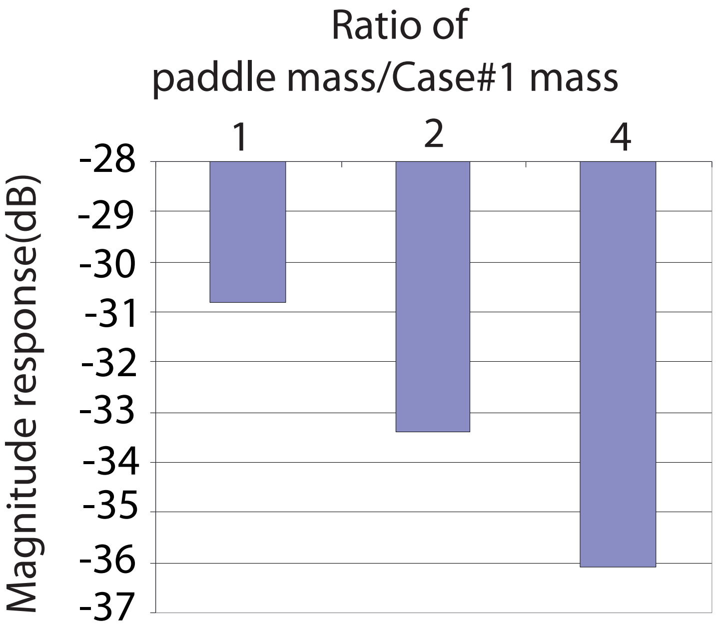

Figure 4.23: Effect of the paddle mass on the paddle pitch response.

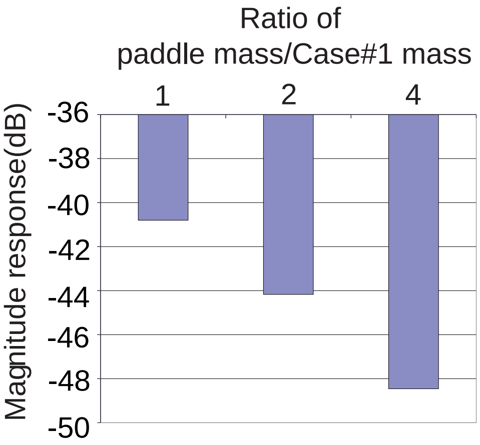

Figure 4.24: Effect of the paddle mass on the coupled blade pitch and paddle flap response.

be made:

1. The concept of the paddle flap-blade pitch coupling was represented in an analytical form. The analysis was input characteristics from the Ecureuil helicopter design. Several cases were run and transfer functions of the responses to a given unit voltage applied to a PZT actuator were obtained. The steady and 1/rev responses, which correspond to the collective and cyclic responses, could be extracted from the transfer functions
2. When a flapping motion for instance was considered, the frequency obtained by the numerical 4 DOF model was in close agreement with the frequency obtained from a simplified analysis based on first principles.
3. The 4 DOF analysis demonstrated the effect of paddle radial location and mass (for a constant area). It was shown that as the paddle is moved outboard, it is subjected to increased centrifugal load and hence flaps less. This leads to a decreased blade pitch response due to the paddle flap-blade pitch coupling. The effect of paddle mass was seen on the paddle natural frequency. If it increased, then the paddle cyclic pitch response decreases as do the paddle flap response and the blade pitch response.
4. The influence of the aerodynamic forces could be seen in terms of damping.
5. The PZT actuator is not chosen yet. So one cannot rely on the magnitude of the responses to design and define the optimum configuration to maximize the blade pitch response. The magnitude is informative and indicates the relative performances of different configurations.
6. The relative magnitude of the analytical responses of different configurations provided guidelines for the choice of experimental parameters.

4.2.2 Experimental results

As mentioned earlier, two tests were performed:

1. Case A': paddles with a 0.187m span, an attachment point at $20\%R^B$ and a $0.00579 kg.m^2$ flapping inertia.
2. Case B': paddles with a 0.374m span, an attachment point at $20\%R^B$ and a $0.01046 kg.m^2$ flapping inertia.

Rotary potentiometers were used to measure pitch and flap angles of all blades and paddles. The rotor RPM was measured using a Hall sensor.

The paddles and blades were assigned a number to be easily recognized. Paddle 2 is connected to blade 3 and paddle 4 is coupled to blade 1 (see

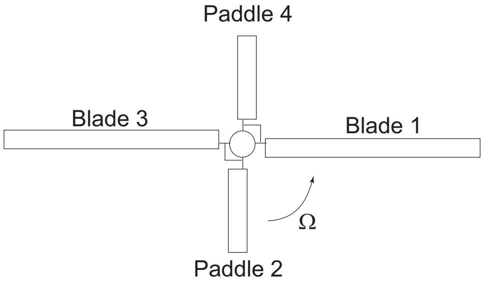

Figure 4.25: Paddles and blades assigned number.

Figure. 4.25

The rotor was spun to 900 RPM quickly to go through modes as fast as possible. The pitch and flap angles can be written as a Fourier transform (Ref. [1]):

$$\theta(\psi) = \theta_0 + \sum_{n=1}^{\infty} (\theta_{nc} \cos n\psi + \theta_{ns} \sin n\psi) \tag{4.5}$$

$$\beta(\psi) = \beta_0 + \sum_{n=1}^{\infty} (\beta_{nc} \cos n\psi + \beta_{ns} \sin n\psi) \tag{4.6}$$

with θ_0 and β_0 the collective pitch and collective flap respectively. These are referred to as static pitch and static flap in the results. θ_{nc}, θ_{ns}, β_{nc} and β_{ns} are the longitudinal cyclic pitch, laterial cyclic pitch, longitudinal flapping angle and lateral flapping angle respectively for the n/rev component. The cyclic pitch and flap angles for blades and paddles can be written as complex numbers. The magnitude of the cyclic pitch is $\sqrt{\theta_{nc}^2 + \theta_{ns}^2}$ and is referred to as dynamic pitch in the experimental results. The magnitude of the cyclic flap is $\sqrt{\beta_{nc}^2 + \beta_{ns}^2}$ and is referred to as dynamic flap in the experimental results. Even though aerodynamic excitation is primarily at $1/rev$, the $1/rev$, $2/rev$ and $4/rev$ components were recorded during the tests. Let us focus on the collective and $1/rev$ (i.e. 15 Hz in the present case) magnitude components. Phase information are not going to be discuss here. In the following figures, the time histories are not zero-ed out but the figures that show angle variations as a function of paddle static or dynamic pitch angles are indexed to zero. Figures. 4.26 and 4.27 present the time history of the static paddle pitch angles in case A' and case B' respectively. It can be seen that the time variation of collective angles of paddles #2 and paddles #4 are not superimposed in Figure. 4.26. If the same input is given by the swashplate to both paddles, their collective pitch angles should be identical. The fact that the two curves do not match exactly means that the paddles reacted differenly to the same swashplate input. This is because of significant

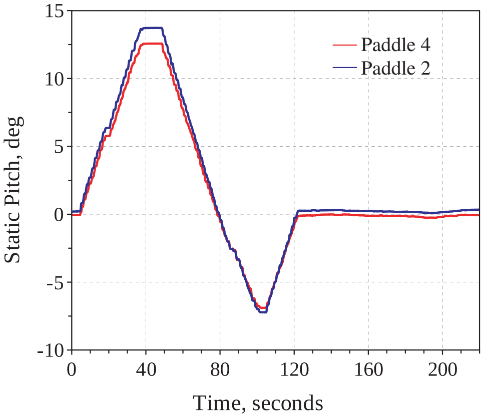

Figure 4.26: Time history of the paddles static pitch in case A'.

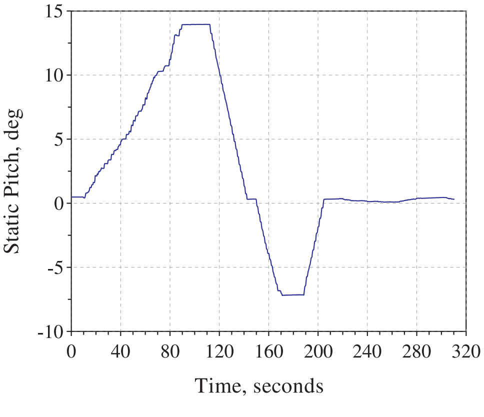

Figure 4.27: Time history of the paddles static pitch in case B'.

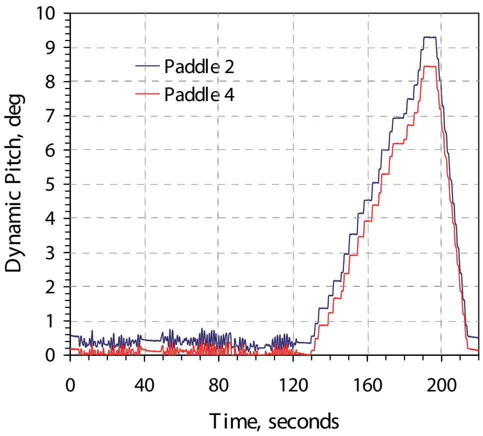

Figure 4.28: Time history of the paddles dynamic pitch in case A'.

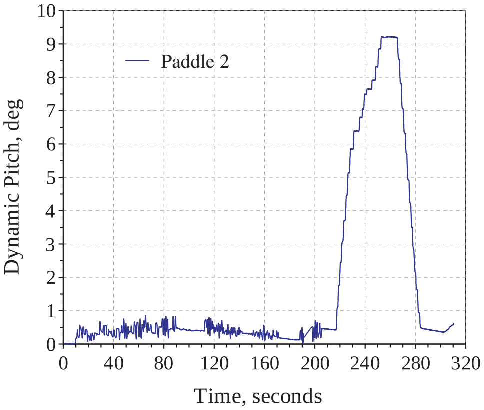

Figure 4.29: Time history of the paddles dynamic pitch in case B'.

friction in the bronze bushings mentioned earlier. These bushings are self lubricated and are located on the flap and pitch hinges of all blades and paddles. When the rotor spins up, their lubricant is pushed towards the outboard of the rotor because of centrifugal load and hence do not lubricate the remaining of the bushings. Sensors provided excellent data readings during spin up and during case A', i.e. for 300 sec. However, a paddle pitch sensor stopped functioning after case A'. Hence, Figure. 4.27 features only one curve.

Figures. 4.28 and 4.29 present the time history of the dynamic paddle pitch angles in case A' and case B' respectively. As in the case of Figure. 4.26, the dynamic pitch of paddle #2 and paddle #4 are not superimposed due to friction in the bushings. A paddle sensor stopped functioning after test A', thus Figure. 4.29 showcases only one curve.

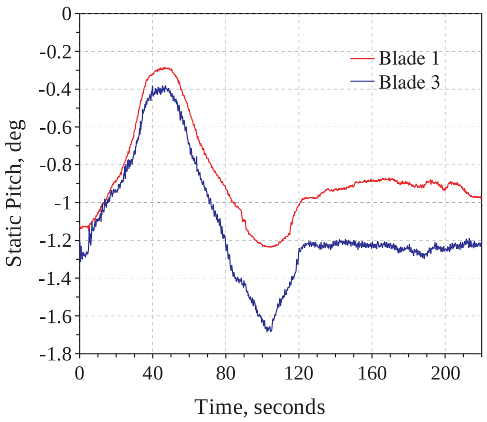

Figure 4.30: Time history of the blades static pitch in case A'.

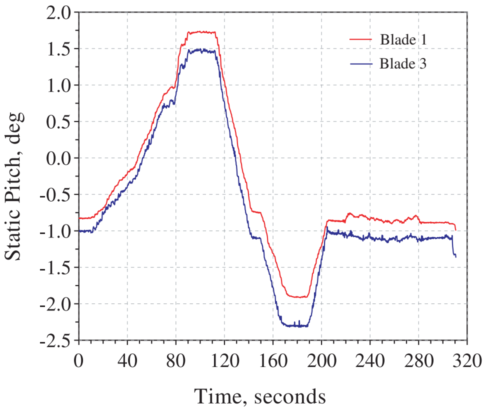

Figure 4.31: Time history of the blades static pitch in case B'.

Figures. 4.30 and 4.31 present the time history of the static blade pitch angles in case A' and case B' respectively.

Figures. 4.32 and 4.33 present the time history of the dynamic blade pitch angles in case A' and case B' respectively. Figures. 4.30, 4.31,. 4.32 and 4.33 show curves that are not superimposed. This again shows the influence of friction, this time in the blades bushings. In addition, the dynamic pitch for blades #1 and #3 in case A' are very different from one another as seen in Figure. 4.32. At $time = 190$ sec, the dynamic pitch for blade #1 is of 1.1° whereas the dynamic pitch for blade #3 at the same time is of 0.45°. These outputs occur at the same time in response to respective inputs of paddle #4 and paddle #2 (see Figure. 4.28). Indeed, friction affects the magnitude of the responses.

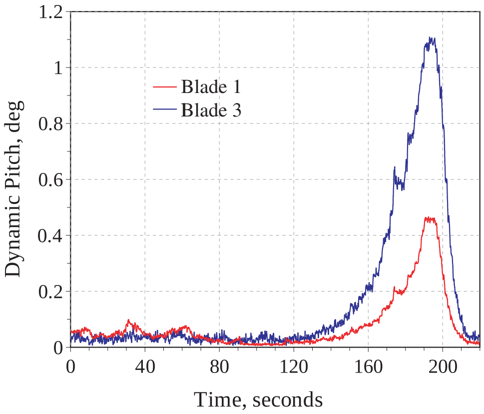

Figure 4.32: Time history of the blades dynamic pitch in case A'.

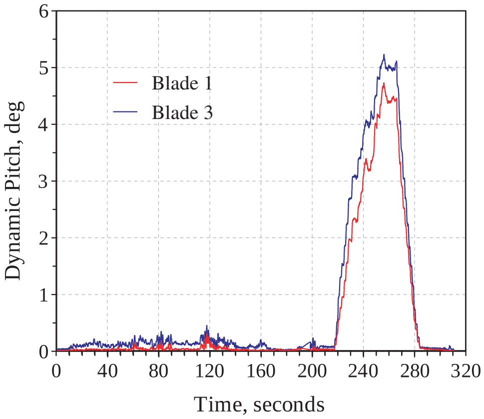

Figure 4.33: Time history of the blades dynamic pitch in case B'.

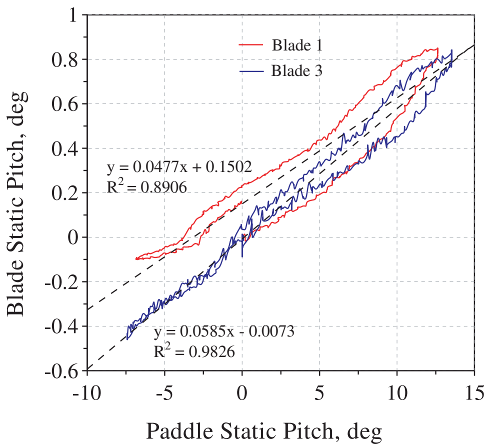

Figure 4.34: Case A', blade static pitch vs. paddle pitch.

Figures. 4.34 and 4.35 present the blade static pitch as a function of the paddle static pitch in case A' and case B' respectively. It is seen that the curve for both blade #1 and blade #3 form a loop. For a given paddle static pitch, there are two values of blade static pitch: if paddle #4 provides a 5° collective input to blade #1, the response of blade #1 is either of 0.2° or of 0.45°. When the paddle collective pitch was varied over its range, the collective pitch was increased first to its maximum then brought back to zero. Depending on if the paddle collective pitch was of 5° when increasing or decreasing the collective pitch input, the blade responses was different, not repeatable. This phenomenon appears for both blade #1 and blade #3. Therefore, the loops in Figure. 4.34 prove the presence of friction caused by the bushings on flap and pitch axes of blades and paddles. The fact that the responses of blade #1 and blade #3 are not on top of each other means the rotor is not tracked. For a paddle collective pitch of 14° in case A', both the blades responded with a collective pitch of $\approx 0.8°$ in case A' (see Figure. 4.34). In case B', however, the blade response was greater: for a paddle collective pitch of 14°, the blade responded with a collective pitch of $\approx 2.5°$ (see Figure. 4.35). This could be explained by two different reasons:

1. In case B', paddles have a much bigger surface area, hence the aerodynamic force they generate for a given pitch angle is greater than in case A'. Therefore, the friction from the bronze bushings cannot counteract the effect of aerodynamic load as much as in case A'.
2. The angle measurements are subjected to a 0.4° error. When measuring small angles, such as in case A', the error is predominant.

In both Figures. 4.34 and 4.35, a linear fit is generated for each curve. The equations y of these linear fits are indicated on each figure. R^2 is the

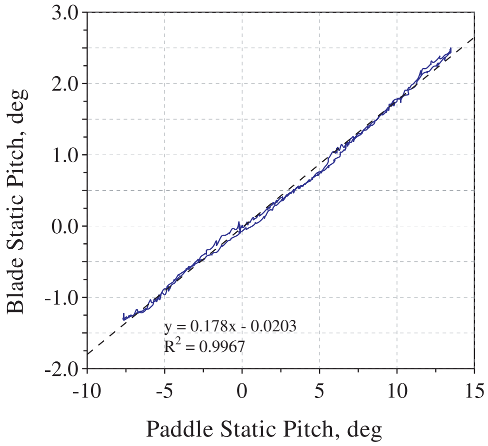

Figure 4.35: Case B', blade static pitch vs. paddle pitch.

regression factor. The closer R^2 is to 1, the closer the actual blade static responses are to their respective linear fit. It can be seen from Figures. 4.34 and 4.35, that the regression factor the closest to 1 is the one observed in case B' : $R^2 = 0.9967$. It shows the blades in case B' showcase a more linear response that in case A'. Based on the linear fits of Figures. 4.34 and 4.35, it is seen that:

1. The greatest blade response for a given paddle pitch input is obtained in case B',
2. In case A', blade #1 produces a greater response to a given pitch input than blade #3.

Figures. 4.36 and 4.37 present the blade dynamic responses as a function of the paddle dynamic pitch for case A' and case B' respectively. Figure. 4.36 showcases the responses of blade #1 and blade #3. Both these curves are non linear. This non linear behavior is suspected to be caused by friction in the bushings. Friction dominates the responses at low angular displacement. In addition, for a given paddle dynamic pitch, the blade response is lower in case A' than in case B'. As mentioned earlier, this is because the paddles in case B' have a greater surface area than in case A', hence they generate more lift that is not as counteracted as in case A'. In addition, the potentiometers have a $0.4°$ error angle which can be predominant in blade dynamic responses in case A' as the greater blade dynamic response to a given paddle dynamic pitch is of $1.1°$ in Figure. 4.36. Figure. 4.37 shows that the blade dynamic pitch response to paddle dynamic pitch is almost linear as the regression factor of its linear fit is $R^2 = 0.9923$. Based on the linear fits in Figure. 4.35 and 4.37, it is seen that the blade dynamic response to a given paddle dynamic pitch is greater than the blade static response to the same given

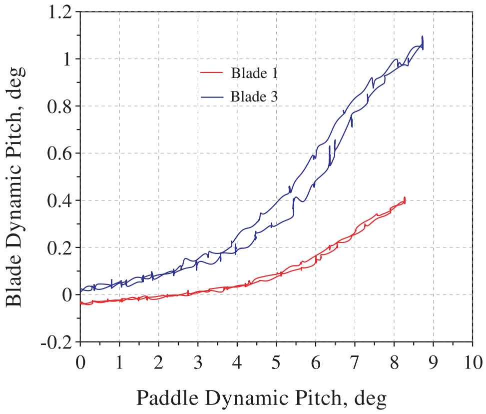

Figure 4.36: Case A', blade dynamic pitch vs. paddle pitch.

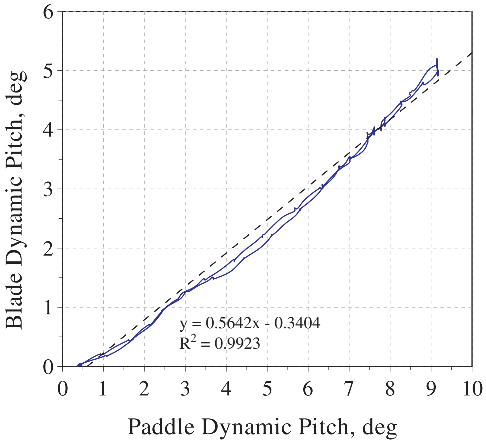

Figure 4.37: Case B', blade dynamic pitch vs. paddle pitch.

paddle static pitch.

Figures. 4.38 and 4.39 present the blade static flap as a function of paddle static pitch in case A' and case B' respectively. Figures. 4.40 and 4.41 present the blade dynamic flap as a function of paddle static pitch in case A' and case B' respectively. The blade flap readings are small because the centrifugal loads on the blade is much larger than on a paddle. Hence, the blade will tend to flap less than a paddle. That can be seen from the blade flap readings and the blade pitch data (because paddle flap and blade pitch are assumed to be equal). In addition, friction further reduces the blade flap responses. Thus, the signals in these figures are non linear. In addition, the data is noisy.

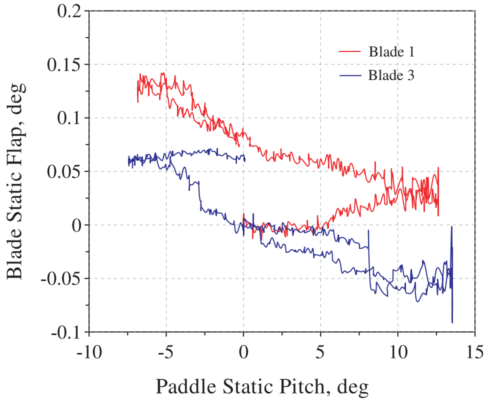

Figure 4.38: Case A', blade static flap vs. paddle static pitch.

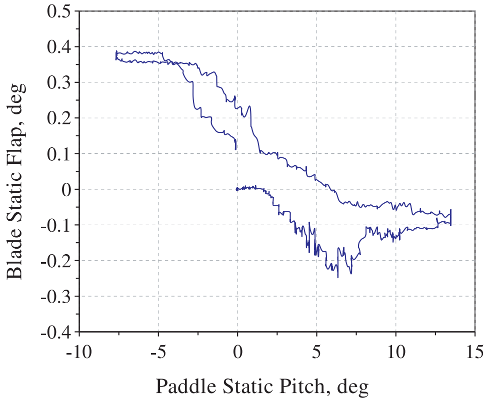

Figure 4.39: Case B', blade static flap vs. paddle static pitch.

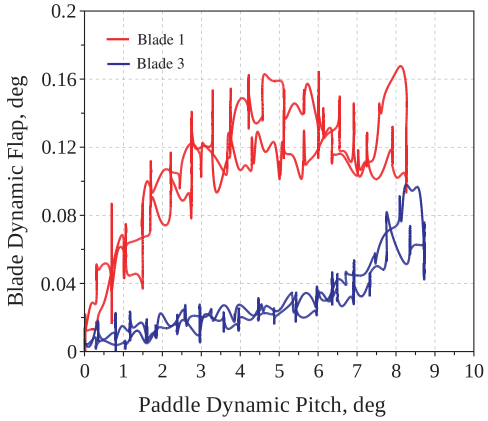

Figure 4.40: Case A', blade dynamic flap vs. paddle dynamic pitch.

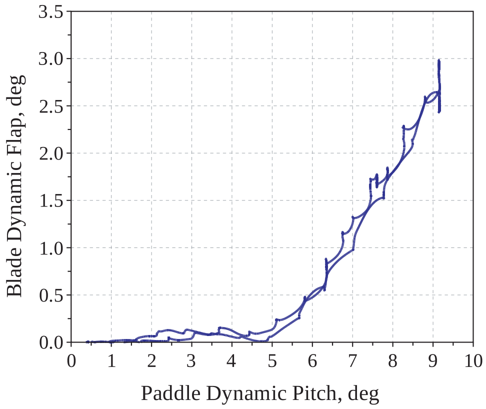

Figure 4.41: Case B', blade dynamic flap vs. paddle dynamic pitch.

4.2.3 Correlation with analysis

The second analysis described in Chapter. 3 is used to obtain analytical results to be compared with the experimental results mentioned above. For pratical reasons, this analysis is hereafter called 3 DOFs analysis. As described in the previous section, case A' exhibited dramatic friction and non linear behavior. As a result, we consider case B' for the present correlation. The paddle characteristics are input into the 3 DOFs analytical study. The collective and $1/rev$ components are extracted from the Bode plots of the blade pitch and the Bode plots of the paddle pitch. Then the collective, or static, component of the blade pitch is divided by the static component of the paddle pitch. This gives a slope that can be compared to the blade static pitch vs. paddle static pitch slope obtained in the experiments. Similarly, the cyclic, or dynamic, compotent of the blade pitch is divided by the dynamic component of the paddle pitch. This gives a slope that can be compared to the blade dynamic pitch vs. paddle dynamic pitch slope obtained in the experiments. Figure. 4.42 presents the static 3 DOFs analytical and experimental results for case B'. Figure. 4.43 presents the dynamic 3 DOFs analytical and experimental results for case B'. The static slope obtained by the 3 DOFs analysis was of 0.245 and the analytical dynamic slope is of 0.6438.

It can be seen that the slopes obtained by the experiments and the 3DOFs analysis are very different. In the previous section, it was mentioned that:

1. The RC-blades used to make paddles included holes and fillings. These holes were drilled and filled with lead by the manufacturer to ensure static moments within a pair of blades were identical. These holes were

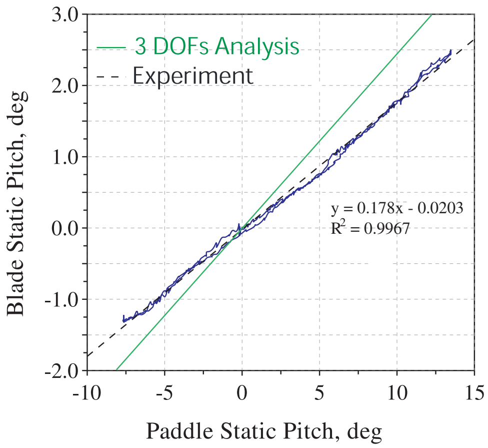

Figure 4.42: Case B', 3DOFs analytical and experimental results of the blade static pitch vs. the paddle static pitch.

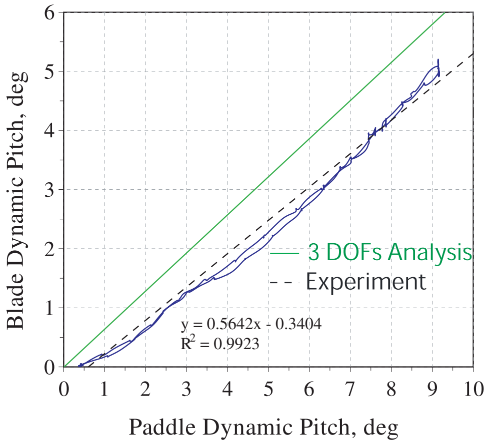

Figure 4.43: Case B', 3DOFs analytical and experimental results of the blade dynamic pitch vs. the paddle dynamic pitch.

randomly drilled along the chord and span of the blades. In addition, two pairs of blades did not feature the same number of holes nor the same holes location. Hence, characteristics of the paddles made from the RC-blades were not precisely known and varied from paddle to paddle.

2. Bushings on the flap and pitch axes of all paddles and blades generated dramatic amount of friction.
3. Blades and paddles were not tracked.
4. Several sensors stopped functioning in case B': a potentiometer measuring a paddle pitch angle, a potentiometer measuring a blade pitch angle and a potentiometer measuring a blade flap angle. For instance, when the paddle pitch angle is measured on both paddle, the measurements trustworthiness increases. Hence the lack of measurements from the aforementioned sensors hampered a good reading of the blades and paddles angles.

Based on these reasons, it is necessary to assess which of the 3DOFs analysis or the experiments results are more trustworthy. A simplified analysis based on first principles is developed to be used as a cross check. This simplified model can be derived to gain insight into the behavior of the system in hover. This model neglects the hinge offsets, assumes quasi-steady aerodynamics and treats the control linkages as infinitely stiff. In this way, the blade-paddle system of equations derived above (Eq.3.102) can be simplified to two degrees of freedom - the blade flap and blade pitch. Because the control linkage is assumed infinitely stiff, the input to the system is the paddle pitch angle. It is expected that this model will be able to predict the hover performance of the system fairly accurately due to the relatively low reduced frequency.

The coupled blade-paddle equations of motion can be written as:

$$\begin{aligned} I_\beta^B\left[\ddot{\beta}^B+\Omega^2\beta^B\right]-\overline{S_\theta^B}\left[\ddot{\theta}^B+\Omega^2\theta^B\right] &= M_\beta^B \\ -\overline{S_\theta^B}\left[\ddot{\beta}^B+\Omega^2\beta^B\right]+I_\theta^B\left[\ddot{\theta}^B+\Omega^2\theta^B\right]+I_\beta^P\left[\ddot{\beta}^P+\Omega^2\beta^P\right] &= M_\theta^B+M_\beta^P \\ &\quad +\overline{S_\theta^P}\left[\ddot{\theta}^P+\Omega^2\theta^P\right] \end{aligned} \tag{4.7}$$

The aerodynamic pitching moment M_θ^B is expected to be small compared to the flapping moments on the blade (M_β^B) and on the paddle (M_β^P). It is seen that the paddle pitch θ^P appears as a forcing on the right hand side of the torsional moment equation.

In hover, the aerodynamic flapping moment on the blade is given by

$$M_\beta^B = \frac{1}{2}\rho_{air} c C_{l\alpha} \left[\theta^B \Omega^2 \frac{R^4}{4} - v_i \Omega \frac{R^3}{3} - \dot{\beta}^B \Omega \frac{R^4}{4}\right] \tag{4.8}$$

where R is the blade radius, and v_i is the induced velocity of the rotor. The aerodynamic flapping moment on the paddle is given by

$$M_\beta^P = \frac{1}{2}\rho_{air} c C_{l\alpha} \left[\theta^P \Omega^2 \frac{(R_o^4 - R_i^4)}{4} - v_i \Omega \frac{(R_o^3 - R_i^3)}{3} - \dot{\beta}^P \Omega \frac{(R_o^4 - R_i^4)}{4}\right] \tag{4.9}$$

It is assumed that the pitching moment coefficient is constant over the range of angles of attack below stall. This yields the blade pitching moment as

$$M_\theta^B = \frac{1}{6}\rho_{air} c^2 C_m \Omega^2 R^3 \tag{4.10}$$

The coupled blade and paddle equations (Eqs. 4.7) can be non-dimensionalized with respect to the rotor revolution and blade parameters. This yields the non-dimensional flapping moment equation as

$$\overset{**}{\beta}{}^B + \frac{\gamma^B}{8}\overset{*}{\beta}{}^B + \beta^B - S_1 \overset{**}{\theta}{}^B - \left[S_1 + \frac{\gamma^B}{8}\right]\theta^B = -\frac{\gamma^B}{6}\lambda_i \tag{4.11}$$

And the non-dimensional torsional moment equation as

$$\begin{aligned}-S_2\left[\overset{**}{\beta}{}^B + \beta^B\right] + I'\left[\overset{**}{\theta}{}^B + \theta^B\right] + \overset{**}{\beta}{}^P + \frac{\gamma^P}{8}(r_o^4 - r_i^4)\overset{*}{\beta}{}^P + \beta^P \\ = S_3\left[\overset{**}{\theta}{}^P + \theta^P\right] + \frac{\gamma^P}{8}(r_o^4 - r_i^4)\theta^P - \frac{\gamma^P \lambda_i}{6}(r_o^3 - r_i^3) + \frac{\gamma^P C_m c}{6 C_{l\alpha R}}\end{aligned} \tag{4.12}$$

where the Lock number of the blade and paddle respectively are defined as

$$\gamma^B = \frac{\rho_{air} c C_{l\alpha} R^4}{I_\beta^B} \tag{4.13}$$

$$\gamma^P = \frac{\rho_{air} c C_{l\alpha} R^4}{I_\beta^P} \tag{4.14}$$

$$\tag{4.15}$$

and the other constants are defined as

$$r_o = \frac{R_o}{R} \tag{4.16}$$

$$r_i = \frac{R_i}{R} \tag{4.17}$$

$$I' = \frac{I_\theta^B}{I_\beta^P} \tag{4.18}$$

$$S_1 = \frac{\overline{S_\theta^B}}{I_\beta^B} \tag{4.19}$$

$$S_2 = \frac{\overline{S_\theta^B}}{I_\beta^P} \tag{4.20}$$

$$S_3 = \frac{\overline{S_\theta^P}}{I_\beta^P} \tag{4.21}$$

The substitution $\theta^B = \beta^P$ was not made in the above equations to account for the 90 degree phase difference between paddle flap and blade pitch. Grouping several terms together results in a more compact set of coupled equations:

$$\overset{**}{\beta}{}^B + K_1\overset{*}{\beta}{}^B + \beta^B - S_1\overset{**}{\theta}{}^B - (S_1 + K_1)\theta^B = M_1 \tag{4.22}$$

$$-S_2\left[\overset{**}{\beta}{}^B + \beta^B\right] + I'\left[\overset{**}{\theta}{}^B + \theta^B\right] + \overset{**}{\beta}{}^P + K_2\overset{*}{\beta}{}^P + \beta^P = M_2 + (K_2 + S_3)\theta^P + S_3\overset{**}{\theta}{}^P \tag{4.23}$$

where

$$M_1 = -\frac{\gamma^B}{6}\lambda_i \tag{4.24}$$

$$M_2 = -\frac{\gamma^P(r_o^3 - r_i^3)\lambda_i}{6} + \frac{\gamma^P C_m c}{6C_{l\alpha}R} \tag{4.25}$$

$$K_1 = \frac{\gamma^B}{8} \tag{4.26}$$

$$K_2 = \frac{\gamma^P(r_o^4 - r_i^4)}{8} \tag{4.27}$$

The goal is to find the effect of small changes in paddle pitch on the blade flap and blade pitch. For this purpose, the inflow is assumed to remain constant, which is justified for small changes in blade pitch angle. Therefore, this approach yields a linearized estimate of the effectiveness of the paddle pitch control input. The same effect can be obtained by deriving the perturbation equations from the flapping and torsional moment equations.

The substitution method is used to find the control effectiveness. The paddle pitch input is assumed as

$$\theta^P = \theta_o^P + \theta_{1c}^P \cos\psi \tag{4.28}$$

Where the phase of the input is taken to be zero. The blade flap and blade pitch response are assumed to be

$$\beta^B = \beta_o^B + \beta_{1c}^B \cos\psi + \beta_{1s}^B \sin_\psi \tag{4.29}$$

$$\theta^B = \theta_o^B + \theta_{1c}^B \cos\psi + \theta_{1s}^B \sin_\psi \tag{4.30}$$

Due to the mechanical coupling between the paddle and the blade, the paddle flap response is

$$\beta^P = \theta_o^B - \theta_{1s}^B \cos\psi + \theta_{1c}^B \sin_\psi \tag{4.31}$$

The assumed input and responses are substituted in the coupled system equations (Eqs. 4.23) and the steady terms, coefficients of cosine terms and coefficients of sine terms are equated.

Equating the steady terms gives the set of equations

$$\beta_o^B - (S_1 + K_1)\theta_o^B = M_1 \tag{4.32}$$

$$-S_2\beta_o^B + (I' + 1)\theta_o^B = (S_3 + K_2)\theta_o^P + M_2 \tag{4.33}$$

From which we get the expressions for steady blade pitch and steady blade flap as

$$\beta_o^B = M_1 + (S_1 + K_1)\theta_o^B \tag{4.34}$$

$$\theta_o^B = \frac{(S_3 + K_2)\theta_o^P + S_2 M_1 + M_2}{I' + 1 - S_2 K_1 - S_2 S_1} \tag{4.35}$$

Recalling the assumption of constant inflow, the effectiveness of the steady paddle pitch control input in creating a steady blade pitch is given by

$$\frac{\Delta\theta_o^B}{\Delta\theta_o^P} = \frac{S_3 + K_2}{I' + 1 - S_2K_1 - S_2S_1} \tag{4.36}$$

And the effectiveness of the steady paddle pitch control input in creating a steady blade flap is given by

$$\frac{\Delta\beta_o^B}{\Delta\theta_o^P} = \frac{(K_1 + S_1)(S_3 + K_2)}{I' + 1 - S_2K_1 - S_2S_1} \tag{4.37}$$

Equating the coefficients of the cosine terms and sine terms yields

$$\beta_{1s}^B = \theta_{1c}^B \tag{4.38}$$

$$\theta_{1c}^B = \theta_{1c}^P \tag{4.39}$$

$$\beta_{1c}^b = 0 \tag{4.40}$$

$$\theta_{1s}^B = 0 \tag{4.41}$$

The result that $\theta_{1s}^B = 0$ is as expected because of the assumption of zero hinge offset and the purely longitudinal paddle pitch input. From these equations, we get the effectiveness of the cyclic paddle pitch inputs.

$$\frac{\Delta\theta_{1c}^B}{\Delta\theta_{1c}^P} = 1 \tag{4.42}$$

$$\frac{\Delta\theta_{1s}^B}{\Delta\theta_{1c}^P} = 0 \tag{4.43}$$

$$\frac{\Delta\beta_{1c}^B}{\Delta\theta_{1c}^P} = 0 \tag{4.44}$$

$$\frac{\Delta\beta_{1s}^B}{\Delta\theta_{1c}^P} = 1 \tag{4.45}$$

These slopes are compared to the sloped obtained from the 3 DOFs analysis from Chapter 3 and from the experiments. Figure. 4.44 shows the blade static pitch vs. the paddle static pitch in case B' for the experiments, the 3 DOFs analysis and the simplified analysis. Figure. 4.45 shows the blade dynamic pitch vs. the paddle dynamic pitch in case B' for the experiments, the 3 DOFs analysis and the simplified analysis. The static slope for the simplified model described above is of 0.28. The dynamic slope for the simplified model described above is of 1.

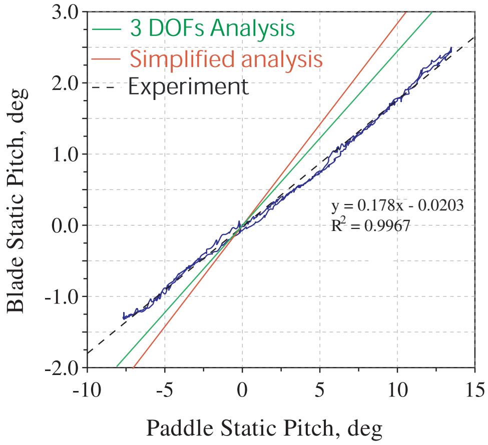

Figure 4.44: Case B', results of the blade static pitch vs. the paddle static pitch for the 3 DOFs analysis of Chapter 3, the simplified model of Chapter 4 and the experiments.

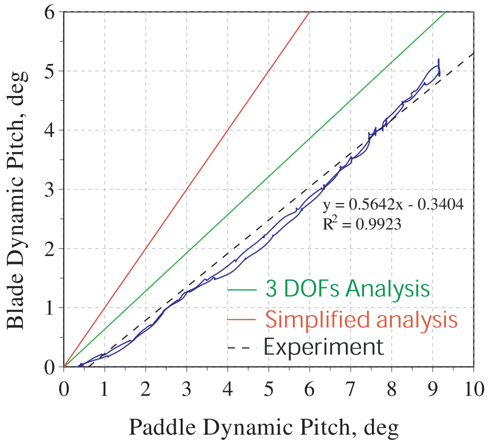

Figure 4.45: Case B', results of the blade dynamic pitch vs. the paddle dynamic pitch for the 3 DOFs analysis of Chapter 3, the simplified model of Chapter 4 and the experiments.

Comparison of the slopes predicted by the simplified analysis and the 3 DOF analysis for both the static and dynamic cases confirms the trends predicted by the 3DOFs analysis and the unreliability of the experimental data. The lower slope of the 3DOF model is due to the inclusion of effects such as hinge offset, CG offset and unsteady aerodynamics. The closer agreement of the dynamic results than the static results is further indicative of large amounts of friction in the rotor hinges, because the dynamic friction coefficient is lower than the static friction coefficient. This can also be seen in the plots of the test data shown above, for example, the large amounts of hysteresis demonstrated by the blade flap response is indicative of hinge friction. The experimental data is determined to be unreliable because:

1. The RC-blades used to make paddles included holes and fillings. These holes were drilled and filled with lead by the manufacturer to ensure static moments within a pair of blades were identical. These holes were randomly drilled along the chord and span of the blades. In addition, two pairs of blades did not feature the same number of holes nor the same holes location. Hence, characteristics of the paddles made from the RC-blades were not precisely known and varied from paddle to paddle.
2. Bushings on the flap and pitch axes of all paddles and blades generated dramatic amount of friction.
3. Blades and paddles were not tracked.
4. Several sensors stopped functioning in case B': a potentiometer measuring a paddle pitch angle, a potentiometer measuring a blade pitch angle and a potentiometer measuring a blade flap angle.

The discrepancies observed between the simplified model and the 3 DOF analysis show the importance of considering hinge offset, CG offset and unsteady aerodynamics.

4.3 Conclusion

The novel coupled blade-paddle control concept was initially tested on a modified model RC helicopter. These flight tests proved the concept of achieving primary control using a coupled blade-paddle system. Qualitative observations by the pilot indicated good control authority in hovering flight even in the presence of strong crossed winds.

A model scale two-bladed rotor system was designed and fabricated for hover testings. The blades and paddles were constructed using commercially available model helicopter blades. The system was equipped with sensors to measure blade and paddle pitch and flap angles. To ensure the system did not enter ground resonance, the load balance was replaced by a dummy balance which did not allow for hub loads measurements. Hover testings were performed on two configurations. Testings were severely constrained by vibrations of the rotor system due to dramatic friction in the hinges as well as untracked rotor blades. For a paddle of span equal to 40% of the blade radius, with a paddle dynamic pitch of 9°, a blade dynamic pitch of 5° was obtained.

Ecureuil characteristics were input into the 4 DOF analysis, described in Chapter 3. Several cases were evaluated using this approach. Transfer functions of the responses to a given unit voltage applied to the PZT actuator were obtained. The steady and 1/rev components were extracted from the transfer functions. When a flapping motion for instance was considered, the frequency obtained by the numerical 4 DOF model was in close agreement with the frequency obtained from a simplified analysis based on first principles. The 4 DOF model proved the effect of paddle radial location and mass on the rotor responses. The outputs indicated which parameters have an effect on the performances. The influence of aerodynamic load could be observed in terms of damping. Since the PZT actuator has not yet been defined, the magnitude of the responses is informative and indicates the relative performances of different configurations. These relative magnitudes provided useful guidelines to chose the geometrical parameters for the hover experiments.

The 3 DOF analysis was then compared to blade pitch measured in hover stand experiments. Three readings were not available for the case B' as two pitch sensors and one flap sensor stopped functioning because of dramatic friction and vibrations.

Several discrepancies were observed between the 3 DOF analysis and the experiments. The experimental results exhibited hysteresis and significant non linearity due to friction in the hinges. So a simplified model was developed to assess the accuracy of the trends indicated by the 3 DOF analysis. This simplified model assumed quasi-steady aerodynamics, neglected hinge offsets and assumed the center of gravity of the blades and paddles lies on their respective feathering axis. The simplified analysis verified the trends predicted by the 3 DOF code by indicating the effects of including hinge offset, CG offset and unsteady aerodynamics, and highlighting the effects of friction in the experimental results. Hence, it was concluded that it was needed to repeat the experiments with a carefully designed rotor minimizing friction and well defined rotor parameters. Moreover, if dynamic inflow is used in the analytical model, it is possible the 3 DOF model and the experiments would show better agreement.

Chapter 5

Summary, conclusions and planned activities

Des études analytiques et expérimentales ont été menées pour étudier le comportement d'un nouveau concept de rotor réalisant la commande des pales sans l'aide de plateaux cycliques. Ce concept est appelé le "Rotor Vert". Les angles de pas cyclique et collectif de chaque pale sont commandés par une palette et son aileron, actionné par un actionneur piezo-électrique. Les exigences de conception sont définies comme suit : le rotor comporte deux pales afin de garder la complexité du système à un minimum, le diamètre rotor est de $1,8$ *m pour s'adapter à l'installation où les essais sont menés et afin d'éviter une résonance sol et des effets de plafond. Dans la présente étude, la palette et son aileron sont situés à* 90° *d'azimut avant par rapport à la pale. L'aileron, situé derrière le bord de fuite de la palette, commande le pas de la palette. Un couplage mécanique lie le pas de la pale et le battement de la palette. L'angle de pas de l'aileron est commandé par un actionneur intelligent, ce qui crée une portance sur l'aileron qui génère un moment en pas autour de l'axe de pas de la palette. L'angle de pas de la palette varie donc et son angle de battement change de par une variation de la force aérodynamique à laquelle la palette est soumise. Grâce au couplage mécanique mentionné ci-dessus, l'angle de pas de la pale change. La commande du rotor principal est alors réalisée. Le rotor a été conçu de telle façon que pour* 1° *de battement de palette, l'angle de pas de la pale varie de* 1°*. Une telle conception devrait présenter des avantages significatifs : la réduction de la traînée parasite et du poids, une diminution du nombre de pièces mobiles et donc de la complexité mécanique et des coûts de maintenance. Les palettes devraient améliorer la stabilité du rotor comme une barre de Hiller. La palette et son aileron sont situés à proximité de l'axe de rotation rotor. Ils sont donc soumis à une moindre charge centrifuge que les gouvernes habituelles, tels les servo-flaps de Kaman. La conception des pales reste identique aux configurations classiques, les coûts de développement devraient être plus bas que dans d'autres études sans plateaux cycliques impliquant des gouvernes incluses dans la pale. Un autre avantage du présent concept est la réduction de la consommation de carburant. Ses coûts d'exploitation et d'acquisition devraient être plus faibles que dans le cas d'un hélicoptère classique équipé de plateaux cycliques. Le "Rotor Vert" pourrait présenter deux inconvénients: la palette et son aileron pourraient générer une traînée parasite qui diminuerait la Figure de Merit. Toutefois, ceci ne pourra pas contrecarrer les effets positifs sur la traînée qu'implique l'élimination du plateau cyclique. D'autre part, dans des conditions de vol avant, la palette et son aileron pourraient opérer dans la région d'écoulement* *inversé. Cela pourrait diminuer leur efficacité. Toutefois, cette question n'est pas abordée dans la présente étude puisque seule la condition de vol stationnaire est considérée.*

Un hélicoptère RC est utilisé pour effectuer un test en vol en plein air. Le rotor d'hélicoptère est modifié pour inclure le couplage battement de la palette-pas de la pale. Les palettes sont actionnées par un petit plateau cyclique afin que le design soit aussi simple que possible. Le rotor a un diamètre de 1.853 *m. Il a été observé que l'hélicoptère était stable dans ces conditions et qu'il pouvait voler en stationnaire avec succès et à plusieurs reprises. Les essais en vol ont servi à prouver la faisabilité du concept à petite échelle. Cependant, la maquette testée en vol n'étant pas équipée de capteurs, ces essais n'ont pas fourni de données quantitatives.*

Deux études analytiques sont présentées. Tout d'abord, un modèle analytique (analyse {Palette, Aileron, Pale}) comprenant quatre degrés de liberté est développé pour étudier le comportement dynamique du système décrit ci-dessus. Les degrés de liberté sont le battement et le pas de la pale, le pas de la palette et le pas de l'aileron. La théorie de Theodorsen est utilisée pour calculer les efforts aérodynamiques. L'analyse comprend également la fonction de Theodorsen qui offre la possibilité de rendre compte des écoulements instationnaires. Des études préliminaires sont réalisées en utilisant une aérodynamique quasi-stable, pour étudier l'effet de certains paramètres géométriques de la palette sur les réponses rotor. Cette étude a fourni des orientations quant au choix des paramètres expérimentaux. Une seconde analyse est développée (analyse {Palette, Pale}). Ce modèle analytique est identique au premier à l'exclusion de l'actionnement de la palette: au lieu de commander le pas de la palette via un aileron commandé par un actionneur PZT, le pas de la palette est commandé en utilisant un petit plateau cyclique. Cette méthode compte trois degrés de liberté: le pas et battement de la pale et le pas de la palette. Le couplage mécanique du battement de la palette au pas de la pale est identique au premier modèle analytique. Cette seconde configuration reflète le système étudié lors de tests en vol stationnaire. Le développement et les tests d'une palette actionnée par plateau cyclique sont en effet moins coûteux et plus sûrs que si un actionneur piezo-électrique est utilisé. Les essais sur une configuration {palette, pale} permettent de vérifier et quantifier l'influence de la palette sur la pale. L'objectif de ce modèle est d'étudier les effets de divers paramètres de commande et de la géométrie du système sur le comportement du mécanisme en vol stationnaire stable.

Des tests en vol stationnaire sont effectués sur un banc rotor principal sur une configuration similaire: un rotor de diamètre de $1,87$ *m équipé de deux pales, deux palettes qui sont actionnées par de petits plateaux cycliques et un couplage liant les angles de battement de la palette et de pas de pale. Plusieurs paires de palettes sont fabriquées à partir de pales disponibles sur étagères, leur inertie et envergure sont modifiées. L'inertie est modifiée en incorporant des masses de plomb en saumon de palette sur son axe de pas. L'envergure est modifiée en coupant une partie du matériau superflu. L'emplacement radial de la palette est un autre paramètre qui est changé par l'utilisation de manchons de palettes de longueurs différentes. Plusieurs capteurs sont utilisés pour recueillir des données afin de valider l'analyse:*

un potentiomètre rotatif est monté sur chaque axe de pas et de battement des pales et palettes. Ils mesurent les angles de battement et de pas. Un capteur Hall est utilisé pour mesurer la vitesse de rotation du rotor. Une balance six axes devait être utilisée pour mesurer les forces et moments au moyeu. Cela aurait permis le calcul de la Figure de Merit du présent système et la comparaison avec l'efficacité des configurations conventionnelles. Toutefois, le rotor a été soumis à une résonance sol et des vibrations. En raison de ces problèmes, la balance n'a pas été utilisée.

Le problème des vibrations mentionné ci-dessus a été causé par l'utilisation de bagues autolubrifiantes en bronze sur chaque axe de pas et de battement des palettes et pales. Sous l'influence de la force centrifuge, les bagues en bronze ont créé des frottements importants qui ont empêché les pales et palettes de répondre de façon voulue. Un balourd était alors observé sur le rotor. De plus, les pales et palettes n'étaient pas alignées. Les pales, à partir desquelles les palettes ont été fabriquées, comprenaient le long de leur corde et envergure des cavités comblées par des poids non référencés. Les caractéristiques d'une palette n'étaient donc pas connues précisément et variaient de palette en palette. Il a été observé que la quantité de vibrations n'est pas reproductible suivant les essais et les montées en régime. Certains tests ont montré peu de vibrations, particulirement lorsque du lubrifiant était ajouté dans les bagues en bronze. Deux séries de palettes ont été testées avec succès. La dernière, d'une envergure de $0,374$ *m et d'un emplacement radial de mi-envergure de* $0,467$ *m, a montré une réponse en pas de pale satisfaisante. A cause des vibrations importantes du rotor, trois capteurs ont cessé de fonctionner après le premier test. Le nombre de mesures initialement prévues pour valider l'analyse {Palette, Pale} s'en est donc trouvé réduit. Des expériences supplémentaires n'ont pu être réalisées pour raison de coûts.*

Une validation de l'analyse {Palette, Pale} a été effectuée en utilisant les données expérimentales des tests en vol stationnaire. Les expériences reproduisent qualitativement les tendances prédites par l'analyse. Un pas cyclique de pale de 5 degrés a été obtenu pour un pas cyclique de palette de 9 degrés. Des différences entre l'approche {Palette, Pale} et les expéciences ont été observées. Elles sont dûes aux importants frottements sur les axes de pas et battement du rotor. Une méthode simplifiée a été conçue pour évaluer la précision de l'analyse {Palette, Pale}. L'approche simplifiée suppose des termes aérodynamiques quasi-constants, néglige les excentricités, suppose un flux constant et un centre de gravité des pales et des palettes se trouvant sur leur axe respectif de pas. Comme prévu, le modèle simplifié fournit des réponses plus élevées que celles obtenues par l'expérience ainsi que par l'analyse {Palette, Pale}. Cela montre l'importance de tenir compte des excentricités, de la position du centre de gravité des pales et palettes et des termes aérodynamiques instationnaires dans le calcul des réponses rotor. De plus, une bonne corrélation entre le modèle simplifié et l'analyse {Palette, Pale} fournie une indication supplémentaire que les données expérimentales ne sont pas fiables. Le manque de données expérimentales précises a été attribué aux raisons détaillées ci-dessus, à savoir des niveaux importants de vibrations subit par le rotor et de sévères frottements sur les axes de pas et battement des pales et palettes.

En conclusion, la faisabilité du nouveau concept de rotor sans plateaux cycliques a été démontrée sur un modèle d'échelle réduite par des essais en vol sur une maquette de modélisme modifiée. La faisabilité du concept a également été constatée par des essais au banc rotor principal sur une maquette d'échelle réduite équipée de capteurs. Cependant comme mentionné ci-dessus, des frottements importants sur les axes de pas et de battement limitent les réponses du rotor. En dépit de ces frottements, une réponse dynamique de pas de pale de 5 degrés a été obtenue pour un pas de de palette dynamique de 9 degrés et montre donc que le concept est viable pour effectuer la commande du rotor. Une corrélation entre l'approche {Palette, Pale}, le modèle simplifié et les expériences a été observée. L'examen des donnés expérimentales indique qu'il est nécessaire de renouveler les expériences avec un rotor soigneusement conçu afin de minimiser les frottements, et des paramètres rotor bien définis. Ces expériences sont essentielles avant une validation plus poussée de l'analyse et une évaluation du concept de couplage pas de pale-battement de palette.

Les travaux futurs devront d'abord inclure le remplacement des bagues autolubrifiantes en bronze sur la maquette expérimentale par des roulements à billes et des butées à billes sur les axes de battement et de pas de chaque pale et palette. Cela devrait réduire considérablement les vibrations subies par le rotor et permettre l'utilisation de la balance à six axes. Par conséquent, des tests complémentaires en stationnaire sur un banc rotor principal pourront être réalisés sur le rotor à échelle réduite afin de recueillir des données supplémentaires pour la validation de l'étude analytique. Le comportement du "Rotor Vert" simplifié doit être étudié de la même façon dans des conditions de vol avant. Par conséquent, le modèle à échelle réduite devra être testé dans une soufflerie. En se basant sur les tests en vol stationnaire et en soufflerie, la Figure de Merit d'une telle configuration pourra être déterminée et comparée à celle d'une conception classique comportant des plateaux cycliques assurant la commande du pas collectif et cyclique des pales.

Si les étapes précédentes sont couronnées de succès, l'adaptation à un hélicoptère d'échelle un pourra débuter. Des études numériques devront être effectuées pour intégrer les caractéristiques de la gamme Ecureuil, telles que les butées sphériques qui pourraient être étudiées en utilisant la méthode des éléments finis. Ceci afin d'obtenir une représentation plus précise du système. L'Ecureuil comptant plus de deux pales, un choix de configuration rotor devra être fait: soit les palettes et les ailerons seront situés dans un autre plan que les pales du rotor principal, soit les palettes et ailerons seront situés sur le même plan que les pales mais à un angle d'azimut de moins de 90°. L'influence d'un angle d'azimut réduit entre une pale et sa palette devra être investiguée analytiquement. Le comportement dynamique et les réponses de la configuration à l'échelle un devront être étudiés. L'étape suivante comprendra le choix d'un mécanisme d'actionnement reposant sur des actionneurs piézo-céramiques. Ce mécanisme fera l'objet d'essais à l'échelle un en vol stationnaire et en soufflerie, d'une palette et de son aileron actionné par matériaux *intelligents. Les données ainsi obtenues seront utilisées pour valider l'étude analytique du système à l'échelle un. Un régulateur devra être développé avant la mise en application d'un tel système sur un hélicoptère à l'échelle un en vue d'un premier vol. Le développement d'un tel régulateur pourra se heurter à quelques difficultés. En vol avant, le comportement du rotor est en effet régi par un système d'équations différentielles comportant des coefficients variant périodiquement. Ces coefficients doivent être identifiés et mis en forme avant de les intégrer au régulateur. De plus, les pales d'un hélicoptère ne sont jamais identiques. Ces dissimilarités engendrent des composantes de contrainte non idéales, telles que en 1/rev et en harmoniques de la vitesse de rotation rotor. Si le rotor n'est pas équilibré, la composante en 1/rev est beaucoup plus importante que les composantes des harmoniques plus élevées. Il peut être alors difficile de mesurer ces dernières et d'en tenir compte dans le régulateur. Par ailleurs, le régulateur devra d'abord être développé en boucle ouverte et ensuite en boucle fermée. Des capteurs seront alors nécessaires pour mesurer les réponses du rotor devant être transmises au régulateur.*

Recently, there has been considerable interest in the development of a swashplateless rotor system to decrease drag, decrease maintenance time and increase reliability. The present research describes analytical and experimental studies carried out to investigate the behavior of a novel swashplateless rotor concept, called the green rotor. In this concept, both the blade cyclic and collective pitch angles are controlled by a servopaddle. The servopaddle itself is free to pitch about its feathering axis and its pitch angle is controlled with an aileron with an embedded PZT actuator. In this manner, the rotor achieves swashplateless primary flight control. The design requirements are defined as:

1. A two bladed rotor to keep the complexity of the system to the minimum.
2. A 1.8 m rotor diameter to fit the test facility and avoid ground and ceiling effects.

In the present study, the paddle and aileron are situated 90° forward of azimuth with respect to the blade. The aileron, located behind the paddle trailing edge, controls the paddle pitch motion. A mechanical linkage couples the blade pitch and paddle flap motions. The smart actuator makes the aileron deflect, thereby creating a lift which generates a pitch moment around the paddle pitch axis. The paddle thus pitches and its flap angle varies due to a change in the aerodynamic load it experiences. Since the paddle flap and blade pitch angles are coupled, the blade pitch angle varies.

The rotor primary control is then achieved. The rotor was designed in such a way that for 1° of paddle flap, the blade pitched of 1°. Such a design is expected to yield significant benefits:

1. A reduction in the aircraft parasitic drag and weight,
2. A decrease in the number of moving parts and hence in the mechanical complexity and maintenance costs.
3. The paddles are expected to improve rotor stability much as a Hiller bar.
4. The paddle and aileron are located close to the rotor rotation axis. Therefore they experience less centrifugal load than common control surfaces, such as Kaman's servo-flap.
5. The blade design remains identical to conventional designs. Hence, development costs are expected to be lower than in other swashplateless designs involving on-blade control surfaces and actuation.
6. A reduction in fuel consumption. Hence its operating and acquisition costs should be lower than in the case of a conventional helicopter equipped with a swashplate.

The green rotor could come across two drawbacks:

1. The paddle and aileron generate a profile drag which decreases the Figure of Merit. However, it will not counteract the positive effect the elimination of the swashplate has on the drag.
2. In forward flight conditions, the paddle and aileron might operate in the reversed flow region. This could impede their efficiency. However, this issue is not addressed in the present study as only hover flight condition is considered.

An off the shelf RC helicopter is used to perform outdoor flight tests. The helicopter rotor is modified to include the paddle flap-blade pitch coupling arm. The paddles are actuated by a small swashplate to keep the design as simple as possible. The rotor diameter is of 1.853 m. The helicopter proved to be stable under these conditions and hover was achieved successfully and repeatedly. Qualitative feedback from the pilots indicated that the coupled paddle-blade rotor control system was responsive, stable and resulted in a helicopter with flying qualities as good as or better than that with a conventional swashplate controlled rotor. Therefore, these flight tests demonstrated proof-of-concept on a reduced scale model rotor system. However, the flight tests were not instrumented and did not yield quantitative data.

Two analytical studies are presented. First, a four degree-of-freedom analytical model (4 DOF analysis) is developed to study the dynamic behavior of the system described above. The degrees-of-freedom are the blade flap, the coupled blade pitch and paddle flap, the paddle pitch and the aileron pitch. Theodorsen's theory is used to compute the aerodynamic components. The analysis also includes Theodorsen's function which offers the possibility to account for unsteady airloads. Preliminary trade studies are performed using the analysis with quasi-steady aerodynamics, to investigate the effect of paddle span, paddle radial location and paddle mass. A second analysis, which counts three degrees-of-freedom (3 DOFs), is developed. This analytical model is identical to the first one except for the paddle actuation: instead of controlling the paddle pitch via a PZT-actuated aileron, it is achieved using a small swashplate. The mechanical linkage coupling the paddle flap and blade pitch angles is identical to the first analytical study. The system features three degrees of freedom: the blade flap and pitch and the paddle pitch. This configuration is investigated to later perform hover stand tests. A swashplate actuated paddle is indeed cheaper and safer to develop and test than a piezoelectric-actuated one. Tests on a {paddle, blade} configuration permits to check and quantify the paddle control authority on the blade. The goal of this model is to study the effects of various control settings and system geometry on the system behavior during steady hover flight. The 4 DOF analytical model is used to perform preliminary trade studies on the rotor geometry. For example, moving the paddle outboard resulted in a decrease in coupled response due to the increased centrifugal loads, similarly an increase in paddle mass resulted in a decrease in coupled response. These trade studies indicated which parameters dominated the behavior of the rotor system, and provided guidelines in the choice of appropriate experimental configurations for the hover tests.

Hover stand tests are performed on a configuration similar to the RC model helicopter flight tests: a 1.87 m diameter rotor equipped with two blades, two paddles (which are actuated by a small swashplate) and a coupling arm linking the paddle flap and blade pitch angles. Several pairs of paddles are manufactured from off-the-shelf blades to modify their inertia and span. The inertia is altered by incorporating lead weights on the outboard side of the paddle on its feathering axis. The span is changed by cutting off any extra material. The paddle radial location is another parameter that is varied by means of paddle grips of different length. Several sensors are used to gather data to validate the analysis:

1. Two rotary potentiometers are mounted on each blade and paddle. They measure the flap and pitch angles.
2. A Hall sensor is used to measure the rotational speed of the rotor.
3. A six-axes balance was to be used to measure hub forces and moments.

> This would have allowed for the computation of the Figure of Merit and hence permit an efficiency comparison with conventional designs. However, the rotor experienced ground resonance and vibrations. Because of these issues the balance was not used.

The vibration problem mentioned above was caused by self lubricated bronze bushings used on each flap and pitch axes. Under the influence of centrifugal load, the bronze bushings created significant friction which prevented blades and paddles alike to flap and pitch in a desired fashion. The spinning rotor could then become unbalanced due to differences in flap and pitch between different blades. In addition, the blades and paddles were found to be untracked. The RC-blades used to make paddles included holes and fillings. These holes were drilled and filled with lead by the manufacturer to ensure static moments within a pair of blades were identical. These holes were randomly drilled along the chord and span of the blades. In addition, two pairs of blades did not feature the same number of holes nor the same holes location. Hence, characteristics of the paddles made from the RC-blades were not precisely known and varied from paddle to paddle. The amount of vibration was not found to be repeatable. Some tests showed little vibration, especially if lubricant had been added in the bronze bushings. However, centrifugal forces resulted in the expulsion of this lubricant as the rotor was spinning during the test. Two sets of paddles were tested. The latter, of a 0.56 m span and 0.467m mid span radial location, showed some blade pitch reponse. Because of the excessive amount of vibration, three sensors stopped functioning after the first test. Because of this, there were less measurements to correlate the 3 DOF analysis than desired. Further experiments could not be performed due to lack of funding.

Validation of the 3DOF analysis was performed using experimental data from the hover stand tests. The experiments qualitatively reproduced the trends predicted by the analysis. A blade cyclic pitch of 5 degrees was obtained for a paddle cyclic pitch of 9 degrees. Some discrepancies were noted between the 3DOF analysis and the the experiments. This was attributed to the poor track of the rotor and the large amount of friction in the hinges. The discrepancy was noted to be larger in the case of the static results which further indicated the presence of excessive friction in the hinges. A simplified model was developed to assess the accuracy of the 3 DOF analysis. The 3 DOF analysis will reduce to the simplified analysis when we assume quasi-steady aerodynamics, neglect hinge offsets, assume constant uniform inflow and assume the center of gravity of the blades and paddles lies on their respective feathering axis. As expected, the simplified model indicated significantly higher response than the experiment as well as the 3DOF analysis. This indicated the importance of considering effects such as hinge offset, CG offset and unsteady aerodynamics in the calculation of rotor response. In addition, the fair correlation of the simplified model and the 3DOF analysis provided further proof that the experimental data was unreliable. The lack of accurate experimental data was attributed to the reasons detailed above, namely unacceptable levels of vibration in the rotor and severe friction in the hinges. Moreover, if dynamic inflow is used in the analytical model, it is possible the 3 DOF model and the experiments would show better agreement.

In conclusion, proof-of-concept of the novel swashplateless rotor concept was demonstrated on a reduced scale model by means of flight tests on a RC model helicopter. The concept was further verified by means of tests on an instrumented, reduced scale model on a hover stand, however severe friction in the rotor hinges limited the response. In spite of the friction, a dynamic blade pitch response of 5 deg was obtained indicating the feasibility of the concept for swashplateless primary control. A fair correlation between a 3DOF numerical model, a simplified first-principles based analysis and experiments was observed. Examination of the experimental data indicates that it is necessary to repeat the experiments with a carefully designed rotor minimizing friction and well documented rotor parameters. These experiments are essential before further validation of the analysis and assessment of the blade-paddle coupled concept. In addition, the analysis can be further refined.

Future work will first involve the replacements of the bronze bushings on the experimental model by ball bearings and thrust bearings on each blade and paddle flap and pitch axes. This should reduced greatly the vibrations encountered by the rotor and permits the use of the six-axes balance. Hence, further hover stand tests could be performed on the small scale rotor to gather further data for analytical validation. It should be noted that blades and paddles characteristics must be known precisely. Once the hover stand tests results are correlated to the analysis, wind tunnel tests must be performed on the same configuration. These wind tunnel tests will provide further data to refine the analysis by adding the forward flight condition to the study. Based on the hover stand and wind tunnel tests, the propulsive efficiency of such a design should be determined and compared to that of a conventional design involving direct blade pitch control by a swashplate.

If previous steps have been successful, full scale adaptation will start. Numerical studies will have to be performed to incorporate Ecureuil characteristics such as the spherical thrust bearings which could be studied using FEM. Since the Ecureuil counts more than two blades, a choice will have to be made whether the paddles and ailerons will be located on a different plane from the main rotor blades or the paddles and aileron will be located on the same plane as the blades but at an azimuth angle lesser than 90°. The influence of a lesser azimuth angle between a blade and its paddle will have to be investigated analytically. The dynamic behavior and the responses of the full scale configuration will have to be studied. The next step will involve the selection of a piezoceramic actuation mechanism. The PZT actuation system is difficult to apply to small scale and cannot be easily scaled-up. Hence, testing of a full scale paddle and PZT-actuated aileron in a hover stand and wind tunnel will be needed. This data will be used to validate the aforementioned full scale analytical study. A controller will have to be developed before implementing such a system on a full scale helicopter in view of a first flight test. The development of such a controller will involve some issues that need to be carefully addressed. In forward flight, the rotor behavior is represented by a system of differential equations that include periodic coefficients. These coefficients must be identified and transmitted in the right format to the controller. Furthermore, helicopter blades are never identical. Hence, non ideal components of forcing appear, such as components at 1/rev or harmonics of the rotor RPM. If the rotor is unbalanced, the 1/rev component is much larger than higher components. Thus, it can become difficult to measure higher harmonics to transmit them to the controller. First, an open loop controller will have to be developed. A closed loop controller will finally be studied and will require sensors to measure rotor responses to be transmitted to the controller.

Bibliography

[1] J.G. Leishman. *Principles of Helicopter Aerodynamics.* Cambridge University Press, 2006.

[2] U.W.E Arnold, D. Fuerst, T. Neuheuser, and R. Bartels. Development of an integrated electrical swashplateless primary and individual blade control system. Virginia Beach, VA, USA, May 2007. American Helicopter Society 63rd Annual Forum.

[3] O. Dieterich. Application of modern control technology for advanced ibc systems. Marseille, France, September 1998. 24^{th} European Rotorcraft Forum.

[4] O. Dieterich, B. Enenkl, and D. Roth. Trailing-edge flaps for active rotor control aeroelastic characteristics of the adasys rotor system. Phoenix, AZ, USA, May 2006. American Helicopter Society 62nd Annual Forum.

[5] D. Roth, B. Enenkl, and O. Dieterich. Active rotor control by flaps for vibration reduction - full scale demonstrator and first flight test results -. Maastricht, The Netherlands, September 2006. 32^{nd} European Rotorcraft Forum.

[6] A. P. F. Bernhard, J. O'Neill, F. Kohlhepp, W. Welsh, and P. Lorber. Active Rotor Control (ARC) of a mach-scale trailing edge flap rotor. *Presented at the American Helicopter Society 57th Annual Forum, Washington DC*, May 9-11 2001.

[7] A.P.F. Bernhard and J. Wong. Wind tunnel evaluation of a sikorsky active rotor controller implemented on the nasa/army/mit active twist rotor. *Journal of the American Helicopter Society*, 50(1):65–80, January 2005.

[8] F.K. Straub. Active flap control for vibration reduction and performance improvement. Fort Worth, TX, USA, 1995. American Helicopter Society 51st Annual Forum.

[9] F.K. Straub and A.A. Hassan. Aeromechanic considerations in the design of a rotor with smart materials actuated trailing-edge flap.

Washington D.C, USA, June 1996. American Helicopter Society 52nd Annual Forum.

[10] P. Crozier. Analytical method to determine dynamic loads on reduced scale helicopter blades at onera. 29^{th} European Rotorcraft Forum, September 2003.

[11] R.A. Ormiston and M.V. Fulton. Aeroelastic and dynamic rotor response with on-blade elevon control. Marseilles, France, September 1998. 24th European Rotorcraft Forum.

[12] J. Shen and I. Chopra. A parametric design study for a swashplateless helicopter rotor with trailing-edge flaps. Montral, Canada, June 2002. American Helicopter Society, 58th Annual Forum.

[13] T. Theodorsen. General theory of aerodynamic instability and the mechanism of flutter. Technical Report 496, NASA, 1935.

[14] T. Theodorsen and L.E. Garrick. Mechanism of flutter a theoretical and experimental investigation of the flutter problem. Technical Report 685, NASA, 1940.

[15] T. Theodorsen and Garrick L.E. Nonstaionary flow about a wing-aileron-tab combination including aerodynamic balance. Technical Report 736, NASA, 1942.

[16] S. Jr Hiller and J. III Stuart. Us patent 2,481,750, September 1949.

[17] S. Jr Hiller and H. H. Sigler. Us patent 2,534,353, December 1950.

[18] W.F. Alex and G.A. McCoubrey. Design and structural features of the SH-2F composite main rotor blade. Washington, D.C., USA, June 1986. American Helicopter Society 42nd Annual Forum.

[19] J. Shen. *Comprehensive Aeroelastic Analysis of Helicopter Rotor with Trailing-Edge Flap for Primary Control and Vibration Control.* PhD thesis, University of Maryland, College Park, MD 20742, USA, 2003.

[20] Kaman's "proof of principle" mmira is formally introduced. Helicopter News, February 1992.

[21] C.H. Kaman. Aircraft of rotary wing type. u.s. patent 2,455,866, December 1948.

[22] R.W. Prouty. *Helicopter Performance, Stability and Control.* PWS Engineering, 1986.

[23] V. Hrishikeshavan, J. Sirohi, M. Tishchenko, and I. Chopra. Design and stability of a shrouded rotor micro air vehicle with anti-torque vanes. Chandler, Arizona, January 2007. AHS International Specialists' Meeting on Unmanned Rotorcraft.

[24] A. Brindejonc. Hélicoptère muni d'une plurarité d'éléments sustentateurs pourvu d'un volet pour commander l'incidence de ses pales. Patent: FR 0801077, February 2008.

[25] C. D'Ascanio. U.s. patent 1,960,141, May 1934.

[26] F.S. Wei and R. Jones. Correlation and analysis for $sh - 2f101$ rotor. *Journal of Aircraft*, 25(7):647–652, July 1988.

[27] A.Z. Lemnios and R. Jones. The servo flap-an advanced rotor control system. San Francisco, CA, USA, January 1990.

[28] F.S. Wei. Design of an integrated servo-flap main rotor. Phoenix, AZ, USA, May 2003. American Helicopter Society 59^{th} Annual Forum Proceedings.

[29] F.S. Wei. Design of soft in torsion rotor systems at kaman aerospace corporation. pages 1264–1273, Montreal, Canada, June 2002. American Helicopter Society 58^{th} Annual Forum Proceedings.

[30] R. Lacy. Aircraft design 2003 – 2004. In *Vertiflite*, volume Winter, pages 32–33. American Helicopter Society, 2004.

[31] F.S Wei and F. Gallagher. Servo-flap rotor performance flight testing and data identification. Washington, D.C., May 2001. American Helicopter Society 57^{th} Annual Forum Proceedings.

[32] B. Rocconella and F.S. Wei. Wind tunnel model testing of the improved k-max servo-flap blade section. Washington, D.C., May 2001. American Helicopter Society 57^{th} Annual Forum Proceedings.

[33] I. Chopra. Perspectives in aeromechanical stability of helicopter rotors. *Vertica*, 14(4):457–508, 1990.

[34] Z.A. Chaudhry, B.E. Wake, A. Bagai, P.F. Lorber, and A.J. Collins. Active rotor development for primary and secondary flight control. Grapevine, TX, USA, May 2009. American Helicopter Society 65^{th} Annual Forum.

[35] M. Bebesel, D. Roth, and R. Pongratz. Reduction of bvi noise on ground-in flight evaluation of closed-loop controller. Bristol, UK, September 2002. 28^{th} European Rotorcraft Forum.

[36] D. Roth. Advanced vibration reduction by ibc technology. Marseille, France, September. 30^{th} European Rotorcraft Forum.

[37] F. Toulmay, V. Kloppel, F. Lorin, B. Enenkl, and J. Gaffiero. Active blade flaps- the needs and current capabilities. Washington D.C, USA, 2001. American Helicopter Society 57^{th} forum.

[38] B. Enenkl, V. Kloeppel, D. Preissler, and P. Janker. Full scale rotor with piezoelectric actuated blade flaps. Bristol, UK, September 2002. 28^{th} European Rotorcraft Forum.

[39] M. Bebesel, E. Schoell, and G. Polz. Aerodynamic and aeroacoustic layout of atr (advanced technology rotor). Montreal, Canada, May 1999. 55^{th} American Helicopter Society Annual Forum.

[40] H. Glassel, J. Kahl, O. Dieterich, and S. Rudolph. Neural networks for bvi system identification. Friedrichshafen, Germany, September 2003. 29^{th} European Rotorcraft Forum.

[41] R.A. Ormiston. Aeroelastic considerations for rotorcraft primary control with on-blade elevons. Washington, D.C., USA, May 2001. American Helicopter Society 57^{th} Annual Forum.

[42] D. Schimke, P. Janker, V. Wendt, and B. Junker. Wind tunnel evaluation of a full scale piezoelectric flap control unit. Marseille, France, September 1997. 24^{th} European Rotorcraft Forum.

[43] N. Hasegawa, Y. andKatayama, N. Kobiki, E. Nakasato, E. Yamakawa, and H. Okawa. Experimental and analytical results of whirl tower test of atic full scale rotor system. Washington, D.C., May 2001. 57^{th} American Helicopter Society Annual Forum.

[44] M.N.H. Priems. Concept studies for a soft torsional rotor without swashplate. Master's thesis, Delft University of Technology, Delft, The Netherlands, June 2006.

[45] D. Schimke, P. Janker, A. Blaas, R. Kube, G. Schewe, and C. Kesser. Individual blade control by servo-flap and blade root control, a collaborative research and development programme. In 23^{rd} *European Rotorcraft Forum*, pages 46.1–46.16, Dresden, Germany, September 1997.

[46] D. Schimke, P. Janker, V. Wendt, and B. Junker. Wind tunnel evaluation of a full scale piezoelectric flap control unit. In 24^{th} *European Rotorcraft Forum*, Marseilles, France, September 1998. Paper TE-02.

[47] P. Janker, K. Kloppel, F. Hermle, T. Lorkowski, S. Storm, M. Christmann, and M. Wettemann. Development and evaluation of a hybrid piezoelectric actuator for advanced flap control technology. In 25^{th} *European Rotorcraft Forum*, Rome, Italy, September 1999. Paper G-21.

[48] R. Kube, B.G. Van der Wall, A. Buter, U. Ehlert, W. Geissler, M. Raffel, and G. Schewe. A multi concept approach for development of adaptive rotor systems. In *8th Army Research Office (ARO) workshop on the aeroelasticity of rotorcraft systems*, State College, PA, October 1999.

[49] T. Lorkowski, P. Janker, F. Hermle, , S. Storm, M. Christmann, and M. Wettemann. Development of a piezoelectrically actuated leading edge flap for dynamic stall delay. In *25th European Rotorcraft Forum*, Rome, Italy, September 1999.

[50] S.A. Jacklin, A. Haber, G. De Simone, T.R. Norman, and P. Shinoda. Full-scale wind tunnel test of an individual blade control system for a

uh-60 helicopter. Montreal, Canada, June 2002. American Helicopter Society 58th Annual Forum.

[51] A. Haber, S.A. Jacklin, and G. De Simone. Development, manufacturing, and component testing of an individual blade control system for a uh-60 helicopter rotor. San Francisco, CA, USA, January 2002. American Helicopter Society Aerodynamics, Acoustics, and Test and Evaluation Specialists Meeting.

[52] T. Neuheuser and U. Carl. Assesment of power consumption of helicopter flight control systems without swashplate. Toulouse, France, 2004. Recent Advances in Aerospace Actuation System and Components.

[53] F.K. Straub and R.J. King. Application of smart materials to helicopter rotor active control. In *SPIE symposium on smart structures and materials, conference on industrial and commercial applications of smart structures technologies*, pages 66–77, San Diego, CA, March 1996.

[54] F.K. Straub, M.A. Ealey, and M.L. Schetky. Application of smart materials to helicopter rotor active control. In *SPIE symposium on smart structures and materials, conference on industrial and commercial applications of smart structures technologies*, pages 99–113, February, CA, March 1997.

[55] F.K. Straub, H.T.N. Ngo, V. Anand, and D.B. Domzalski. Development of a piezoelectric actuator for trailing-edge flap control of rotor blades. In *SPIE symposium on smart structures and materials, conference on smart structures and integrated systems*, pages 2–13, Newport Beach, CA, March 1999.

[56] F.K. Straub and B.D. Charles. Comprehensive modeling of rotors with trailing edge flaps. In *55th American Helicopter Society Forum*, Montreal, Canada, May 1999.

[57] F.K. Straub. Development of a full scale smart rotor system. In *8th Army Research Office (ARO) workshop on the aeroelasticity of rotorcraft systems*, State College, PA, October 1999.

[58] F.K. Straub. Development of an active flap rotor. Ann Arbor, MI, USA, October 2001. 9th ARO International Conference on Aeroelasticity of Rotorcraft Systems.

[59] F.K. Straub, D.K. Kennedy, A.D. Stemple, V.R. Anand, and T.S. Birchette. Development and whirl tower test of the smart active flap rotor. San Diego, CA, USA, March 2004. SPIE's International Symposium on Smart Structures and Materials.

[60] F.K. Straub and D.K. Kennedy. Design, development, fabrication and testing of an active flap rotor system. Grapevine, TX, USA, June 2005. American Helicopter Society 61^{st} Annual Forum.

[61] F.K. Straub, V.R. Anand, T.S. Birchette, and B.H. Lau. Wind tunnel test of the smart active flap rotor. Grapevine, TX, USA, May 2009. American Helicopter Society 65^{th} Annual Forum.

[62] S.R. Hall, V.R. Anand, F.K. Straub, and Lau B.H. Active flap control of the smart rotor for vibration reduction. Grapevine, TX, USA, May 2009. American Helicopter Society 65^{th} Annual Forum.

[63] S. Kottapalli and F. Straub. Correlation of smart active flap rotor loads. Grapevine, TX, USA, May 2009. American Helicopter Society 65^{th} Annual Forum.

[64] F.K. Straub. Smart rotor technology developments - challenges and payoffs. In *The 12th International Conference on Adaptive Structures Technology*, University of Maryland, College Park, MD, October 2001.

[65] L. Taeoh and I. Chopra. Design and static testing of a trailing-edge flap actuator with piezostacks for a rotor blade. In *SPIE symposium on smart structures and materials, conference on smart structures and integrated systems*, pages 321–332, San Diego, CA, March 1998.

[66] L. Taeoh and I. Chopra. Development and validation of a refined piezostack-actuated trailing-edge flap actuator for a helicopter rotor. In *SPIE symposium on smart structures and materials, conference on smart structures and integrated systems*, Newport Beach, CA, March 1999.

[67] L. Taeoh. *Design of a High Displacement Smart Trailing-Edge Flap Actuator Incorporating Dual-Stage Mechanical Stroke Amplifier for Rotors*. PhD thesis, University of Maryland, 2000.

[68] D.A. Fink, T.J. Hawkey, M. Gaudreau, B. Wellman, and R.A. Ormiston. An electromagnetic actuator for individual blade control. *Presented at the American Helicopter Society 57th Annual Forum, Virginia Beach, Virginia*, May 2000.

[69] D.A. Fink, T.J. Hawkey, M. Gaudreau, B. Wellman, and R.A. Ormiston. An electromagnetic actuator for individual blade control. *AHS National Specialists' Meeting "Improving Rotorcraft Acceptance Through Active Controls Technology, Bridgeport, Connecticut*, October 2000.

[70] L.R. Centolanza and E.C. Smith. Design and experimental testing of an induced-shear piezoelectric actuator for rotor blade trailing edge flaps. In *41th AIAA/ASME/ASCE/AHS/ASC structures, structural dynamics and materials conference and AIAA/ASME/AHS adaptive structures forum*, Atlanta, GA, April 2000. Paper AIAA-2000-1713.

[71] A.E. Glazounov, Q.M. Zhang, and C. Kim. New torsional actuator based on shear piezoelectric response. In *SPIE symposium on smart structures and materials, conference on smart materials technologies*, pages 82–93, San Diego, CA, March 1998.

[72] M. Tarascio, M. Gervais, T. Gowen, J. Ma, K. Singh, G. Gopalan, K. Kleinhesselink, Y. Zhao, and I. Chopra. Raven SAR Rotorcaft. Technical report, Alfred Gessow Rotorcraft Center, University of Maryland, College Park, MD 20742, 2001. In response to the 2001 Annual AHS International Student Design Competition - Graduate Category.

[73] S. Dawson and F.K. Straub. Design, validation and testing of a model rotor with tip mounted active flaps. 1994.

[74] F.K. Straub. Active flap control for vibration reduction and performance improvement. Fort Worth, TX, USA, May 1995. American Helicopter Society 51^{st} Annual Forum.

[75] S. Dawson, A. Hassan, and F.K. Straub. Wind tunnel test of an active flap rotor: Bvi noise and vibration reduction. Fort Worth, 1995 1995. American Helicopter Society 51^{st} Annual Forum.

[76] C.C. Hennes and K. Brentner. Acoustics 2006. In *Vertiflite*, volume Winter, pages 33–34. American Helicopter Society, 2006.

[77] P. Leconte, M. Rapin, and B.G. Van Der Wall. Main rotor active flaps: Numerical assessment of vibration reduction. Washington D.C, USA, May 2001. American Helicopter Society 57^{th} forum.

[78] P. Leconte and H. Mercier des Rochettes. Experimental assessment of an active flap device. Montreal, Canada, May 2002. American Helicopter Society 58^{th} forum.

[79] P. Crozier, P. Leconte, Delrieux Y., B. Gimonet, A. Le Pape, and H. Mercier des Rochettes. Wind tunnel tests of a helicopter rotor with active flaps. Maastricht, The Netherlands, September 2006. 32^{nd} European Rotorcraft Forum.

[80] Y. Delrieux, A. Le Pape, P. Leconte, P. Crozier, B. Gimonet, and H. Mercier des Rochettes. Wind tunnel assessment of the concept of active flaps on a helicopter rotor. Virginia Beach, Virginia, USA, May 2007. American Helicopter Society 63^{rd} forum.

[81] H. Mainz, B.G. Van Der Wall, P. Leconte, F. Ternoy, and H. Mercier des Rochettes. Abc rotor blades: design, manufacturing and testing. Florence, Italy, September 2005. 31^{st} European Rotorcraft Forum.

[82] D. Feszty, F. Nitzsche, A. Mander, G. Coppotelli, F. Vetrano, J. Riemenschneider, and P. Wierach. Whirl tower demonstrations of

the sharcs hybrid control concept. Grapevine, TX, USA, May 2009. American Helicopter Society 65^{th} Annual Forum.

[83] R. Barrett, P. Frye, and M. Schliesman. Design, construction and characterization of a flightworthy piezoelectric solid state adaptive rotor. *Smart Materials and Structures*, 7(3), 1998.

[84] P.C. Chen. *Development of a smart rotor with induced-strain actuation of blade twist.* PhD thesis, University of Maryland, Aerospace Department, College Park, MD, 1996.

[85] P.C. Chen and I. Chopra. Hover test of a smart rotor with induced strain actuation of blade twist. *AIAA Journal*, 35(1):6–16, January 1997.

[86] P.C. Chen and I. Chopra. Wind tunnel test of a smart rotor model with individual blade twist control. *Journal of Intelligent Material Systems and Structures*, 8(5):414–425, May 1997.

[87] N.A. Koratkar. *Smart Helicopter Rotor with Piezoelectric Bender Actuated Trailing-Edge Flaps.* PhD thesis, University of Maryland, College Park, MD 20742, USA, 2000.

[88] A.A. Bent and N.W. Hagood. Anisotropic actuation with piezoelectric fiber composites. *Journal of Intelligent Material Systems and Structures*, 6(3):338–349, 1995.

[89] J.P. Rodgers and N.W. Hagood. Manufacture of adaptive composite plates incorporating piezoelectric fiber composite plies. In *36th AIAA/ASME/ASCE/AHS/ASC Structures, Structural Dynamics and Materials Conference and AIAA/ASME Adaptive Structures Forum*, pages 2824–2835, New Orleans, LA, April 1995.

[90] J.P. Rodgers, A.A. Bent, and N.W. Hagood. Characterization of interdigitated electrode piezoelectric fiber composites under high electrical and mechanical loading. In *SPIE symposium on smart structures and materials, conference on smart structures and integrated systems*, pages 642–659, San Diego, CA, March 1996.

[91] J.P. Rodgers. *Development of an Integral Twist-Actuated Rotor Blade For Individual Blade Control.* PhD thesis, Massachusetts Institute of Technology, Cambridge, MA 02139, USA, 1998.

[92] H.B. Strock, M.R. Pascucci, M.V. Parish, and A.A. Bent. Active pzt fibers: a commercial production process. In *SPIE symposium on smart structures and materials, conference on smart materials technologies*, pages 22–31, Newport Beach, CA, March 1999.

[93] M.L. Wilbur, P.H. Mirick, W.T. Yeager, W.L. Chester, C.E.S. Cesnik, and S. Shin. Vibratory loads reduction testing of the nasa/army/mit active twist rotor. *Journal of the American Helicopter Society*, 47(2), 2002.

[94] M.L. Wilbur and M.K. Sekula. The effect of tip geometry on active-twist rotor response. Firenze, Italy, September 2005. 31^{st} European Rotorcraft Forum.

[95] W. Keats Wilkie, M.L. Wilbur, P.H. Mirick, C.E.S. Cesnik, and S. Shin. Aeroelastic analysis of the NASA/ARMY/MIT active twist rotor. In *55th American Helicopter Society Forum*, Montreal, Canada, May 1999.

[96] C.E.S. Cesnik, S. Shin, W. Keats Wilkie, M.L. Wilbur, and P.H. Mirick. Modeling, design and testing of the NASA/ARMY/MIT active twist rotor prototype blade. In *55th American Helicopter Society Forum*, Montreal, Canada, May 1999.

[97] M.L. Wilbur, W. Keats Wilkie, W.T. Yeager, R.C. Lake, C. Langston, C.E.S. Cesnik, and S. Shin. Hover testing of the NASA/ARL/MIT active twist rotor. In *8th Army Research Office (ARO) workshop on the aeroelasticity of rotorcraft systems*, State College, PA, October 1999.

[98] M.L. Wilbur, W.T. Yeager Jr, W. Keats Wilkie, C.E.S. Cesnik, and S. Shin. Hover testing of the nasa/army/mit active twist rotor prototype blade. Virginia Beach, VA, USA, May 2000. American Helicopter Society 56^{th} Annual Forum,.

[99] R. Derham. The aeromechanics of (smart) active rotors. Atlanta, GA, USA, November 2000. American Helicopter Society Aeromechanics Specialists Meeting.

[100] Robert Derham, Douglas Weems, M. Bobby Mathew, and Richard Bussom. The design evolution of an active materials rotor. *Presented at the American Helicopter Society 57th Annual Forum, Washington DC*, May 9-11 2001.

[101] C. Walz and I. Chopra. Design and testing of a helicopter rotor model with smart trailing edge flaps. In *35th AIAA/ASME/ASCE/AHS/ASC structures, structural dynamics and materials conference and AIAA/ASME/AHS adaptive structures forum*, Hilton Head, SC, April 1994.

[102] O. Ben-Zeev and I. Chopra. Advances in the development of an intelligent helicopter rotor employing smart trailing edge flaps. *Smart Materials and Structures*, 5(1):11–25, February 1996.

[103] N.A. Koratkar and I. Chopra. Analysis and testing of a Froude scaled rotor with piezoelectric bender actuated trailing-edge flaps. *Journal of Intelligent Material Systems and Structures*, 8(7):555–70, July 1997.

[104] N.A. Koratkar and I. Chopra. Analysis and testing of a Mach scaled helicopter rotor in hover with piezoelectric bender actuated trailing-edge flaps. In *SPIE symposium on smart structures and materials,*

conference on smart structures and integrated systems, pages 266–290, San Diego, CA, March 1998.

[105] N.A. Koratkar and I. Chopra. Analysis and testing of a Mach scaled rotor model with piezoelectric bender actuated trailing-edge flaps. In *40th AIAA/ASME/ASCE/AHS/ASC structures, structural dynamics and materials conference and AIAA/ASME/AHS adaptive structures forum*, pages 2380–2402, St. Louis, MO, April 1999.

[106] N.A. Koratkar and I. Chopra. Design, fabrication and testing of a Mach scaled-rotor model with trailing edge flaps. In *55th American Helicopter Society Forum*, pages 558–578, Montreal, Canada, May 1999.

[107] N.A. Koratkar and I. Chopra. Hover testing of a Mach-scaled rotor with trailing-edge flaps. In *SPIE symposium on smart structures and materials, conference on smart structures and integrated systems*, Newport Beach, CA, March 2000.

[108] N.A. Koratkar and I. Chopra. Wind tunnel testing of a Mach-scaled rotor with trailing-edge flaps. In *56th American Helicopter Society Forum*, Virginia Beach, VA, May 2000.

[109] B. Roget. *Individual Blade Control for Vibration Reduction of a Helicopter with Dissimilar Blades.* PhD thesis, University of Maryland, College Park, MD 20742, USA, 2004.

[110] M.V. Fulton and R.A. Ormiston. Hover testing of a small-scale rotor with on-blade elevons. Virginia Beach, VA, USA, April-May 1997. American Helicopter Society 53^{rd} Annual Forum.

[111] M.V. Fulton and R.A. Ormiston. Small-scale rotor experiments with on-blade elevons to reduce blade vibratory loads in forward flight. Washington, D.C., May 1998. American Helicopter Society 54^{th} Annual Forum.

[112] M.V. Fulton. Analysis of an active rotor and comparison with small scale experimental data. In *8th Army Research Office (ARO) workshop on the aeroelasticity of rotorcraft systems*, State College, PA, October 1999.

[113] A.P.F. Bernhard. *Smart Helicopter Rotor with Active Blade Tips.* PhD thesis, University of Maryland, College Park, MD 20742 USA, February 2000.

[114] A.P.F. Bernhard and I. Chopra. Development of a smart moving blade tip activated by a piezo-induced bending-torsion coupled beam. In *SPIE symposium on smart structures and materials, conference on smart structures and integrated systems*, pages 63–79, San Diego, CA, February 1996.

[115] A.P.F. Bernhard and I. Chopra. Hover testing of an active rotor blade tip and structural analysis of the actuator beam. In *39th AIAA/ASME/ASCE/AHS/ASC structures, structural dynamics and materials conference and AIAA/ASME/AHS Adaptive structures forum*, pages 3299–3325, Longbeach, CA, April 1998.

[116] A.P.F. Bernhard and I. Chopra. Hover testing of active rotor blade-tips using a piezo-induced bending-torsion coupled beam. *Journal of Intelligent Material Systems and Structures*, 9(12):963–974, December 1998.

[117] M.G. Spencer, R.M. Sanner, and I. Chopra. An adaptive neurocontroller for vibration suppression and shape control of a flexible beam. *Journal of Intelligent Material Systems and Structures*, 9(3):160, 1998.

[118] M.G. Spencer, R.M. Sanner, and I. Chopra. Neurocontrol of simulated full scale rotor vibrations using trailing edge flaps. In *40th AIAA/ASME/ASCE/AHS/ASC structures, structural dynamics and materials conference and AIAA/ASME/AHS adaptive structures forum*, pages 2744–2752, St. Louis, MS, April 1999.

[119] M.G. Spencer. *Development of a real time adaptive neural network controller for active rotorcraft vibration reduction.* PhD thesis, University of Maryland, Aerospace Department, College Park, MD, March 2000.

[120] N. Koratkar. Wind tunnel testing of a smart rotor with trailing edge flaps. In *The 12th International Conference on Adaptive Structures Technology*, University of Maryland, College Park, MD, October 2001.

[121] C.M. Bothwell, R. Chandra, and I. Chopra. Torsional actuation with extension-torsional composite coupling and magnetostrictive actuators. *AIAA Journal*, 33(4):723–729, April 1995.

[122] A.J. Moskalik and D. Brei. Force-deflection behavior of piezoelectric c-block actuator arrays. *Smart Materials and Structures*, 8(5):531–543, October 1999.

[123] J.W. Clement, D. Brei, A.J. Moskalik, and R. Barrett. Bench-top characterization of an active rotor blade flap system incorporating c-block actuators. In *39th AIAA/ASME/ASCE/AHS/ASC structures, structural dynamics and materials conference and AIAA/ASME/AHS adaptive structures forum*, pages 2857–2869, Longbeach, CA, April 1998.

[124] J.W. Clement, D. Brei, and R. Barrett. Wind tunnel testing of a high authority, airspeed insensitive, rotor blade flap. In *40th AIAA/ASME/ASCE/AHS/ASC structures, structural dynamics and materials conference and AIAA/ASME/AHS adaptive structures forum*, pages 2414–2424, St. Louis, MO, April 1999.

[125] E.F. Prechtl and S.R. Hall. An x-frame actuator servo-flap actuation system for rotor control. In *SPIE symposium on smart structures and materials, conference on smart structures and integrated systems*, pages 309–320, San Diego, CA, March 1998.

[126] E.F. Prechtl and S.R. Hall. Design of a high efficiency, large stroke, electromechanical actuator. *Smart Materials and Structures*, 8(1):13–30, February 1999.

[127] E.F. Prechtl and S.R. Hall. Preliminary testing of a Mach-scaled active rotor blade with trailing-edge servo flap. In *SPIE symposium on smart structures and materials, conference on smart structures and integrated systems*, pages 14–21, Newport Beach, CA, March 1999.

[128] E.F. Prechtl and S.R. Hall. Hover testing of a Mach-scaled rotor with an active trailing edge flap. In *8th Army Research Office (ARO) workshop on the aeroelasticity of rotorcraft systems*, State College, PA, October 1999.

[129] E.F. Prechtl. Development of a piezoelectric servo-flap actuator for helicopter rotor control. Master's thesis, Massachusetts Institute of Technology, Cambridge, MA, USA, May 1994.

[130] E.F. Prechtl. *Design and Implementation of a Piezoelectric Servo-Flap Actuation System for Helicopter Rotor Individual Blade Control.* PhD thesis, Massachusetts Institute of Technology, Department of Aeronautics and Astronautics, Cambridge, MA, February 2000.

[131] I. Chopra. Status of application of smart structures technology to rotorcraft systems. *Journal of the American Helicopter Society*, 45(4):228–252, October 2000.

[132] I. Chopra. Review of current status of smart structures and integrated systems. *SPIE Smart Structures and Integrated Systems*, 2717:20–62, 1996.

[133] I. Chopra. Status of application of smart structures technology to rotorcraft systems. *Innovations in Rotorcraft Technology, Royal Aeronautical Society*, 2717:20–62, June 1997.

[134] I. Chopra. Review of state of art of smart strucutres and integrated systems. *AIAA journal*, 40(11):2145–2187, November 2002.

[135] D.J. Jendritza and H. Jonocha, editors. *Adaptronics and Smart Structures.* Springer Verlag GmbH, 1999.

[136] B.K. Wada, J.L. Fanson, and E.F. Crawley. Adaptive structures. *Journal of Intelligent Material Systems and Structures*, 1(2):157–174, April 1990.

[137] P.W. Stevens and E.C. Smith. Active interrogation of helicopter rotor faults using trailing edge flap actuation. *Presented at the American*

Helicopter Society 57th Annual Forum, Washington DC, May 9-11 2001.

[138] E.F. Crawley. Intelligent structures for aerospace: a technology overview and assessment. *AIAA Journal*, 32(8):1689–1699, August 1994.

[139] J. Sirohi. *Piezoelectric Hydraulic Hybrid Actuator for a Potential Smart Rotor Application.* PhD thesis, University of Maryland, College Park, MD 20742, USA, 2002.

[140] QuickPack actuators. Active Control eXperts, ACX.

[141] S. Yoshikawa, M. Farrell, D. Warkentin, R. Jacques, and E. Saarmaa. Monolithic piezoelectric actuators and vibration dampers with interdigitated electrodes. In *SPIE symposium on smart structures and materials, conference on smart structures and integrated systems*, pages 578–585, Newport Beach, CA, March 1999.

[142] M.W. Hooker. Properties and performance of RAINBOW piezoelectric actuator stacks. In *SPIE symposium on smart structures and materials, conference on industrial and commercial applications of smart structures technologies*, pages 413–420, San Diego, CA, March 1997.

[143] Thunder actuators. Face International Corporation, http://www.faceinternational.com, Norfolk, VA, 1999.

[144] K.M. Mossi and R.P. Bishop. Characterization of different types of high-performance THUNDER actuators. In *SPIE symposium on smart structures and materials, conference on smart materials technologies*, pages 43–52, Newport Beach, CA, March 1999.

[145] C.D. Near. Piezoelectric actuator technology. In *SPIE symposium on smart structures and materials, conference on smart structures and integrated systems*, pages 246–258, San Diego, CA, February 1996.

[146] *Piezoelectric Actuators and Ultrasonic Motors.* Kluwer Academic Publishers, Boston, 1997.

[147] *Piezoelectric Ceramics.* Academic Press Ltd, 1971.

[148] J. Epps and I. Chopra. Shape memory alloy actuators for in-flight tracking of helicopter rotor blades. *Smart Materials and Structures*, 10(1):104–111, 2001.

[149] J. Epps. *In-Flight Tracking of Helicopter Rotor Blades with Tabs Using Shape Memory Alloys.* PhD thesis, University of Maryland, College Park, MD 20742 USA, 2000.

[150] H. Prahlad and I. Chopra. Design of a variable twist tilt-rotor blade using shape memory alloy (SMA) actuators. In *Proceedings of SPIEs Annual Symposium on Smart Structures and Materials, Newport Beach, CA*, volume 4327, pages 46–59, 2001.

[151] J.N. Kudva, B.P. Sanders, J. Pinkerton-Florance, and E. Carcia. Overview of the darpa/afrl/nasa smart wing phase ii program. volume 4332, pages 383–389, Newport Beach, CA, USA, MArch 2001. Proceedings of the 8th SPIE Conference on Smart Structures and Materials: Industrial and Commercial Applications of Smart Structures Technologies.

[152] J.N. Kudva, C.A. Martin, L.B. Scherer, P.A. Jardine, A. Rivas McGowan, R.C. Lake, G.P. Sendeckyi, and B.P. Sanders. Overview of the darpa/afrl/nasa smart wing program. volume 3674, pages 230–236, Newport Beach, CA, USA, March 1999. Proceedings of the 6th SPIE Conference on Smart Structures and Materials: Industrial and Commercial Applications of Smart Structures Technologies.

[153] Product catalog. http://www.adaptamat.com/, Adaptamat Limited, Yrityspiha 5, FIN-00390 Helsinki, Finland, 2001.

[154] P.P. Friedmann. Rotary-wing aeroelasticity: Current status and future trends. *AIAA Journal*, 42(10):1953–1972, October 2004.

[155] J. Shaw, N. Albion, E.J. Hanker, and R.S. Teal. Higher harmonic control: Wind tunnel demonstration of fully effective vibratory hub forces suppression. *Journal of the American Helicopter Society*, 34(1):14–25, January 1989.

[156] K. Nguyen. *Higher Harmonic Control Analysis for Vibration Reduction of Helicopter Rotor Systems*. PhD thesis, University of Maryland, College Park, MD 20742, USA, 1989.

[157] F.S. Wei, J.P. Basile, and R. Jones. Vibration reduction on servo flap controlled rotor using hhc. Arlington, Texas, USA, November 1989. American Helicopter Society National Specialists Meeting on Rotorcraft Dynamics.

[158] R.P. Cheng, C.R. Theodore, and R. Celi. Effects of two/rev higherharmonic control on rotor performance. *Journal of the American Helicopter Society*, (1):18–27, January 2003.

[159] N.D. Ham. Helicopter individual-blade-control and its applications. St Louis, MO, USA, May 1983. American Helicopter Society 39^{th} Annual Forum Proceedings.

[160] P.P. Friedmann. Vibration reduction in rotorcraft using actively controlled flaps-from theoretical concept to flight ready hardware. American Helicopter Society 4th Decennial Specialists Conference on Aeromechanics, January 2004.

[161] D. Patt, L. Liu, and P.P Friedmann. Rotorcraft vibration reduction and noise prediction using a unified aeroelastic response simulation. *Journal of the American Helicopter Society*, 50(1):95–106, January 2005.

[162] J.S. Kim. *Design and Analysis of Rotor Systems with Multiple Trailing-Edge Flaps and Resonant Actuators.* PhD thesis, Pennsylvania State University, 2005.

[163] D.A Peters and C.J. He. Finite state induced flow models part ii: Three dimensional rotor disk. *Journal of Aicraft*, 32(2):323–333, 1995.

[164] D.A Peters, S. Karunamoorthy, and W. Cao. Finite state induced flow models part i: Two dimensional thin airfoil. *Journal of Aicraft*, 32(2):313–322, 1995.

[165] D.A Peters, D.D. Boyd, and C.J. He. Finite state induced flow model for rotor in hover and forward flight. *Journal of the American Helicopter Society*, 34(4):5–17, 1989.

[166] D.A Peters and C.J. He. A closed-form unsteady aerodynamic theory for lifting rotorsin hover and forward flight. Alexandria, VA, USA, May 1987. American Helicopter Society 43^{rd} Annual Forum.

[167] A. Bagai and J.G. Leishman. Rotor free-wake modeling using a pseudo-implicit technique- including comparisons with experimental data. *Journal of the American Helicopter Society*, 40(3):29–41, 1995.

[168] D. Petot. Differential equation modeling of dynamic stall. *La Recherche Aerospaciale*, 5:59–71, June 1989.

[169] J.G. Leishman and T.S. Beddoes. A generalized model for unsteady aerodynamic behavior and dynamic stall using indicial methods. *Journal of the American Helicopter Society*, 34(3):3–17, 1989.

[170] G. Bir and I. et. al. Chopra. *University of Maryland Advanced Rotor Code (UMARC) Theory Manual.* Center for Rotorcraft Education and Research, University of Maryland, College Park, MD, USA, 1994. UM-AERO 94-18.

[171] J. Milgram, I. Chopra, and F. Straub. A comprehensive rotorcraft aeroelastic analysis with trailing edge flap model: Validation with experimental data. Washington D.C, USA, June 1996. American Helicopter Society 52nd Annual Forum.

[172] J. Milgram and I. Chopra. A parametric design study for actively controlled trailing edge flaps. *Journal of the American Helicopter Society*, 43(2), 1998.

[173] J. Milgram, I. Chopra, and F.K. Straub. Rotors with trailing-edge flaps: Analysis and comparison with experimental data. *Journal of the American Helicopter Society*, 43(4):1603–1610, August 1998.

[174] Judah H. Milgram. *A comprehensive aeroelastic analysis of helicopter main rotors with trailing edge flaps for vibration reduction.* PhD thesis, University of Maryland, Aerospace Department, College Park, MD, January 1997.

[175] J. Shen and I. Chopra. Aeroelastic modeling of smart trailing-edge flaps with smart material actuators. Atlanta, GA, USA, April 2000. 41^{st} Structures, Strutural Dynamics and Materials Conference and Adaptive Structures.

[176] J. Shen and I. Chopra. Aeroelastic stability of smart trailing-edge flap helicopter rotors. Seattle, WA, USA, April 2001. 42^{nd} Structures, Strutural Dynamics and Materials Conference and Adaptive Structures.

[177] J. Shen and I. Chopra. Actuation requirements for a swashplateless helicopter control system with trailing-edge flaps. Denver, CO, USA, April 2002. 43^{rd} Structures, Strutural Dynamics and Materials Conference and Adaptive Structures.

[178] J. Shen and I. Chopra. Ultralight helicopter with trailing-edge flap for primary control. Tochigi, Japan, November 2002. Heli Japan.

[179] J. Shen, I. Chopra, and W. Johnson. Performance of swashplateless ultralight helicopter rotor with trailing edge flaps for primary flight control. American Helicopter Society, 59th Annual Forum, May 2003.

[180] J. Shen, M. Yang, and I. Chopra. Swashplateless helicopter rotor system with active trailing-edge flaps for primary and vibration controls. Palm Springs, CA, USA, April 2004. 45th AIAA/ASME/ASCE/AHS/ASC Structures, Structural Dynamics and Materials Conference,.

[181] J. Shen and I. Chopra. Swashplateless helicopter rotor with trailing-edge flaps. *Journal of Aircraft*, 41(2), March-April 2004.

[182] J. Shen and I. Chopra. Aeroelastic modeling of trailing-edge flap helicopter rotors including actuator dynamics. *Journal of Aircraft*, 41(6), November-December 2004.

[183] J. Shen, M. Yang, and I. Chopra. Swashplateless helicopter rotor with trailing-edge flaps for flight and vibration control. *Journal of Aircraft*, 43(2):346–352, March-April 2006.

[184] N. Hariharan and J.G. Leishman. Unsteady aerodynamics of a flapped airfoil in subsonic flow by indicial concepts. *Journal of Aircraft*, 5(33):855–868, September-October 1996.

[185] A.A. Hassan, F.K. Straub, and K.W. Noonan. Experimental/numerical evaluation of intergral trailing edge flaps for helicopter rotor applications. Virginia Beach, VA, USA, May 2000. American Helicopter Society, 56th Annual Forum.

[186] A.A. Hassan, F.K. Straub, and K.W. Noonan. Experimental/numerical evaluation of intergral trailing edge flaps for helicopter rotor applications. *Journal of the American Helicopter Society*, 50(1):3–18, January 2005.

[187] *Fluid-dynamic drag.* Hoerner, S.F., 1965.

[188] W. Johnson. Technology drivers in the development of camrad ii. San Francisco, CA, USA, January 1994. American Helicopter Society Aeromechanics Specialists Conference.

[189] H. Yeo. Assessment of active controls for rotor performance enhancement. *Journal of the American Helicopter Society*, 53(2):152–163, April 2008.

[190] L. Coulet. Definition of flying controls and servo-controls. Aerospatiale, Note Technique, June 1977.

[191] W. Johnson. *Helicopter Theory.* Dover, 1994.

[192] A. Brindejonc, F. Malburet, and P.A. Aubourg. Analysis of a swashplateless helicopter rotor with active servopaddles. Jacksonville, Florida, USA, August 2008. Fluids Engineering Division Summer Conference, American Society of Mechanical Engineers.

[193] A. Brindejonc and F. Malburet. Green swashplateless helicopter rotor. American Helicopter Society, May 2009.

[194] D.M. Pitt and D.A. Peters. Theoretical prediction of dynamic-inflow derivatives. *Vertica*, 5(1):21–34, 1981.

[195] *Bramwell's Helicopter Dynamics.* American Institute of Aeronautics and Astronautics, June 2001.

ETUDE D’UN ROTOR D’HELICOPTERE SANS PLATEAU CYCLIQUE AVEC DES SERVOPADDLES ACTIVES

RESUME: Cette thèse présente la conception, la fabrication et l'étude analytique d'un nouveau concept basé sur la barre de Hiller pour réaliser la commande du rotor sans plateau cyclique. Les pales sont couplées à des palettes. Un aileron, commandé par des actionneurs piezo-électriques, est situé derrière le bord de fuite de chaque palette. L'aileron est incliné par l’actionneur, et génère ainsi une portance. Le moment en pas de la palette change ainsi que le pas, la portance et le battement de la palette. L'angle de battement de la palette et l'angle de pas de la pale étant couplés, ce dernier varie. Chaque ensemble {pale palette aileron} est indépendant d'un autre. La palette peut donc générer du pas collectif et cyclique en entrée de la pale. Comparé aux rotors conventionnels, un tel système présente divers avantages tels la réduction de la complexité mécanique, de la traînée et du poids. La consommation en fuel de l'hélicoptère devrait donc décroître fortement et la disponibilité de l’aéronef augmenter. Un hélicoptère de modélisme a été piloté en milieu extérieur et sert à valider le concept de couplage. Le système a pu maintenir un vol stationnaire stable malgré la présence de vent. Une analyse comprenant la dynamique de l'aileron et quatre degrés de liberté est développée pour évaluer le comportement dynamique et apprécier la faisabilité d'un tel concept de rotor sans plateau cyclique. L'analyse est utilisée pour investiguer l'effet des paramètres du système sur l'influence que la palette et l'aileron peuvent exercer sur la pale. Des tests en stationnaire ont été réalisés sur un banc rotor principal qui représente un environnement plus maîtrisé. Le but de ces tests est de valider l'étude théorique et d'évaluer l'effet de différentes variables de conception sur la réponse en pas de la pale. Pour ce faire, le système est équipé de capteurs. Dans le cas des essais en vol comme au banc rotor principal, la commande en pas de la palette est réalisé par de petits plateaux cycliques assurant une conception rapide, simple et peu coûteuse. Le reste du système est inchangé. Pour une palette d'envergure égale à 40% du rayon de la pale, avec un pas cyclique de 9°, un angle de pas cyclique de pale de 5° a été obtenu.

Mots-clés: *Commande, Rotor, Hélicoptère, Sans Plateau Cyclique, Servopaddles actives*

STUDY OF A SWASHPLATELESS HELICOPTER ROTOR WITH ACTIVE SERVOPADDLES

ABSTRACT: This thesis presents the design, fabrication, testing and analytical study of a novel concept of actively controlled Hiller type servopaddle to achieve rotor primary control. The blades on the swashplateless rotor are coupled to a servopaddle equipped with a piezo electrically actuated aileron located behind the paddle trailing edge. The aileron is deflected because of the actuator and generates a lift. This leads to a variation of the paddle pitch moment, as well as of the paddle pitch and lift. Hence, a change in paddle flap and in blade pitch via a mechanical linkage is created. The system {blade, paddle, aileron} is independent from any other {blade, paddle, aileron} assembly. Thus, the active servopaddle can generate both cyclic and collective inputs. Such a system presents the advantage of reduced mechanical complexity, parasitic drag and weight. The fuel consumption of the aircraft is thus expected to significantly decrease and its availability to increase. A small scale RC helicopter has been flown outdoor and served as a proof of concept. The system showed good hover capability under windy and non predictable conditions. A four degree-of-freedom analysis including aileron dynamics has been developed to predict the dynamic behavior and assess the feasibility of such a swashplateless rotor. The analysis is used to investigate the effect of system parameters on the blade control authority. Hover stand tests are performed in a more controlled environment. The aim of these tests is to validate the theory and to investigate the effects of different design variables on the blade pitch response. To this end, the system is equipped with sensors. In the case of both the outdoor and hover stand tests, the paddle actuation is achieved by a small swashplate to ensure a quick, affordable and simple design. The rest of design remains the same as described earlier. For a paddle of span equal to 40% of the blade radius, with a cyclic pitch input of 9°, a 5° blade cyclic pitch output was observed.

Keywords: *Primary Control, Swashplateless, Helicopter Rotor, Active Servopaddles*

ARTS
ET MÉTIERS
ParisTech